

ABSTRACT

Title of Dissertation: **ANALYZING THE STAR FORMATION EFFICIENCY
AND PHYSICAL CONDITIONS OF THE
MOLECULAR GAS IN NEARBY GALAXIES**

Vicente Antonio Villanueva Llanos
Doctor of Philosophy, 2023

Dissertation Directed by: **Dr. Alberto D. Bolatto
Dr. Stuart N. Vogel
Department of Astronomy, University of Maryland**

Star formation activity plays a key role in driving galaxy evolution, and it depends on the amount of cold gas available (as traced by CO emission) and on the physical conditions and dynamical state of this gas. This work focuses on investigating the star formation efficiency of the gas, both molecular and total, as a function of local and global galaxy properties. The galaxy samples studied in this thesis are representative of the nearby universe, and we use a combination of interferometric CO observations and integral field unit optical spectroscopy for most of our analyses.

First, we show that in a sample of galaxies dominated by “field galaxies” the disk scale lengths for the molecular and stellar components are very similar, reflecting the close relation between CO emission and star formation activity. Our analysis of the radial dependence of the star formation efficiency of the total gas on morphological, structural, and dynamical properties of the galaxies shows that there is a smooth, continuous exponential decline with increasing

radius and a systematic increase in the average star formation efficiency from early to late type galaxies. Our results also show a morphological dependence of the efficiency per orbital time, which may reflect star formation quenching due to the presence of a bulge.

Next, we test the impact of environmental processes on galaxies immersed in the rich environment of the Virgo cluster. We show that in these galaxies the CO emission is more centrally concentrated than the stars, unlike what we saw in the field. Moreover, in the central regions of galaxies with an increasing level of perturbation (as determined by the morphology and kinematics of their atomic gas emission), the mean molecular-to-atomic gas ratio increases while the star formation efficiency of the molecular gas in the same region decreases. This demonstrates that the cluster environment not only affects the outskirts of galaxy disks and their atomic gas, but deeply changes the distribution and efficiency of the centrally located molecular gas component.

Finally, we study the onset of star formation cessation in galaxies (“quenching”) by investigating a complete sample of galaxies spanning from the main sequence (normal star forming objects) to the green valley (galaxies which are starting to quench) to the red cloud (galaxies that are mostly quiescent, that is, “red and dead” objects). We find that the star formation activity and the molecular gas-to-stellar mass ratio track each other. We also note that green valley galaxies have lower molecular star formation efficiencies than galaxies on the main sequence. On average, we find that within the bulges of green valley galaxies the molecular gas star formation efficiency is lower than in the bulges of main sequence galaxies. Also in green valley galaxies, we find that the molecular gas to stellar ratio, the molecular gas star formation efficiency, and the specific star formation rate all increase with increasing distance to the center. Our results suggest that gas depletion or removal does not fully explain the star-formation quenching in galaxies transiting through the green valley, and that a reduction in star formation efficiency is also required during

this stage. This is reminiscent of the so-called “morphological quenching.”

ANALYZING THE STAR FORMATION EFFICIENCY AND PHYSICAL
CONDITIONS OF THE MOLECULAR GAS IN NEARBY GALAXIES

by

Vicente Antonio Villanueva Llanos

Dissertation submitted to the Faculty of the Graduate School of the
University of Maryland, College Park in partial fulfillment
of the requirements for the degree of
Doctor of Philosophy
2023

Advisory Committee:

Professor Alberto D. Bolatto, Chair/Advisor
Professor Stuart N. Vogel, Co-Advisor
Professor Sylvain Veilleux, Committee Member
Professor Adam K. Leroy, External Member
Professor Ricardo C. Araneda, Dean's Representative

© Copyright by
Vicente Villanueva
2023

Preface

The work presented in this thesis has been published or under collaboration review. The research in Chapter 2 is published in *The Astrophysical Journal* as “The EDGE-CALIFA Survey: The Resolved Star Formation Efficiency and Local Physical Conditions” [1]. This work has been presented in several conferences and meeting, including the *SOCHIAS XVII Annual Meeting 2022, Chile* and *SM 2021: Structure, characteristic scales, and star formation, Beirut* (both virtual). The work in Chapter 3 is also published in *The Astrophysical Journal* as “VERTICO.IV. Environmental Effects on the Gas Distribution and Star Formation Efficiency of Virgo Cluster Spirals” [2], and was presented in the meeting *Our Galactic Ecosystem: Opportunities and Diagnostics in the Infrared and Beyond* in Los Angeles, USA. Finally, Chapter 4 is currently undergoing the revision of the EDGE collaboration and will be submitted to *The Astrophysical Journal* shortly as “The EDGE-CALIFA survey: Molecular Gas and Star Formation Activity Across the Green Valley”. Also, during my PhD I have had the opportunity to contribute actively as a co-author of at least 12 publication by the EDGE¹ and VERTICO² collaborations.

¹<https://www.astro.umd.edu/EDGE/>

²<https://www.verticosurvey.com/>

¿Qué era el hombre?

¿En qué parte de su conversación abierta,

entre los almacenes y los silbidos,

en cuál de sus movimientos metálicos,

vivía lo indestructible,

lo imperecedero,

la vida?

–“La Poderosa Muerte,” Pablo Neruda, Los Jaivas

Dedication

To my parents,

who never let me down and always encouraged

my passion for astronomy along this journey.

Acknowledgments

The time I spent in graduate school was a period of an overwhelming personal and professional enrichment, but it also represented the culmination of a long journey that I started almost 17 years ago. Throughout this path, I had the chance to meet inspiring and kindness people from all around the world, with who I built up either a meaningful friendship or a prolific scientific collaboration. Although most of them are still part of my life, I do not want to leave behind those who at some point also gave me their confidence and motivation to pursue in this field (even though our pathways had split apart).

I want to thank my advisors, Alberto Bolatto and Stuart Vogel. I will be eternally grateful for giving me the opportunity to work with you. From you I have learnt not only to boost my research skills but also to emphasise the importance of neatness and rigorous. Thank you so much for your patience, dedication, for sharing your vast knowledge in radioastronomy with me, but mainly for the lessons that both of you gave me even beyond astronomy.

To my defense committee members, Sylvain Veilleux, Adam Leroy, and Ricardo Araneda. To Sylvain, for our valuable talks about AGNs, but also for his kindness and support during our experience together teaching ASTR101. To Adam Leroy, for being part of my “Astronomy Mount Rushmore” of my heroes in extragalactic research; without his outstanding research and inspiration I took from his work this thesis would not have been possible. To Ricardo Araneda, for his kindness and being a good example of the scientist I want to become some day. Thanks

for hosting me during my first years at Maryland and for taking the time to read my thesis. To all of them: it is a real honor to have you as part of my defense committee.

To all the members of the galaxy-research group fellows and LMA people along my time at UMD: Laura, Rye, Serena, Jialu, Peter, among others. Special thanks to Liz Tarantino, Becca Levy, Ramsey Karim, Milena Crnogorčević, Julian Marohnic, and Jegug Ih for your company and our experiences together. Your friendship and research skills helped me to cope with the toughest part of grad life. To Maitraiye Tiwari, for your friendship and support during the once in a lifetime pandemic.

To all my closest grad classmates and roomies: Tomás, Teal, Umisha, Sergio, Johnny, Ben, Erica, Calvin, Joe, among others. Thank you for being so kind and for the amazing time hanging out around the DMV area, at camping, or wherever.

A mis padres, María Llanos y Julio Villanueva: De ustedes aprendí que la rigurosidad, responsabilidad, y el trabajo duro finalmente traen frutos. Gracias por haberme dado la oportunidad (dentro de sus posibilidades) de poder elegir el camino que quería seguir. A mis hermanos Bárbara, Joaquín, María Ignacia, Agustín, y también a abuelita María y Hector Ortiz, por entregarme su cariño y soporte a lo largo de toda mi vida.

A mis amigos y compañeros de vida, especialmente a Ivania Mijic por haber estado tan cerca durante estos años a pesar de la distancia. A David Ramirez, Marcelo Calderón y Carola Gacitúa, por su valiosa amistad a lo largo de mi vida. A Natalia Calderón y a toda su familia, por creer en mi cuando daba mis primeros pasos en la astronomía. A Tati Perez, Alex Ortiz, Leo Silva, Memo Retamales y Miguel Fernández. Un fraterno agradecimiento a Diego Hurtado-Torres por su apoyo y amistad durante mis años en USA.

A pesar de que ya no todos caminen a mi lado, de alguna manera cada uno de ellos forma

parte de mi.

Gracias a cada uno de ustedes.

Table of Contents

Preface	ii
Foreword	iii
Dedication	iv
Acknowledgements	v
Table of Contents	viii
List of Tables	xi
List of Figures	xiii
List of Abbreviations	xxiv
Chapter 1: Introduction	1
1.1 The baryon cycle	1
1.2 Galaxies and morphology	4
1.3 The connection between star formation, molecular/atomic hydrogen, and carbon monoxide	7
1.4 Radio and mm/submm telescopes	10
1.4.1 The VLA telescope	13
1.4.2 The CARMA telescope	14
1.4.3 The ALMA telescope	15
1.5 The star-formation activity in the local Universe	17
1.6 Main aims of this thesis	20
Chapter 2: The EDGE-CALIFA Survey: The Resolved Star Formation Efficiency and Local Physical Conditions	25
2.1 Introduction	25
2.2 Data products	28
2.2.1 The EDGE and CALIFA surveys	28
2.2.2 edge_pydb database	29
2.3 Methods	30
2.3.1 Stacking of the CO spectra	30
2.3.2 Extracting fluxes from stacked spectra	33

2.3.3	Basic equations and assumptions	35
2.4	Results and Discussion	40
2.4.1	Exponential scale lengths	40
2.4.2	SFE and Local Parameters	43
2.5	Summary and conclusions	67
Chapter 3: VERTICO.IV. Environmental Effects on the Gas Distribution and Star Formation Efficiency of Virgo Cluster Spirals		71
3.1	Introduction	71
3.2	Data products	75
3.2.1	The VERTICO Survey	77
3.2.2	Ancillary Data and Data Selection	78
3.3	Methods	80
3.3.1	Stacking of the CO Spectra	80
3.3.2	Basic Equations and Assumptions	84
3.3.3	CO Radial Profiles	88
3.4	Results and Discussion	90
3.4.1	Scale Lengths and Environment	90
3.4.2	Effective Radii and Environment	93
3.4.3	R_{mol} , SFE, and Environment	94
3.5	Summary and conclusions	109
Chapter 4: The EDGE-CALIFA survey: Molecular Gas and Star Formation Activity Across the Green Valley		113
4.1	Introduction	113
4.2	OBSERVATIONS	116
4.2.1	The ACA EDGE sample	116
4.2.2	The CO data	119
4.2.3	Data reduction and products	123
4.2.4	The CALIFA survey and ancillary data	127
4.3	Methods and products	128
4.3.1	Basic equations and assumptions	128
4.3.2	Radial profiles	131
4.3.3	Bulge radii and masses	134
4.4	Results and Discussion	136
4.4.1	Global quantities and relations	136
4.4.2	Spatially resolved relations	141
4.5	Summary and conclusions	154
Chapter 5: Conclusions & Future Work		158
5.1	About the Star-formation Efficiency in EDGE-CALIFA galaxies	158
5.2	About galaxy cluster environmental effects in VERTICO galaxies	159
5.3	About the Star Formation Activity in ACA EDGE galaxies	162
5.4	Future projects	165

Appendix A: Emission line intensity, velocity, and peak-SNR maps for ACA EDGE galaxies	168
Appendix B: Facilities and Software used in this Thesis	177
B.0.1 Facilities	177
B.0.2 Software	177
Bibliography	179
Bibliography	179

List of Tables

2.1	Main properties of the 81 EDGE-CALIFA galaxies analyzed in this work. The columns Distance, M_* , Morphological Class, and M_{mol} are taken from [3], where M_{mol} is computed using $\alpha_{\text{CO}} = 4.36 M_{\odot} (\text{K km s}^{-1} \text{ pc}^2)^{-1}$. The column Nuclear corresponds to the emission-line diagnostic for the optical nucleus spectrum for CALIFA galaxies by [4], who classify the galaxies (with signal-to-noise larger than three) into star forming (SF), active galactic nuclei (AGN), and LINER-type galaxies. The columns l_* , l_{mol} , $R_{50,*}$, and $R_{50,\text{mol}}$ are the exponential scale lengths and the radii that enclose 50% of the molecular gas and the stellar mass computed in Section 4.4.1.2, respectively.	51
3.1	Main properties of the 38 VERTICO galaxies analyzed in this work. The columns are (1) galaxy name; (2) HI-Class from [5]; (3) logarithm of the total molecular gas mass derived as explained in Section 4.4.1.2; (4) logarithm of the total stellar mass derived as explained in Section 3.4.2; (5) exponential scale length of the molecular gas; (6) exponential scale length of the stars; (7) effective radius of the molecular gas; (8) effective radius of the stars.	95
3.2	Median and 1σ scatter values of the mass and star formation rate distributions for the galaxy groups in column (1). The columns are: (2) logarithm of the median stellar mass; (3) logarithm of median molecular gas mass; (4) logarithm of median atomic gas mass; from Class 0 to Class IV, atomic gas masses are taken from [6]; (5) logarithm of total median star formation rate; (6) logarithm of total molecular gas mass derived from the $M_{\text{mol}}-M_*$ relation for main sequence xGASS-CO galaxies by [7], using the stellar mass from column (2); (7) logarithm of total atomic gas mass derived similarly as in column (6); (8) logarithm of the total molecular-to-stellar ratio derived from the M_{mol}/M_*-M_* relation for xGASS-CO galaxies by [7], using the stellar mass from column (2), as shown by the black errorbars in the top panel of the right plot in Fig. 3.7; (9) logarithm of the total atomic-to-stellar ratio derived similarly as in column (8). For both columns (8) and (9), according to [7] the scatter is within ~ 0.3 dex.	102
4.1	The ACA EDGE target sample. Notes: Column (1): galaxy name; (2) R.A. (J2000) of the galaxy optical center; (3) Decl. (J2000) of the galaxy optical center; (4) optical SDSS r -band inclination; (5) optical SDSS r -band position angle, calculated east of north; (6) stellar redshift; (7) root mean square flux in 10 km s^{-1} channels; (8) minor axis of the synthesized beam; (9) major axis of the synthesized beam; (10) position angle of the synthesized beam; (11) distance; (12) effective radius; (13) optical size of the major axis measured at $25 \text{ mag arcsec}^{-2}$ in the B band. Columns (2) and (3) are drawn from the NASA/IPAC Extragalactic Database, NED. Column (4) is derived by finding the best fit for the SDSS z -band contours at $r \sim r_{25}$ as described in §4.3.1. Columns (5) and (6) are drawn from HyperLEDA. Column (11) is derived from column (6) assuming a Λ CDM cosmology with $\Omega_{\Lambda} = 0.7$, $\Omega_{\text{DM}} = 0.3$, and $H_0 = 69.7 \text{ km s}^{-1} \text{ Mpc}^{-1}$. Column (12) is taken from CALIFA. Column (13) is taken from [8].	120

4.2 Main properties of the ACA EDGE galaxies. Column (1): galaxy name. Column (2) and (3): logarithmic of the total stellar masses and SFRs from CALIFA. Column (4): logarithmic of the total molecular gas mass as derived explained in §4.3.1. Column (5): morphological classification drawn from NED. Column (6): emission line diagnostics for the optical nucleus spectrum for CALIFA galaxies by [4], who classify them into star-forming (SF), active galactic nuclei (AGN), and LINER-type galaxies. These groups are also complemented by the type-I and type-II AGN classification by [9]. Column (7): Galaxy classification according to their quenching stage as explained in §4.4.1.1: main sequence (MS), green valley (GV), and red cloud (RS). Columns (8) and (9): exponential scale lengths of the molecular gas and stars, respectively, as derived in §4.4.1.2. Columns (10) and (11): radius and mass of bulges, as derived in §4.3.3. ^aGalaxies with two-dimensional emission line classification (column 7) from [10], who classify galaxies in star-forming (SF), quiescent-nuclear-ring (QnR), centrally quiescent (cQ), mixed (MX), nearly retired (nR), and fully retired (fR). 133

List of Figures

1.1	The baryon cycling inside galaxies. Picture by A. Kepley.	2
1.2	Schematic picture of the different structures of the interstellar medium, where molecular clouds are the nurseries where new star are born. Picture taken from Van der Tak et al. (2018) [11].	3
1.3	Schematic of galaxy structural components. Figure taken from Astrobites.org ³	5
1.4	The de Vaucouleur-Hubble tuning fork diagram. The figure represents an empirical classification based on directly observed properties like morphology, stellar mass, substructures, among others. The diagram also group galaxies in two main classes accordingly to their evolutionary stage: early-type (which encompasses both elliptical and lenticular galaxies: left side), and early-type (including spiral, irregular, and dwarf galaxies; right side).	7
1.5	Sampling data for seven molecular gas-rich spiral galaxies selected from the HERACLES survey, as shown in Bigiel et al. (2008) [12]. <i>Left</i> : The resolved SFR surface density, Σ_{SFR} , versus the resolved atomic hydrogen surface density, Σ_{HI} . <i>Right</i> : Σ_{SFR} versus the resolved molecular gas surface density, Σ_{H_2}	8
1.6	<i>Left</i> : The atomic hydrogen (proton and electron) spins aligned (top) undergoes a flip of the electron spin, resulting in emission of a photon with a 21-cm wavelength (bottom). <i>Right</i> : Molecules can emit radiation by changing either their rotational or vibrational states. A change in the roto-vibrational state of the CO molecule (H_2 tracer) results in a photon emitted at millimeter wavelengths. Image taken from COSMOS ⁴	9
1.7	Schematics of a single dish antenna (left), and an interferometer (right), in their most basic configurations. While single antennas collect radiation only over the area defined by the surface of the dish, an interferometer collects radiation from several antennas (two or more). Although single dish telescopes are better at recovering the total flux than interferometers, the latter can spaces dishes at separations much larger than the diameter of a single dish and thereby achieve the higher angular resolution essential to resolving disks of galaxies. Images from <i>How ALMA Works Vol. 2: Combining Multiple Antennas into One Radio Interferometer</i>	11
1.8	VLA antennas at the Plains of San Agustin, New Mexico, USA. Credits to the National RadioAstronomy Observatory, NRAO.	13
1.9	CARMA antennas at Cedar Flat in the Inyo Mountains, California. Photo by R. L. Plambeck.	15
1.10	ALMA antennas at the Chajnantor Plateau, 5000 m above the sea level. <i>Credits</i> : ALMA (ESO/NAOJ/NRAO)/W. Garnier (ALMA).	17

³<https://astrobites.org/2013/12/06/finding-relics-of-galaxy-formation/>

⁴<https://astronomy.swin.edu.au/cosmos/m/Molecular+Cloud>

1.11	Integrated M_* versus SFR relation for galaxies selected from the Calar Alto Legacy Integral Field Area survey, CALIFA [13], as shown in Colombo et al. (2020; [14]). Points in the plot, which represent galaxies, are conveniently colored according to how efficient is the conversion from molecular gas into stars within them. Main sequence galaxies (blue points) tend to have high SFRs and are well represented by the best-linear fit for main sequence galaxies from Cano-Diaz et al. (2016; [15]). Conversely, SFRs seem to be uncorrelated with M_* in red sequence galaxies (red points), which also have lower star-formation rates than main sequence galaxies. The green dotted line marks the “green valley”, i.e. galaxies transiting from the main to the red sequence and experiencing star-formation quenching.	18
1.12	Ram pressure stripping of the HI gas in four galaxies from the Virgo cluster. The optical images are a color composite of three filters from the Sloan Digital Sky Survey, SDSS, overlaid with HI contours from the VIVA survey [16]. Since gas is less gravitationally bound to galaxies than stars, HI is noticeably more disturbed by ram pressure stripping than the stellar disk. Image taken from Wong et al. (2014; [17]).	23
2.1	Example showing effects of spectral stacking. The average CO spectrum within an annulus that spans from 0.65 to 0.75 r_{25} in NGC 0551 is shown. The left panel shows the average of all spectra in the annulus in the observed velocity frame. The right panel shows the average in the velocity frame relative to $H\alpha$, along with the best Gaussian fit profile (green dashed line).	32
2.2	<i>Left:</i> FWHM of CO line as a function of galactocentric radius. Small colored dots show the FWHM of a Gaussian fit to the stacked spectrum in an annulus. Large green squares indicate the FWHM lying above 80% of the points at that radius, and the dashed green line is the fit to the squares; we use this function to define the window of flux integration as a function of r_{gal} . The gray-dashed line marks the limit at which we reject spectra with a Gaussian fit narrower than 40 km s^{-1} (2 channels in the CO datacubes). <i>Right:</i> Ratio between the final stacked and unstacked integrated CO(1–0) line intensity per annulus for annuli located at $r/r_{25} > 0.5$, which include just 2σ detection spaxels.	34
2.3	<i>Left:</i> Comparison between the stellar, l_* , and molecular length scales, l_{mol} , computed by fitting exponential profiles to the respective surface densities as a function of galactocentric radius. The colored circles correspond to 61 EDGE-CALIFA galaxies color-coded by stellar mass derived from SED fitting (see Section 3.2.1). The inset panel shows the comparison between l_{mol} and the isophotal radius r_{25} . The triangles represent uncertain results for which measurements are smaller than 3σ . The solid red and dashed blue lines illustrate the 1:1 scaling and the OLS linear bisector fit (forced through the origin) for all the sources, respectively. <i>Right:</i> Relationship between the radii that enclose 50% of the molecular gas and the stellar mass, $R_{50,\text{mol}}$ and $R_{50,*}$, respectively. Conventions and symbols are as in the left panel.	42
2.4	SFE_{gas} vs galactocentric radius. Each line indicates the average SFE_{gas} for individual galaxies in $0.1r_{25}$ -wide tilted annuli after stacking. The morphological group for the galaxies in each panel is indicated by the legend in that panel. The plot shows that the SFE_{gas} in individual galaxies generally decreases as a function of galactocentric radius and that the dispersion in SFE_{gas} at particular radii is due mostly to differences between galaxies.	44

- 2.5 Histogram of galactocentric radii at which Σ_{H_2} drops to $6 M_{\odot} \text{pc}^{-2}$, which is the value of Σ_{atom} assumed for EDGE-CALIFA galaxies in this work. The dashed vertical black line is the mean value of r/R_e at which this occurs, corresponding to 1.1 ($0.4r_{25}$; see inset panel). The gray area represents the uncertainty in mean value of r/R_e . The inset shows a similar histogram for r/r_{25} 45
- 2.6 *Top:* SFE_{gas} vs galactocentric radius for different morphological types of galaxies. SFE is averaged at each radius over all galaxies of the selected morphological type; types are indicated by shaded color as described in the legend. The vertical extent of the shaded area for each morphological type is the 1σ scatter distribution for that type (see Figure 2.4). Circular dots indicate the average SFE_{gas} and galactocentric radius in stacked annuli for all EDGE-CALIFA galaxies; the black solid line is the OLS linear bisector fit to those points using the model $A_{\text{SFE}} \times \exp(-r/r_{\text{SFE}})$. The error bars are the uncertainties of the mean SFE values in each bin. The two dashed black lines show the effect of increasing and decreasing Σ_{atom} by a factor of two from its assumed value of $6 M_{\odot} \text{pc}^{-2}$. The shaded gray band indicates the amount by which the binned SFE_{gas} would increase if we use the metallicity dependent prescription for α_{CO} . The green squares are the HERACLES data for spiral galaxies. The figure shows that SFE_{gas} depends on radius, stellar mass and morphological type. 46
- 2.7 *Left:* Sample distribution of the oxygen abundances, $12 + \log(\text{O}/\text{H})$, with the O3N2 as metallicity indicator. The dashed-black line is the assumed solar value, which corresponds to $12 + \log(\text{O}/\text{H})_{\odot} = 8.69$. *Right:* The star formation efficiency of the molecular gas, $\text{SFE}_{\text{mol}} = \Sigma_{\text{SFR}}/\Sigma_{\text{mol}}$, vs the ratio between the molecular and the atomic gas surface densities, $R_{\text{mol}} = \Sigma_{\text{mol}}/\Sigma_{\text{atom}}$. Colors code for galactocentric radius (in R_e) are as indicated by the color bar. Black contours are 80%, 60%, 40%, and 20% of the points just for detections. Large black filled circles show the mean of EDGE-CALIFA data at each stellar surface density bin; the error bars are the uncertainties of the mean SFE_{mol} values in each bin. The black-solid line shows the OLS linear bisector fit for averaged points of SFE_{mol} over annuli by using the model $y = ax + b$. The shaded region represents uncertainty of the slope derived from the OLS linear bisector fit. The horizontal dashed-blue line is the average SFE_{mol} , including the 3σ detection, for the sample. The inset panel shows the SFE_{mol} for detections only as a function of galactocentric radius. The blue-dashed line is the average SFE_{mol} 49
- 2.8 *Top left:* SFE_{gas} as a function of stellar surface density, Σ_{\star} . Circular dots indicate the average SFE_{gas} and Σ_{\star} in stacked annuli for the EDGE-CALIFA data. The ‘r’ term represents the Pearson correlation coefficient, including the binned annuli, for the relation between the SFE_{gas} and Σ_{\star} . Conventions are as in bottom panel of Figure 2.7. *Top right:* The H_2 -to- H_I ratio, R_{mol} , as a function of Σ_{\star} ; we use $\Sigma_{\text{atom}} = 6 M_{\odot} \text{pc}^{-2}$. Conventions are as in top panel. *Bottom:* SFE_{gas} as a function of gas surface density. The grey dashed line marks the point at which $\Sigma_{\text{gas}} = \Sigma_{\text{atom}} = 6 M_{\odot} \text{pc}^{-2}$. Conventions are as in top panel. 52
- 2.9 *Left:* SFE_{gas} as a function of dynamical equilibrium pressure, P_{DE} . The dashed-blue line corresponds to 1% of gas converted to stars per disk free-fall time. *Right:* Star formation rate surface density, Σ_{SFR} , as a function of P_{DE} . The black dashed line is the OLS linear bisector fit for all points. The ‘r’ term is the Pearson correlation coefficient of this subsample. The shaded region represents uncertainty of the slope derived from the OLS linear bisector fit. Conventions are as in Figure 2.8. 55

2.10	<p><i>Left:</i> SFE_{gas} as a function of the orbital timescale, τ_{orb}. Color coding and symbols are as described in Figure 2.8. The black-dashed line is the best fit of the binned data and shows 5% of gas converted into stars per τ_{orb}. The ‘r’ term represents the Pearson correlation coefficient, including the binned annuli, for the relation between the SFE_{gas} and τ_{orb}. <i>Right:</i> SFE_{gas} averaged over τ_{orb} bins over all galaxies of selected morphological types as in Figure 2.6. Black-dashed lines, from top to bottom, represent the 50%, 17%, 5%, 1.7%, and 0.5% efficiency of gas converted into stars per τ_{orb}.</p>	59
2.11	<p>SFE_{gas} as a function of Toomre’s gravitational instability Q parameter for two different scenarios. <i>Left:</i> The SFE_{gas} is plotted as a function of the Toomre Q parameter for gas, Q_{gas}. <i>Right:</i> The SFE_{gas} is plotted as a function of the Toomre Q parameter redefined by [18] to include the contribution of stars and gas, $Q_{\text{stars+gas}}$. Green squares in the upper left and right panels correspond to HERACLES spiral galaxies; black dashed line sets the limit where the gas is unstable or stable. The center left and right panels show the same points included in the upper ones but this time divided into low and high galaxy stellar mass sets; red points correspond to binned annuli which belong to galaxies with $\log_{10}(M_{\star}) > 10.7$, while blue points belong to galaxies with stellar masses below this limit. Blue and red contours are the 66% and 33% of the points for each mass set. The bottom left and right panels provide information about the morphological type of the host galaxy for a given annulus. The crosses correspond to the center of mass of the $\log_{10} SFE_{\text{gas}}$ vs center of mass of $\log_{10} Q$ points for each set of morphological types.</p>	62
2.12	<p><i>Top:</i> Molecular gas surface density, Σ_{mol}, as a function of Toomre’s instability parameter for gas and stars, $Q_{\text{stars+gas}}$, for annuli with galactocentric radii within $0.3r_{25}$ (red points), between $0.3r_{25}$ and $0.5r_{25}$ (yellow points), and outside $0.5r_{25}$ (blue points). Each point represents the value of Σ_{mol} averaged over a r/r_{25}-wide annuli. Points are color-coded by galactocentric radius (in r_{25}), as indicated by the color bar on the right side. Solid-lines are PCA major and minor axes for which each of the groups vary most. The axes are normalized to fit the major and minor axes of the elliptical contours that enclose 50% of the annuli within a given range. The ratio between the major and the minor axes from the PCA, $R_{\text{maj/min}} = r_{\text{maj}}/r_{\text{min}}$, is in the upper left. Typical $1-\sigma$ error bars are shown in bottom left. The horizontal black-dotted line represents the assumed $\Sigma_{\text{atom}} = 6 M_{\odot} \text{pc}^{-2}$. <i>Bottom:</i> Distribution of the Spearman rank correlation coefficients for the three r ranges in the top panel after randomizing the Σ_{mol} data, per range, in 200 realizations to test for the degree of internal correlation of the axes. The horizontal dashed-red, dashed-yellow, and dashed-blue lines are the Spearman rank coefficients for the actual data, from inner to outer ranges, respectively. This shows that the correlations observed in the top panel are completely consistent with being a result of the definition of $Q_{\text{gas+stars}}$ (see discussion in the text), and thus (although tantalizing) are not particularly meaningful.</p>	64
3.1	<p>Background-subtracted, exposure-corrected ROSAT All Sky Survey mosaic of the Virgo Cluster (hard band: 0.4-2.4 keV), with an overlay of 49 VERTICO CO(2-1) peak temperature maps, increased in angular size by a factor of 20 for illustration. Image taken from [6].</p>	76

3.2	Distribution of offsets between the CO(2–1) and HI velocities, $\Delta V = V_{\text{CO}(2-1)} - V_{\text{HI}}$, in spaxels within the 38 VERTICO galaxies analyzed here. The red bars correspond to spaxels with ΔV offsets that place CO outside the integration window (see text) for stacking CO. The vertical black-dashed line is the median value of $\Delta V = -0.7 \text{ km s}^{-1}$. The figure shows that, on average, the differences between the CO(2–1) and HI velocities are smaller than the integration window in most cases ($\sim 98\%$).	81
3.3	Spectral stacking example. The average CO(2–1) spectrum within an annulus that spans from 0.6 to 0.7 r_{25} in NGC 4536 is shown. The left panel shows the average of all spectra in the annulus in the observed velocity frame. The inset panel includes the SDSS r -band image (background), CO(2–1) data (blue contours), and the annulus that spans from 0.6 to 0.7 r_{25} (red ellipses). The right panel shows the average in the velocity frame relative to HI along with the best Gaussian fit profile (green dashed line).	82
3.4	Ratio of the integrated CO(2–1) line intensity in an annulus after stacking to that before stacking. The vertical black-dashed line is the median value of $\log_{10}[I_{\text{CO,Stack}}/I_{\text{CO,Unstack}}] = 0.21$; this shows that, on average, stacking recovers $\sim 60\%$ more emission. On average, we are reaching a characteristic rms noise of 0.1 mK at 10 km s^{-1} , which corresponds to a sensitivity of $\sim 0.1 M_{\odot} \text{ pc}^{-2}$. The inset panel compares $\log_{10}[I_{\text{CO,Stack}}/I_{\text{CO,Unstack}}]$ vs galactocentric radius, and shows that annuli with the most CO flux enhancement are at $r \geq 0.5r_{25}$	83
3.5	Stacked molecular gas (Σ_{mol} , solid-blue line) and stellar (Σ_{\star} , solid-orange line) surface densities, in units of $M_{\odot} \text{ pc}^{-2}$, as a function of galactocentric radius, in units of r_{25} , for the 38 VERTICO galaxies analyzed in this work (sorted by HI-Class). The shaded-blue area is the Σ_{mol} uncertainty. The brown-dotted line is the star formation rate surface density, Σ_{SFR} . The purple-dashed line is the atomic gas surface density derived from HI moment 0 maps at $15''$, resolution from the VIVA survey. The shaded-gray area is the region within the stellar effective radius $R_{e,\star}$. The dashed-green and dashed-red lines represent the best-fit exponential profiles for Σ_{mol} and Σ_{\star} , respectively, when an exponential fit was appropriate. The vertical-dashed lines correspond to $r_{\text{gal}} = 3\text{kpc}$	89
3.6	<i>Left:</i> Comparison between the stellar, l_{\star} , and molecular scale lengths, l_{mol} , computed by fitting exponential profiles to the respective surface densities as a function of galactocentric radius. The colored circles correspond to 33 VERTICO galaxies with $\Sigma_{\text{mol}} > 1 M_{\odot} \text{ pc}^{-2}$ for all the annuli within $0.25r_{25}$, color-coded by HI-Class from [5]. The blue-solid line is the OLS linear bisector fit (forced through the origin) for them, and the dashed-dotted-red and dashed-green lines illustrate the 1:1 scaling and the OLS linear bisector fit for EDGE-CALIFA galaxies (see Chapter 2), respectively. The ‘ r_p ’ value noted corresponds to the Pearson correlation parameter. <i>Right:</i> The molecular, $R_{e,\text{mol}}$, vs stellar, $R_{e,\star}$, effective radii, which enclose 50% of the total molecular gas and stellar masses, respectively, for the 38 VERTICO galaxies analyzed in this work. Conventions are as in left panel.	91

- 3.7 *Left:* The resolved molecular-to-stellar mass ratio R_{\star}^{mol} colored by HI-Class vs galactocentric radius for annuli within the 38 VERTICO galaxies analyzed in this work. The black contours enclose, from outside-in, the 66% and 33% of the R_{\star}^{mol} of the points. The green shaded area is the range covered by EDGE-CALIFA spiral galaxies within 1σ scatter about the mean values for radial bins of $0.1r_{25}$ wide. *Right:* The resolved atomic-to-stellar mass ratio R_{\star}^{atom} vs galactocentric radius. Conventions are as in left panel. 96
- 3.8 *Left:* The molecular-to-stellar mass ratio within R_e , $R_{\star}^{\text{mol}}(r < R_e) = M_{\text{mol}}(r < R_e)/M_{\star}(r < R_e)$ (top) and the atomic-to-stellar mass ratio within R_e , $R_{\star}^{\text{atom}}(r < R_e) = M_{\text{atom}}(r < R_e)/M_{\star}(r < R_e)$ (bottom), vs HI-Class defined by [5]. The black bars show the values obtained from the $M_{\text{mol}}/M_{\star}-M_{\star}$ and $M_{\text{atom}}/M_{\star}-M_{\star}$ relations for xGASS-CO MS galaxies from [7] using the mean stellar masses for the [5] HI-Classes listed in Table 3.2. The violin errorbars represent the distribution of values for each HI-Class. The white dot is the median value of the distribution. The shaded-green area in the top panel is the $R_{\star}^{\text{mol}}(r < R_e)$ range covered by EDGE-CALIFA spiral galaxies within 1σ scatter. *Right:* $R_{\star}^{\text{mol}}(r < R_e)$ (top) and the $R_{\star}^{\text{atom}}(r < R_e)$ (bottom) vs HI-Class after clustering them in three broader groups: i) unperturbed galaxies (HI-Class 0), ii) asymmetric galaxies (HI-Classes I and II galaxies); and iii) symmetric-truncated galaxies (HI-Classes III and IV galaxies). Conventions are as in the left panel. While $R_{\star}^{\text{mol}}(r < R_e)$ values for VERTICO galaxies are within the ranges covered by the xGASS-CO MS galaxies, $R_{\star}^{\text{atom}}(r < R_e)$ values show a systematic decrease with increasing HI-Class. 97
- 3.9 *Left:* The resolved molecular-to-atomic gas ratio $R_{\text{mol}} = \Sigma_{\text{mol}}/\Sigma_{\text{atom}}$ vs galactocentric radius, with circles colored by HI-Class. The black contours enclose, from outside-in, the 66% and 33% of the points. *Middle:* The molecular-to-atomic gas ratio, in logarithmic space, computed using the molecular and atomic gas masses within R_e , $R_{\text{mol}}(r < R_e) = M_{\text{mol}}(r < R_e)/M_{\text{atom}}(r < R_e)$, vs HI-Class. The black bars show the R_{mol} values obtained from the $M_{\text{mol}}/M_{\text{atom}}-M_{\star}$ relation for xGASS-CO MS galaxies from [7] using the mean stellar masses for the [5] HI-Classes listed in Table 3.2. There is an increase of $R_{\text{mol}}(r < R_e)$ that is up to about an order of magnitude going from lower to higher HI-Classes (e.g., from Class I to III); the more disturbed the HI the higher the molecular-to-atomic ratio within R_e . *Right:* $R_{\text{mol}}(r < R_e)$ vs HI-Class groups as in the right panel of Fig. 3.8. Conventions and symbols are as in Fig. 3.8. 101
- 3.10 *Top:* The molecular gas mass within R_e , $M_{\text{mol}}(r < R_e)$ (M_{\odot}), vs HI-Class. *Bottom:* The star formation rate within R_e , $\text{SFR}(r < R_e)$ ($M_{\odot} \text{ yr}^{-1}$), vs HI-Class. Conventions are as in left panel of Fig. 3.8. While $M_{\text{mol}}(r < R_e)$ remains almost constant, there is a systematic decrease of $\text{SFR}(r < R_e)$ with HI-Class (particularly from HI-Classes II to IV). 103

3.11	<p><i>Left:</i> The resolved star formation efficiency of the molecular gas, SFE_{mol}, vs galactocentric radius. The black contours enclose, from outside-in, the 66% and 33% of the points. <i>Middle:</i> The star formation efficiency of the molecular gas within R_e, $SFE_{\text{mol}}(r < R_e)$, vs HI-Class. The horizontal black bars are the SFR/M_{mol} median values for HI-Classes 0, I, II, III, and IV VERTICO galaxies using the $SFR/M_{\text{mol}}-M_*$ relation derived from the molecular depletion times, $\tau_{\text{dep}} = M_{\text{mol}}/SFR$, for xGASS-CO MS galaxies by [7]. The shaded-green area is the $SFE_{\text{mol}}(r < R_e)$ range covered by EDGE-CALIFA spiral galaxies within 1σ scatter. <i>Right:</i> $SFE_{\text{mol}}(r < R_e)$ vs HI-Groups. Conventions are as in left panel of Fig. 3.8. The results shown in Figs. 3.10 and 3.11 suggest that the systematic decrease of $SFE_{\text{mol}}(r < R_e)$ is a consequence of changes to the state of the gas or the star-formation process caused by the source of the morpho-kinematic perturbations that affect the HI in the outer disks of VERTICO galaxies.</p>	104
3.12	<p>The star formation efficiency of the molecular mass within R_e, $SFE_{\text{mol}}(r < R_e)$, vs the best-fit power-law index of the resolved Kennicutt-Schmidt, N_{rKS}, from [19]. Although without a significant correlation between $SFE_{\text{mol}}(r < R_e)$ and N_{rKS} (Pearson $r_p = 0.3$), HI-Classes III and IV (blue circles) seem to group at both lower N_{rKS} and $SFE_{\text{mol}}(r < R_e)$ than HI-Classes 0 and I (red circles), and vice versa.</p>	106
3.13	<p>The star formation efficiency of the molecular mass within the radius of the bulge R_b, $SFE_{\text{mol}}(r < R_b)$, vs the bulge mass M_b (in units of the total stellar mass) for HI-Classes II, III, and IV. Symbols are colorcoded by HI-Class as in Figure 3.12. The horizontal arrows are upper-limits for M_b since no clear breaks in the stellar radial profiles due to bulges are identified; therefore, M_b in these cases is the mass enclosed within $0.1r_{25}$, which corresponds to $r_{\text{gal}} \approx 1.0$ kpc at the Virgo cluster distance (16.5 Mpc; [20]).</p>	109
4.1	<p>SFR-M_* relation for the 60 galaxies in the ACA EDGE survey (blue circles), sampling the whole range of $z = 0$ galaxy behavior for $\log[M_*/M_\odot] \approx 10 - 11.5$, including the star formation main sequence and quenched systems below it. Gray circles are the 126 galaxies CARMA EDGE galaxies included in [3]. The black-solid and dashed-green lines correspond to the best-linear fit for star-formation main sequence ([15]) and green valley ([14]) galaxies, respectively. ACA EDGE galaxies constitute a sample of the local universe with good statistical characteristics and are easy to volume-correct to characterize the star formation activity in nearby massive galaxies.</p>	117
4.2	<p>Menagerie of stellar distributions presented in the local Universe. SDSS r (red channel), i (green channel), and z-bands (blue channel) composite images for the 60 galaxies encompassed by the ACA EDGE survey. These local galaxies show a broad variety of morphologies, which is one of the main ACA EDGE goals to analyze the star-formation quenching mechanisms at different evolutionary stages.</p>	118
4.3	<p>CO(2-1) spectra for ACA datacubes convolved to $1.1'$ and 30 km s^{-1} channel width for the 60 galaxies. The spectra are taken from the central pixel located at the optical center (columns 2 and 3 in Table 4.1), and velocities are centered on the stellar redshift.</p>	121

4.4	ACA EDGE data products for each galaxy. Panels cover an area of $1.25' \times 1.25'$. The first panel shows the SDSS <i>riz</i> multicolor image with contours from our integrated intensity masked map overlaid. Contours correspond to 2σ and 5σ CO(2-1) emission line levels. From left to right, the following panels show the CO(2-1) emission line intensity (moment 0, in units of Jy/beam km s^{-1}), velocity (moment 1, in units of km s^{-1}), and signal-to-noise peak maps, respectively. The red crosses are the optical centers (columns 2 and 3 of Table 4.1). The black ellipses in the left bottom corner are the beam size of the CO(2-1) data. Panels for the remainder of the survey can be found in the Appendix.	122
4.5	Comparison of the integrated CO($J=2-1$) emission line flux between ACA (this work) and APEX [14] datasets for 51 ACA galaxies. ACA fluxes are derived after convolving datacubes to match the APEX angular resolution ($26.3''$). The red dots correspond to NGC 0768, NGC 7321, and UGC 12250, which have incomplete ACA spectral coverage (see Fig. 4.3). The green arrows are UGC 08322 and UGC 12274, which are detected by ACA but not APEX (see Table 4.2). The figure shows good agreement between ACA and APEX fluxes. However, fluxes measured by APEX are on average $\sim 20\%$ brighter than in ACA, likely due to calibration differences. Note that a lack of a detection by ACA in a $26''$ beam does not imply the source is not detected by ACA: for interferometric data convolution results in removing visibilities in long baselines (and thus collecting area and sensitivity).	125
4.6	Stellar (Σ_* ; red solid line) and molecular gas (Σ_{mol} ; blue solid line) surface densities, in units of $M_\odot \text{pc}^{-2}$, as a function of galactocentric radius, in units of the stellar effective radius (R_e), for the 30 ACA EDGE galaxies with 5σ CO detections and inclinations $i \leq 70^\circ$. The blue shaded area is the Σ_{mol} uncertainty. The brown dotted line is the SFR surface density, Σ_{SFR} . The gray shaded area is the region within the bulge radius, R_{bulge} . Dashed black lines correspond to the best exponential function fit for stellar and molecular gas radial profiles, from top to bottom. The dashed green line corresponds to $r = r_{25}$. The code on the left bottom corner corresponds to the Hubble type and the nuclear activity (columns 5 and 6 in Table 4.2, respectively). SFRs at $r < 0.5R_e$ have been removed for LINER and AGN galaxies since $\text{H}\alpha$ in this region is susceptible to LINER/AGN contamination (see §4.4.2.2). Galaxies are classified based on their quenching stage as defined in §4.4.1, i.e., in main sequence (blue panels), green valley (green panels), and red cloud (red panels). When using stellar profiles as a benchmark, we note a systematic flattening of the molecular gas profiles with quenching stage. See also Fig. 4.12.	132

- 4.7 *Top left:* SFR- M_* diagram integrated over CALIFA SFR and stellar maps, color-coded by the total molecular gas mass, M_{mol} . The solid black line is the SFMS fit by [15]. Blue, green, and red dashed areas define main sequence, green valley, and red cloud galaxies, respectively, as defined by the bands (see §4.4.1 for more details). *Top right:* SFR- M_{mol} relation color-coded by stellar mass. The dashed black lines, from top to bottom, correspond to molecular gas depletion times $\tau_{\text{dep}} = 0.1, 1.0,$ and 10 Gyr, respectively. Blue, green, and red circles are the centroids of SFR and M_{mol} values for galaxies with 5σ CO detections (filled circles) of the groups as defined by the bands in the top left panel. The blue and green squares correspond to the centroid of SFR and M_{mol} values for main sequence and green valley CARMA EDGE detected galaxies. *Bottom:* Distributions for the molecular-to-stellar mass fraction ($R_*^{\text{mol}} = M_{\text{mol}}/M_*$; left) and the molecular gas depletion time ($\tau_{\text{mol}} = M_{\text{mol}}/\text{SFR}$; right) for the three categories (excluding CO upper-limits), as defined in top left panel. Vertical and horizontal lines correspond to the average values and the standard deviations of the distributions, respectively. The plots suggest that while the transition from main sequence to green valley galaxies is mostly driven by gas removal/depletion, the movement from the latter to the red cloud may be determined by a reduction in the star formation efficiency of the molecular gas ($\text{SFE}_{\text{mol}} = \tau_{\text{dep}}^{-1}$). 137
- 4.8 Comparison between the stellar, l_* , and molecular, l_{mol} , scale lengths, computed by fitting exponential profiles to the respective surface densities as a function of galactocentric radius. Blue circles and green triangles correspond to 23 ACA EDGE galaxies with $\Sigma_{\text{mol}} > 1 M_{\odot} \text{pc}^{-2}$ for all the annuli within 1 kpc. The blue solid line is the best fit for the model $y = \alpha x$ for main sequence, omitting galaxies with low-quality l_{mol} fits (symbols with pale colors). The gray dotted and orange-dotted lines are the best fit relation for CARMA EDGE [1] and VERTICO [2], respectively. The shaded gray area correspond to the median physical resolution of ACA EDGE galaxies. On average, the figure shows a $\sim 6:5$ relation between the molecular and stellar scale lengths. 140
- 4.9 *Left:* SFR surface density, Σ_{SFR} , versus stellar surface density, Σ_* , color-coded by the resolved star formation efficiency of the molecular gas, $\text{SFE} = \Sigma_{\text{SFR}}/\Sigma_{\text{mol}}$, for pixels with 5σ CO detections and selected from the 30 galaxies included in Figure 4.6. Blue and green density contours are 90%, 60%, and 30% of the points for main sequence and green valley galaxies. *Right:* The resolved SFR- M_{mol} relation, color-coded by the resolved molecular-to-stellar mass gas fraction, $rR_*^{\text{mol}} = \Sigma_{\text{mol}}/\Sigma_*$. Conventions are as in left panel. The black dashed lines corresponds to the OLS bisector fit for main sequence galaxies using the model $y = \alpha x + \beta$ for the resolved SFMS (left) and the resolved Kennicutt-Schmidt (right) relations. While the left panel exhibits an increasing in Σ_* for pixels transiting from the main sequence to the green valley, the right panel shows that pixels from these two populations cover a similar parameter space although with a mild decreasing in Σ_{SFR} . This suggests that changes in star formation activity during the transition are driven not only by a lowering in the molecular gas, but also due to a decrease of the star formation efficiency. 142

- 4.10 *Top:* The resolved SFE_{mol} versus galactocentric radius for SF pixels within R_b , color-coded by quenching stage. Black crosses are pixels drawn for PHANGS-ALMA spirals. Solid blue and green lines correspond to 90%, 60%, and 30% density contours of main sequence and green valley pixels, respectively. Dashed lines are density contours for pixels when adopting a variable $\alpha_{\text{CO}}(Z', \Sigma_{\text{total}})$ prescription (see Eq. 4.6). *Middle:* The resolved SFE_{mol} versus the resolved specific star formation rate, sSFR, for the same groups as in top panel. *Bottom:* Distribution of the resolved molecular-to-stellar mass fraction, rR_{\star}^{mol} , for main sequence and green valley galaxies included in the upper panel. The vertical and horizontal lines are the mean and the standard deviation values of the distributions, respectively. We note that the spatially resolved SFE_{mol} , sSFR, and rR_{\star}^{mol} within the bulges have a systematic decrease with quenching stage, and these trends seem to not depend on the adopted α_{CO} prescription. 145
- 4.11 Distributions of the bulge density (in units of $M_{\odot} \text{pc}^{-3}$), for the 23 main sequence and 5 green valley galaxies included in Figure 4.6. The vertical and horizontal lines are the mean and the standard deviation values of the distributions, respectively. Although we do not see a statistically significant difference between green valley and main sequence bulge densities, we note that the former have on average denser bulges than the latter. 147
- 4.12 The resolved star formation efficiency of the molecular gas, $SFE_{\text{mol}} = \Sigma_{\text{SFR}}/\Sigma_{\text{mol}}$ (panels A and B), the resolved molecular-to-stellar mass fraction, $rR_{\star}^{\text{mol}} = \Sigma_{\text{mol}}/\Sigma_{\star}$ (panels C and D), and the specific star formation rate, sSFR = $\Sigma_{\text{SFR}}/\Sigma_{\star}$ (panels E and F), in radial bins of $0.3R_e$ (~ 1.5 kpc) versus galactocentric radius for pixels from the 30 galaxies included in Figure 4.6. The figure is color-coded according to the three main groups. Panels A, C, and E encompass pixels from 20 galaxies classified as SF (or with No Nuclear Activity, NNA; see column 5 in Table 4.2), split by their quenching stage (i.e., main sequence, green valley, and red cloud) of the host galaxy. Panels B, D, and F include pixels from 30 ACA EDGE galaxies grouped according to the nuclear activity of the host galaxy. The grey shaded areas correspond to the regions where our $H\alpha$ -based SFR estimator is susceptible to AGN/LINER contamination, so SFR and quantities related are only taken as upper-limits. In all panels, the vertical extent of the shaded areas is the 1σ scatter distribution for any group. Also, the vertical black dashed lines are located at $r = R_e$, which we use to divide galaxy regions in central and disk pixels. While efficiencies in main sequence galaxies remain almost constant with galactocentric radius, in green valley galaxies we note a systematic increase of SFE_{mol} , rR_{\star}^{mol} , and sSFR, with increasing radius. We also observe slightly higher SFE_{mol} in the regions near the centers ($0.5R_e \leq r \leq 1.2R_e$) of AGNs when compared to their outskirts. 149
- 4.13 SFE_{mol} distributions for pixels from no nuclear activity galaxies (NNA), split in main sequence (blue bars) and green valley (green bars) galaxies (from left to right panels, respectively). The two groups are split by two radial bins according to the breaks identified in Fig. 4.12, thus between pixels within the central (hatched unfilled bars) and outer (solid bars) regions. To compute the SFE_{mol} , we adopt a fixed CO-to- H_2 conversion factor (top panels), and the variable $\alpha_{\text{CO}}(Z', \Sigma_{\text{total}})$ from Equation 4.6 (bottom panels). While the distributions of SFE_{mol} for main sequences pixels within the two radial bins are similar when adopting the two α_{CO} prescriptions, green valleys show a more clear bimodal behaviour when using a constant α_{CO} 151

4.14	SFE _{mol} distributions for pixels from star-forming (i.e., no nuclear activity galaxies, NNA; purple bars), LINER (orange bars), and AGN (yellow bars) galaxies (from left to right panels, respectively). Conventions are as in Fig. 4.13. While NNA and LINER pixels have similar SFE _{mol} distributions for the two radial bins and when testing the two α_{CO} prescriptions, we note a mild bimodal behaviour for AGNs.	154
A.1	Images for ACA EDGE galaxies. See caption in Figure 4.4.	169
A.2	Images for ACA EDGE galaxies. See caption in Figure 4.4.	170
A.3	Images for ACA EDGE galaxies. See caption in Figure 4.4.	171
A.4	Images for ACA EDGE galaxies. See caption in Figure 4.4.	172
A.5	Images for ACA EDGE galaxies. See caption in Figure 4.4.	173
A.6	Images for ACA EDGE galaxies. See caption in Figure 4.4.	174
A.7	Images for ACA EDGE galaxies. See caption in Figure 4.4.	175
A.8	Images for ACA EDGE galaxies. See caption in Figure 4.4.	176

List of Abbreviations

ACA	Atacama Compact Array
ALMA	Atacama Large Millimeter/submillimeter Array
ALMaQUEST	ALMA-MaNGA Quenching and STar formation
AGN	Active Galactic Nuclei
BIMA	Berkeley-Illinois-Maryland Association
CASA	Common Astronomy Software Applications
CALIFA	Calar Alto Legacy Integral Field Area
CARMA	Combined Array for Research in Millimeter-wave Astronomy
COMING	CO Multi-line Imaging of Nearby Galaxies survey
EDGE	Extragalactic Database for Galaxy Evolution
ETG	Early-Type Galaxies
FUV	Far UltraViolet
GALEX	GALaxy Evolution EXplorer
GASP	GAs Stripping Phenomena survey
GEMS	Group Evolution Multiwavelength Study survey
GMC	Giant Molecular Clouds
FWHM	Full Width Half Maximum
HERACLES	HERA CO Line Extragalactic Survey
HRS	Herschel Reference Survey
ICM	Intracluster Medium
IGM	Intergalactic Medium
IFS	Integrated Field Spectroscopy
IFU	Integrated Field Unit
IMF	Initial Mass Function
ISM	Interstellar Medium
KS	Kennicutt–Schmidt
LINER	Low Ionization Nuclear Emission-line Region
LTG	Late-Type Galaxies
LITTLE THINGS	Local Irregulars That Trace Luminosity Extremes, The HI Nearby Galaxy Survey
LOFAR	LOW Frequency ARray
MGMS	Molecular Gas Main Sequence
MS	Main Sequence
NGLS	James Clerk Maxwell Telescope Nearby Galaxies Legacy Survey
NMSFR	Normalized Massive Star-Formation Rate

ODR	Orthogonal Distance Regression
OLS	Ordinary Least-Square
PHANGS	Physics at High Angular resolution in Nearby Galaxies
PCA	Principal Component Analysis
RPS	Ram Pressure Stripping
RMS	Root-to-Mean Square
SED	Spectral Energy Distribution
SDSS	Sloan Digital Sky Survey
SFE	Star-Formation Efficiency
SFMS	Star-Formation Main Sequence
SFR	Star Formation Rate
sSFR	specific Star-Formation Rate
SNe	Supernovae
TP	Total Power
URC	Universal Rotation Curve
ULIRG	Ultra Luminous Infra-Red Galaxy
VERTICO	Virgo Environment Traced In CO
VIVA	VLA Imaging survey of Virgo galaxies in Atomic
VLA	Very Large Array
WALLABY	Widefield ASKAP L-band Legacy All-sky Blind Survey
WISE	Wide-field Infrared Survey Explorer

Chapter 1: Introduction

Just as bricks are piled up to build a house, galaxies represent the basic building blocks of the Universe. Gathered together, galaxies can form galaxy clusters, which are structures hosting a significant fraction of the known matter in the Universe. Galaxies are composed of billion of stars, gas, dust and even planets like those in the Solar System. As a whole, these components are referred as baryonic matter (constituted by atoms made of protons and neutrons). In addition, galaxies are dominated by the gravity from a strange type of material called “dark matter”—although still invisible for modern astrophysics (“dark” since it lacks the capability to interact with or emit electromagnetic radiation).

1.1 The baryon cycle

Galaxies are active systems that change and evolve over time. That is possible because gas, mostly made of hydrogen (the most common element in the Universe), enables the formation of new stars over time. Several processes related to gaseous hydrogen maintain galaxies as active systems; these together are usually referred as the “baryon cycle” (e.g., [21]). The current consensus in astronomy states that there is a cycle in which gas is pulled in and out of galaxies and regulates the formation of stars (therefore the galaxy growth) across the history of the Universe (e.g., [22, 23]). The production of these new stars, also referred as “star formation”, is one of

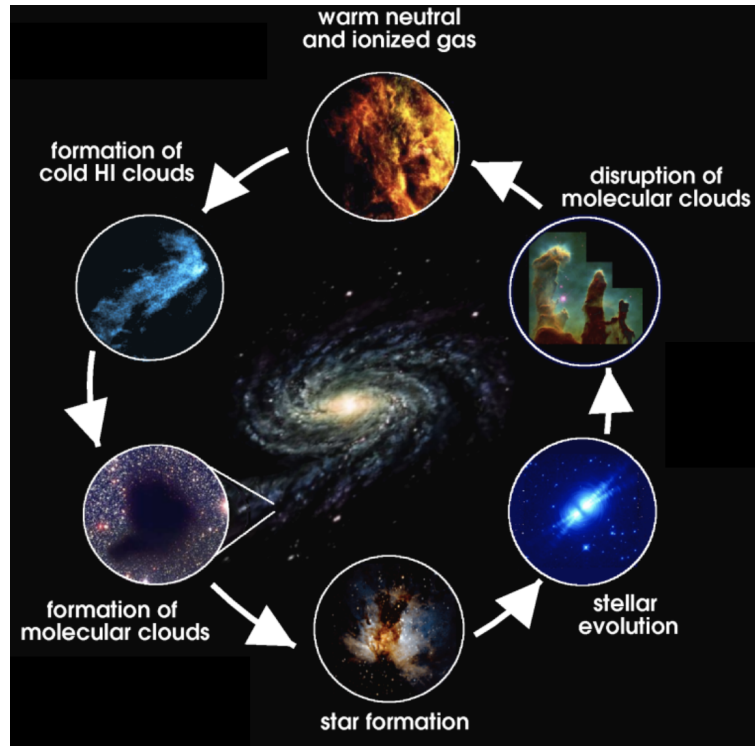


Figure 1.1: The baryon cycling inside galaxies. Picture by A. Kepley.

the most important evolutionary processes that shape galaxies over cosmic times. In practice, the star formation is the process that keeps galaxies alive: when it stops, because the blue stars soon die (because they are mostly massive and therefore short-lived) we refer to the galaxy as “red and dead”.

Galaxies are usually gathered in groups; therefore, the processes related to the baryon cycle may also involve interactions between galaxies and their environments (gas reservoirs outside/between galaxies, tidal forces from other galaxies, among others). All of these together play an important role in the different stages of the baryon cycle. In a nutshell, the baryon cycle can be characterized by the interplay between the following processes (see Fig. 1.1):

1. *Star-formation*: Stars are formed inside molecular clouds (e.g., [24]), which are regions of the interstellar medium (hereafter ISM) in which the gas is predominantly in the molecular

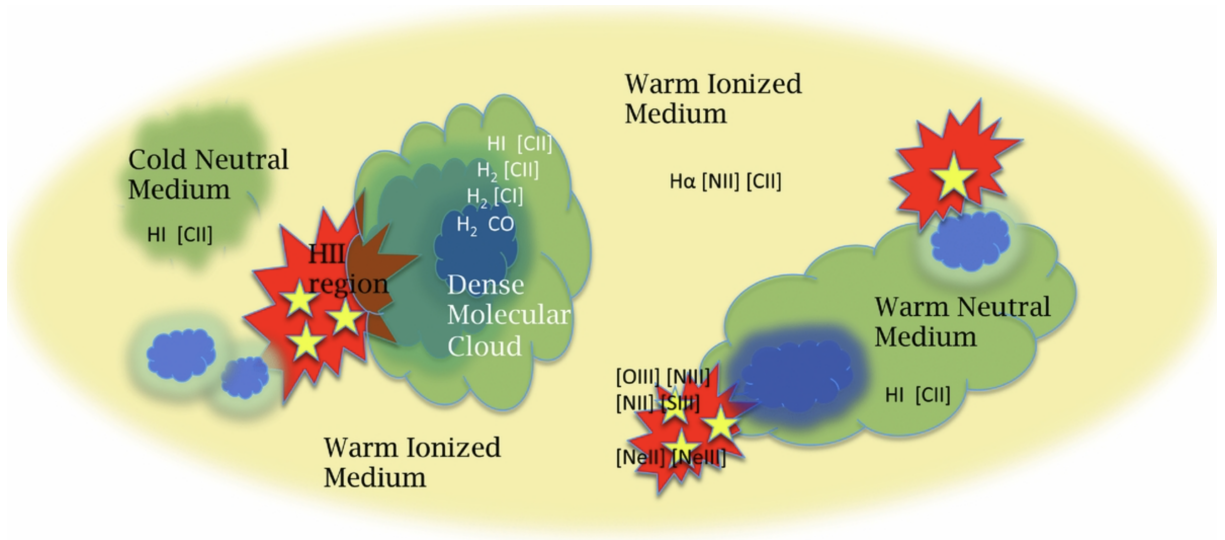


Figure 1.2: Schematic picture of the different structures of the interstellar medium, where molecular clouds are the nurseries where new stars are born. Picture taken from Van der Tak et al. (2018) [11].

phase. Molecular clouds are cloudy complexes composed of hydrogen; they are among the densest and coldest regions within the ISM. Some dense clumps within molecular clouds can collapse due to their self-gravity and form new stars (usually called protostars). At some point, protostars start to increase their temperature due to the accretion of gas that increases the density eventually making the gas optically thick to its cooling radiation, allowing the gas pressure to increase and eventually counteract the infalling gas with growing internal pressure. Young stars (which are protostar entering to the main sequence) are capable of affecting the surrounding gas, even ionizing the atomic hydrogen. All these processes carve out a series of structures within the ISM, such as HII regions (or hydrogen “one time ionized” – as part of the not quite obvious nomenclature that astronomers have adopted) one of the most distinctive (see Fig. 1.2).

2. *Stellar evolution:* Eventually the core of star becomes hot enough for nuclear fusion of hydrogen into helium and the star enters a stable phase in which the energy radiated by the

star is balanced by energy release by fusion in the core and gas pressure balances gravity. A star spends most of its “lifetime” in this phase. After a period time ranging from a few million years for the most massive (more luminous, hotter, and therefore bluer) stars to more than a trillion years for the more numerous least massive (less luminous, cooler, and therefore redder) stars, the nuclear fuels available to the star are exhausted.

3. *Supernovae remnants & stellar ejecta:* As stars exhaust their nuclear fuels in their last evolutionary stages, stars undergo several processes depending on their mass that release material to their surroundings in different ways. These processes are able to disrupt, push out, and warm up a significant fraction of gas in molecular clouds, allowing some gas even to leave the disk of galaxies. Among these processes, the stellar winds in massive stars, planetary nebulae (i.e., the expulsion of outermost layers in low massive stars), and supernovae explosions are some of the most important.
4. *Accretion of gas:* Gas is accreted from the intergalactic medium, providing galaxies with fresh gas reservoirs to sustain the production of new stars across cosmic times. In addition, a substantial portion of the ejected material in the previous stage may recycle back into galaxies, giving an extra source of gas (“wind recycling”; [21]) that may fuel star formation at later times. These processes are also able to enrich the interstellar medium with heavy elements.

1.2 Galaxies and morphology

As mentioned previously, a galaxy is primarily a gravitationally-bound collection of multiple stars, gas, dust, and dark matter. Since there is a close connection between gas, the production

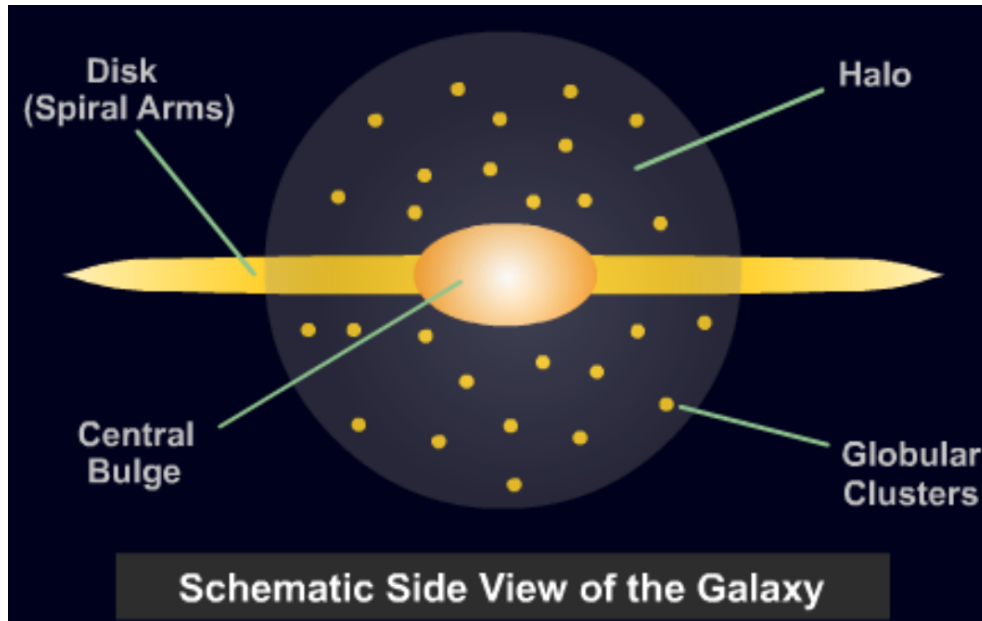


Figure 1.3: Schematic of galaxy structural components. Figure taken from [Astrobit.es.org](https://astrobit.es.org)¹.
¹<https://astrobit.es.org/2013/12/06/finding-relics-of-galaxy-formation/>

of new stars, and the total stellar content, the availability of atomic and molecular gas is a key component for determining the appearance (i.e. structure, distribution of mass between baryon components, etc) of a galaxy. In addition, both the environment and the history of a given galaxy (e.g., the number of galaxy-galaxy interactions, age of their stellar populations, among others) are important factors driving their final mass, shape, or size. For instance, galaxies that have undergone mergers would in principle look different than those just growing from intergalactic gas.

Before we start to analyze the different morphologies of galaxies, we need to understand the structures that, together, give the final appearance to a galaxy. To do so, we can describe the different galaxy structures present in our galaxy, the Milky Way, using Figure 1.3. Briefly, the Milky Way (a stereotypical spiral galaxy) is composed of three main components where stars and gas interact: i) The disk, which contains the spiral arms and/or bars; ii) the central bulge, which is defined by a spherical distribution of packed stars in the galaxy center; and iii) the halo,

which is the most extended structure and comprises a cloud of stars (typically old populations) surrounding the galaxy.

Based on pure observational evidence and on how prominent these structural components are, galaxies can be classified according to their 2D projection on the sky. One of the first and most important galaxy classifications is the one introduced by Edwin Hubble (originally included in his book *The Realm of the Nebulae* published in 1926). Hubble found a useful way to classify galaxies according to their morphological features. The “Hubble Sequence” (also known as the Hubble turning-fork diagram) consists of four main galaxy categories: Elliptical, Lenticular, Spiral, and Barred Spiral. Although this classification adopted a very simplistic methodology, the Hubble Sequence seems to reflect an evolutionary trend of galaxies, going from spirals (with and without bars; also known as late-type galaxies, LTGs), to elliptical/lenticular (known also as early-type galaxies, ETGs). The evolutionary picture comes basically from the fact that spiral galaxies are observed to have young stars and regions of active star formation, while elliptical galaxies tend to host mostly old stellar populations. As mentioned earlier, more massive stars are more luminous, hotter, and bluer, but shorter-lived than low-mass stars; once star-formation ceases, the color of a galaxy becomes dominated by its long-lived low mass stars, which are red. In contrast to elliptical/lenticular galaxies, stars with short lifetimes seem to reside mostly in spiral galaxies, maintaining a continuous production of new massive stars to reflect the characteristic blue colors of spiral arms. There are different hypotheses to explain this difference (which will be discussed later in this work), but apparently gas depletion and removal are the main factors controlling the star formation activity and making the distinction between early- and late-type galaxies.

Since Hubble’s work, the Hubble Sequence has been complemented with more recent ob-

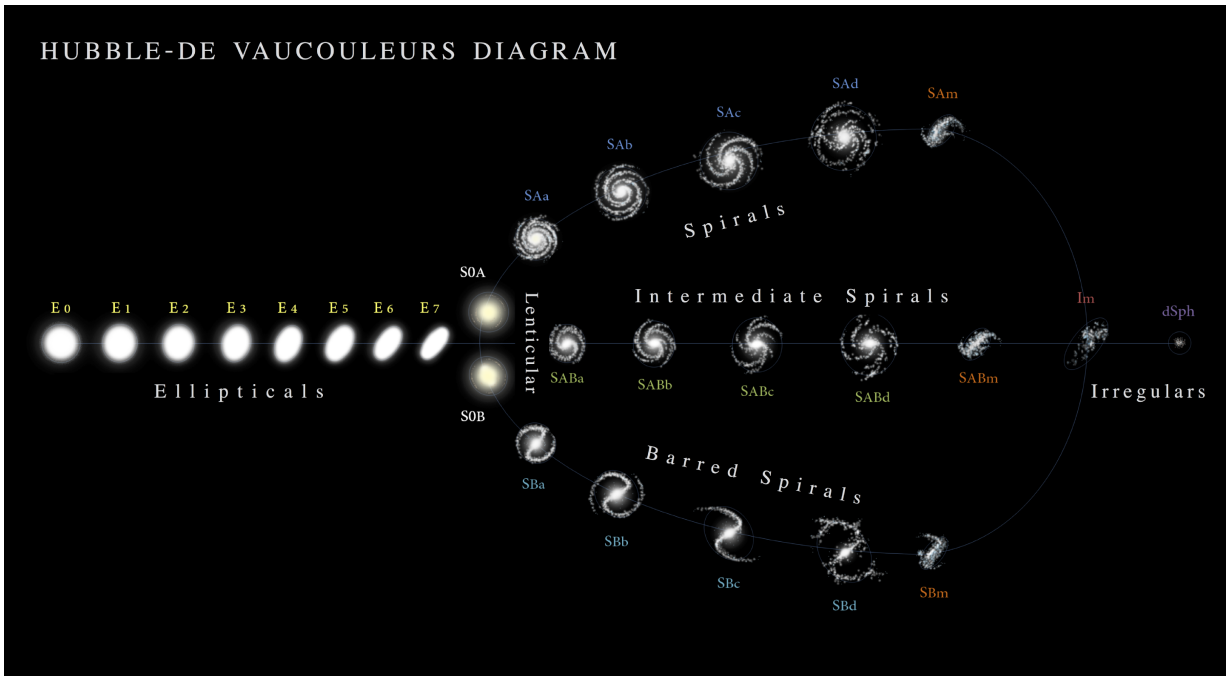


Figure 1.4: The de Vaucouleur-Hubble tuning fork diagram. The figure represents an empirical classification based on directly observed properties like morphology, stellar mass, substructures, among others. The diagram also group galaxies in two main classes accordingly to their evolutionary stage: early-type (which encompasses both elliptical and lenticular galaxies: left side), and early-type (including spiral, irregular, and dwarf galaxies; right side).

servational evidence and a better understanding of galaxy evolution (e.g., [25]). Currently, the de Vaucouleur-Hubble diagram (see Fig. 1.4) is a widely used extension. While the former does not capture the full range of observed galaxy morphologies, the latter incorporates rings and lenses as an important structural component of spiral galaxies.

1.3 The connection between star formation, molecular/atomic hydrogen, and carbon monoxide

In the last decades, studies of the galaxy-integrated star formation and gas have shown there is a tight correlation between the number of stars produced per unit time (known as the

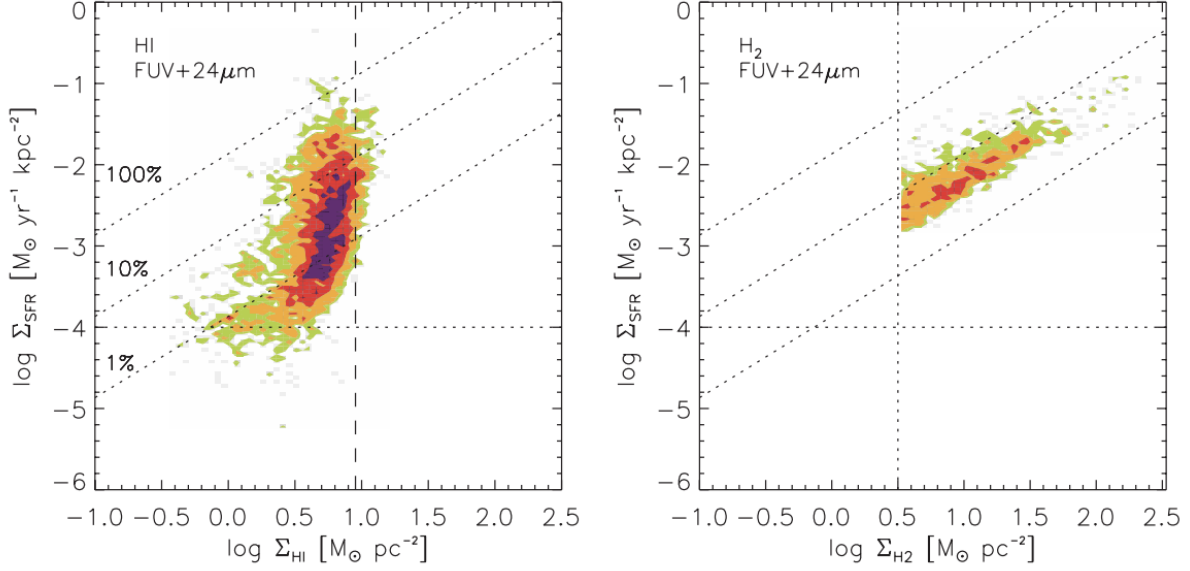


Figure 1.5: Sampling data for seven molecular gas-rich spiral galaxies selected from the HERACLES survey, as shown in Bigiel et al. (2008) [12]. *Left*: The resolved SFR surface density, Σ_{SFR} , versus the resolved atomic hydrogen surface density, Σ_{HI} . *Right*: Σ_{SFR} versus the resolved molecular gas surface density, Σ_{H_2} .

star-formation rate, SFR), and the gas content (e.g., [26,27]). As discussed earlier, stars appear to form in molecular rather than atomic gas. Fig. 1.5 compares the correlation of the star formation rate per unit area (called the SFR surface density, Σ_{SFR}) with atomic hydrogen (HI) and molecular hydrogen (H₂) surface density for a sample of gas-rich spiral galaxies. The figure shows the excellent linear correlation of SFR and (H₂) gas surface densities where H₂ (traced by CO) is detected (see also [28–32], among others). HI shows a non-linear correlation with SFR presumably reflecting its conversion into H₂ as density increases. In other words, as long as there is enough molecular gas susceptible to gravitational collapse, there will be a continuous production of stars.

Similarly to previous studies, one of the main aims of this thesis is to extend the environments and galaxy types probed by studies of molecular gas beyond the molecular-rich regions usually covered mostly in gas-rich spirals galaxies (e.g., [33–36]). This will give us a better understanding about what is the actual impact of the molecular gas content (and its physical con-

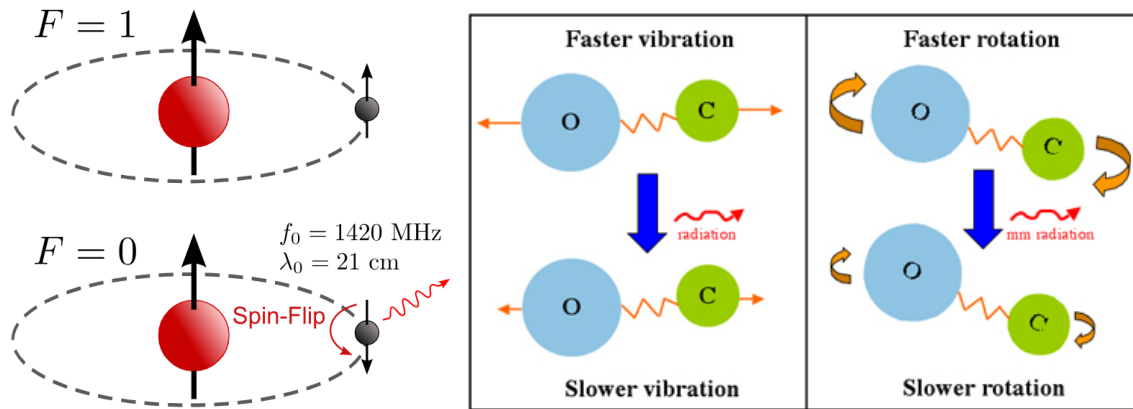


Figure 1.6: *Left:* The atomic hydrogen (proton and electron) spins aligned (top) undergoes a flip of the electron spin, resulting in emission of a photon with a 21-cm wavelength (bottom). *Right:* Molecules can emit radiation by changing either their rotational or vibrational states. A change in the roto-vibrational state of the CO molecule (H_2 tracer) results in a photon emitted at millimeter wavelengths. Image taken from COSMOS ².

² <https://astronomy.swin.edu.au/cosmos/m/Molecular+Cloud>

ditions) on the production of new stars. Since H_2 reservoirs are strongly tied to the extended atomic hydrogen content in galaxies, the presence of HI is crucial to maintain the production of H_2 molecules (e.g. [37]), which will form new stars and sustain their production over long timescales. In consequence, HI data are also essential to complete the panoramic picture of the star-formation activity and its dependence on molecular gas.

Atoms and molecules can be identified by the specific frequencies in the electromagnetic spectrum at which their emission/absorption lines are located. These emission/absorption lines are the “fingerprints” of atoms, since they reflect the different transitions between discrete energy states which are unique to any atomic or molecular species. This means that for a given species there is a well defined set of possible energetic states that their electrons can take. Transitions between these energy levels can happen spontaneously (due to the probabilistic nature of quantum mechanics), or can be triggered due to either interaction with light (also referred as photons; i.e., light particles) or other atoms. Emission lines can also respond to some changes in the physical

properties of atoms, molecules, or the sub-atomic particles within them, like changes in their “spin” (or angular momentum in case of molecules). Hydrogen atoms in the neutral state (i.e. HI) can be traced with the well known 21-cm wavelength line due to changes in electron spin (known as hyperfine-structure lines; see left panel of 1.6). In regions where H₂ can be excited (only a small fraction of the molecular gas in the ISM), such emission lines are located at frequencies inaccessible to ground-based telescopes since Earth’s atmosphere block them, which makes them more “expensive” to observe (there are only accessible using space telescopes).

We usually trace the molecular gas through observations from rotation or vibration transitions (together usually called ro-vibrational lines) of a more easily excited molecule: the main isotope of carbon monoxide (¹²C¹⁶O; hereafter CO; see right panel of Fig. 1.6). Since CO is easily excited and one of the most abundant molecules except for H₂, it provides a good tracer of the total molecular mass emitting at frequencies observable from ground-based telescopes operating at radio, millimeter, and submillimeter frequencies, where the Earth atmosphere is transparent (to some degree) under good weather conditions. Both the CO($J = 1 - 0$) and CO($J = 2 - 1$) rotational transitions are commonly used as a tracer of H₂ mass (e.g., [38]).

1.4 Radio and mm/submm telescopes

As explained in previous sections, CO and HI observations are crucial to investigate the stellar production through the gas content in galaxies. While the HI can be directly detected using the 21-cm line ($f_{\text{HI}} \approx 1.42$ GHz) with radio telescopes, the bright CO rotational lines (the most commonly used H₂ tracer) are emitted at mm wavelengths (e.g., $\lambda_{\text{CO}(1-0)} \approx 2.6$ mm and $\lambda_{\text{CO}(2-1)} \approx 1.3$ mm) must be observed with mm/submm telescopes.

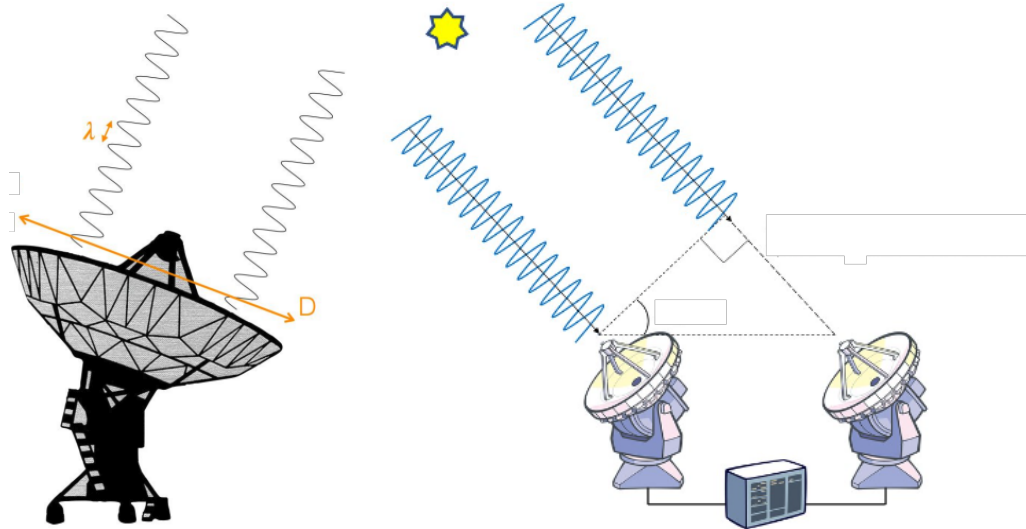


Figure 1.7: Schematics of a single dish antenna (left), and an interferometer (right), in their most basic configurations. While single antennas collect radiation only over the area defined by the surface of the dish, an interferometer collects radiation from several antennas (two or more). Although single dish telescopes are better at recovering the total flux than interferometers, the latter can space dishes at separations much larger than the diameter of a single dish and thereby achieve the higher angular resolution essential to resolving disks of galaxies. Images from *How ALMA Works Vol. 2: Combining Multiple Antennas into One Radio Interferometer*.

Although HI is observed with cm-wave telescopes and CO with mm/submm-wave telescopes, the basic concepts of radio astronomy apply for both bands. Astronomical observations at these wavelengths can be performed using mostly two categories of telescopes: single-dish telescopes (i.e., only one radio dish –also called an antenna– collecting radiation; left panel of Fig. 1.7), and interferometers (i.e., multiple radio dishes, effectively synchronized and operating as a whole instrument; right panel of Fig. 1.7). Even though these telescopes complement more than exclude each other, a given instrument can perform some tasks better than the other one. For instance, to obtain a precise measurement of a large-scale structure on the sky and its total line emission flux, single-dish telescopes could be the best option. Covering a large area on the sky with several pointings, they provide a good balance between sensitivity of the detector (reasonable time spent on source) and the level of detail of the structure. For other tasks, like to see

the detailed structure of a compact source, an interferometer is the best solution. Interferometers can achieve a better angular resolution compared to single-dish telescopes. In simple terms, the angular resolution of a telescope is well described by $\theta \approx 1.22 \lambda/D$, where λ is the wavelength of the radiation detected and D is the size of the instruments. For single antennas, D is given by the diameter of the dish; the size of θ (i.e., the smaller theta, the finer the amount of detail that can be resolved) is thus limited by the capability to construct highly precise and large parabolic dishes (which at some point becomes impossible). For interferometers, D corresponds to the distance between antennas, which is more straightforward to be well calibrated (in terms of the setup of antennas). In summary, for a single dish or an interferometer operating at the same wavelength, the final decision of the instrument should rely on the main scientific aim to achieve.

Large single-dish single-pointing CO and HI surveys have made remarkable contributions to understand how the gas content varies with galactic mass. Nevertheless, spatially resolved data are critical to understand the complete picture of the baryon cycle in galaxies, how the gas is transported within galaxies, and how its local physical conditions modulates the star-formation activity. In this regard, the new generation of radio, millimeter, and sub-millimeter telescopes are now enabling observations and analysis of how physical conditions in the molecular gas vary between the different structural components in galaxies in the local Universe via high angular resolution CO data. Since in this work we base our analysis on data taken from the CARMA, ALMA, and VLA telescopes, we describe briefly the main features of these three radio and mm/submm facilities in the following sub-sections.



Figure 1.8: VLA antennas at the Plains of San Agustin, New Mexico, USA. Credits to the National RadioAstronomy Observatory, NRAO.

1.4.1 The VLA telescope

The Karl G. Jansky Very Large Array, VLA (see Fig. 1.8) is a radio-interferometer (operating at wavelengths between 1 and 50 GHz), using 27 25-m antennas located on the Plains of San Agustin in New Mexico, USA. The location was chosen based on the low-humidity desert climate, which is critical for observations at the frequencies of some VLA's bands (e.g., 23 GHz). Water molecules distort radio waves since they can absorb and emit radiation at similar wavelengths that interfere astronomical observations, for instance altering the radiation path-length and the signal phase of the calibrator source. Therefore, radio detectors are required to be in desertlike environments and at high altitudes to reduce the background emission from Earth-based water molecules.

The antennas are sorted in a well known “Y” shape; the main reason is to increase the space coverage of large-scales structures of the observed sources. As briefly explained in the previous

section, the size of the interferometer's aperture depend on the maximum distances between antennas; the wider the array is, the higher the angular resolution at which a specific source can be seen. Antennas can be moved to set the four VLA configurations (assigned with letters A-D), yielding different compromises between brightness sensitivity and angular resolution. The maximum distance between antennas (also called baseline) varies among the different configurations, which span from ~ 37 km for A to ~ 1 km for D. For the 21-cm line (at the 1.4 GHz band), this translates in angular resolutions between ~ 46 and 1.3 arcseconds³ (an arcsecond is $1^\circ/3600$ on the sky).

After 40 years of operation, VLA observations have made important contributions to the understanding of the effects of black holes, protoplanetary disks around young stars, the discovery of magnetic filaments in the Milky Way, probing and constraint cosmological parameters, and to construct a more complete picture of the atomic hydrogen distribution within galaxies and the Universe, among others.

1.4.2 The CARMA telescope

The Combined Array for Research in Millimeter-wave Astronomy (CARMA, [39]) was constructed from nine of the 6.1-m antennas of the Berkeley-Illinois-Maryland Association (BIMA) array, and the six 10.4-m antennas of Caltech's Owens Valley Radio Observatory (OVRO) millimeter array, along with eight 3.5-m antennas from the University of Chicago. The antennas were located at Cedar Flat in the Inyo Mountains of eastern California, at an elevation of 2200 m. The two more extended array configurations contained baselines that ranged in length from 100 m to 1000 m (B configuration) and 250 m to 1900 m (A configuration) to achieve angular

³<https://science.nrao.edu/facilities/vla/docs/manuals/oss/performance/resolution>



Figure 1.9: CARMA antennas at Cedar Flat in the Inyo Mountains, California. Photo by R. L. Plambeck.

resolutions of $0.''33$ and $0.''15$, respectively, at a frequency of 230 GHz. The array was composed by 6 m and 10 m antennas operating in the 1.3 or 3 mm atmospheric windows, and the reference array comprised the 3.5 m antennas and operated in the 1 cm window.

Until its cessation of operations in April 2015 and commencement of ALMA observations, CARMA was one of the most successful millimeter radio observatories in the world. The array made many discoveries in the areas of stellar birth, early planet formation, supermassive black holes (as part of the Event Horizon Telescope), galaxies (e.g., the EDGE-CALIFA survey), galaxy mergers, and more.

1.4.3 The ALMA telescope

The Atacama Large Millimeter/submillimeter Array (ALMA) is the premium telescope for mm-submm astronomy currently operating. Benefitting from the extreme dry climate of the

Atacama desert, Chile, ALMA is located at ~ 5000 m above the sea level to further mitigate mm/submm absorption and emission from water vapor in the atmosphere. ALMA uses 66 high-precision antennas, including 54 12-m dishes and 12 7-m dishes, which corresponds to a collecting area for the array of about 6600 m^2 . The 12-m antennas can be moved to different locations by custom-made Antenna Transporters to form arrays in different configurations. Fifty of the 12-m dishes are deployed in the main array; from the most compact to the most extended arrays, configurations have baselines that range between 160 m to 16 km, respectively. The other 16 dishes are designated as the Atacama Compact Array (ACA), including the 12 7-m and four 12-m antennas deployed in a compact configuration for imaging large-scale structures. The ALMA angular resolution depends on both the baseline and the wavelength observed. For instance, in ALMA's most compact configuration the resolution can range from $0''.5$ at $\lambda = 0.5$ mm (650 GHz) to $8''.5$ at $\lambda = 7.5$ mm (40 GHz). In the most extended 12-m configuration, ALMA's resolution range from 9 milliarcseconds at 0.7 mm (460 GHz) to 110 milliarcseconds at 7.5 mm (40 GHz).

ALMA has revolutionized radio astronomy during its first decade of operations, broadening our knowledge in several fields. The telescope has allowed the study of the cosmic light that straddles the boundary between radio and infrared. Most objects in the Universe emit this kind of energy, so the ability to detect it has been a driver for astronomers for decades. In this way, ALMA has opened a new window on the Universe, capturing never-before-seen details about the very first stars and galaxies, probing the heart of the Milky Way, and directly imaging the formation of planets.



Figure 1.10: ALMA antennas at the Chajnantor Plateau, 5000 m above the sea level. *Credits:* ALMA (ESO/NAOJ/NRAO)/W. Garnier (ALMA).

1.5 The star-formation activity in the local Universe

In the last decades, the increasing amount of data from the new generation of telescopes has allowed the construction of multi-wavelength galaxy surveys, which provide statistically significant results and are essential for understanding ensemble trends in galaxy evolution. Analysing these databases, studies have revealed that there is a tight connection between the total star formation rate and the total stellar mass for a large fraction of galaxies. That is, as long as a galaxy has a sufficient gas reservoir available to form new stars, the amount of stars it produces will be directly proportional to its current stellar mass (the sum of the masses of all the stars within the galaxy, M_*). In such cases, we say that a given galaxy forms new stars on the galaxy star-formation main sequence (hereafter SFMS, see 1.11; e.g., [14, 15, 40–43]). The existence of the SFMS suggests a useful galaxy classification based on how active galaxies are in terms their stellar production, which can be summarized in the following categories (as shown in Fig. 1.11):

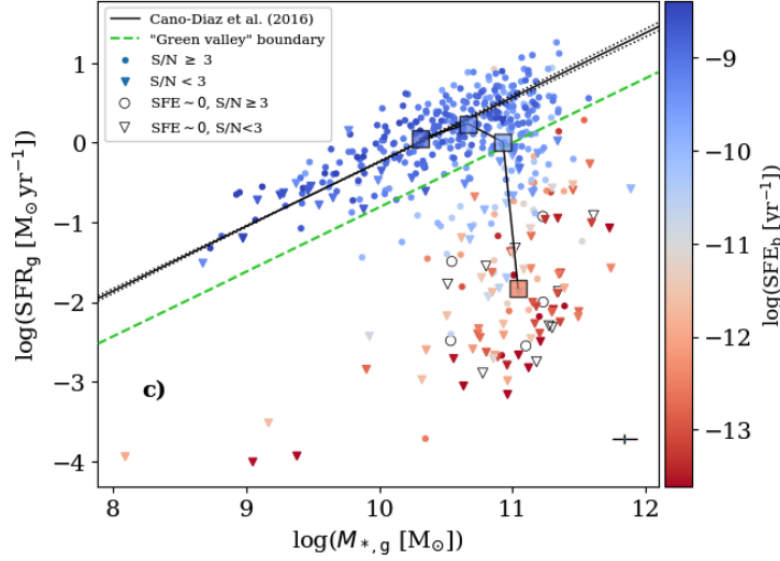


Figure 1.11: Integrated M_* versus SFR relation for galaxies selected from the Calar Alto Legacy Integral Field Area survey, CALIFA [13], as shown in Colombo et al. (2020; [14]). Points in the plot, which represent galaxies, are conveniently colored according to how efficient is the conversion from molecular gas into stars within them. Main sequence galaxies (blue points) tend to have high SFRs and are well represented by the best-linear fit for main sequence galaxies from Cano-Diaz et al. (2016; [15]). Conversely, SFRs seem to be uncorrelated with M_* in red sequence galaxies (red points), which also have lower star-formation rates than main sequence galaxies. The green dotted line marks the “green valley”, i.e. galaxies transiting from the main to the red sequence and experiencing star-formation quenching.

1. *Blue cloud (or Main Sequence)*: These galaxies have a direct proportionality between their M_* and their star-formation rate (blue symbols). The behaviour of these galaxies can be well described by the blue line in Fig. 1.11.
2. *Red cloud (or Red Sequence)*: Galaxies having star-formation rates significantly lower than those for main sequence galaxies (10s-100s times lower or even null), and with a poor or null correlation between M_* and SFR (red symbols in Fig. 1.11).
3. *Green valley (or transition galaxies)*: These galaxies are have SFR and stellar masses that place them between the blue cloud and the red sequence (see green dashed line in Fig. 1.11).

The bimodal tendencies shown by main sequence and red cloud galaxies suggest interesting questions regarding the physical processes that may produce the transition from the former to the latter. It seems that galaxies halt the production of new stars at a certain point in their evolution; this phenomena is usually referred as the star-formation “quenching” (which makes reference to “cessation”). Some studies (e.g., [44]) have proposed the idea of two general categories of quenching processes:

- *Environmental quenching*: Environment (i.e. the amount of gas, dust, and other galaxies around the galaxy under study) can play a key role in regulating the star formation activity. On the one hand, galaxies rich in gas with low or intermediate stellar masses are commonly found in environments with low density, suggesting a strong interplay between environment and the baryon cycle (e.g., [45, 46]). On the other hand, high-density environments tend to preferentially host red galaxies (e.g., [47–49]), since galaxies can lose the ability to accrete gas from their surroundings when they are immersed in a cluster of galaxies (e.g., [50–55]).
- *Mass quenching*: Intrinsic mechanisms are usually associated with the activation and regulation of the physical processes relevant for the star-formation activity. These mechanisms are also expected to act differently depending on the structural components within galaxies, resulting in variations of the stars production when comparing bulges, bars, or disks. This form of star-formation quenching has been broadly associated with different ways to alter the physical conditions of the gas and how this impacts the production of new stars.

Although the two quenching modes represent a well defined evolutionary stage of galaxies, it is still not clear if the star-formation quenching is primarily driven by a change in the star formation efficiency, the reduction of the molecular gas content, or a combination of multiple

processes.

1.6 Main aims of this thesis

Since the production of new stars takes place in molecular clouds, the characterization of the processes that control the amount of molecular gas and the rate at which it is converted into stars is essential. Although considerable progress in this area has been accomplished, our conceptual understanding has been limited due to the challenges in connecting global studies (i.e., sampling of large numbers of spatially unresolved galaxies) with spatially resolved studies, which are frequently restricted to a handful of galaxies and do not span a significant range of masses, environments, and types. The synergies between multiwavelength galaxy surveys represent a powerful tool to overcome these limitations, providing a unique opportunity to address the key questions regarding galaxy evolution. Some of the topics that can be uniquely investigated using this combination are:

- *What local factors regulate the conversion of H_2 into stars?* The efficiency of the conversion from H_2 into stars can be described using the depletion time of the molecular gas $\tau_{\text{dep}} = \Sigma_{\text{mol}}/\Sigma_{\text{SFR}}$, where Σ_{mol} and Σ_{SFR} are the molecular gas and the star formation rate per unit area, respectively. Due to the close relation between star formation and gravitational collapse, an easy exercise is to compare τ_{dep} with some dynamical time scales related to gravity. On the one hand, τ_{dep} is usually compared to the free-fall time $\tau_{\text{ff}} = (G\rho_{\text{tot}})^{-1/2}$ on physical scales of GMCs, where ρ_{tot} is the volume density of the total stellar and molecular gas mass and G is the gravitational constant. On the other hand, the depletion time can be compared on galaxy scales to the orbital time scale $\tau_{\text{orb}} = \Omega^{-1}$, where Ω is the angular

velocity of the gas around the galaxy. Based on these definitions, τ_{dep} being longer than both τ_{ff} and τ_{orb} should reflect the inefficiency of the conversion from H_2 into stars, suggesting that some mechanisms may be modifying the natural rate of the star formation. In this regard, our understanding of these spatial and time scales is still limited, as well as how these may depend on some global galaxy properties, like morphology or total molecular gas content. In Chapter 2, we try to address these questions by analyzing a subsample of 81 galaxies selected from the EDGE-CALIFA survey [3], which is one of the best samples currently available due to its good statistical representation of galaxy morphologies and/or environments in the local Universe.

- *Are the atomic and molecular gas affected similarly by environmental effects?* A particular interest in modern astrophysics is focused on verifying if environmental factors affecting the HI content of a galaxy (e.g., those related to galaxy clusters, which are groups of galaxies gravitationally bound and interacting) are reflected in the H_2 content within that galaxy (impacting the production of stars as well). For instance, one of the most common environmental processes affecting the gas distribution within galaxies in a cluster is the ram pressure stripping (or RPS; Gunn & Gott 1972 [56]), who suggest that the gas in these galaxies can be removed by “winds” due to the interaction with the hot intracluster medium (ICM; see Fig. 1.12). If we use RPS as a stereotypical environmental process, three different scenarios can be identified: i) Both HI and H_2 are removed and/or disturbed simultaneously by the same environmental process(es); ii) most of the atomic gas is removed before the molecular gas starts being affected; and iii) although both the atomic and molecular gas are affected, they are altered in different ways. Some studies (e.g., [57]) have identified

an increase in the H_2 deficiency (i.e., how low the HI content is compared to normal star-forming galaxies) for HI-deficient galaxies, which suggests that both the molecular and atomic gas are affected similarly. Also, they have shown that even though HI deficiencies are not significantly correlated with global H_2 deficiencies, the resolved properties of molecular gas do correlate with HI deficiency. They find that HI deficient galaxies have more centrally concentrated H_2 . In other words, for disks that are more truncated due to atomic gas removal in the outermost parts of galaxies, we should expect an increase in their central H_2 surface densities. Spatially resolved HI and H_2 observations allow us to compute the molecular-to-atomic gas ratio in high detail, which is a useful indicator of the gas phase balance. They can help us to understand how the HI-to- H_2 transition is affected by environmental effects and their impact on the star-formation efficiency across a wide variety of galaxy structures. In Chapter 3, we investigate these topics in 38 galaxies selected from the VERTICO survey [6], which comprises CO(2-1) and HI observations for 51 galaxies from the Virgo galaxy cluster undergoing different stages of environmental quenching.

- *How do galaxies grow and age?* Although the continuing accretion of gas is crucial to maintain the star formation activity in a galaxy, studies suggest that gas depletion alone and galaxies transformed into “red” ellipticals due to merging events cannot explain completely the ultimate fate of galaxies. For instance, gas can be removed by powerful starburst or via active-galactic nuclei activity (e.g., strong winds due to powerful gravitational effects from supermassive black holes in some galaxy centers). On the one hand, the conversion of gas into stars could potentially stop smoothly due to a slow aging process as cold gas inflow decreases or is quenched on short timescales in galaxies within high-density en-

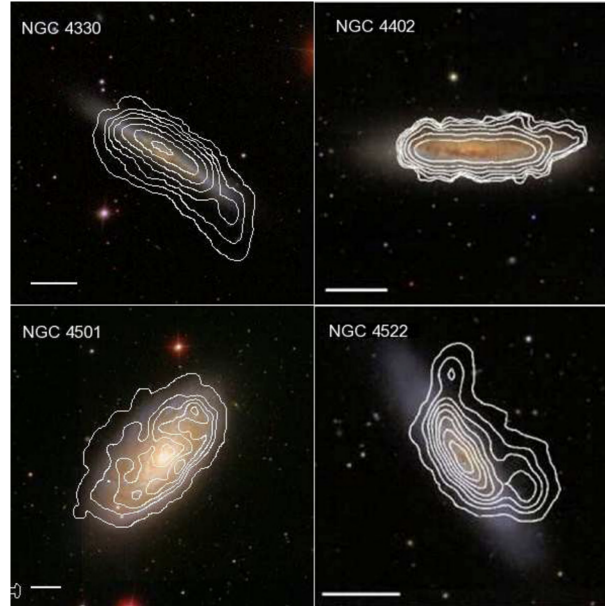


Figure 1.12: Ram pressure stripping of the HI gas in four galaxies from the Virgo cluster. The optical images are a color composite of three filters from the Sloan Digital Sky Survey, SDSS, overlaid with HI contours from the VIVA survey [16]. Since gas is less gravitationally bound to galaxies than stars, HI is noticeably more disturbed by ram pressure stripping than the stellar disk. Image taken from Wong et al. (2014; [17]).

vironments. On the other hand, star formation may depend also on the local physical processes and conditions in the gas, which could vary with galactocentric radius, galaxy structures, among others. Therefore, it is crucial to determine if the ageing/quenching is mostly driven by gas depletion, or perhaps it is induced by local physical processes. In Chapter 4, we study some of these star-formation quenching mechanisms using CO(2-1) and optical data for 60 galaxies selected from CALIFA as part of the ACA EDGE survey. Compared to other local galaxy surveys, ACA EDGE is designed to mitigate selection effects based on CO brightness and morphological type, which makes it ideal to investigate the quenching mechanisms modulating the transition from main sequence to red sequence galaxies.

In this thesis, we investigate these topics by implementing an holistic approach. We an-

alyzed three sets of dissimilar galaxy samples in order to test how the molecular gas varies depending on the galaxy environments, total galaxy stellar mass, or galaxy morphology, among others. To do so, we designed a common methodology and a variety of computational tools that allowed us to characterize the star-formation efficiency in the different galaxy surveys. Although with some limitations, our idea is to give a broad picture of the main properties and factors that impact the efficiency of the star formation activity in the local Universe.

Chapter 2: The EDGE-CALIFA Survey: The Resolved Star Formation Efficiency and Local Physical Conditions

2.1 Introduction

Star formation is one of the most important evolutionary processes that shape galaxies over cosmic times. Either from the inter-galactic medium or through galaxy-galaxy interactions, the accretion of gas into a galaxy potential well provides the fuel for future star formation (e.g., [22, 23]). The mechanisms behind the conversion of gas into stars have been investigated in both distant and nearby galaxies [58, 59]. The [26, 27] seminal studies of the galaxy star formation scaling relations in terms of both the star formation rate and neutral gas surface densities (Σ_{SFR} and Σ_{gas} , respectively), showed they are strongly correlated. More recent studies of the scaling laws between gas, stars, and star formation activity show that the latter is most closely related to molecular gas (H_2), and focus on the mechanisms that convert H_2 into stars, as the main gas reservoir for star formation [12, 28–32].

Stars form in Giant Molecular Clouds (GMCs) in which the molecular gas is the main constituent (e.g., [24]). We usually trace molecular gas through observations of the low- J transitions of the carbon monoxide (CO) molecule which provide a good measure of the total molecular mass. The $^{12}\text{C}^{16}\text{O}(J = 1 - 0)$ transition has been commonly used as a tracer of H_2 since it is

the second most abundant molecule and it can be easily excited in the cold Interstellar Medium (ISM). The CO(1-0) emission line is usually optically thick, and the conversion of CO luminosity, $L'_{\text{CO}1-0}$, into molecular gas mass, M_{H_2} , is done through a CO-to-H₂ conversion factor α_{CO} (e.g., [38]) which appears reasonably constant in the molecular regions of galactic disks but changes at low-metallicities and frequently in galaxy centers in response to environmental conditions (e.g., [60, 61]).

In the last decades a sharp increase in optical data on galaxies has enabled the detailed study of structure assembly in the Universe, with the goal of understanding the mechanisms that drive the Universe from the very smooth state imprinted on the cosmic microwave background radiation to the galaxies we observe today. Optical spectroscopic surveys (e.g. zCOSMOS, [62]; Sloan Digital Sky Survey III, [63]; KMOS^{3D}, [64]; SINS, [65]) have shown the relations between star formation, stellar population, nuclear activity, and metal enrichment for unresolved galaxies in a broad range of redshifts. Meanwhile, gas surveys of nearby galaxies have enabled the exploration of the physics behind the star formation relations (e.g., [30, 32, 66, 67]). These data have revealed that the star formation rate responds to two main factors: the molecular gas content and the stellar potential of the system. An important piece of information is the internal structure of the galaxies. The new generation of Integrated Field Unit (IFU) spectroscopy surveys (e.g., Calar Alto Legacy Integral Field Area, CALIFA, [13]; SAMI, [68]; MaNGA, [69]) have provided detailed spectral imaging data with unprecedented spectral and spatial coverage and good resolution, giving the opportunity to map metallicities, dynamics, extinctions, SFRs, stellar mass density, and other quantities across galaxies. In addition, imaging spectroscopy of the molecular gas from millimeter-wave interferometers [3, 70, 71] adds invaluable information to understand the baryon cycle in galaxies in the local Universe, where star formation has experienced a drastic

decline since the peak of cosmic activity [59].

The study of star formation in galaxies demands a holistic approach, since the phenomenon is controlled by multiple processes and it covers a broad range of scales and environments. The analysis of a broad range of galaxy types with multi-waveband datasets is therefore essential to understand the physical conditions that drive star formation activity. The Extragalactic Database for Galaxy Evolution (EDGE) survey is one of the legacy programs completed by the Combined Array for Millimeter-wave Astronomy (CARMA) interferometer [39], spanning imaging observations of CO emission in 126 local galaxies. The EDGE survey, combined with the IFU spectroscopy from the CALIFA survey [13], constitute the EDGE-CALIFA survey [3], which provides ^{12}CO and ^{13}CO ($J = 1 - 0$) images at good sensitivity and angular resolution covering the CALIFA field-of-view.

In this work, we investigate the star formation efficiency (SFE_{gas} , where $\text{SFE}_{\text{gas}} [\text{yr}^{-1}] = \Sigma_{\text{SFR}}/\Sigma_{\text{gas}}$) in the EDGE-CALIFA survey taking advantage of its large multiwavelength data for 81 local galaxies with low inclinations. In particular, we investigate how the SFE_{gas} depends on physical quantities such as galactocentric radius, stellar surface density, mid-plane gas pressure, orbital timescale, and the stability of the gas disk to collapse. This paper is organized as follows: Section 4.2 explains the main characteristics of the EDGE-CALIFA survey and the sample selection. In section 2.3 we present the methods employed for data analysis, including the CO stacking procedure and the equations we used to derive the basic quantities. Finally, in sections 2.4 and 2.5 we present our results, discussion, summary and conclusions of this work, respectively.

2.2 Data products

2.2.1 The EDGE and CALIFA surveys

The EDGE-CALIFA survey [3] is based on the optical Integrated Field Spectroscopy (IFS) CALIFA and CO EDGE surveys. In the next paragraphs, we briefly summarize the main features of these two datasets.

The Calar Alto Legacy Integral Field Area survey, CALIFA [13], comprises a sample of approximately 800 galaxies at $z \approx 0$. The data were acquired by using the combination of the PMAS/PPAK IFU instrument [72] and the 3.5 m telescope from the Calar Alto Observatory. PMAS/PPAK uses 331 fibers each with a diameter of $2''.7$ sorted in an hexagonal shape which covers a field-of-view (FoV) of $\sim 1 \text{ arcmin}^2$. Its average resolution is $\lambda/\Delta\lambda \sim 850$ at $\sim 5000\text{\AA}$ with a wavelength range that spans from 3745 to 7300 \AA . CALIFA galaxies are selected such that their isophotal diameters, D_{25} , match well the PMA/PPAK FoV, and they range from 45 to 80 arcsec in the SDSS r -band [73]. The CALIFA survey uses a data reduction pipeline designed to produce data cubes with more than 5000 spectra and with a sampling of $1 \times 1 \text{ arcsec}^2$ per spaxel. For more details, see [13].

The Extragalactic Database for Galaxy Evolution, EDGE, is a large interferometric CO and $^{13}\text{CO } J = 1 - 0$ survey which comprises 126 galaxies selected from the CALIFA survey. The observations were taken using the CARMA in a combination of the E and D configurations for a total of roughly 4.3 hr per source, with a typical resolution of 8 and 4 arcsec, respectively. The observations used half-beam-spaced seven-point hexagonal mosaics giving a half-power power field-of-view of radius $\sim 50 \text{ arcsec}$. The data are primary-gain corrected and masked where

the primary beam correction is greater than a factor of 2.5. The final maps, resulting from the combination of E and D array data, have a velocity resolution of 20 km s^{-1} and typical velocity coverage of 860 km s^{-1} , a typical angular resolution of 4.5 arcsec, and a rms sensitivity of 30 mK at the velocity resolution. For more details, see [3].

2.2.2 `edge_pydb` database

The EDGE-CALIFA survey provides global (integrated) and spatially resolved information about the molecular/ionized gas and stellar components in 126 nearby galaxies, comprising ~ 15000 individual lines-of-sight. In the context of this work, and to provide easy yet robust access to this large volume of data, we have used one main source of data to perform our analysis.

The `edge_pydb` database (Wong et al. in prep.) is a versatile PYTHON environment that allows easy access and filtering of the EDGE-CALIFA data in the variety of analyses we aim to perform. `edge_pydb` encompasses a combination of global galaxy properties and spatially resolved information, with a special emphasis on estimation of the CO moments from smoothed and masked versions of the CARMA CO datacubes. All data have been convolved to a common angular resolution of $7''$. By using the PIPE3D data analysis pipeline (see [74, 75] for more details), the convolved optical datacubes are reprocessed to generate two dimensional maps at $7''$ resolution. The pipeline fits the stellar continuum to the emission lines for each spaxel in each datacube (adopting a Salpeter [76] Initial Mass Function, IMF), generating maps sampled on a square grid with a spacing of $3''$ in RA and DEC. To identify a given pixel in the grid, the data are organized by using a reference position (taken from HyperLEDA¹) and an offset

¹<http://leda.univ-lyon1.fr/>

indicating spatial position. The final database also contains ancillary data, including information from HyperLEDA, NED², among others.

2.3 Methods

2.3.1 Stacking of the CO spectra

Although many EDGE-CALIFA galaxies have high signal-to-noise detections of CO emission in their central regions, emission is generally faint in their outer parts. Typically, the decrease in emission takes place from $r = 0.5r_{25}$ outwards (around $1.1R_e$, by assuming that $r_{25} \approx 2.7R_e$; [77]). [3] published maps of velocity-integrated CO emission and discussed various masking techniques for recovering flux and producing maps with good signal to noise; even so, they tend to miss flux in regions of weak emission and to underestimate the CO flux (see Figure 9 in [3]). Since one of the main goals of this work is to find how the H_2 content changes as a function of radius, it is essential to recover low-brightness CO emission line in the outermost parts of galaxies.

Maps with both good spatial coverage and sensitivity are crucial to set thresholds and timescales for these dependencies. In order to cover a broad range of galactocentric radii, we perform spectral stacking of the ^{12}CO ($J = 1 - 0$) emission using the $H\alpha$ velocities to coherently align the spectra while integrating in rings. The CO spectral stacking helps recover CO flux in the outer parts of our galaxies, improving our ability to probe the SFE_{gas} in a variety of environments. Many of the molecular gas surveys have measured some of these dependencies in a similar fashion (e.g., using the CO [$J = 2 - 1$] spectral stacking; [78]), although they mostly covered a small

²<https://ned.ipac.caltech.edu/>

range of morphological types and/or stellar masses, or were limited to very local volumes that are subject to cosmic variance because they represent our particular local environment. Although the EDGE-CALIFA survey does not yet encompass resolved HI observations, we will explore the efficiency with respect to total gas and compare it to previous results by assuming a prescription for the atomic gas while keeping in mind the limitations of this methodology.

We perform a CO emission line stacking procedure following the methodology described by [78]. The method relies on using the IFU $H\alpha$ velocity data to define the velocity range for integrating CO emission. The key assumption of this method is that both the $H\alpha$ and the CO velocities are similar at any galaxy location. This assumption is consistent with results by [79], who found a median value for the difference between the CO and $H\alpha$ rotation curve of $\Delta V = V_{\text{rot}}(\text{CO}) - V_{\text{rot}}(H\alpha) = 14 \text{ km s}^{-1}$ (within our 20 km s^{-1} channel width) when analyzing a sub-sample of 17 EDGE-CALIFA rotation-dominated galaxies. As we will discuss later, after shifting CO spectra to the $H\alpha$ velocity, we integrate over a window designed to minimize missing CO flux. The smaller the velocity differences between CO and $H\alpha$, the better the signal-to-noise. Similarly, the smaller the velocity window we implement, the smaller the noise in the integrated flux estimate.

We constructed an algorithm coded in PYTHON that implements this procedure. Since we are interested in radial variations in galactic properties, we stack in radial bins $0.1r_{25}$ wide. In practice, galactocentric radius is usually a well determined observable and it is covariant with other useful local parameters, which makes it a very useful ordinate [78].

We recover the CO line emission by applying radial stacking based on the following steps: We convert $H\alpha$ velocity from the optical into the radio velocity convention. Then, for each spaxel in an annulus we shift the CO spectrum by the negative $H\alpha$ velocity. This step aligns

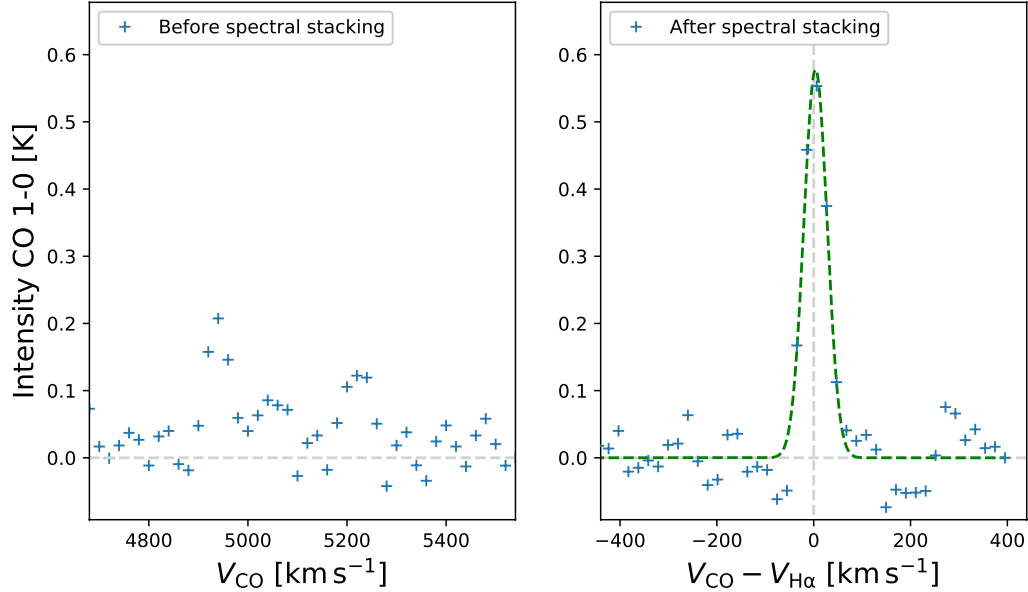


Figure 2.1: Example showing effects of spectral stacking. The average CO spectrum within an annulus that spans from 0.65 to $0.75 r_{25}$ in NGC 0551 is shown. The left panel shows the average of all spectra in the annulus in the observed velocity frame. The right panel shows the average in the velocity frame relative to $H\alpha$, along with the best Gaussian fit profile (green dashed line).

the CO spectrum for each line-of-sight at zero velocity if the intrinsic $H\alpha$ and CO velocities are identical. We then average all the velocity-shifted CO spaxels in an annulus, and integrate the resulting average spectrum over a given velocity window to produce the average intensity in the annulus.

Figure 2.1 shows the usefulness of the stacking procedure in recovering CO emission. As an example, we show the average CO spectrum of NGC 0551 within an annulus that spans from 0.65 to $0.75 r_{25}$ ($\sim 1.3 - 1.7 R_e$). The left panel contains the average CO spectra within the given annulus using the observed velocity frame, while the right panel shows the average CO spectra after shifting by the observed $H\alpha$ velocity. If the CO and $H\alpha$ velocities are identical for all spaxels, then the resulting CO emission would appear at zero velocity. This procedure allows us to co-add CO intensities coherently and reject noise. Figure 2.1 also shows the best

Gaussian fit for the averaged-stacked spectra. We expect that in an ideal case the total intensity integrated over the full velocity range ($\sim 860 \text{ km s}^{-1}$) is exactly the same in both cases, but the noise would be much larger without the spectral stacking. Without performing the stacking procedure the CO line emission is not evident, and the signal-to-noise ratio in the measurement of CO velocity-integrated intensity is lower. Interferometric deconvolution artifacts that produce negative intensities at some velocities, resulting from incomplete uv sampling and spatial filtering, would also get into the integration more easily without stacking and artificially reduce the intensity.

2.3.2 Extracting fluxes from stacked spectra

After we compute the stacked spectra, we extract the total CO fluxes for each annulus as a function of galactocentric radius. To do this in a way that is likely to include all the CO flux but minimizes the noise, we want to select a matched velocity range that is just large enough to include all CO emission and exclude the baseline (which only adds noise). In order to investigate the ideal integration range we fit Gaussian profiles to each averaged-stacked CO spectrum with a detection. We reject fits which have central velocities more than $\pm 80 \text{ km s}^{-1}$ from zero velocity. We also reject spectra with FWHMs narrower than 40 km s^{-1} (2 channels). Results for valid stacked spectra fits are shown in the left panel of Figure 2.2, color coded by the reduced chi-squared of the fit and plotted against normalized galactocentric radius.

We use these data to define a velocity window for the integrated CO line emission fluxes in the stacked spectra. For each radial bin, we define an integration range that guarantees that we integrate the CO line profile between $\pm \text{FWHM}$ in at least 80% of annuli. This is represented

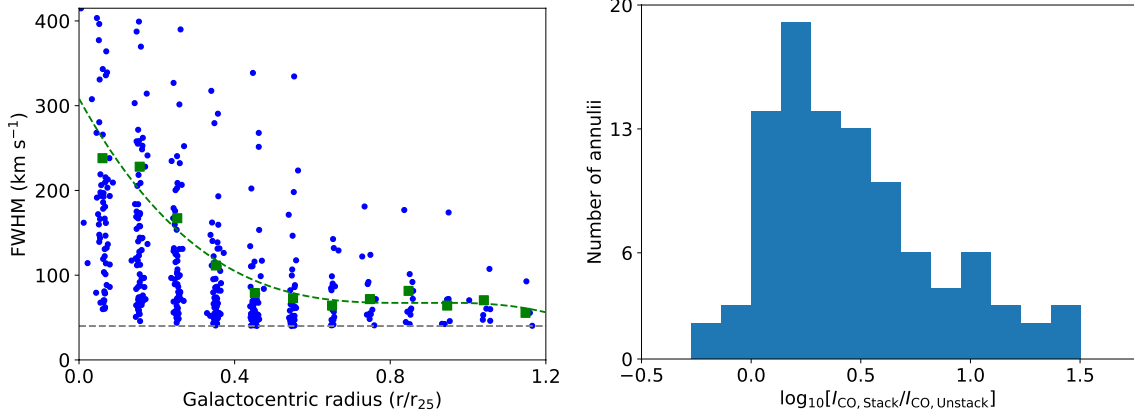


Figure 2.2: *Left*: FWHM of CO line as a function of galactocentric radius. Small colored dots show the FWHM of a Gaussian fit to the stacked spectrum in an annulus. Large green squares indicate the FWHM lying above 80% of the points at that radius, and the dashed green line is the fit to the squares; we use this function to define the window of flux integration as a function of r_{gal} . The gray-dashed line marks the limit at which we reject spectra with a Gaussian fit narrower than 40 km s^{-1} (2 channels in the CO datacubes). *Right*: Ratio between the final stacked and unstacked integrated CO(1–0) line intensity per annulus for annuli located at $r/r_{25} > 0.5$, which include just 2σ detection spaxels.

by the green dots in Figure 2.2. We assume that this window is sufficient to contain most of the CO flux, and we can use it to compute errors where no CO is detected. To obtain a prescription we fit the best third-order polynomial to the green squares (green dashed-line) as a function of galactocentric radius, $\text{FWHM}(r_{\text{gal}})$. Finally, we recompute the CO line emission fluxes for the stacked spectra by integrating the CO stacked spectrum over $\pm \text{FWHM}(r_{\text{gal}})$. We extract the integrated flux uncertainties by taking the rms from the emission free part of the stacked CO spectra.

Using spectral stacking we reach a typical deprojected CO intensity 3σ uncertainty of $I_{\text{CO}} \approx 0.25 \text{ K km s}^{-1}$, or a 3σ surface density sensitivity of $\Sigma_{\text{mol}} \approx 1.1 M_{\odot} \text{ pc}^{-2}$, which represents the typical sensitivity in the outermost regions of galaxy disks. The right panel of Figure 2.2 shows the ratio between the final stacked and unstacked integrated CO(1-0) line intensity, per annulus, located at $r > 0.5r_{25}$ (or $r > 1.3R_e$), and includes just 2σ detection spaxels. The

histogram shows that the distribution peaks at $\log[I_{\text{CO,Stack}}/I_{\text{CO,Unstack}}] \sim 0.47$, meaning that, in overall, we are recovering ~ 3 times more flux with the stacking procedure.

2.3.3 Basic equations and assumptions

To compute the extinction-corrected SFRs, we estimate the extinction (based on the Balmer decrement; see [3]) for each $7''$ spaxel using

$$A_{\text{H}\alpha} = 5.86 \log \left(\frac{F_{\text{H}\alpha}}{2.86 F_{\text{H}\beta}} \right) \quad (2.1)$$

where $F_{\text{H}\alpha}$ and $F_{\text{H}\beta}$ are the fluxes of the respective Balmer lines, and the coefficients assumes a [80] extinction curve and an unextincted flux ratio of 2.86 for case B recombination. Then, the corresponding SFR (in $M_{\odot} \text{ yr}^{-1}$) is obtained using [81]

$$\text{SFR} = 1.61 \times 7.9 \times 10^{-42} F_{\text{H}\alpha} 10^{\frac{A_{\text{H}\alpha}}{2.5}}, \quad (2.2)$$

which adopts a Salpeter Initial Mass Function (IMF) corrected by a factor of 1.61 to move it to a Kroupa IMF [82]. We use this to compute the Star Formation Rate surface density, Σ_{SFR} in $M_{\odot} \text{ yr}^{-1} \text{ kpc}^{-2}$, by dividing by the face-on area corresponding to a $7''$ spaxel, given the angular diameter distance to the galaxy.

The gas surface density is computed as $\Sigma_{\text{gas}} = \Sigma_{\text{mol}} + \Sigma_{\text{atom}}$, where Σ_{H_2} is derived from the integrated CO intensity, I_{CO} , by adopting a Milky-Way constant CO-to- H_2 conversion factor, $X_{\text{CO}} = 2 \times 10^{20} \text{ cm}^{-2} (\text{K km s}^{-1})^{-1}$ (or $\alpha_{\text{CO}} = 4.3 M_{\odot} [\text{K km s}^{-1} \text{ pc}^{-2}]^{-1}$). For the CO $J = 1-0$

emission line, we use the following expression to obtain Σ_{mol} (i.e., [30])

$$\Sigma_{\text{mol}} = 4.4 \cos i I_{\text{CO}}, \quad (2.3)$$

where I_{CO} is in K km s^{-1} , Σ_{mol} is in $\text{M}_{\odot} \text{pc}^{-2}$, and i is the inclination of the galaxy. This equation takes into account the mass correction due to the cosmic abundance of Helium.

To include in our calculations Σ_{atom} despite the fact that we do not have resolved HI data, we assume a constant $\Sigma_{\text{atom}} = 6 \text{ M}_{\odot} \text{pc}^{-2}$ for face-on disks. This is approximately correct (within a factor of 2) for spiral galaxies out to $r \sim r_{25}$ [30, 83]. This value is also in agreement with Monte Carlo simulations performed by [84] to test different values of Σ_{atom} ; they obtain a normal distribution of $\Sigma_{\text{atom}} = 7 \text{ M}_{\odot} \text{pc}^{-2}$, with a standard deviation of $2 \text{ M}_{\odot} \text{pc}^{-2}$. We also test the influence of metallicity in the CO-to-H₂ conversion factor, α_{CO} , by using the following equation (from Equation 31 in [38]):

$$\alpha_{\text{CO}} = 2.9 \exp\left(\frac{+0.4}{Z' \Sigma_{\text{GMC}}^{100}}\right) \left(\frac{\Sigma_{\text{total}}}{100 \text{ M}_{\odot} \text{pc}^{-2}}\right)^{-\gamma}, \quad (2.4)$$

in $\text{M}_{\odot} (\text{K kms}^{-1} \text{pc}^{-2})^{-1}$, $\gamma \approx 0.5$ for $\Sigma_{\text{total}} > 100 \text{ M}_{\odot} \text{pc}^{-2}$ and $\gamma = 0$ otherwise. We adopt the empirical calibrator based on the O3N2 ratio from [85], and then we use equation 2 from [85] to obtain the oxygen abundances, $12 + \log(\text{O}/\text{H})$. Finally, we derive the metallicity normalized to the solar value, $Z' = [\text{O}/\text{H}]/[\text{O}/\text{H}]_{\odot}$, where $[\text{O}/\text{H}]_{\odot} = 4.9 \times 10^{-4}$ [86].

Although there are many definitions for star formation efficiency (SFE_{gas}), in this work we use SFR surface density per unit neutral gas surface density (atomic and molecular), $\Sigma_{\text{gas}} = \Sigma_{\text{mol}} + \Sigma_{\text{atom}}$, in units of yr^{-1} for each line-of-sight (LoS),

$$\text{SFE}_{\text{gas}} = \frac{\Sigma_{\text{SFR}}}{\Sigma_{\text{gas}}}. \quad (2.5)$$

Midplane gas pressure, P_{h} is computed using the expression by [87],

$$P_{\text{h}} \approx \frac{\pi}{2} G \Sigma_{\text{gas}}^2 + \frac{\pi}{2} G \frac{\sigma_{\text{g}}}{\sigma_{\star,z}} \Sigma_{\star} \Sigma_{\text{gas}}, \quad (2.6)$$

where σ_{g} and $\sigma_{\star,z}$ are the gas and stars dispersion velocities, respectively. We correct the Σ_{\star} by the same 1.61 factor used for the SFR to translate them to a Kroupa IMF. We assume $\sigma_{\text{g}} = 11 \text{ km s}^{-1}$, which has been found to be a typical value in regions where HI is dominant ([30]). This value is also in agreement with the second moments maps included in [88], and is also consistent with the CO velocity dispersion for a subsample of EDGE-CALIFA galaxies [79]. $\sigma_{\star,z}$ is the vertical velocity dispersion (in km s^{-1}) of stars. Although the EDGE-CALIFA database includes σ_z measurements that could allow us to model $\sigma_{\star,z}$, the instrumental resolution of the survey constrains us to use them just in the central parts of the galaxies (for details, see [13]). Therefore, and following the assumptions and derivation included in [30], we use the following expression for $\sigma_{\star,z}$:

$$\sigma_{\star,z} = \sqrt{\frac{2\pi G l_{\star}}{7.3} \Sigma_{\star}^{0.5}}, \quad (2.7)$$

where l_{\star} is the disk stellar exponential scale length obtained by fitting azimuthally averaged profiles to Σ_{\star} in the SDSS r -band and $G = 4.301 \times 10^{-3} \text{ pc M}_{\odot}^{-1} \text{ km}^2 \text{ s}^{-2}$. In cases where we do not have l_{\star} measurements, we use the relation $l_{\star} = [0.25 \pm 0.01] r_{25}$ since it corresponds to the best linear fit for our data. See Section 4.4.1.2 for more information about how both l_{\star} and the

l_\star - r_{25} relation are derived.

The dynamical equilibrium pressure (P_{DE}) is computed following a similar methodology as for P_{h} (e.g., [89–92]). Assuming that the gas disk scale height is much smaller than the stellar scale height, and neglecting the gravity from dark matter, we write P_{DE} as [93]:

$$P_{\text{DE}} \approx \frac{\pi}{2} G \Sigma_{\text{gas}}^2 + \Sigma_{\text{gas}} \sigma_{\text{gas},z} \sqrt{2 G \rho_\star}. \quad (2.8)$$

Here, we assume that $\sigma_{\text{gas},z} = \sigma_{\text{g}} = 11 \text{ km s}^{-1}$, and ρ_\star is the mid-plane stellar volume density from the observed surface density in a kpc-size aperture,

$$\rho_\star = \frac{\Sigma_\star}{0.54 l_\star}. \quad (2.9)$$

This equation assumes that the exponential stellar scale height, h_\star , is related to the stellar scale length, l_\star , by $h_\star/l_\star = 7.3 \pm 2.2$ [94].

The orbital timescale, τ_{orb} , is usually used in the analysis of star formation law dependencies since it can be comparable to timescale of the star formation (e.g., [95, 96]). Following [27] and [28], we compute τ_{orb} using:

$$\tau_{\text{orb}}^{-1} = \frac{v(r_{\text{gal}})}{2\pi r_{\text{gal}}} \quad (2.10)$$

where $v(r_{\text{gal}})$ is the rotational velocity at a galactocentric radius r_{gal} . We obtain the $\text{H}\alpha$ rotation curves for EDGE-CALIFA galaxies from [79]. We use them to adjust an Universal Rotation Curve (URC, [97]) for each galaxy to avoid the noise in the inner and outer edges of the $\text{H}\alpha$ rotation curves.

We compute the Toomre's instability parameter (Q , [98]) including the effect of stars [18].

The Toomre's instability parameter for the stellar component (Q_{star}) is

$$Q_{\text{stars}} = \frac{\sigma_{*,r}\kappa}{\pi G \Sigma_{*}}, \quad (2.11)$$

where $\sigma_{*,r}$ is the radial velocity dispersion of the stars. We compute it using $\sigma_{*,r} = 1.67 \sigma_{*,z}$, valid for most late-type galaxies ([99]). The parameter κ is the epicyclic frequency and can be computed as

$$\kappa = 1.41 \frac{v(r)}{r} \sqrt{1 + \beta}, \quad (2.12)$$

where $\beta = \frac{d \log v(r)}{d \log r}$. This derivative is computed based on the URC fit to the H α rotation curve.

The Toomre's instability parameter for the gas (Q_{gas}) is

$$Q_{\text{gas}} = \frac{\sigma_{\text{gas}}\kappa}{\pi G \Sigma_{\text{gas}}} = \frac{(11 \text{ km s}^{-1})\kappa}{\pi G \Sigma_{\text{gas}}}. \quad (2.13)$$

Since Σ_{*} and Σ_{gas} are averaged and stacked by annuli, respectively, then both Q_{stars} and Q_{gas} are derived radially. The condition for instability in the gas+stars disk is then given by

$$\frac{1}{Q_{\text{star+gas}}} = \frac{2}{Q_{\text{stars}}} \frac{q}{1+q^2} + \frac{2}{Q_{\text{gas}}} R \frac{q}{1+q^2 R^2} > 1, \quad (2.14)$$

where $q = k\sigma_{*,r}/\kappa$. Here, $k = 2\pi/\lambda$ is the wavenumber at maximum instability. Finally,

$$R = \sigma_g/\sigma_{*,r}.$$

2.4 Results and Discussion

2.4.1 Exponential scale lengths

To investigate the spatial relationship between molecular and stellar components, we compute their exponential scale lengths, l_{mol} and l_{\star} , respectively, for a subsample of 68 galaxies. Out of the 81 EDGE-CALIFA galaxies with $i < 75^{\circ}$, these galaxies are selected since their disks are well fitted by exponential profiles and they have at least three annuli available for the fitting. To avoid annuli within the bulge or with significant variations in α_{CO} usually found in central regions of galaxies (e.g., [100]), we do not include Σ_{mol} and Σ_{\star} for $r_{\text{gal}} \leq 1.5$ kpc.

It is well known that the CO distribution and star formation activity are closely related (e.g., [32]). For instance, [101] showed that HERACLES spiral galaxies can be well described by exponential profiles for CO emission in the H_2 -dominated regions of the disk, with similar CO scale lengths to those for old stars and star-forming tracers, and an early study on the EDGE sample found similar results [3]. Here we use the stacking technique to extend the molecular radial profiles and obtain a better measurement of the distribution.

Although molecular clouds have lifetimes spanning a few to several Myr (similar to the stars that give rise to the $\text{H}\alpha$ emission used to compute SFR; e.g., [102–104]), these are quite short compared with lifetimes of the stellar population in galaxies in the EDGE-CALIFA survey (0.4 to 3.9 Gyr; [84]). Consequently, it is not necessarily expected to have comparable distributions for the molecular and the stellar components. However, stellar and CO emission distributions can be similar when the process of converting atomic gas to molecular is driven by the stellar potential [105, 106]. For instance, [78] showed a clear correspondence between l_{CO} and r_{25} ;

this correlation is maintained even in the HI-dominated regions of the disk, supporting the role that molecular gas plays in a scenario when the stellar potential well is relevant in collecting material for star formation [107]. Thus, it is interesting to use the CO stacked data to verify if the exponential decay of Σ_{mol} holds in the outer parts of EDGE-CALIFA galaxies.

The left panel of Figure 2.3 shows the relation between l_{mol} and l_{\star} . The l_{\star} values were obtained by fitting exponential profiles to $\Sigma_{\star}(r_{\text{gal}})$, after averaging it in annuli, while l_{mol} values were determined from $\Sigma_{\text{mol}}(r_{\text{gal}})$ derived from the CO stacking procedure. The left panel of Figure 2.3 also shows the ordinary least-square (OLS) bisector fit weighted by the uncertainties for all scale lengths measured with better than 3σ significance (blue dashed line); we find that $l_{\text{mol}} = [0.89 \pm 0.04] l_{\star}$. This result is in agreement with the relation found by [3] for 46 EDGE-CALIFA galaxies, who obtain $l_{\text{mol}} = [1.05 \pm 0.06] l_{\star}$. Compared with [3], however, the CO radial stacking allows us to compute exponential length scales for a larger galaxy sample (68 in our case) and to constrain them better over a broader range of galactocentric radii. Our results are also in agreement with the exponential length scales for HERACLES ($l_{\text{mol}} = [0.9 \pm 0.2] l_{\star}$; [30]). The inset in the left panel of Figure 2.3 shows the relation between l_{mol} and r_{25} . Using an OLS bisector fit, we find that $l_{\text{mol}} = [0.22 \pm 0.01] \times r_{25}$, which agrees reasonably with [108], who find $l_{\text{mol}} \approx 0.22r_{25}$.

In general, resolved molecular gas surveys exhibit similarity between the stellar light and the CO distributions. [109], using the CO distribution from the BIMA SONG CO survey, showed that when comparing the scale lengths from exponential fits to the CO and the K-band galaxy profile data for 15 galaxies, the typical CO to stellar scale length ratio is 0.88 ± 0.14 . Additionally, single-dish CO measurements plus $3.6\mu\text{m}$ data from the HERACLES galaxies show a correspondence between the stellar and molecular disk ([30, 78]), with an exponential scale length for CO

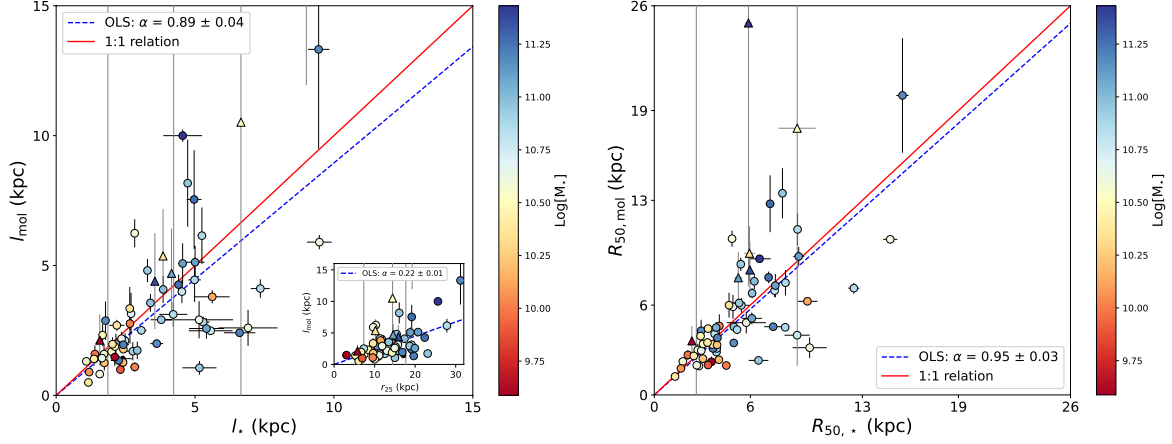


Figure 2.3: *Left*: Comparison between the stellar, l_* , and molecular length scales, l_{mol} , computed by fitting exponential profiles to the respective surface densities as a function of galactocentric radius. The colored circles correspond to 61 EDGE-CALIFA galaxies color-coded by stellar mass derived from SED fitting (see Section 3.2.1). The inset panel shows the comparison between l_{mol} and the isophotal radius r_{25} . The triangles represent uncertain results for which measurements are smaller than 3σ . The solid red and dashed blue lines illustrate the 1:1 scaling and the OLS linear bisector fit (forced through the origin) for all the sources, respectively. *Right*: Relationship between the radii that enclose 50% of the molecular gas and the stellar mass, $R_{50,\text{mol}}$ and $R_{50,*}$, respectively. Conventions and symbols are as in the left panel.

that follows $l_{\text{mol}} \approx 0.2 r_{25}$.

If the radial distributions for molecular gas and stars are similar, we would expect the radii containing 50% of the CO emission and the star light to also be similar. The right panel of Figure 2.3 demonstrates that our data confirm this expectation, as it shows the relation between the radii that enclose 50% of the molecular gas and the stellar mass, $R_{50,\text{mol}}$ and $R_{50,*}$, respectively. The dashed blue line represents an ordinary least-square bisector fit (weighted by the uncertainties) for all our 3σ detections; we find that $R_{50,\text{mol}} = [0.95 \pm 0.03] \times R_{50,*}$.

Table 3.1 summarizes the properties of the 81 EDGE-CALIFA galaxies included in this work and together with the values for l_{mol} , l_* , $R_{50,\text{mol}}$, and $R_{50,*}$ for the 68 galaxies analyzed in this section.

2.4.2 SFE and Local Parameters

In this section, we will look at how local physical parameters affect the star formation efficiency of the total gas, $\text{SFE}_{\text{gas}} = \Sigma_{\text{SFR}} / [\Sigma_{\text{atom}} + \Sigma_{\text{mol}}]$, following methodologies similar to those used by HERACLES [30], against which we will compare results. We compute efficiencies by dividing the star formation rate surface density obtained from $\text{H}\alpha$ corrected for extinction using the Balmer decrement (Eq. 4.5) by the total gas surface density (Eq. 4.10). As discussed in §4.3.1 we assume a constant $\Sigma_{\text{atom}} = 6 M_{\odot} \text{pc}^{-2}$.

The EDGE-CALIFA galaxies are generally at larger distances (~ 23 to 130 Mpc) than the much more local HERACLES sample (3 to 20 Mpc). Both samples have stellar masses spanning a similar range ($\log[M_{\star}/M_{\odot}] = 9.4\text{--}11.4$), but EDGE a larger representation of more massive disks and bulges as HERACLES includes mostly late Sb and Sc objects and lower mass galaxies. The parent sample CALIFA galaxies are selected in a large volume to allow adequate representation of the $z = 0$ population and numbers that allow statistically significant conclusions for all classes of galaxies represented in the survey [13]. The EDGE follow-up selection is biased toward IR-bright objects, but otherwise tries to preserve the variety and volume of the mother sample. CALIFA does not include dwarf galaxies. EDGE otherwise spans a larger range of properties and has a larger sample size than HERACLES, although with lower spatial resolution (~ 1.5 kpc versus ~ 200 pc).

We correct our calculations by the inclination of the galaxy (with a $\cos i$ factor, where i is the inclination angle) to represent physical “face-on” deprojected surface densities (see §4.3.1). Our typical 1σ uncertainty in the SFE_{gas} is 0.22 dex, dominated by the CO line emission uncertainties derived from the stacking procedure after error propagation.

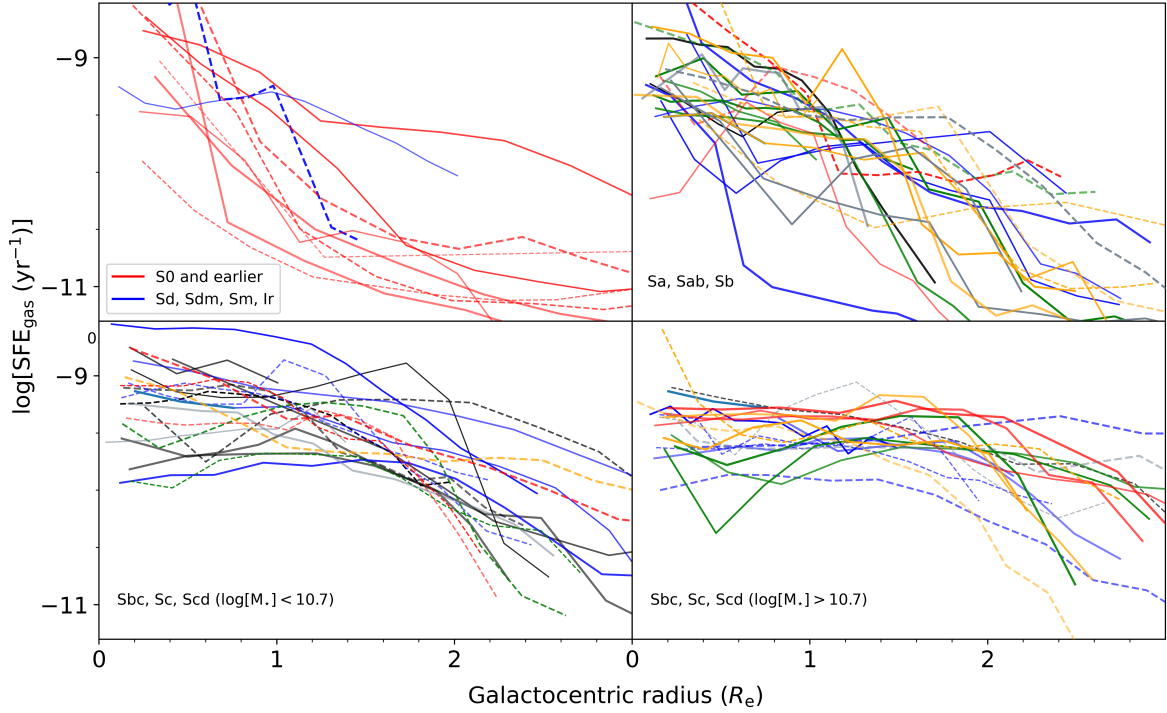


Figure 2.4: SFE_{gas} vs galactocentric radius. Each line indicates the average SFE_{gas} for individual galaxies in $0.1r_{25}$ -wide tilted annuli after stacking. The morphological group for the galaxies in each panel is indicated by the legend in that panel. The plot shows that the SFE_{gas} in individual galaxies generally decreases as a function of galactocentric radius and that the dispersion in SFE_{gas} at particular radii is due mostly to differences between galaxies.

2.4.2.1 SFE and Galactocentric Radius

Figure 2.4 shows the relation between SFE_{gas} and galactocentric radius; the four different panels show grouping of the 81 galaxies. Following modern studies, we use R_e to normalize galactocentric distances, except when we need to compare to published data which use r_{25} . Note that for the EDGE galaxies in this sample, $r_{25} \approx 2.1R_e$. In this figure for clarity we split the Sbc, Sc, and Scd galaxies in two groups by choosing the median of stellar masses of the EDGE-CALIFA sample $\log_{10}[M_*] = 10.7$ [3]. In general, there is a decreasing trend for SFE_{gas} with radius. It is important to note that SFE_{gas} is a fairly smooth function of radius for a given galaxy.

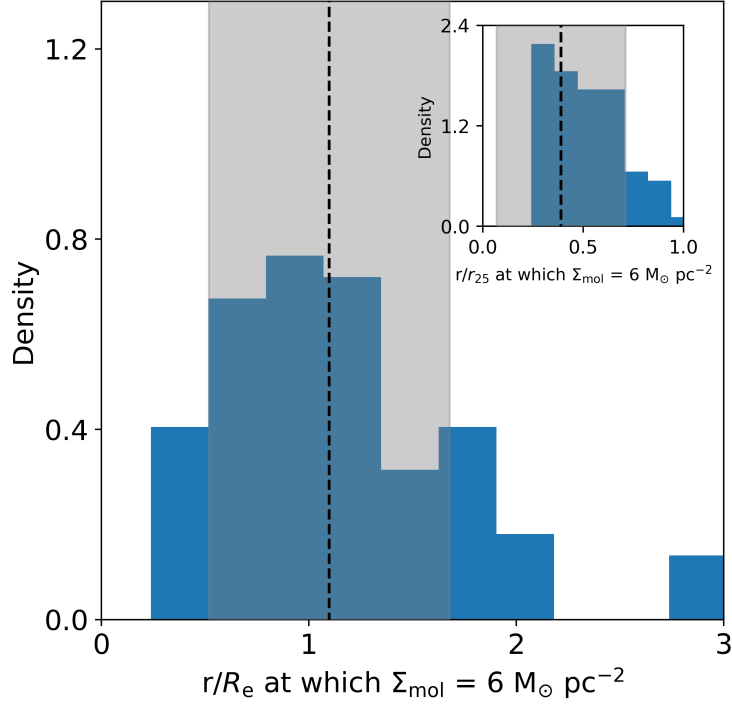


Figure 2.5: Histogram of galactocentric radii at which Σ_{H_2} drops to $6 M_{\odot} \text{pc}^{-2}$, which is the value of Σ_{atom} assumed for EDGE-CALIFA galaxies in this work. The dashed vertical black line is the mean value of r/R_e at which this occurs, corresponding to 1.1 ($0.4r_{25}$; see inset panel). The gray area represents the uncertainty in mean value of r/R_e . The inset shows a similar histogram for r/r_{25} .

In fact, variations between galaxies are frequently larger than variations between most annuli in a galaxy, indicating that the radial decrease in SFE_{gas} within a galaxy is often smooth and that galaxy to galaxy variations are significant.

Figure 2.5 shows the radius at which our measured molecular surface density, averaged over an annulus, is the same as our assumed constant surface density in the atomic disk, $\Sigma_{\text{mol}} = \Sigma_{\text{atom}} = 6 M_{\odot} \text{pc}^{-2}$. The typical radius at which this happens is $r/R_e \sim [1.1 \pm 0.5]$, or $r/r_{25} \sim [0.47 \pm 0.28]$ (see inset panel), which agrees with the value of $r/r_{25} \sim 0.43 \pm 0.18$ found by [30]. Note that in Figure 2.4 the SFE_{gas} is generally smooth across that radius, suggesting that our assumption of a constant Σ_{atom} does not play a major role at determining the shape of the total gas SFE_{gas} .

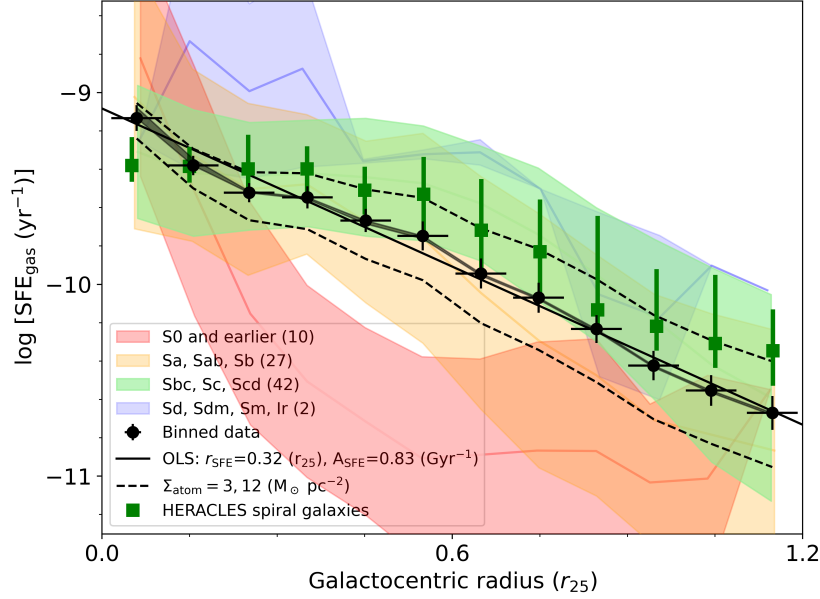


Figure 2.6: *Top*: SFE_{gas} vs galactocentric radius for different morphological types of galaxies. SFE is averaged at each radius over all galaxies of the selected morphological type; types are indicated by shaded color as described in the legend. The vertical extent of the shaded area for each morphological type is the 1σ scatter distribution for that type (see Figure 2.4). Circular dots indicate the average SFE_{gas} and galactocentric radius in stacked annuli for all EDGE-CALIFA galaxies; the black solid line is the OLS linear bisector fit to those points using the model $A_{\text{SFE}} \times \exp(-r/r_{\text{SFE}})$. The error bars are the uncertainties of the mean SFE values in each bin. The two dashed black lines show the effect of increasing and decreasing Σ_{atom} by a factor of two from its assumed value of $6 M_{\odot} \text{pc}^{-2}$. The shaded gray band indicates the amount by which the binned SFE_{gas} would increase if we use the metallicity dependent prescription for α_{CO} . The green squares are the HERACLES data for spiral galaxies. The figure shows that SFE_{gas} depends on radius, stellar mass and morphological type.

Figure 2.6 shows the average SFE_{gas} as a function of the normalized galactocentric radius for each of the four different groups of morphological classification used in Figure 2.4, with $\pm 1\sigma$ variation indicated by the color bands. We note a systematic increase in the average SFE_{gas} from early type (red shaded area) to late type galaxies (blue shaded area). The SFE_{gas} tend to be lower for the early spirals (i.e., S0 and earlier; ten galaxies), which have a steeper profile when compared with the rest of the morphological groups, and therefore showing a significant anticorrelation between SFE_{gas} and r_{gal} (Pearson correlation coefficient of $r = -0.6$). This steepening may reflect the degree of central concentration seen in earlier-type galaxies. Sd-Ir galaxies

show a SFE_{gas} flattening at $r_{\text{gal}} < 0.45 r_{25}$; however, their small amount (only 2 galaxies in our sample) does not allow to conclude that this flattening is statistically significant. When looking at the average SFE_{gas} value, over r_{gal} for all the radial profiles (black-circular dots), we find that the SFE_{gas} decreases exponentially even in regions where the gas is mostly molecular. In EDGE we see an continuous exponential profile for the SFE_{gas} averaged over all galaxies (black line in Figure 2.6). Although still within the error bars, this is in contrast to HERACLES, which sees a leveling of the SFE_{gas} in the inner regions. The greater range of SFE_{gas} s in our sample may be a reflection of the larger range of galaxy spiral types spanned by EDGE compared to HERACLES, which consisted mostly of late types. In fact the Sbc, Sc, and Scd galaxies in EDGE-CALIFA (green band) are very consistent with the measurements of HERACLES. Where the gas is dominated by the atomic component, $r \geq 0.4r_{25}$, the SFE_{gas} decreases rapidly to the galaxy edge. Because we assume a constant Σ_{atom} , this is fundamentally a reflection of the rapid decrease of SFR in the atomic disks.

We can describe the behaviour of the SFE_{gas} for our sample using an ordinary least-square (OLS) linear bisector method to fit a simple exponential decay:

$$\text{SFE}_{\text{gas}} = [0.83 \pm 0.07 (\text{Gyr}^{-1})] \exp\left(\frac{-r_{\text{gal}}}{[0.31 \pm 0.02] r_{25}}\right). \quad (2.15)$$

We note that we do not see clear breaks in this trend; instead, we find a continuous smooth exponential decline of SFE_{gas} as a function of r_{gal} . This is consistent with the rapid decline of star formation activity in the outer parts of galaxies (e.g., [26, 30, 110], and also is in agreement with previous results for low-redshift star-forming galaxies (e.g., [111, 112]. In particular, our results agree with the inside out monotonic decrease of the SFE_{gas} shown by [111]. [111] also

find that galaxies are segregated by morphology; for a given stellar mass, they show that late-type galaxies present larger SFE_{gas} than earlier ones at any r_{gal} , which is consistent with the trend we observe in Figure 2.6. In the outer parts, our steeper profiles may be influenced by our assumption of constant HI surface density. However, this does not explain our steeper profiles we also observe in the inner galaxy. The top and bottom dashed lines in Fig. 2.6 show how SFE_{gas} changes if instead of $6 M_{\odot} \text{pc}^{-2}$ we use $\Sigma_{\text{atom}} = 3$ and $12 M_{\odot} \text{pc}^{-2}$, which are the two extremes of Σ_{atom} values found in HERACLES [30]. A better match between EDGE and HERACLES would require using $\Sigma_{\text{atom}} = 3 M_{\odot} \text{pc}^{-2}$, which appears extremely low. Note that these two studies use different SFR tracers: our extinction-corrected $\text{H}\alpha$, may behave differently from the GALEX FUV that dominates the SFR estimate in the outer disks of HERACLES (e.g., [113]).

How sensitive is the SFE_{gas} determination to the CO-to- H_2 conversion factor? To test this we adopt a variable CO-to- H_2 conversion factor, α_{CO} , using equation 2.4. This includes changes in the central regions caused by high stellar surface densities, and changes due to metallicity. When comparing the effects of a constant and a variable prescription of α_{CO} (shaded area in Figure 2.6) we observe that the central regions present larger SFE_{gas} variations than the outer disks within the range of galactocentric distances we study, as the latter do not exhibit $12 + \log(\text{O}/\text{H})$ significantly below 8.4 according to the O3N2 indicator, as shown in the top panel of Figure 2.7. Therefore, the variations of the CO-to- H_2 conversion factor are generally small and consistent with the assumption of a constant α_{CO} .

So far, we have analyzed the SFE of the total gas, but it is also interesting to test whether the star formation efficiency responds to the phase of the ISM. The bottom panel of Figure 2.7 shows the star formation efficiency of the molecular gas, $\text{SFE}_{\text{mol}} = \Sigma_{\text{SFR}}/\Sigma_{\text{mol}}$ (in yr^{-1}), as a function of the ratio between the molecular and the atomic surface densities, $R_{\text{mol}} = \Sigma_{\text{mol}}/\Sigma_{\text{atom}}$. Since

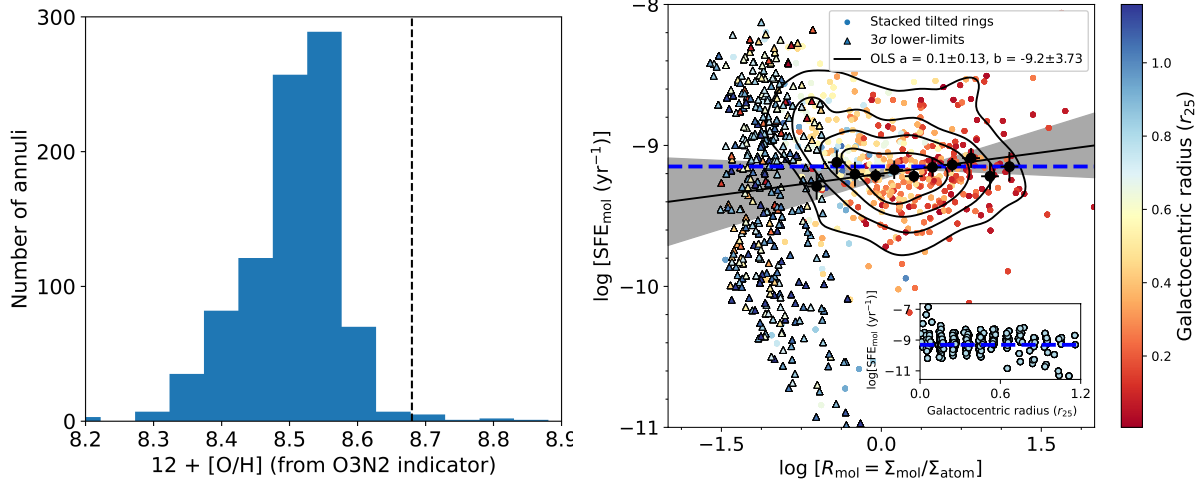


Figure 2.7: *Left*: Sample distribution of the oxygen abundances, $12 + \log(\text{O}/\text{H})$, with the O3N2 as metallicity indicator. The dashed-black line is the assumed solar value, which corresponds to $12 + \log(\text{O}/\text{H})_{\odot} = 8.69$. *Right*: The star formation efficiency of the molecular gas, $\text{SFE}_{\text{mol}} = \Sigma_{\text{SFR}}/\Sigma_{\text{mol}}$, vs the ratio between the molecular and the atomic gas surface densities, $R_{\text{mol}} = \Sigma_{\text{mol}}/\Sigma_{\text{atom}}$. Colors code for galactocentric radius (in R_e) are as indicated by the color bar. Black contours are 80%, 60%, 40%, and 20% of the points just for detections. Large black filled circles show the mean of EDGE-CALIFA data at each stellar surface density bin; the error bars are the uncertainties of the mean SFE_{mol} values in each bin. The black-solid line shows the OLS linear bisector fit for averaged points of SFE_{mol} over annuli by using the model $y = ax + b$. The shaded region represents uncertainty of the slope derived from the OLS linear bisector fit. The horizontal dashed-blue line is the average SFE_{mol} , including the 3σ detection, for the sample. The inset panel shows the SFE_{mol} for detections only as a function of galactocentric radius. The blue-dashed line is the average SFE_{mol} .

we assume $\Sigma_{\text{atom}} = 6 M_{\odot} \text{pc}^{-2}$, R_{mol} is a prescription for the Σ_{mol} normalized by a factor of 6.

Although there is large scatter, the figure shows that the SFE_{mol} , averaged by R_{mol} bins (filled-black dots), remains almost constant over the R_{mol} range, with an average $\log[\text{SFE}_{\text{mol}}] \sim -9.15$ (blue-dashed line in bottom panel of Fig. 2.7). The inset panel shows that the SFE_{mol} is also fairly constant over the range of galactocentric radii. These results are in agreement with [114], who find a similar flattening in SFE_{mol} for annuli at $r \leq 0.6r_{25}$ when analyzing 80 nearby-spiral galaxies selected from the CO Multi-line Imaging of Nearby Galaxies survey (COMING; [115]). Using CO, FUV+24 μm and H $_{\alpha}$ +24 μm data for 33 nearby-spiral galaxies selected from the IRAM HERACLES survey [101], [78] found that H $_2$ -dominated regions are well parameterized by a

fixed SFE_{mol} equivalent to a molecular gas depletion time of $\tau_{\text{dep,mol}} = \text{SFE}_{\text{mol}}^{-1} \sim 1.4$ Gyr, which is consistent with our average $\tau_{\text{dep,mol}} \sim 1.45 \pm 0.23$ Gyr. As for previous studies, these results support the idea that the vast majority of the star formation activity takes place in the molecular phase of the ISM instead of the atomic gas (e.g., [12, 78, 110]).

We explore possible trends between SFE_{gas} , galactocentric radius, and nuclear activity. We adopt the nuclear activity classification performed by [4], who classify CALIFA galaxies (with signal-to-noise larger than three) into star forming (SF), active galactic nuclei (AGN), and LINER-type galaxies, and we apply it, when available, for the 81 galaxies analyzed in this work (see column Nuclear in Table 3.1). We do not identify significant trends as a function of galactocentric radius for any of the these three categories.

2.4.2.2 SFE versus Stellar and Gas Surface Density

Since in the previous section we show a clear dependence of SFE_{gas} on galactocentric distance, it is expected that SFE_{gas} will also depend on the stellar surface density, Σ_{\star} . Indeed, the top left panel of Figure 2.8 shows an approximately power-law relationship between SFE_{gas} and Σ_{\star} . We quantify this relation by using an OLS linear bisector method in logarithmic space to estimate the best linear fit to our data (excluding upper-limits), obtaining

$$\log[\text{SFE}_{\text{gas}} (\text{yr}^{-1})] = [0.32 \pm 0.27] \times \log[\Sigma_{\star} (\text{M}_{\odot} \text{pc}^{-2})] - [10.13 \pm 1.75]. \quad (2.16)$$

When comparing the EDGE average SFE_{gas} , over Σ_{\star} bins (black dots) with similar HERACLES bins (green squares), we find consistently slightly larger efficiencies at $\log[\Sigma_{\star} (\text{M}_{\odot} \text{pc}^{-2})] \leq$

Name	Dist. (Mpc)	$\log[M_*/M_\odot]$	Morph. Class	$\log[M_{\text{mol}}/M_\odot]$	Nuclear	l_* (kpc)	l_{mol} (kpc)	$R_{50,*}$ (kpc)	$R_{50,\text{mol}}$ (kpc)
ARP220	78.0	10.91±0.09	Sm	9.72±0.0	LINER	2.76±0.24	1.7±0.35	3.88±0.24	2.86±0.35
IC0944	100.8	11.26±0.1	Sa	10.0±0.02	SF	4.41±0.11	4.26±0.39	7.14±0.11	7.85±0.39
IC1151	30.8	10.02±0.1	SBc	7.93±0.14	...	2.66±0.07	2.76±0.78	4.06±0.07	4.61±0.78
IC1199	68.3	10.78±0.1	Sbc	9.35±0.04	SF	4.53±0.06	3.99±0.44	7.52±0.06	6.97±0.44
IC1683	69.7	10.76±0.11	Sb	9.68±0.02	SF	5.56±0.79	2.49±0.13	8.92±0.79	3.99±0.13
IC4566	80.7	10.76±0.11	SABb	9.68±0.02	...	<3.55	<4.4	<5.97	<8.35
NGC0447	79.7	11.43±0.1	S0-a	9.33±0.05	...	4.56±0.7	10.0±0.23	6.58±0.7	9.09±0.23
NGC0477	85.4	10.9±0.12	Sc	9.54±0.05	SF	<9.01	<21.78	<14.43	<35.98
NGC0496	87.5	10.85±0.13	Sbc	9.48±0.04	SF	7.35±0.34	4.11±0.36	12.46±0.34	7.13±0.36
NGC0528	68.8	11.06±0.1	S0	8.36±0.13
NGC0551	74.5	10.95±0.11	SBbc	9.39±0.04	...	4.73±0.07	8.17±1.68	8.01±0.07	13.47±1.68
NGC1167	70.9	11.48±0.09	S0	9.28±0.06	LINER
NGC2253	51.2	10.81±0.11	Sc	9.62±0.02	SF	2.48±0.07	2.1±0.28	3.77±0.07	4.07±0.28
NGC2347	63.7	11.04±0.1	Sb	9.56±0.02	LINER	2.15±0.06	1.99±0.38	3.86±0.06	4.5±0.38
NGC2486	67.5	10.79±0.09	Sa	<9.05
NGC2487	70.5	11.06±0.1	Sb	9.47±0.05	...	<4.23	<16.66	<5.88	<24.85
NGC2639	45.7	11.17±0.09	Sa	9.36±0.02	LINER	1.78±0.01	2.88±0.74	2.93±0.01	4.29±0.74
NGC2730	54.8	10.13±0.09	Sd	9.0±0.06	...	5.62±0.62	3.79±0.25	9.57±0.62	6.25±0.25
NGC2880	22.7	10.56±0.08	E-S0	<7.93
NGC2906	37.7	10.59±0.09	Sc	9.11±0.03	INDEF	1.72±0.08	1.59±0.4	2.71±0.08	3.0±0.4
NGC2916	53.2	10.96±0.08	Sb	9.05±0.06	AGN
NGC3303	89.8	11.17±0.1	Sa	9.57±0.04	LINER	3.62±0.23	1.99±0.11	4.97±0.23	3.47±0.11
NGC3381	23.4	9.88±0.09	SBb	8.11±0.08
NGC3687	36.0	10.51±0.11	Sbc	<8.42	...	<1.86	<39.56	<2.63	<66.35
NGC3811	44.3	10.64±0.11	SBc	9.28±0.03	...	2.36±0.09	2.18±0.26	2.93±0.09	2.96±0.26
NGC3815	53.6	10.53±0.09	Sab	9.16±0.04	...	2.0±0.16	1.68±0.27	3.05±0.16	3.4±0.27
NGC3994	44.7	10.59±0.11	Sc	9.26±0.03	...	1.09±0.04	1.31±0.08	1.78±0.04	2.23±0.08
NGC4047	49.1	10.87±0.1	Sb	9.66±0.02	SF	2.37±0.02	1.26±0.25	3.9±0.02	3.11±0.25
NGC4185	55.9	10.86±0.11	SBbc	9.08±0.07	INDEF	4.98±0.23	4.45±0.85	8.19±0.23	7.49±0.85
NGC4210	38.8	10.51±0.1	Sb	8.86±0.05	LINER
NGC4211NED02	96.9	10.53±0.13	S0-a	9.29±0.06	...	<6.65	<10.52	<8.93	<17.82
NGC4470	33.4	10.23±0.09	Sa	8.59±0.06	SF	1.73±0.05	1.25±0.29	3.04±0.05	2.42±0.29
NGC4644	71.6	10.68±0.11	Sb	9.2±0.05	...	2.7±0.05	3.15±0.8	4.91±0.05	5.88±0.8
NGC4676A	96.6	10.86±0.1	S0-a	9.88±0.02	SF
NGC4711	58.8	10.58±0.09	SBb	9.18±0.05	SF	2.83±0.06	6.24±0.54	4.86±0.06	10.44±0.54
NGC4961	36.6	9.98±0.1	SBc	8.41±0.08	...	1.39±0.08	1.59±0.33	2.1±0.08	2.67±0.33
NGC5000	80.8	10.94±0.1	Sbc	9.45±0.04	SF	5.16±0.61	1.06±0.26	6.51±0.61	2.31±0.26
NGC5016	36.9	10.47±0.09	SABb	8.9±0.04	...	1.67±0.02	2.32±0.42	2.89±0.02	3.93±0.42
NGC5056	81.1	10.85±0.09	Sc	9.45±0.04	...	4.22±0.51	3.12±0.48	5.44±0.51	5.99±0.48
NGC5205	25.1	9.98±0.09	Sbc	8.37±0.07	LINER	<1.57	<2.13	<2.35	<3.61
NGC5218	41.7	10.64±0.09	SBb	9.86±0.01	...	1.65±0.08	1.43±0.18	2.79±0.08	1.93±0.18
NGC5394	49.5	10.38±0.11	SBb	9.62±0.01	SF	2.18±0.27	2.7±0.21	3.36±0.27	4.43±0.21
NGC5406	77.8	11.27±0.09	Sbc	9.69±0.04	LINER	4.97±0.26	7.54±1.9	7.23±0.26	12.77±1.9
NGC5480	27.0	10.18±0.08	Sc	8.92±0.03	LINER	2.41±0.1	1.27±0.2	4.04±0.1	2.35±0.2
NGC5485	26.9	10.75±0.08	S0	<8.09	LINER
NGC5520	26.7	10.07±0.11	Sb	8.67±0.03	...	1.19±0.07	0.9±0.11	1.67±0.07	1.77±0.11
NGC5614	55.7	11.22±0.09	Sab	9.84±0.01	...	2.25±0.28	1.34±0.16	3.67±0.28	3.1±0.16
NGC5633	33.4	10.4±0.11	Sb	9.14±0.02	SF	1.36±0.03	1.4±0.26	2.47±0.03	2.61±0.26
NGC5657	56.3	10.5±0.1	Sb	9.11±0.04	...	2.11±0.07	1.88±0.13	3.63±0.07	3.37±0.13
NGC5682	32.6	9.59±0.11	Sb	<8.29	SF	2.11±0.05	1.47±0.34	3.57±0.05	2.21±0.34
NGC5732	54.0	10.23±0.11	Sbc	8.82±0.07	SF	2.42±0.09	1.78±0.11	3.92±0.09	3.34±0.11
NGC5784	79.4	0.0±0.0	S0	9.4±0.04	...	2.4±0.32	1.41±0.13	3.28±0.32	3.46±0.13
NGC5876	46.9	10.78±0.1	SBab	<8.56
NGC5908	47.1	10.95±0.1	Sb	9.94±0.01	...	2.92±0.01	1.73±0.34	4.98±0.01	4.55±0.34
NGC5930	37.2	10.61±0.11	SABa	9.33±0.02	...	1.57±0.07	0.82±0.03	2.66±0.07	1.98±0.03
NGC5934	82.7	10.87±0.09	Sa	9.81±0.02	...	3.07±0.18	2.5±0.17	5.17±0.18	4.36±0.17
NGC5947	86.1	10.87±0.1	SBbc	9.26±0.06	AGN	<4.15	<4.7	<5.25	<7.83
NGC5953	28.4	10.38±0.11	S0-a	9.49±0.01	...	1.16±0.17	0.5±0.07	1.3±0.17	1.23±0.07
NGC6004	55.2	10.87±0.08	Sc	9.33±0.04	...	5.29±0.23	2.82±0.21	8.18±0.23	4.52±0.21
NGC6027	62.9	11.02±0.1	S0-a0	8.01±0.22
NGC6060	63.2	10.99±0.09	SABc	9.68±0.03	SF	3.85±0.11	4.08±0.52	6.25±0.11	7.59±0.52
NGC6063	40.7	10.36±0.12	Sc	<8.53	SF	2.65±0.08	3.34±0.83	4.67±0.08	5.99±0.83
NGC6125	68.0	11.36±0.09	E	<8.83
NGC6146	128.7	11.72±0.09	E	<9.36
NGC6155	34.6	10.38±0.1	Sc	8.94±0.03	SF	2.03±0.06	1.97±0.27	3.32±0.06	3.5±0.27
NGC6186	42.4	10.62±0.09	Sa	9.46±0.02	...	9.48±0.45	5.9±0.28	14.74±0.45	10.39±0.28
NGC6301	121.4	11.18±0.12	Sc	9.96±0.03	INDEF	9.45±0.39	13.32±3.83	15.5±0.39	20.01±3.83
NGC6314	95.9	11.21±0.09	Sa	9.57±0.03	INDEF	6.6±0.57	2.41±0.07	7.43±0.57	4.56±0.07
NGC6394	124.3	11.11±0.1	SBb	9.86±0.04	AGN	5.0±0.34	5.13±0.63	9.02±0.34	9.25±0.63
NGC7738	97.8	11.21±0.11	Sb	9.99±0.01	LINER	2.42±0.2	1.95±0.02	3.95±0.2	3.81±0.02
NGC7819	71.6	10.61±0.09	Sb	9.27±0.04	SF	6.91±1.06	2.6±0.69	9.71±1.06	3.15±0.69
UGC03253	59.5	10.63±0.11	Sb	8.88±0.06	SF	5.15±1.22	2.91±0.72	5.74±1.22	4.83±0.72
UGC03973	95.9	10.94±0.08	Sb	9.51±0.05	AGN	3.78±0.38	2.91±0.11	5.3±0.38	6.14±0.11
UGC05108	118.4	11.11±0.11	SBab	9.75±0.04	...	4.55±0.16	5.08±0.78	7.56±0.16	7.31±0.78
UGC05359	123.2	10.86±0.13	SABb	9.65±0.05	SF	5.25±0.15	6.15±1.09	8.95±0.15	11.06±1.09
UGC06312	90.0	10.93±0.12	Sa	<9.08	...	3.29±0.07	4.81±0.44	5.41±0.07	8.73±0.44
UGC07012	44.3	11.0±2.9	SBc	9.9±0.11	SF	2.31±0.1	0.99±0.17	3.36±0.1	2.0±0.17
UGC09067	114.5	10.96±0.12	Sab	9.83±0.04	SF	3.39±0.06	3.56±0.34	6.11±0.06	6.8±0.34
UGC09476	46.6	10.43±0.11	SABc	9.15±0.04	SF	<3.85	<5.37	<5.95	<9.46
UGC09759	49.2	10.02±0.1	Sb	9.07±0.04	...	2.83±0.16	1.09±0.17	4.5±0.16	1.96±0.17
UGC10205	94.9	11.08±0.1	Sa	9.6±0.04	SF	5.41±0.63	2.57±0.39	6.09±0.63	5.12±0.39

Table 2.1: Main properties of the 81 EDGE-CALIFA galaxies analyzed in this work. The columns Distance, M_* , Morphological Class, and M_{mol} are taken from [3], where M_{mol} is computed using $\alpha_{\text{CO}} = 4.36 M_\odot (\text{K km s}^{-1} \text{pc}^2)^{-1}$. The column Nuclear corresponds to the emission-line diagnostic for the optical nucleus spectrum for CALIFA galaxies by [4], who classify the galaxies (with signal-to-noise larger than three) into star forming (SF), active galactic nuclei (AGN), and LINER-type galaxies. The columns l_* , l_{mol} , $R_{50,*}$, and $R_{50,\text{mol}}$ are the exponential scale lengths and the radii that enclose 50% of the molecular gas and the stellar mass computed in Section 4.4.1.2, respectively.

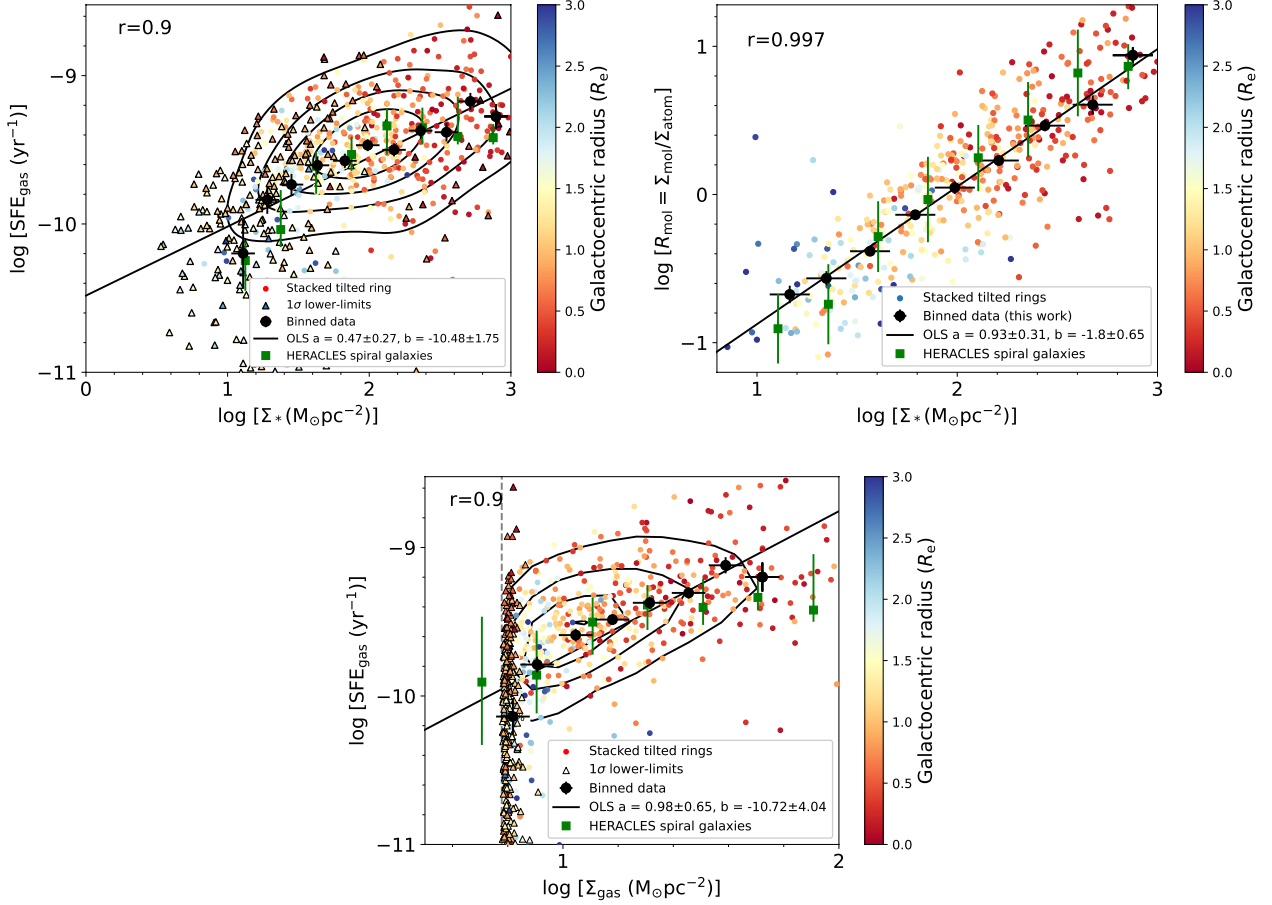


Figure 2.8: *Top left*: SFE_{gas} as a function of stellar surface density, Σ_* . Circular dots indicate the average SFE_{gas} and Σ_* in stacked annuli for the EDGE-CALIFA data. The ‘r’ term represents the Pearson correlation coefficient, including the binned annuli, for the relation between the SFE_{gas} and Σ_* . Conventions are as in bottom panel of Figure 2.7. *Top right*: The H_2 -to- H_I ratio, R_{mol} , as a function of Σ_* ; we use $\Sigma_{\text{atom}} = 6 \text{ M}_{\odot} \text{ pc}^{-2}$. Conventions are as in top panel. *Bottom*: SFE_{gas} as a function of gas surface density. The grey dashed line marks the point at which $\Sigma_{\text{gas}} = \Sigma_{\text{atom}} = 6 \text{ M}_{\odot} \text{ pc}^{-2}$. Conventions are as in top panel.

1.4 although the HERACLES points are still within the error bars of our data. Since these points are in the outer regions of the EDGE galaxies, this result may be sensitive to the adoption of $\Sigma_{\text{atom}} = 6 \text{ M}_{\odot} \text{ pc}^{-2}$. In the inner regions with $\log[\Sigma_*(\text{M}_{\odot} \text{ pc}^{-2})] \geq 2.6$, our average efficiencies are also higher, although we do not expect these regions to be sensitive to the choice of Σ_{atom} . Between these two extremes, however, there is good general agreement between the EDGE and HERACLES results.

The top right and bottom panels of Figure 2.8 show the relation between the H₂-to-H_I ratio ($R_{\text{mol}} = \Sigma_{\text{mol}}/\Sigma_{\text{atom}} = \Sigma_{\text{mol}}/6 M_{\odot} \text{ pc}^{-2}$), Σ_{\star} , and the gas surface density, $\Sigma_{\text{gas}} = \Sigma_{\text{mol}} + \Sigma_{\text{atom}}$, respectively. In the right panel, we observe a tight correlation between R_{mol} and Σ_{\star} . The relation is well described by a power-law and there is overall reasonable consistency between EDGE and HERACLES. Our measurements are also consistent with the resolved Molecular Gas Main Sequence relation (rMGMS, $\Sigma_{\text{gas}}-\Sigma_{\star}$; [70]) found for EDGE-CALIFA galaxies by [84]. The bottom panel shows very good agreement between the EDGE and HERACLES results in the range $0.9 \leq \log[\Sigma_{\text{gas}}] \leq 1.5$; outside this range there are small differences, although there is still consistency within the error bars. Therefore, the discrepancies seen in the top panel are not the result of differences in efficiency at a given H₂-to-H_I ratio nor gas surface density, but likely reflect small systematic differences in the relation between gas and stellar surface density in HERACLES and EDGE. Since we have both a broader morphological and a more numerous sample selection than HERACLES (particularly in the H_I-dominated regions), our results reflect on a more general power-law dependence of the SFE_{gas} on Σ_{\star} . Observations have shown that the fraction of gas in the molecular phase in which star formation takes place depends on the pressure in the medium ([107, 116]). These results suggest that high stellar densities in the inner regions of EDGE-CALIFA galaxies are helping self-gravity to compress the gas, resulting in H₂ dominated regions. Once the gas is predominantly molecular, our data suggests that a dependence of the SFE_{gas} on Σ_{\star} persists even in high Σ_{\star} , predominantly molecular regions.

Other studies have given different insights of the relation between star formation activity and the stellar surface density. For instance, analyzing 34 galaxies selected from the ALMA-MaNGA Quenching and STar formation (ALMaQUEST; [70]), [117] find that Σ_{SFR} is mainly regulated by Σ_{mol} , with a secondary dependence on Σ_{\star} . Conversely, analyzing 39 galaxies se-

lected from EDGE-CALIFA, [118] find a strong correlation between Σ_{SFR} and Σ_{mol} ; they show that the $\Sigma_{\text{SFR}} - \Sigma_{\star}$ relation is statistically more significant. [119], however, used the `edge_pydb` database to show that secondary correlations can be driven purely by errors in correlated parameters, and it is necessary to be particularly careful when studying these effects. Errors in Σ_{gas} , for example, will tend to flatten the relation between SFE_{gas} and Σ_{gas} because of the intrinsic correlations between the axes, and will have the same effect on the relation between SFE_{gas} and Σ_{\star} because of the positive correlation between Σ_{\star} and Σ_{gas} .

2.4.2.3 SFE, Pressure and SFR

We explore the dependency of SFE_{gas} on the dynamical equilibrium pressure, P_{DE} . While the midplane gas pressure, P_{h} [87], is a well studied pressure prescription in a range of previous works (e.g., [30, 116]), P_{DE} has been extensively discussed recently (e.g., [84, 90, 93, 120]). In both pressure prescriptions, it is assumed that the gas disk scale height is much smaller than the stellar disk scale height and the gravitational influence from dark matter is neglected. P_{h} and P_{DE} have an almost equivalent formulation, although they slightly differ in the term related to the gravitational influence from the stellar component (second term in equations 2.6 and 2.8; see section 4.3.1). We quantify this difference by computing the mean P_{DE} -to- P_{h} ratio averaged in annuli for our sample, obtaining $P_{\text{DE}}/P_{\text{h}} \approx 1.51 \pm 0.19$. We use this value to convert the P_{h} from HERACLES into P_{DE} , since we perform our qualitative analysis using the dynamical equilibrium pressure.

The left panel of Figure 2.9 shows the SFE_{gas} as a function of P_{DE} (in units of K cm^{-3}). The slope of the SFE_{gas} vs P_{DE} relation (averaged over P_{DE} bins (black dots) has a break at

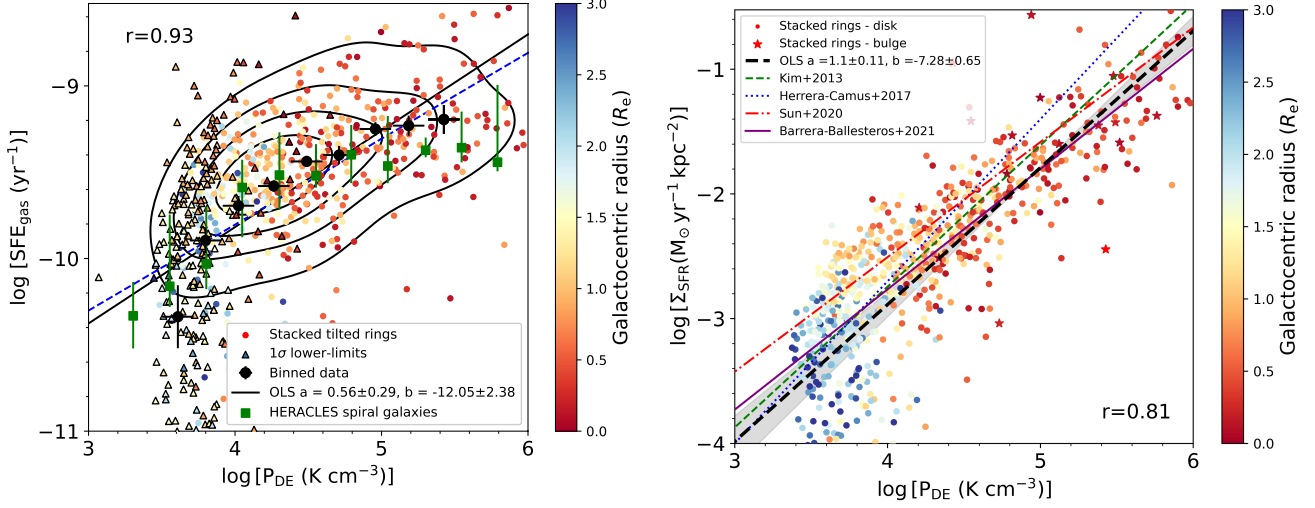


Figure 2.9: *Left*: SFE_{gas} as a function of dynamical equilibrium pressure, P_{DE} . The dashed-blue line corresponds to 1% of gas converted to stars per disk free-fall time. *Right*: Star formation rate surface density, Σ_{SFR} , as a function of P_{DE} . The black dashed line is the OLS linear bisector fit for all points. The ‘r’ term is the Pearson correlation coefficient of this subsample. The shaded region represents uncertainty of the slope derived from the OLS linear bisector fit. Conventions are as in Figure 2.8.

$\log[P_{\text{DE}}] \sim 3.7$. Below $\log[P_{\text{DE}}] \leq 3.7$ (i.e., where the ISM is HI-dominated) we do not see a clear correlation between SFE_{gas} and P_{DE} . This is at the sensitivity limit existing data for EDGE, but it is also consistent with the overall behaviour seen in HERACLES corresponding to a steepening of their mean relation. Above this pressure we find a clear linear trend in log-log space. For higher P_{DE} values (e.g., H_2 -dominated regions) the EDGE average efficiencies are somewhat higher than observed in HERACLES, which flatten out at high P_{DE}) although with a scatter that is within the respective 1σ error bars. For $\log[P_{\text{DE}}] \geq 3.7$ the EDGE average efficiencies are well described by the blue-dashed line, which corresponds to 1% of the gas converted to stars per disk free-fall time, $\tau_{\text{ff}} = (G\rho)^{-1/2}$. To quantify this relation, we use an OLS linear bisector method to estimate the best linear fit to our data, obtaining

$$\log[\text{SFE}_{\text{gas}} (\text{yr}^{-1})] = [0.41 \pm 0.29] \times \log[P_{\text{DE}}/k (\text{Kcm}^{-3})] - [11.32 \pm 2.24]. \quad (2.17)$$

The right panel of Figure 2.9 shows the Σ_{SFR} versus P_{DE} , color-coded by galactocentric radius. When compared with other recent measurements (e.g., KINGFISH, [90]; PHANGS, [93]), our annuli have the advantage of covering a somewhat wider dynamic range in both Σ_{SFR} and P_{DE} . We find a strong correlation between Σ_{SFR} and P_{DE} that is approximately linear for annuli at $\log[P_{\text{DE}}/k] \geq 3.7$, although below this limit we observe a break in the trend. As shown by the color coding of the symbols, indicating r_{gal} in Figure 2.9, this limit is apparently related to the r_{gal} at which the transition from H₂-dominated to HI-dominated annuli happens. This transition may be due to the large range of physical properties covered by our sample, which span from molecular dominated to atomic dominated regimes. Where the ISM weight is higher (e.g., H₂-dominated regions), the SFR is stabilized by the increasing feedback from star formation to maintain the pressure that counteracts the P_{DE} [93]. The lack of correlation we observe at $\log[P_{\text{DE}}/k] \leq 3.7$ ($r \geq 0.7R_e$) is mainly because we are reaching our CO sensitivity in the HI-dominated regions. To quantify the correlation, we estimate the best linear fit by using an OLS linear bisector method in logarithmic space for annuli at $r \geq 0.7R_e$,

$$\log[\Sigma_{\text{SFR}} (\text{M}_{\odot} \text{yr}^{-1})] = [1.10 \pm 0.11] \times \log[P_{\text{DE}}/k (\text{K cm}^{-3})] - [7.28 \pm 0.65]. \quad (2.18)$$

Note that these results are potentially sensitive to the method we employ for the fitting. Nonethe-

less, using an orthogonal distance regression (ODR) to fit the same subsample, we obtain very comparable values $\log[\Sigma_{\text{SFR}} (\text{M}_{\odot} \text{yr}^{-1})] = [1.09 \pm 0.05] \times \log[P_{\text{DE}}/k (\text{Kcm}^{-3})] - [7.25 \pm 0.25]$. [84] analyze 4260 resolved star-forming regions of kpc size located in 96 galaxies from the EDGE-CALIFA survey, using a similar sample selection (e.g., inclination, σ_{gas} and Σ_{atom} constant values, among others) but they just consider Equivalent Widths for the $\text{H}\alpha$ line emission $\text{EW}(\text{H}\alpha) > 20\text{\AA}$. Using an ODR fitting technique, they obtain $\log[\Sigma_{\text{SFR}} (\text{M}_{\odot} \text{yr}^{-1})] = [0.97 \pm 0.05] \times \log[P_{\text{DE}}/k (\text{Kcm}^{-3})] - [7.88 \pm 0.48]$, which is in agreement with the distribution shown in the bottom panel of Figure 2.9. The figure also shows that the correlation agrees with hydrodynamical simulations performed by [120] (green dashed line), in which they obtain a slope of 1.13. These results are also consistent with measurements obtained in other galaxy samples. [93] obtain a slope of 0.84 ± 0.01 for 28 well-resolved CO galaxies ($\sim 1''.5$, corresponding to ~ 100 pc) selected from the ALMA-PHANGS sample by using a methodology very similar to ours. Smaller slopes have been referenced in local very actively star-forming galaxies (e.g., local ultra luminous infra-red galaxies, ULIRGs), which at the same time may resemble some of the conditions in high-redshift sub-millimeter galaxies (e.g., [121]). [90] analyzed the [CII] emission in atomic-dominated regions of 31 KINGFISH galaxies to determine the thermal pressure of the neutral gas and related it to P_{DE} , obtaining a slope of 1.3 (dotted blue line). Our results bridge these two extremes; the strong correlation between Σ_{SFR} and P_{DE} and its linearity supports the idea of a feedback-regulated scenario, in which star formation feedback acts to restore balance in the star-forming region of the disk [93].

2.4.2.4 SFE and Orbital Timescale

In the next two sections, we exclude 21 galaxies (out of the 81) since their $H\alpha$ rotation curves (taken from [79]) are either too noisy or not well fitted by the universal rotation curve parametric form. The top panel of Figure 2.10 shows SFE_{gas} versus τ_{orb} , the orbital timescale (in units of yr), color-coded by galactocentric radius. When analyzing our efficiencies averaged over orbital timescale bins (black symbols), we note that there is a slightly flattening of the SFE_{gas} at $\log[\tau_{\text{orb}}] \sim 7.9 - 8.1$. We also note that annuli at $\log[\tau_{\text{orb}}] \leq 8.1$ are usually within the bulge radius in the SDSS i -band (reddish-stars symbols). However, the error bars are consistent with SFE_{gas} decreasing as a function of τ_{orb} including at $\log[\tau_{\text{orb}}] < 8.1$. These results are in agreement with what is found in other spatially resolved galaxy samples (e.g., [28, 30]). The average gas depletion time for our subsample, $\tau_{\text{dep}} = \Sigma_{\text{gas}}/\Sigma_{\text{SFR}} \approx 2.8_{-1.0}^{+1.1}$ Gyr, which agrees fairly with the depletion time $\tau_{\text{dep}} = 2.2$ Gyr found for HERACLES (not including early-type galaxies; [32]). [122] computed the depletion times for 52 EDGE-CALIFA galaxies using annuli in the region within $0.7 r_{25}$ (just considering the molecular gas); their average $\tau_{\text{dep}} \approx 2.4$ Gyr is in good agreement with our results.

The orbital timescale has a strong correlation with radius, and theoretical arguments expect SFE_{gas} to be closely related to orbital timescale in typical disks [27, 95, 96]. A correlation between SFE_{gas} and τ_{orb} is based on the ‘‘Silk-Elmegreen’’ relation, which states that $\Sigma_{\text{SFR}} = \epsilon_{\text{orb}} \Sigma_{\text{gas}}/\tau_{\text{orb}}$, where ϵ_{orb} is the fraction of the gas converted into stars per orbital time (also called ‘‘orbital efficiency’’). Therefore, because $SFE_{\text{gas}} = \Sigma_{\text{SFR}}/\Sigma_{\text{gas}}$, SFE_{gas} and τ_{orb} are related by

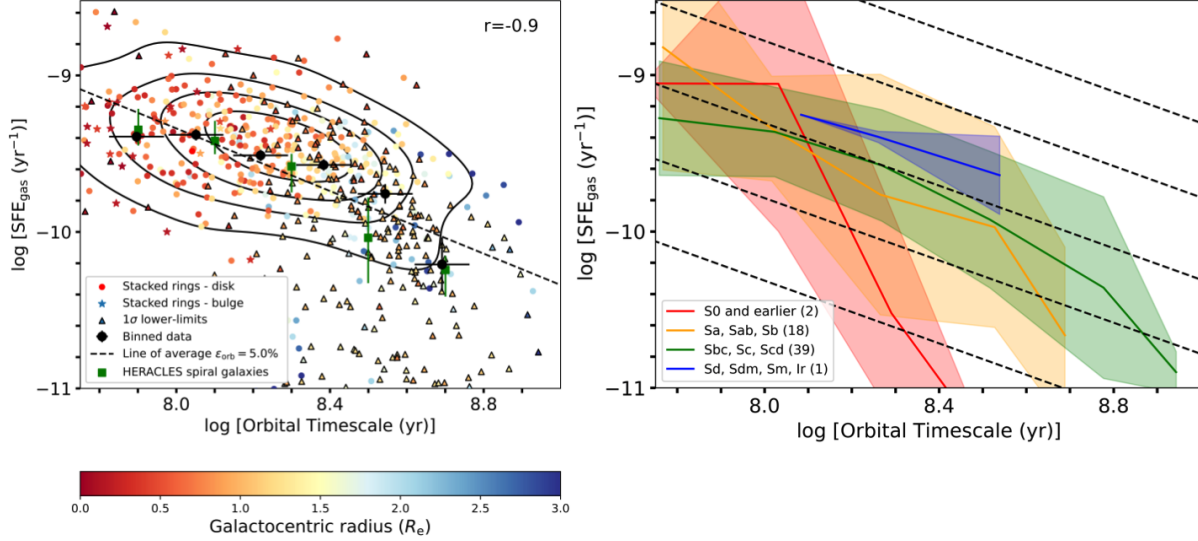


Figure 2.10: *Left*: SFE_{gas} as a function of the orbital timescale, τ_{orb} . Color coding and symbols are as described in Figure 2.8. The black-dashed line is the best fit of the binned data and shows 5% of gas converted into stars per τ_{orb} . The ‘r’ term represents the Pearson correlation coefficient, including the binned annuli, for the relation between the SFE_{gas} and τ_{orb} . *Right*: SFE_{gas} averaged over τ_{orb} bins over all galaxies of selected morphological types as in Figure 2.6. Black-dashed lines, from top to bottom, represent the 50%, 17%, 5%, 1.7%, and 0.5% efficiency of gas converted into stars per τ_{orb} .

$$SFE_{\text{gas}} = \frac{\epsilon_{\text{orb}}}{\tau_{\text{orb}}}. \quad (2.19)$$

It is interesting to analyze the relations between the different timescales since they can give intuition about the physical processes underlying the star formation activity (e.g., [123, 124]). Equation 2.19 shows that the timescale to deplete the gas reservoir and the orbital timescale are related through ϵ_{orb} . Although there is large scatter, the median values of τ_{orb} and τ_{dep} for our sample are $(2.0^{+0.9}_{-0.7}) \times 10^8$ yr and $(2.8^{+1.1}_{-1.0}) \times 10^9$ yr, respectively. These values are in good agreement with previous EDGE-CALIFA sample results found by [124], who analyze a more limited subsample of 39 galaxies without the benefit of CO line stacking and more constrained to inclination below 65° , with $\tau_{\text{orb}} = (3.2^{+2.0}_{-1.2}) \times 10^8$ yr and $\tau_{\text{dep}} = (2.8^{+2.3}_{-1.2}) \times 10^9$ yr. The black-dashed line in the right panel of Figure 2.10 corresponds to the best fit to our binned data

(black symbols); our fit excludes lower limits (shown as triangles in the figure), and it shows that $\epsilon_{\text{orb}} \approx 5\%$ of the total gas mass is converted to stars per τ_{orb} . This average efficiency is lower but similar to the $\epsilon_{\text{orb}} \approx 7\%$ of efficiency found by [28] and [27], and the $\epsilon_{\text{orb}} \approx 6\%$ efficiency for HERACLES [30]. Also, this efficiency is the same to the average molecular gas orbital efficiency found by [124] for their subsample of EDGE-CALIFA galaxies ($\epsilon_{\text{orb}} \approx 5\%$). Similar to our results, all of these studies did not find a clear correlation between SFE_{gas} and τ_{orb} in the inner regions of disks, where the ISM is mostly molecular.

Like [124], however, we find that a constant ϵ_{orb} is not a good approximation for the data. The efficiency per orbital time depends on the Hubble morphological type, with ϵ_{orb} increasing from early- to late-types. This is shown in the right panel of Figure 2.10, which shows the data grouped according to the same four morphological classes used in Figure 2.6. Our results show that annuli from Sbc, Sc, and Scd galaxies, which are the most numerous in our sample, seem to group around $\epsilon_{\text{orb}} \sim 5\%$. This value is also representative of the typical ϵ_{orb} seen for the morphological bins comprised by Sa, Sab, and Sb and Sd, Sdm, Sm, and Ir types in the range $8.0 < \log[\tau_{\text{orb}}] < 8.4$. However, these groups also show $\epsilon_{\text{orb}} \leq 5\%$ in the ranges $\log[\tau_{\text{orb}}] < 8.0$ and $\log[\tau_{\text{orb}}] > 8.4$. However, early-type galaxies (with admittedly limited statistics, 21 annuli in total) show substantially lower ϵ_{orb} , with a median of $\epsilon_{\text{orb}} = 1.2\%$. These values are in agreement with previous results for EDGE-CALIFA galaxies by [124], even though sample selection and processing were different. They observe a $\epsilon_{\text{orb}} \sim 10\%$ for Sbc galaxies (most numerous in their sub-sample), and a systematic decrease in orbital efficiencies from late- to early-type galaxies.

As concluded in [124], our results support the idea of a non-universal efficiency per orbit for the ‘‘Silk-Elmegreen’’ law. Figure 2.10 shows that ϵ_{orb} depends not just on morphological type, but the behavior also varies with galactocentric radius: at short orbital time scales ($\log[\tau_{\text{orb}}] \leq$

8.3), or small radii ($\log[r/R_e] \leq 1.1-1.3$) the efficiency per unit time SFE_{gas} tends to be constant, and as a consequence the observed ϵ_{orb} tends to systematically decrease as τ_{orb} decreases. This is best seen in the top panel in the departure of the binned data (black symbols) from the dashed line of constant ϵ_{orb} . Note that this is also the approximate radius of the molecular disk, the region where molecular gas dominates the gaseous disk (Figure 2.5).

Other studies have also reported SFE_{gas} deviations as a function of morphology. [125] analyze CO observations of 28 nearby galaxies to compute the C-index = $R90_{\text{petro},r}/R50_{\text{petro},r}$ as an indicator of the bulge dominance in galaxies (where $R90_{\text{petro},r}$ and $R50_{\text{petro},r}$ are the radius containing the 90% and 50% of Petrossian flux for SDSS r -band photometric data, respectively). Although they do not detect a significant difference in the SFE_{gas} for bulge- and disk-dominated galaxies, they identify some CO-undetected bulge-dominated galaxies with unusual high SFE_{gas} . Their results may reflect the galaxy population during the star formation quenching processes caused by the presence of a bulge component, and they could explain the flattening shown in top panel (mostly dominated by annuli within bulges) and bottom panel (mainly due by early-type and Sb-Scd galaxies annuli) of Figure 2.10.

2.4.2.5 Gravitational instabilities

The formulation of the Toomre Q gravitational stability parameter (see Section 4.3.1 for more details; [98]) provided a useful tool to quantify the stability of a thin disk disturbed by axisymmetric perturbations. Some studies have shown that the star formation activity is widespread where the gas disk is Q -unstable against large-scale collapse (e.g., [26, 110]).

First we examine the case where only gas gravity is considered; the top left panel of Figure

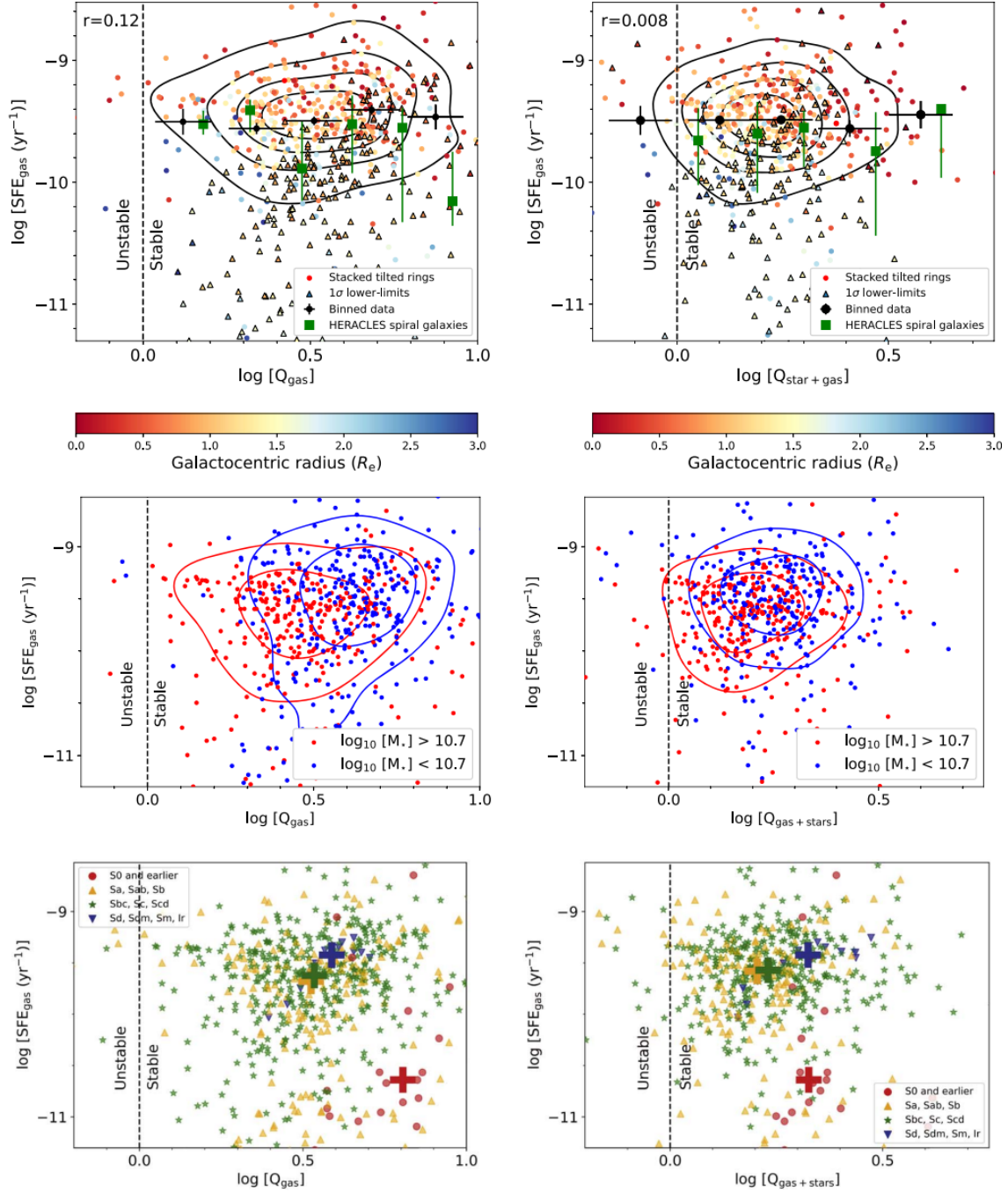


Figure 2.11: SFE_{gas} as a function of Toomre’s gravitational instability Q parameter for two different scenarios. *Left:* The SFE_{gas} is plotted as a function of the Toomre Q parameter for gas, Q_{gas} . *Right:* The SFE_{gas} is plotted as a function of the Toomre Q parameter redefined by [18] to include the contribution of stars and gas, $Q_{\text{stars+gas}}$. Green squares in the upper left and right panels correspond to HERACLES spiral galaxies; black dashed line sets the limit where the gas is unstable or stable. The center left and right panels show the same points included in the upper ones but this time divided into low and high galaxy stellar mass sets; red points correspond to binned annuli which belong to galaxies with $\log_{10}(M_*) > 10.7$, while blue points belong to galaxies with stellar masses below this limit. Blue and red contours are the 66% and 33% of the points for each mass set. The bottom left and right panels provide information about the morphological type of the host galaxy for a given annulus. The crosses correspond to the center of mass of the $\log_{10}\text{SFE}_{\text{gas}}$ vs center of mass of $\log_{10} Q$ points for each set of morphological types.

2.11 considers this case, showing the SFE_{gas} as a function of both the Toomre instability parameter for a thin disk of gas (x-bottom axis), Q_{gas} , and galactocentric radius (indicated by dot color). The vertical black-dashed line marks the limit where the gas becomes unstable to axisymmetric collapse. The vast majority of our points are in stable (or marginally stable) annuli with an average $Q_{\text{gas}} = 3.2$. There is no apparent correlation of SFE_{gas} with Q_{gas} (Pearson correlation coefficient of 0.17), and that is independent of galaxy mass (middle left panel) or type (bottom left panel). In other words, SFE_{gas} does not decrease as stability increases (i.e as Q_{gas} increases). This is in agreement with similar results reported in previous studies. For example, using H_I observation for 20 dwarf Irregular galaxies selected from the Local Irregulars That Trace Luminosity Extremes, The H_I Nearby Galaxy Survey (LITTLE THINGS; [126]), [127] find that dIrr galaxies are Q_{gas} -stable, with a mean $Q_{\text{gas}} \sim 4$. They also find their galaxies have relatively thick disk, with typical (atomic) gas scale heights of $h_{\text{gas}} \sim 0.3 - 1.5\text{kpc}$. Consequently, they are more stable than the infinitely thin disks for which the $Q_{\text{gas}} = 1$ criterion is derived.

Stars represent the dominant fraction of mass in disks at galactocentric radii with active star formation. Thus, it makes sense to account for their gravity when determining the stability of the ISM in these regions. The top right panel of Figure 2.11 shows the SFE_{gas} as a function of Toomre’s instability parameter modified by [18] to include the effects of both gas and stars, $Q_{\text{stars+gas}}$, again galactocentric radius is indicated by color. As expected, we find that disks become more unstable when stellar gravity is included in addition to gas with a few points appearing in the nominally unstable region for thin disks. The bulk of the annuli, however, are found at around $Q_{\text{stars+gas}} \approx 1.6$. This is roughly consistent with calculations of Q in other samples [128]. There is, however, no correlation of SFE_{gas} with Q .

The center panels of Figure 2.11 show the SFE_{gas} s versus Q_{gas} and $Q_{\text{stars+gas}}$ but this time

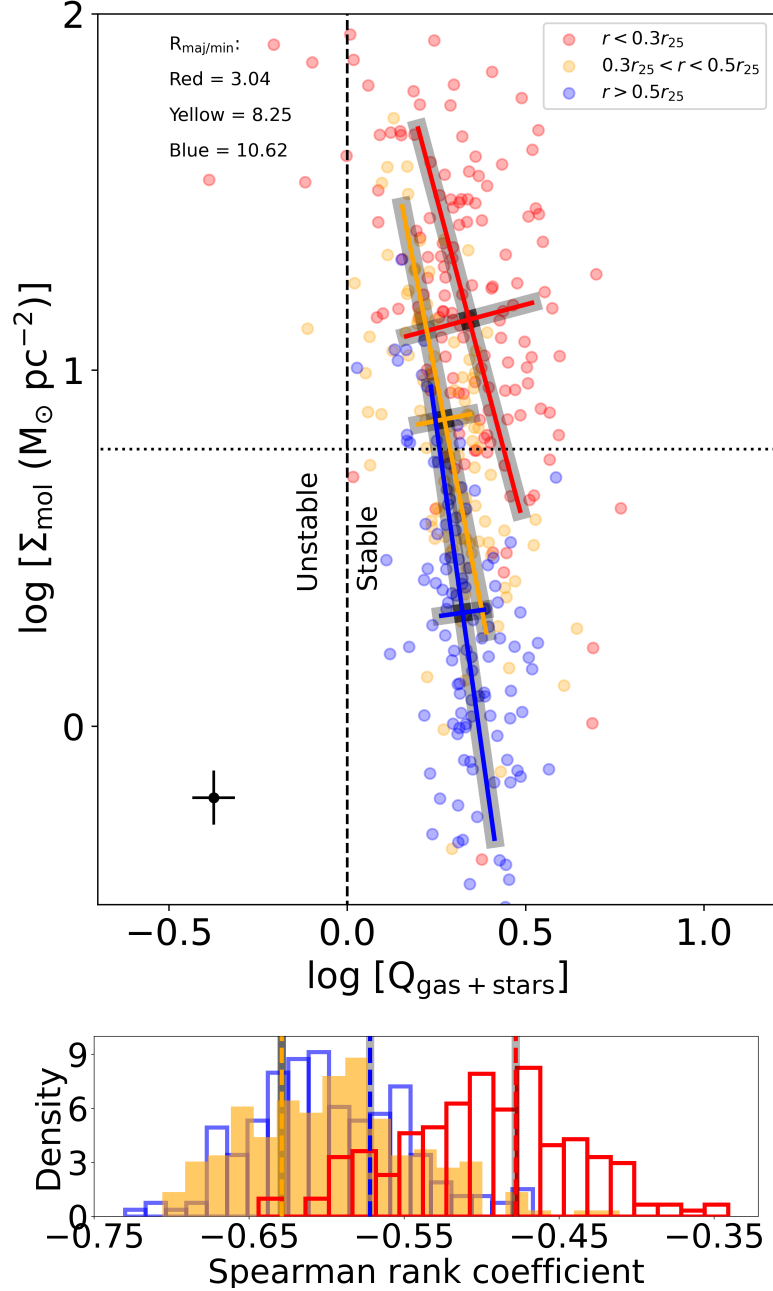


Figure 2.12: *Top:* Molecular gas surface density, Σ_{mol} , as a function of Toomre’s instability parameter for gas and stars, $Q_{\text{stars}+\text{gas}}$, for annuli with galactocentric radii within $0.3r_{25}$ (red points), between $0.3r_{25}$ and $0.5r_{25}$ (yellow points), and outside $0.5r_{25}$ (blue points). Each point represents the value of Σ_{mol} averaged over a r/r_{25} -wide annuli. Points are color-coded by galactocentric radius (in r_{25}), as indicated by the color bar on the right side. Solid-lines are PCA major and minor axes for which each of the groups vary most. The axes are normalized to fit the major and minor axes of the elliptical contours that enclose 50% of the annuli within a given range. The ratio between the major and the minor axes from the PCA, $R_{\text{maj}/\text{min}} = r_{\text{maj}}/r_{\text{min}}$, is in the upper left. Typical 1- σ error bars are shown in bottom left. The horizontal black-dotted line represents the assumed $\Sigma_{\text{atom}} = 6 \text{ M}_{\odot} \text{pc}^{-2}$. *Bottom:* Distribution of the Spearman rank correlation coefficients for the three r ranges in the top panel after randomizing the Σ_{mol} data, per range, in 200 realizations to test for the degree of internal correlation of the axes. The horizontal dashed-red, dashed-yellow, and dashed-blue lines are the Spearman rank coefficients for the actual data, from inner to outer ranges, respectively. This shows that the correlations observed in the top panel are completely consistent with being a result of the definition of $Q_{\text{gas}+\text{stars}}$ (see discussion in the text), and thus (although tantalizing) are not particularly meaningful.

splitting the points in two groups of different galaxy stellar mass; as in Section 2.4.2.1, we choose $\log_{10}[M_{\star}] = 10.7$ to split the groups. Although the two groups separate in Q_{gas} , with annuli from galaxies with $\log_{10}[M_{\star}] < 10.7$ tending to be in general more stable, the separation disappears once the stars are taken into account in the Q calculation.

In one of the ideas on how stars relate to SFE_{gas} , [129] show that star-formation may be associated with the fastest growing mode of instabilities. In that case, the relation between SFR and gas in spiral galaxies may be modulated by the stellar mass, which will contribute to the gravitational instability and regulation of star formation (like in the case of NGC 628; [129]). Also, the $\Sigma_{\text{SFE}_{\text{gas}}} - \Sigma_{\star}$ relation, known as the “extended Schmidt law”, suggests a critical role for existing stellar populations in ongoing star formation activity, and it may be a manifestation of more complex physics where Σ_{\star} is a proxy for other variables or processes [130]. Our results may reflect the importance of instabilities in enhancing the SFE_{gas} due to the strong gravitational influence from stars, particularly in galaxies with $\log_{10}[M_{\star}] > 10.7$. But in the aggregate there is no apparent evidence for a trend showing that annuli with more unstable Q have higher star formation efficiencies.

The bottom panels of Figure 2.11 show the same relations as upper panels but this time the data are grouped in four bins by morphological type. In both panels crosses correspond to the “center of mass” for each morphological group. Although annuli in early-type galaxies are more “Toomre stable”, the statistics are very sparse and the Toomre calculation may not apply (since these are not thin disks). Otherwise, we do not find a clear trend between morphology and stability based on the Toomre parameter for stars and gas. Previous studies have reported that $Q_{\text{star+gas}}$ increases towards the central parts of spirals. For example, [30] found that although molecular gas is the dominant component of the ISM in the central regions, HERACLES galaxies

seems to be more stable there than near the H₂-to-H_I transition. If the type of gravitational instability that Q is sensitive to plays a role in star formation in galaxies, we would expect to see some links between Q and molecular gas abundance. It is therefore interesting to test if there is dependence of the H₂-to-H_I ratio, $R_{\text{mol}} = \Sigma_{\text{mol}}/\Sigma_{\text{atom}}$ on the degree of gravitational instability in EDGE galaxies. Since we assume a constant Σ_{atom} , however, for us R_{mol} is simply a normalized molecular gas surface density, Σ_{mol} . We use the typical H₂-to-H_I transition radius found in §2.4.2.1 to split the annuli into three groups: i) annuli at $r < 0.3r_{25}$ ($r < 0.6R_e$; red points) which should be strongly molecular, ii) annuli between $0.3r_{25} < r$ and $r < 0.5r_{25}$ ($0.6R_e < r < 1.4R_e$; yellow points) which should be around the molecular to atomic transition region, and iii) annuli at $r > 0.5r_{25}$ ($r > 1.4R_e$; blue points) which should be dominated by atomic gas. The top panel of Figure 2.12 shows that Σ_{mol} has a large scatter and does not seem to depend strongly on $Q_{\text{star+gas}}$. Within the each range, however, we find that annuli with smaller galactocentric radii tend to be slightly more stable.

A suggestive trend emerges when we limit the range of galactocentric radii. We compute a Principal Component Analysis (PCA; [131]) to find the main axis along which the three populations vary most. The top panel of Figure 2.12 shows the PCA major and minor axis for annuli in the three defined zones. The axes have been normalized to fit the minor of major axes of the elliptical contours that enclose 50% of the annuli over a given range. The figure suggest that, within a given range, we tend to find more plentiful molecular gas in regions where annuli are more Toomre unstable. A concern, however, is that the axes in this plot have a degree of intrinsic correlation since the computation of $Q_{\text{star+gas}}$ includes Σ_{mol} . Therefore to assert that the correlation we observe is physically meaningful we need to show that it is stronger than that imposed by the mathematics of the computation. We quantify the strength of the correlations using the

Spearman rank correlation coefficient, which is a non-parametric measure of the monotonicity of the observed correlations. To investigate the degree to which the axes are internally correlated, we randomize the Σ_{mol} data (within each range) and recompute $Q_{\text{star+gas}}$ in 200 realizations, to obtain the distributions of the Spearman rank correlation coefficient for each randomized group. Clearly in the randomized data we would expect only the degree of correlation caused by the mathematical definition of the quantities. The bottom panel of Figure 2.12 shows that the Spearman rank correlation coefficients for the actual data (dashed-red, dashed-yellow, and dashed-blue vertical lines) are consistent with the distributions seen in the randomized histograms. These results suggest that the correlation between Σ_{mol} and $Q_{\text{star+gas}}$ seen in the top panel of Figure 2.12 is purely driven by the implementation of equation 2.14, in which $Q_{\text{star+gas}}$ depends on Σ_{mol} .

2.5 Summary and conclusions

We present a systematic study of the star formation efficiency and its dependence on other physical parameters in 81 galaxies from the EDGE-CALIFA survey. We analyse CO 1-0 datacubes which have $7''$ angular resolution and 20 km s^{-1} channel width, along with $\text{H}\alpha$ velocities extracted from the EDGE database, `edge_pydb` (Wong et al. in prep.). We implement a spectral stacking procedure for CO spectra shifted to the $\text{H}\alpha$ velocity to enable detection of faint emission and obtain surface densities averaged over annuli of width $0.1r_{25}$ ($\sim 3.5''$), and measure Σ_{mol} out to typical galactocentric radii of $r \approx 1.2r_{25}$ ($r \sim 3R_e$). We assume a constant [83], a Milky-Way constant conversion factor of $\alpha_{\text{CO}} = 4.3 \text{ M}_{\odot} [\text{K km s}^{-1} \text{ pc}^{-2}]^{-1}$, and a constant $\sigma_g = 11 \text{ km s}^{-1}$ [30, 88]. We perform a systematic analysis to explore molecular scale lengths and the dependence of the star formation efficiency $\text{SFE}_{\text{gas}} = \Sigma_{\text{SFR}} / (\Sigma_{\text{mol}} + \Sigma_{\text{atom}})$ on various physical

parameters. Our main conclusions are as follows:

1. We determine the molecular and stellar exponential disk scale lengths, l_{mol} and l_{\star} , by fitting the radial Σ_{mol} and Σ_{\star} profiles, respectively. We also obtain the radii that encloses 50% of the total molecular mass, $R_{50,\text{mol}}$, and stellar mass, $R_{50,\star}$ (see Fig. 2.3). To quantify the relations, we use an OLS linear bisector method to fit all our 3σ detections beyond $r > 1.5$ kpc. We find that $l_{\text{mol}} = [0.86 \pm 0.07] \times l_{\star}$, $l_{\text{mol}} = [0.24 \pm 0.01] \times r_{25}$, and $R_{50,\text{mol}} = [0.93 \pm 0.05] \times R_{50,\star}$. These results are in agreement with values from the current literature, and indicate that on average the molecular and stellar radial profiles are similar.
2. We find that on average the SFE_{gas} exhibits a smooth exponential decline as a function of galactocentric radius, without a flattening towards the centers of galaxies seen in some previous studies (see Fig. 2.6), in agreement with recent results (e.g., [132, 133]). We note a systematic increase in the average SFE_{gas} from early to late type galaxies. In HI-dominated regions, this conclusion depends strongly on our assumption of a constant HI surface density for the atomic disk. The EDGE-CALIFA survey encompasses a galaxy sample that has not been well represented by prior studies, which includes a larger number of galaxies with a broader range of properties and morphological types. This may explain the differences we observe when we compare our result with previous work.
3. The SFE_{gas} has a clear dependence on Σ_{\star} (see Fig. 2.8), a relation that holds for both the atomic-dominated and the molecular-dominated regimes. The SFE_{gas} has a comparatively flatter dependence on Σ_{gas} for high values of the gas surface density. This suggests that the stellar component has a strong effect on setting the gravitational conditions to enhance the star formation activity, not just converting the gas from HI to H₂. However, statistical

tests, which are beyond the scope of this work, may be required to demonstrate that this secondary relation is not induced by errors [119].

4. There is a clear relationship between SFE_{gas} and the dynamical equilibrium pressure, P_{DE} , particularly in the innermost regions of galactic disks. Moreover, we find a strong correlation between Σ_{SFR} and P_{DE} . We identify a transition at $\log[P_{\text{DE}}/k(\text{K cm}^{-3})] \sim 3.7$, above which we find a best-linear-fit slope of 1.11 ± 0.15 . Our results are in good agreement with the current literature and support a self-regulated scenario in which the star formation acts to restore the pressure balance in active star-forming regions.
5. We find a power-law decrease of SFE_{gas} as a function of orbital time τ_{orb} (see Fig. 2.10). The average τ_{orb} within $0.7r_{25}$ for our galaxies is 2.6 ± 0.2 Gyr, with a typical efficiency for converting gas into stars of $\sim 5\%$ per orbit. Note, however, that there are systematic trends in this efficiency. In particular, we note that there is a flattening of the SFE_{gas} for $\log[\tau_{\text{orb}}(\text{yr})] \sim 7.9 - 8.1$ which may reflect star formation quenching due to the presence of a bulge component. Although our methodology is different, our findings support the conclusion that the star formation efficiency per orbital time is a function of morphology [124].
6. Finally, under the assumption of a constant velocity dispersion for the gas, we do not find clear correlations between the SFE_{gas} and Q_{gas} or $Q_{\text{stars+gas}}$. It is possible that larger samples of galaxies may be required to confidently rule out any trends. Our typical annulus has $Q_{\text{stars+gas}} \sim 1.6$, independent of galaxy mass or morphological type. The range of Σ_{mol} is very broad, and we do not find any meaningful trends.

Future VLA HI and ALMA CO data may improve the spatial coverage and sensitivity,

allowing us remove some limitations and extend this analysis to fainter sources (e.g., earlier galaxy types), contributing to a more extensive and representative sample of the local universe.

Chapter 3: VERTICO.IV. Environmental Effects on the Gas Distribution and Star Formation Efficiency of Virgo Cluster Spirals

3.1 Introduction

A major aim in modern astrophysics is to understand how the local physical conditions of the interstellar medium (ISM) that lead to the production of stars respond to environmental effects. That is, whether there are differences between galaxies residing in a low-density environment and those immersed in galaxy clusters.

Galaxies are known to not be evenly distributed in the Universe. For low/intermediate stellar masses, gas-rich galaxies are mainly found in low-density environments, suggesting a strong interplay between environment, gas cycle, and star-formation activity (e.g., [45, 46]). High-density environments also tend to preferentially host red galaxies (e.g., [47–49]). Numerical simulations and observational evidence have shown that galaxies lose the ability to accrete gas from the cosmic web when they fall into a more massive halo (e.g., [50–55]), resulting in quenching of the star-formation activity once their original gas is depleted.

Galaxy clusters are the largest bound structures in the Universe, containing large number of galaxies tied by the cluster dark matter halos. Seminal studies have proposed several environmental mechanisms that may contribute to the quenching of star-formation. They range from stran-

gulation/starvation (i.e., galaxies cease to accrete gas cosmologically, and they continue forming stars until their remaining disk gas is consumed; [134, 135]), ram pressure stripping (hereafter RPS, i.e. the removal of gas by ‘winds’ due to the hot intra cluster medium, ICM; [56]), galaxy interactions (e.g., galaxy harassment; [136–138]), to the increase of gas stability through morphological quenching (hereafter MQ; [139]). However, the interplay between these different mechanisms and their relative contribution to changes in the gas content are still not *precisely* understood (e.g., [140]).

Star-formation activity takes place in giant molecular clouds, GMCs (e.g., [12, 24, 28, 29, 31, 32]). However, H₂ reservoirs depend on the extended HI component (e.g., [141]), and the presence of atomic gas is thus important for sustaining the production of new stars over a long time scale. Observations reveal that the atomic gas can be strongly affected by high-density environments. Cluster galaxies typically contain less atomic gas than their field counterparts, and commonly show signs of truncation and perturbed HI morphologies (e.g., [5, 16, 142–147]). Although the molecular gas is closer to galaxy centers and more tightly bound than the HI [148], several studies show that the H₂ is also susceptible to significant variations due to environmental effects (e.g., [6, 57, 149–155]).

How the molecular gas is affected by environment, and how this impacts the star-formation activity in galaxy clusters, is a topic of current research. Several scenarios have been proposed; they span from molecular and atomic gas being disturbed and removed simultaneously, atomic gas being removed before the molecular gas, or even an enhancement in the efficiency of the atomic-to-molecular gas transition due to the compression of HI by ram pressure (e.g., [156]). Although using a small sample of galaxies with an heterogeneous set of molecular gas data, [57] find a mild statistically significant correlation between the H₂ and HI deficiencies in Virgo galax-

ies from the Herschel Reference Survey (HRS; [157]), supporting the hypothesis that they are simultaneously affected. [155] note that VERTICO galaxies with larger HI deficiencies (an indicator of how poor in HI individual galaxies are when compared to field galaxies of the same size and morphological type, [142, 158, 159]; see also [140] for a detailed description) also have more compact and steeper H₂ radial profiles. Although with significantly different physical properties than the Virgo cluster, [160] find however a significant scatter in the global molecular-to-atomic ratios, R_{mol} , in galaxies selected from the Fornax cluster, which suggests that the effects of environmental mechanisms on the atomic-to-molecular gas transition may not be straightforward (e.g., [154]).

In recent decades, a broad variety of studies on the physical conditions within local field galaxies have shown that, for the H₂-dominated regions of galaxy disks, the star formation rate (SFR) per unit molecular gas mass, the star formation efficiency of the molecular gas, $\text{SFE}_{\text{mol}} = \Sigma_{\text{SFR}}/\Sigma_{\text{mol}}$, does not vary strongly with radius (except for the galaxy centers; e.g., [1, 32, 161]). However, [162] found an anticorrelation between the H α central concentration parameter and the normalized massive star-formation rate ($\text{NMSFR} = F_{\text{H}\alpha}/F_R$, where $F_{\text{H}\alpha}$ and F_R are the H α and the R -band fluxes, respectively) in Virgo galaxies. Moreover, detailed studies of Virgo's NGC 4654 galaxy by [156] show that, even though R_{mol} values in the north-west appear to be lower when compared to other regions with similar total gas surface density, both the atomic gas surface density, Σ_{atom} , and the SFE_{mol} seem to be higher. They associate this effect with atomic gas being compressed, which consequently increases the molecular gas surface density, Σ_{mol} . Similar results are also found by [163], who note an enhancement of the efficiencies in low mass galaxies on their first infall into the Fornax cluster. They suggest that this is likely due gas compression by environmental effects (e.g., by RPS and tidal interactions). The relations between

scale lengths might be therefore significantly different in cluster galaxies due to environmental effects. [16] observed that in galaxies closer to the center of the Virgo cluster (and also in some galaxies at the outskirts), HI disks are much smaller than optical disks. Similar results are also found by [164], who find HI disks smaller than optical disks in Hydra I cluster galaxies selected from the Widefield ASKAP L-band Legacy All-sky Blind Survey (WALLABY; [165]). However, it is less known how much the cluster environment might change the *molecular* gas distribution (e.g., [166]). Molecular gas is distributed closer to galaxy centers than HI and it is thus more tightly bound and more difficult to affect, and some removal mechanisms such as RPS may be considerably less effective on the denser molecular medium.

According to [37], the HI-to-H₂ transition takes place through gas condensation of the atomic gas when it reaches a critical surface density of $\Sigma_{\text{crit}} \approx 10 M_{\odot} \text{pc}^{-2}$. Therefore, a plausible scenario is that RPS effects may be helping the HI to reach the critical column density. As result, the enhancement of the H₂ production in Virgo galaxies may correspond to a more efficient HI-to-H₂ transition. Several studies have reported observational evidence consistent with these ideas (e.g., [153, 167, 168]). For instance, [153] note that NGC 4654 shows some strongly compressed atomic gas that exceeds Σ_{crit} . They also found a CO-to-H₂ conversion ratio a factor ~ 2 higher than the Galactic value and SFE_{mol} values around $\sim 1.5 - 2$ higher than the rest of the disk.

Galaxy surveys can be very helpful to understand the ensemble tendencies of the star-formation activity and how these depend on the physical conditions of the molecular gas (e.g., the HERA CO Line Extragalactic Survey, HERACLES, [30, 32]; the Herschel Reference Survey, HRS, [157]; the James Clerk Maxwell Telescope Nearby Galaxies Legacy Survey, NGLS, [169]; the CO Legacy Database for GALEX Arecibo SDSS Survey, COLD GASS, and the extended

COLD GASS, xCOLD GASS, [66, 67]). In this work, we determine radial length scales, mass ratios, and star formation efficiencies of molecular gas in the Virgo Environment Traced in CO survey (VERTICO; [6]), using ALMA Compact Array observations and ancillary data available for 38 galaxies with low inclinations. VERTICO is an ALMA Large Program designed to investigate the effect of the cluster environment on galaxies by mapping the star-forming molecular gas in 51 galaxies selected from the Virgo cluster. Since galaxy clusters are natural laboratories to test star-formation quenching processes due to environmental mechanisms, VERTICO gives us a unique opportunity to study not only their impact on molecular gas disturbances at sub-kiloparsec scales, but also to analyze how these processes affect the efficiency of the atomic-to-molecular gas transition and the star formation activity.

This paper is organized as follows: Section 3.2 presents the main features of the VERTICO survey and the sample selection. In Section 3.3 we explain the methods applied to analyze the data and the equations used to derive the physical quantities. Finally, in Section 3.4 we present our results and discussion, and Section 3.5 we summarize the main conclusions of this work.

3.2 Data products

One of the main advantages of carrying out a systematic analysis on the VERTICO survey is the vast ancillary data gathered by studies of Virgo cluster galaxies. The VERTICO sample selection and data reduction are described in detail in [6]; here we summarize the main features.

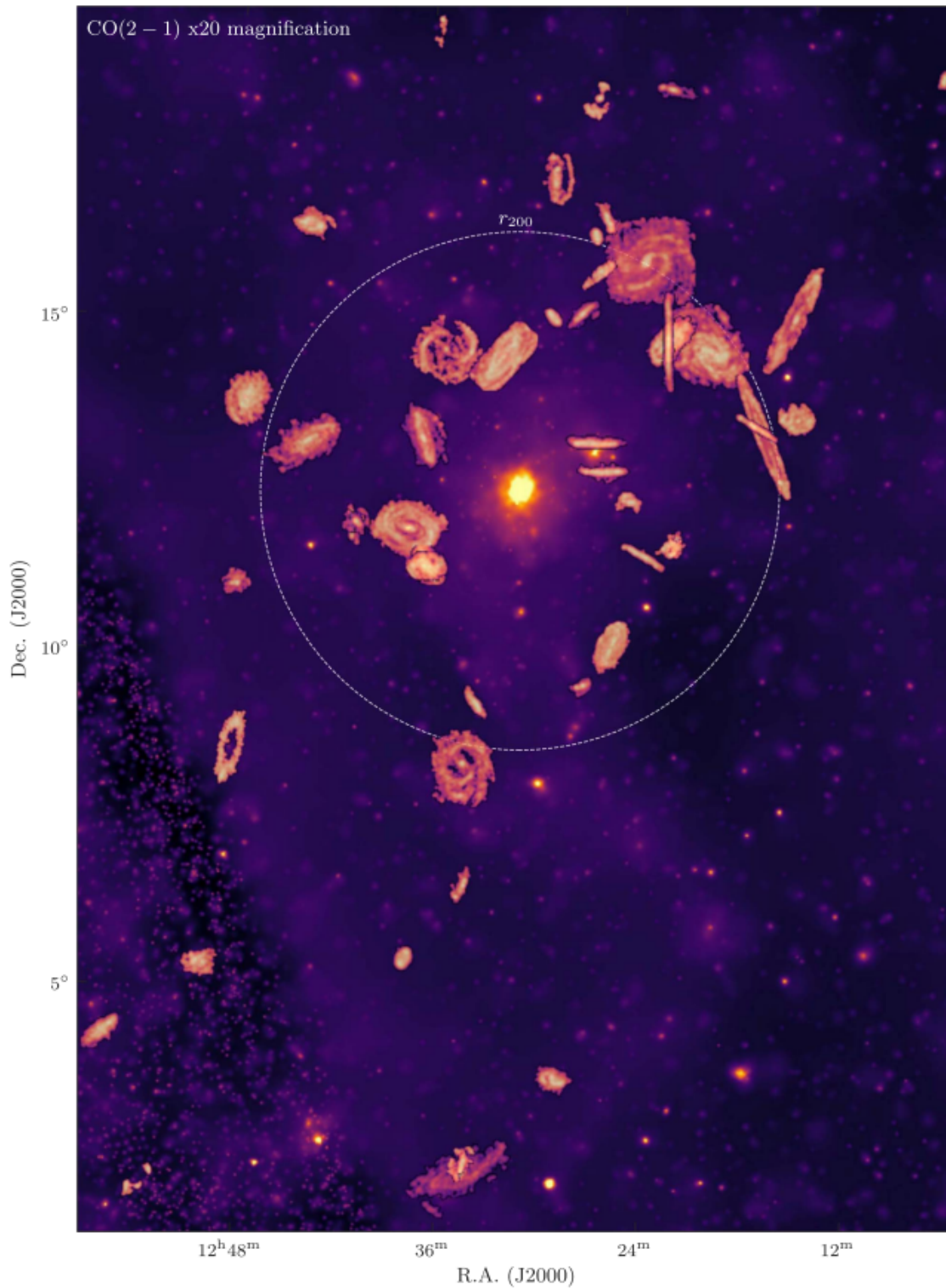


Figure 3.1: Background-subtracted, exposure-corrected ROSAT All Sky Survey mosaic of the Virgo Cluster (hard band: 0.4-2.4 keV), with an overlay of 49 VERTICO CO(2-1) peak temperature maps, increased in angular size by a factor of 20 for illustration. Image taken from [6].

3.2.1 The VERTICO Survey

We use molecular gas data from VERTICO¹, which maps the CO(2-1) emission in 51 late-type spirals galaxies selected from the VIVA HI survey [16]. The galaxies were observed with the ALMA Morita Array, including total power observations. Out of its 51 sources, 15 galaxies are taken from the ALMA archive [168, 170]. VERTICO contains a broad diversity of galaxies experiencing different environmental effects, with stellar masses in the range $10^{8.3} \leq M_*/M_\odot \leq 10^{11}$, and specific star formation rates, $\text{sSFR} = \text{SFR}/M_*$, of $10^{-11.5} \leq \text{sSFR}/\text{yr}^{-1} \leq 10^{-9.5}$. VERTICO cover a variety of star formation properties in Virgo cluster galaxies, including normal (SFRs similar to the global median), enhanced (galaxies above 3 times the global median), anemic (galaxies with significantly low SFRs), and truncated galaxies (sharp cutoff in the star-forming disk), based on the spatial distribution of H α and *R*-band emission (see § 2 in [162] for a detailed description of these categories).

VERTICO encompasses spectroscopic observations of the $J = 2 - 1$ transition of ¹²CO and its isotopologues (i.e., ¹³CO(2-1) and ¹⁸CO(2-1)), as well as the 1-mm continuum. The galaxies were mapped using Nyquist-sampled mosaicking; while total power (TP) plus 7-m arrays were required for 25 galaxies, the rest of the observations were performed with 7-m array only. The archival data and raw visibilities were processed using the Common Astronomy Software Applications package v. 5.6 (CASA; [171]). The Compact Array data and the TP observations were combined using feathering and imaged with the PHANGS-ALMA Imaging Pipeline (v. 1.0; [172]).

For the analysis performed in this work, we use the CO(2-1) 9'', (~ 750 pc at Virgo cluster

¹<https://www.verticosurvey.com>

distance of 16.5 Mpc; [20]) datacubes with 10 km s^{-1} channel width. Since NGC 4321 has a native angular resolution poorer than $9''$, ($\sim 10''$), we used CO(2-1) datacubes at $15''$, ($\sim 1 \text{ kpc}$). When we compute the resolved molecular-to-atomic ratios (see § 4.3.1), we use the $15''$, CO(2-1) datacubes, which have been matched to VIVA’s HI angular resolution. The CO datacubes have a characteristic rms noise of $\sim 15 \text{ mJy beam}^{-1}$ at 5 km s^{-1} (see [6] for more details).

3.2.2 Ancillary Data and Data Selection

To complement the $9''$ CO(2-1) datacubes from VERTICO, we use the SFR surface density, Σ_{SFR} , and stellar mass surface density, Σ_{\star} , derived from a combination of near UV and near/mid-infrared photometry. Specifically, we use the resolved star formation rate maps from GALEX and WISE photometry, which were derived by following the procedure laid out in [173]. All images are convolved from their native resolution to a $9''$, Gaussian beam with the [174] convolution kernels. All Gaia DR2 stars within the image area are masked. Image backgrounds are estimated and subtracted with the `Astropy` Background 2D function. SFR maps are constructed from a combination of GALEX NUV and WISE3 photometry as our obscured tracer in order to match the $9''$, resolution which is not possible with WISE4 (see Appendix of [173] for more details). We apply a local WISE3-to-WISE4 colour correction to the WISE3 images by fitting a linear relationship between W3/W4 colour and galactocentric radius and then modify the WISE3 image on a pixel-by-pixel basis according to the galactocentric radius of each pixel and the expected W3/W4 ratio from the linear fit. For a more detailed description, see [19]. With GALEX NUV and colour-corrected WISE3 images for each galaxy, we then apply the NUV+WISE4 SFR calibration from [173] to derive spatially resolved SFR maps in units of $M_{\odot} \text{ kpc}^{-2} \text{ yr}^{-1}$. All the

pixels in the maps where the S/N of the NUV or the WISE3 imaging is below 3 are masked. Stellar mass maps are derived from WISE1 photometry. For each pixel, the procedure determines the local mass-to-light ratio (at $3.4\mu\text{m}$) using the WISE3 to WISE1 colour as an ‘sSFR-like’ proxy and following the calibrations given in the Appendix of [173]. The WISE1 images are then combined with the derived mass-to-light ratios to produce resolved stellar mass maps in units of $M_{\odot}\text{pc}^{-2}$. Both SFR and stellar maps at $9''$, are derived by assuming a Kroupa initial mass function (IMF; [175]). It would be interesting to verify that similar results are obtained using SFR estimators that respond on shorter timescales, such as $\text{H}\alpha$.

Optical inclination and position angles are obtained from fits to the SDSS using r -band photometry. In order to measure the atomic gas content and velocities, we use 21-cm moment-0 and moment-1 maps from the VLA Imaging survey of Virgo galaxies in Atomic gas (VIVA; [16]), which were re-imaged to $15''$ resolution to match the resolution of VERTICO data [6]. Finally, the isophotal radius, r_{25} , is derived from the optical size of the major axis measured at 25 mag arcsec^{-2} in the B -band, r_{25} from the *The Third Reference Catalogue of Bright Galaxies* (RC3; [8]).

To reduce the beam-smearing effects when deriving the molecular gas profiles, we select galaxies with inclinations $i \leq 75^{\circ}$. Out of the 51 VERTICO galaxies, and rejecting the two nondetections of the survey (IC 3418 and VCC 1581; see Table 2 in [6]), we obtain a final subsample of 38 galaxies that fulfill the selection criteria.

3.3 Methods

3.3.1 Stacking of the CO Spectra

To investigate how the H_2 content (and associated quantities) changes as a function of radius, it is important to recover CO emission in the outermost parts of galaxies, which host the faintest CO emission. To achieve this, we perform a spectral stacking of the ^{12}CO ($J = 2 - 1$) emission line using the HI velocities to coherently align the spectra while integrating in rings. The CO spectral stacking recovers CO flux over a broad range of galactocentric radii, thus allowing us to test how both R_{mol} and SFE_{mol} are affected by the environment from the inner- to the outermost parts of VERTICO galaxies.

We perform the CO emission line stacking procedure following the methodology described in the previous chapter, which is based on the approach detailed in [78]. The method relies on using the HI velocity data to define the velocity range for integrating CO emission. The key assumption of this method is that both the HI and CO velocities are similar at any galaxy location, which is consistent with the results shown by [79] for star-forming galaxies selected from the EDGE-CALIFA survey. Since this may not be the case for cluster galaxies due to environmental effects perturbing the HI and H_2 in a distinct way, we test this by computing the differences between the CO(2–1) and HI velocities, $\Delta V = V_{\text{CO}(2-1)} - V_{\text{HI}}$, in spaxels within the 38 VERTICO galaxies included in this work. Figure 3.2 shows that typically the differences between the atomic gas and the CO velocities are almost always smaller than the size of the velocity integration window (discussed below). To make sure that we recover as much CO intensity as possible, we implement a “smart stacking”. We only take the stacked CO intensities in annuli where we

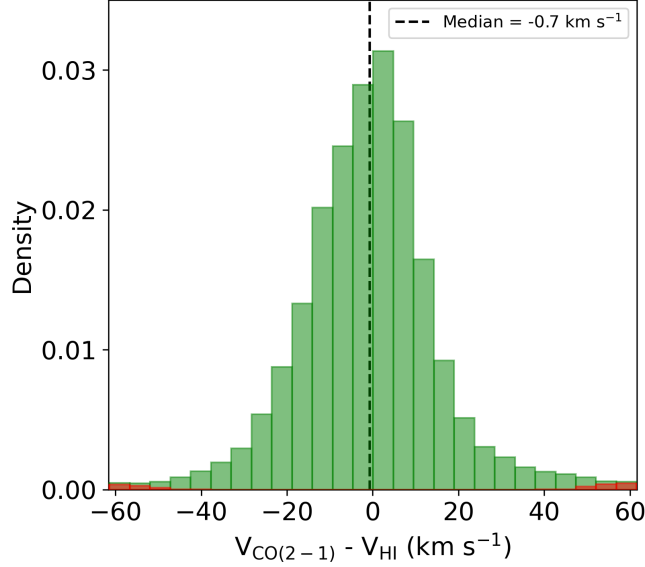


Figure 3.2: Distribution of offsets between the CO(2–1) and HI velocities, $\Delta V = V_{\text{CO}(2-1)} - V_{\text{HI}}$, in spaxels within the 38 VERTICO galaxies analyzed here. The red bars correspond to spaxels with ΔV offsets that place CO outside the integration window (see text) for stacking CO. The vertical black-dashed line is the median value of $\Delta V = -0.7 \text{ km s}^{-1}$. The figure shows that, on average, the differences between the CO(2–1) and HI velocities are smaller than the integration window in most cases ($\sim 98\%$).

have a strong HI signal (i.e., HI surface densities $> 1 \text{ M}_{\odot} \text{ pc}^{-2}$, yielding reliable HI velocity measurements); otherwise, we take the unstacked CO intensities. Because of beam smearing in the HI, intensities in the innermost parts of the galaxies ($r \leq 0.3r_{25}$) can produce unreliable HI velocity estimates, we employ stacked CO intensities only in annuli where their SNR is larger than that of the unstacked data.

Since we are interested in radial variations of the galaxy properties of VERTICO galaxies, we stack in radial bins $\sim 0.1r_{25}$ wide. In practice, galactocentric radius is usually a well-determined observable and it is covariant with other useful local parameters, which makes it a very useful ordinate [78]. As discussed in Chapter 2 and later in this section, after shifting the CO spectra to match the HI velocity in each spaxel within a given annulus, we integrate over a spectral window designed to minimize missing CO flux to compute the CO (2–1) line emission

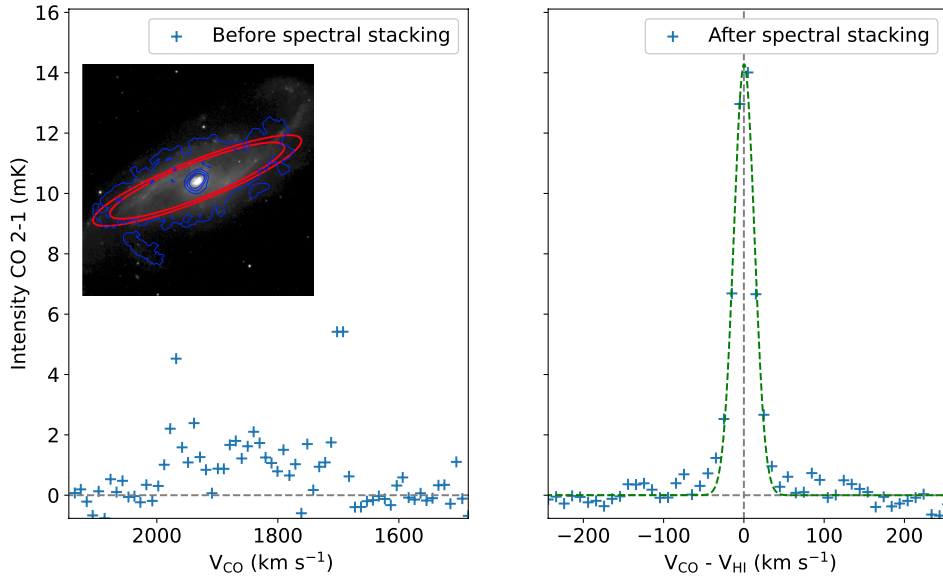


Figure 3.3: Spectral stacking example. The average CO(2–1) spectrum within an annulus that spans from 0.6 to 0.7 r_{25} in NGC 4536 is shown. The left panel shows the average of all spectra in the annulus in the observed velocity frame. The inset panel includes the SDSS r -band image (background), CO(2–1) data (blue contours), and the annulus that spans from 0.6 to 0.7 r_{25} (red ellipses). The right panel shows the average in the velocity frame relative to HI along with the best Gaussian fit profile (green dashed line).

intensity, $I_{\text{CO}(2-1)}$. To define the integration window for the annuli, we use the third-order polynomial included in the top panel of Figure 2 in Chapter 2. They analyze the variation of molecular velocity dispersion as a function of radius for a sample of galaxies, and found a velocity envelope that is characterized as a polynomial. We use the same relation here to define our integration window.

Figure 3.3 shows the usefulness of the stacking procedure in recovering the average CO(2–1) line emission. As an example, we show the average CO spectrum of NGC 4536 within an annulus that spans from 0.6 to 0.7 r_{25} . The left panel contains the average CO spectra within the given annulus using the observed velocity frame, while the right panel shows the average CO spectra after shifting by the observed HI velocity. This procedure allows us to co-add CO intensities coherently and minimize noise. Figure 3.3 also shows the best Gaussian fit for the

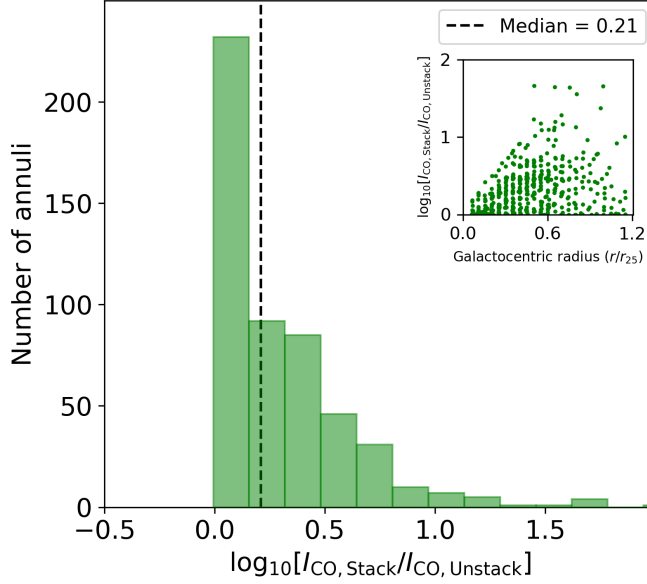


Figure 3.4: Ratio of the integrated CO(2–1) line intensity in an annulus after stacking to that before stacking. The vertical black-dashed line is the median value of $\log_{10}[I_{\text{CO,Stack}}/I_{\text{CO,Unstack}}] = 0.21$; this shows that, on average, stacking recovers $\sim 60\%$ more emission. On average, we are reaching a characteristic rms noise of 0.1 mK at 10 km s^{-1} , which corresponds to a sensitivity of $\sim 0.1 M_{\odot} \text{ pc}^{-2}$. The inset panel compares $\log_{10}[I_{\text{CO,Stack}}/I_{\text{CO,Unstack}}]$ vs galactocentric radius, and shows that annuli with the most CO flux enhancement are at $r \geq 0.5r_{25}$.

averaged-stacked spectra (green-dashed line); as can be seen, the signal-to-noise ratio in the measurement of CO velocity-integrated intensity is lower and without performing the stacking procedure the CO line emission is not clearly detected. To quantify the improvement of the flux recovery, we compute the ratios between the final stacked and unstacked integrated CO(2–1) line intensity, $I_{\text{CO,Stack}}/I_{\text{CO,Unstack}}$, for each annulus. A histogram of the distribution of ratios is shown in Figure 3.4. We find a median ratio of $\log_{10}[I_{\text{CO,Stack}}/I_{\text{CO,Unstack}}] \sim 0.21$; on average, the intensity in an annulus is increased by nearly $\sim 60\%$. We emphasize that most of the annuli with significant enhancements have weak CO emission and are found at large galactocentric radii. Thus, while stacking does not result in a large increase in total CO flux from a galaxy, it does extend the range of radii over which CO is detected, and results in a more accurate (larger) measurement of flux at larger radii. To compute the integrated flux uncertainties, we take the

RMS from the emission-free part of the stacked CO spectra. We adopt a clipping level of 3 in order to consider a valid detection. On average, we reach a characteristic rms noise of 0.1 mK at 10 km s^{-1} (in the range of $\text{rms} \sim 0.05 - 1 \text{ mK}$), which corresponds to a sensitivity of $\sim 0.1 M_{\odot} \text{ pc}^{-2}$ per 10 km s^{-1} channel. Since we are interested in comparing of the radial profiles of the molecular gas, atomic gas, stellar mass, and star formation rate, it is appropriate to average over the entire annulus rather than limiting the average to spaxels where emission is detected.

3.3.2 Basic Equations and Assumptions

The molecular gas surface density, Σ_{mol} , is derived from the integrated CO intensity, $I_{\text{CO}(2-1)}$, by adopting a constant CO-to- H_2 conversion factor, that is based on observations of the Milky Way; $X_{\text{CO}} = 2 \times 10^{20} \text{ cm}^{-2} (\text{K km s}^{-1})^{-1}$, or $\alpha_{\text{CO,MW}} = 4.3 M_{\odot} (\text{K km s}^{-1} \text{ pc}^2)^{-1}$ for the CO(J=1-0) line ([83]), following the analysis by [6]. We also test how our results depend on the α_{CO} prescription that we adopt by using the CO-to- H_2 conversion factor from Equation 31 in [38]:

$$\alpha_{\text{CO}} = 2.9 \exp\left(\frac{+0.4}{Z' \Sigma_{\text{GMC}}^{100}}\right) \left(\frac{\Sigma_{\text{total}}}{100 M_{\odot} \text{ pc}^2}\right)^{-\gamma}, \quad (3.1)$$

in $M_{\odot} (\text{K kms}^{-1} \text{ pc}^{-2})^{-1}$, $\gamma \approx 0.5$ for $\Sigma_{\text{total}} > 100 M_{\odot} \text{ pc}^{-2}$ and $\gamma = 0$ otherwise, and the metallicity normalized to the solar one, $Z' = [\text{O}/\text{H}]/[\text{O}/\text{H}]_{\odot}$, where $[\text{O}/\text{H}]_{\odot} = 4.9 \times 10^{-4}$ [86], $\Sigma_{\text{GMC}}^{100}$ is the average surface density of molecular gas in units of $100 M_{\odot} \text{ pc}^{-2}$, and Σ_{total} is the combined gas plus stellar surface density on kpc scales. Since we are interested in the global variations of the $\alpha_{\text{CO}}(Z', \Sigma_{\text{total}})$, we mainly focus our analysis on its dependence on Σ_{total} , since variations in this have the dominant effect for the regions studied in our sample. Therefore, we

adopt a constant solar metallicity (i.e., $Z' = 1.0$). We use the following expression to obtain Σ_{mol}

$$\Sigma_{\text{mol}} = \frac{\alpha_{\text{CO}}}{R_{21}} \cos(i) I_{\text{CO}(2-1)}, \quad (3.2)$$

which adopts the average VERTICO survey’s line luminosity ratio of $R_{21} = I_{\text{CO}(2-1)}/I_{\text{CO}(1-0)} = 0.77 \pm 0.05$ obtained by [6], and i is the inclination of the galaxy. This equation takes into account the mass “correction” due to the cosmic abundance of helium.

The atomic gas surface density, Σ_{atom} , is computed from the integrated 21 cm line intensity taken from the VIVA survey [16], $I_{21\text{cm}}$, by using the following equation (e.g., [30])

$$\frac{\Sigma_{\text{atom}}}{\text{M}_{\odot} \text{pc}^{-2}} = 0.02 \cos(i) \frac{I_{21\text{cm}}}{\text{K km s}^{-1}}, \quad (3.3)$$

which includes both the inclination and a factor of 1.36 to account for the presence of helium.

Recent observational evidence has shown that molecular gas content and its distribution in the disk of cluster galaxies depends on the effect of the environment on the HI distribution (e.g., [57, 140, 155, 156]). In order to characterize the behavior of the molecular gas as a function of the cluster environmental effects on the atomic gas, we use the HI classification from [5] (hereafter HI-Class). The classification is designed to quantify the perturbation level of atomic radial profiles based on morpho-kinematic HI features and HI-deficiency (e.g., [140, 142]) present in the VIVA survey. In total, 48 sources were selected by [5] to construct the classification, which are a good representation of Virgo galaxies undergoing various strengths of gas stripping. Note that this is different from classifying the galaxies in order of increasing HI deficiency, although more highly disturbed galaxies tend to be more HI deficient. According to [5], the 38 VERTICO

galaxies analyzed in this work can be categorized into the following five classes (including the number of galaxies in each of them):

0. Class 0 (11 galaxies): The HI profiles are symmetric, not truncated, and have extended and similar HI content compared to most normal field galaxies. These are therefore the cases showing no definite signs of gas stripping due to the ICM.
1. Class I (7 galaxies): One-sided HI feature, such as a tail, and no truncation of the HI disk within the relatively symmetric stellar disk; range of HI deficiencies shown, but overall comparable to those of field galaxies.
2. Class II (5 galaxies): A highly asymmetric HI disk, with one-sided gas tails, extraplanar gas, and/or HI disk truncation on at least one side of the stellar disk; quite deficient in HI with an average of only $\sim 17\%$ of the typical HI mass of a field counterpart.
3. Class III (9 galaxies): A symmetric, but severely truncated HI disk; extremely deficient in HI with an average of $<4\%$ of the HI mass of a field galaxy counterpart.
4. Class IV (6 galaxies): A symmetric HI disk with marginal truncation within the radius of the stellar disk; lower HI surface density than the other subclasses; quite deficient in HI with on average $\sim 15\%$ of the HI mass of a field galaxy counterpart.

A more quantitative description of these galaxy categories can be found in [5]. Since a definition of the HI-Classes based on a single criterion is not trivial, we also complement this classification by categorizing these five HI-Classes in three broader groups as follows: i) Unperturbed galaxies (HI-Class 0); ii) asymmetric galaxies (HI-Classes I and II); and iii) symmetric-truncated galaxies

(HI-Class III and IV). These HI-Groups represent a powerful classification, which boost the statistics and provide a simpler analysis framework.

The spatially-resolved molecular-to-atomic gas ratio, R_{mol} , is calculated as

$$R_{\text{mol}} = \frac{\Sigma_{\text{mol}}}{\Sigma_{\text{atom}}}. \quad (3.4)$$

Similarly, we compute the spatially resolved molecular-to-stellar and the atomic-to-stellar ratios, $R_{\star}^{\text{mol}} = \Sigma_{\text{mol}}/\Sigma_{\star}$ and $R_{\star}^{\text{atom}} = \Sigma_{\text{atom}}/\Sigma_{\star}$, respectively, where Σ_{\star} is the stellar surface density derived from the WISE band-1 data. To obtain the integrated values for these ratios (i.e. mass ratios), we integrate the surface densities for the molecular gas, atomic gas, and stars (assuming that they are distributed along a thin disk) to obtain the total masses as:

$$M_i(r < R_{e,\star}) = 2\pi \int_0^{R_{e,\star}} \Sigma_i(r) r dr, \quad (3.5)$$

where $R_{e,\star}$ is the effective radius for the stellar component (see §3.4.2 for more details), and $i = \text{mol}, \text{atom}, \star$. We then calculate the integrated ratios as the ratio of the masses. We compute the resolved SFR surface density per unit molecular gas surface density, i.e. the star formation efficiency of the molecular gas (SFE_{mol} , in units of yr^{-1}) for each annulus,

$$\text{SFE}_{\text{mol}} = \frac{\Sigma_{\text{SFR}}}{\Sigma_{\text{mol}}}, \quad (3.6)$$

where Σ_{SFR} is the resolved SFR surface density. We also obtain the integrated star formation efficiency of the molecular gas within $R_{e,\star}$, $\text{SFE}_{\text{mol}}(r < R_{e,\star})$, using $\Sigma_{\text{SFR}}(r)$, $\Sigma_{\text{mol}}(r)$, and Equation 4.9, so

$$\text{SFE}_{\text{mol}}(r < R_e) = \frac{2\pi \int_0^{R_e} \Sigma_{\text{SFR}} r dr}{M_{\text{mol}}(r < R_e)}. \quad (3.7)$$

Finally, to calculate the galactocentric radius of each annulus for each galaxy we use the inclinations from [6] and we adopt the distance to the Virgo cluster of 16.5 Mpc from [20].

3.3.3 CO Radial Profiles

As discussed in §3.3.1, we derive the molecular gas radial profiles by measuring the averaged azimuthal CO surface density, after performing a spectral stacking, in elliptical annuli in the 9", CO(2–1) datacubes. Although CO radial profiles for VERTICO galaxies are already presented in [6] and [155] (both using the same methodology described in §4.3 of [6]), the CO spectral stacking expands the radial coverage and recovers faint CO emission especially in the outermost regions of most cases. Figure 3.5 shows the molecular gas radial profiles derived in this work (blue-solid line), and their $\pm 1\sigma$ uncertainties (blue-shaded areas) for the 38 VERTICO galaxies selected here. Although radial profiles in [6] and used in [155] are not corrected for inclination, they agree fairly with those included in Figure 3.5 (particularly at $r < 0.3r_{25}$) when we multiply them by $\cos(i)$. Annuli are centered on the optical galaxy position and aligned with the major-axis position angle, taken from Table 1 in [6]. After summing the velocity-integrated CO line emission pixel intensities in an annulus, we divide the sum by the total number of pixels to obtain the average $I_{\text{CO}(2-1)}$ for the annulus. We then use Equation 4.7 to obtain the molecular gas surface density, Σ_{mol} .

Galaxies in Figure 3.5 are sorted by HI-Class. Although Σ_{mol} tends to be lower than Σ_{atom} for HI-Classes 0 and I (except for some galaxies with $\Sigma_{\text{mol}} > \Sigma_{\text{atom}}$ at $r \leq 0.3r_{25}$), we note that

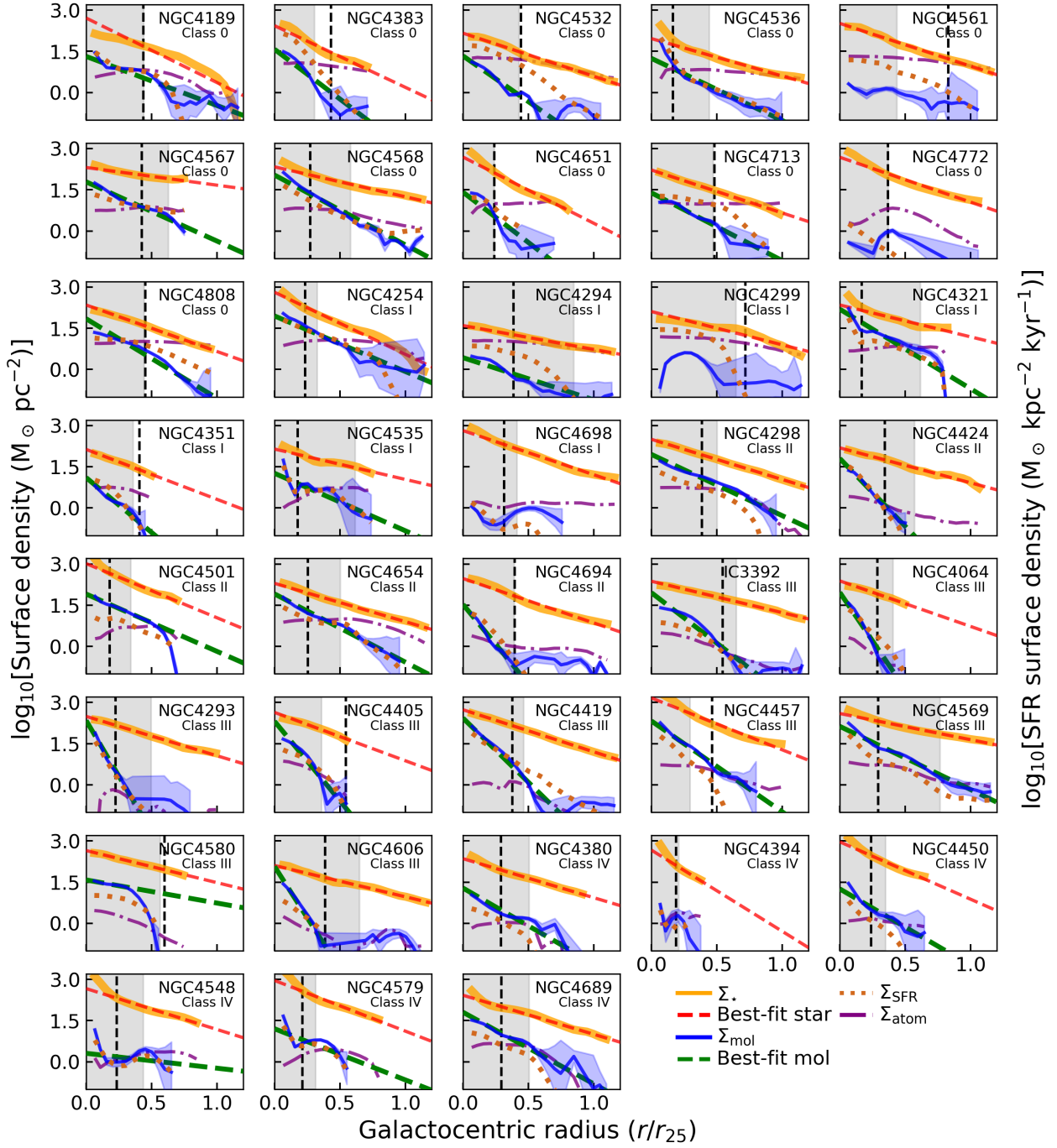


Figure 3.5: Stacked molecular gas (Σ_{mol} , solid-blue line) and stellar (Σ_* , solid-orange line) surface densities, in units of $M_{\odot} \text{pc}^{-2}$, as a function of galactocentric radius, in units of r_{25} , for the 38 VERTICO galaxies analyzed in this work (sorted by HI-Class). The shaded-blue area is the Σ_{mol} uncertainty. The brown-dotted line is the star formation rate surface density, Σ_{SFR} . The purple-dashed line is the atomic gas surface density derived from HI moment 0 maps at $15''$, resolution from the VIVA survey. The shaded-gray area is the region within the stellar effective radius $R_{e,*}$. The dashed-green and dashed-red lines represent the best-fit exponential profiles for Σ_{mol} and Σ_* , respectively, when an exponential fit was appropriate. The vertical-dashed lines correspond to $r_{\text{gal}} = 3\text{kpc}$.

the molecular gas seems to extend at least up to $\sim 0.5r_{25}$ (i.e., $\Sigma_{\text{mol}} > 1 \text{ M}_{\odot} \text{ pc}^{-2}$; excluding NGC 4772, NGC 4299, and NGC 4698). Conversely, HI-Classess II-IV show clear signs of truncation in both molecular and atomic gas radial profiles (except for NGC 4298, NGC 4654, and NGC 4569), with $\Sigma_{\text{mol}} > \Sigma_{\text{atom}}$ at any galactocentric radius. Interestingly, we note a systematic correlation in the truncation between Σ_{mol} and Σ_{atom} radial profiles with increasing HI-Class.

To estimate how Σ_{mol} depends on the α_{CO} prescription, we compute the ratio between the variable and the constant CO-to-H₂ conversion factors, $\alpha_{\text{CO}}(\Sigma_{\text{total}})/\alpha_{\text{CO,MW}}$. We find that $\alpha_{\text{CO}}(\Sigma_{\text{total}})/\alpha_{\text{CO,MW}}$ ranges from 0.2 to 1.0 in the region within $\sim 0.6r_{25}$ (with a median of 0.95); for $r > 0.6r_{25}$, we find that $\alpha_{\text{CO}}(\Sigma_{\text{total}})/\alpha_{\text{CO,MW}} = 1.0$. Although these results show that Σ_{mol} depends on the adopted conversion factor, we note that $\alpha_{\text{CO}}(\Sigma_{\text{total}})$ has very small departures from $\alpha_{\text{CO,MW}}$ for most of the annuli; consequently, the trends that we find in this work do not vary significantly due to the prescriptions for α_{CO} selected for this work. We emphasize however that our exploration of the effects of α_{CO} dependence is limited and it deserves a careful analysis in future VERTICO projects.

Except for the spectral stacking used for CO, we implement the same method (averaging over all pixels in an annulus) for the star-formation rate, atomic gas, and stars. The latter two are shown in Figure 3.5 by the purple-solid and orange-solid lines, respectively.

3.4 Results and Discussion

3.4.1 Scale Lengths and Environment

How do the relations between spatial distributions of the molecular gas and the stellar components depend on galaxy environment? Several studies have revealed the close relation

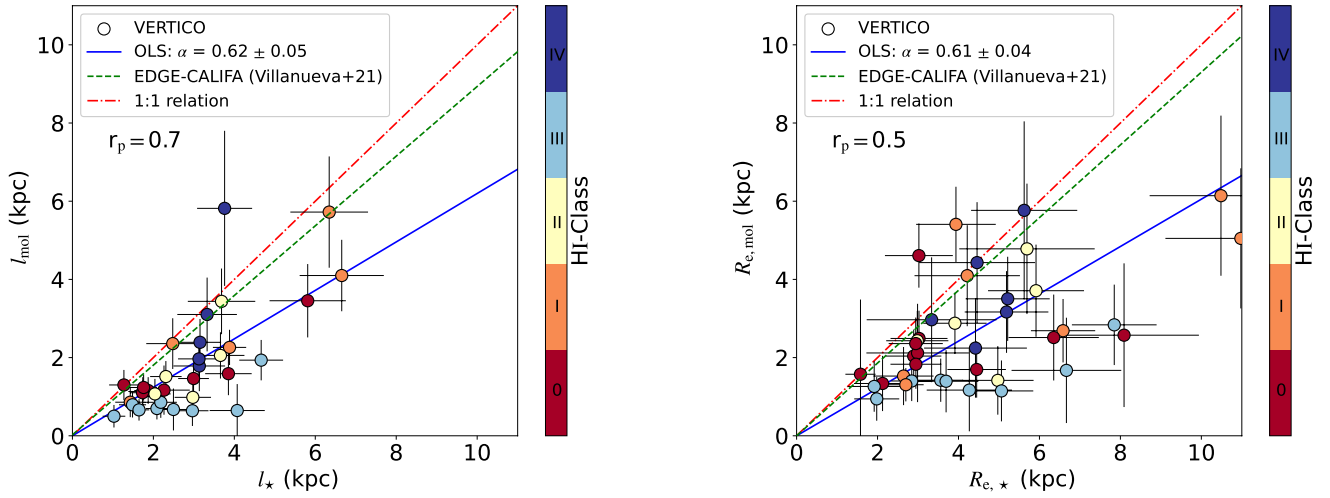


Figure 3.6: *Left:* Comparison between the stellar, l_* , and molecular scale lengths, l_{mol} , computed by fitting exponential profiles to the respective surface densities as a function of galactocentric radius. The colored circles correspond to 33 VERTICO galaxies with $\Sigma_{\text{mol}} > 1 \text{ M}_{\odot} \text{ pc}^{-2}$ for all the annuli within $0.25r_{25}$, color-coded by HI-Class from [5]. The blue-solid line is the OLS linear bisector fit (forced through the origin) for them, and the dashed-dotted-red and dashed-green lines illustrate the 1:1 scaling and the OLS linear bisector fit for EDGE-CALIFA galaxies (see Chapter 2), respectively. The ‘ r_p ’ value noted corresponds to the Pearson correlation parameter. *Right:* The molecular, $R_{e,\text{mol}}$, vs stellar, $R_{e,*}$, effective radii, which enclose 50% of the total molecular gas and stellar masses, respectively, for the 38 VERTICO galaxies analyzed in this work. Conventions are as in left panel.

between the spatial distribution of molecular gas and stars in galaxies selected from the field (e.g., [108, 109]). For instance, analyzing the molecular gas, l_{mol} , and stellar, l_* , exponential scale lengths (the brightness of the disc has fallen off by a factor of e , or ~ 2.71828 , from the center) for spiral galaxies selected from HERACLES ([101]), [30] showed a roughly 1:1 relation between them, with a best-fitting relation of $l_{\text{mol}} = [0.9 \pm 0.2] \times l_*$. A larger recent survey of 68 galaxies from the EDGE-CALIFA survey which covers a broad variety of morphologies finds a similar relation, $l_{\text{mol}} = [0.89 \pm 0.04] \times l_*$ (see Chapter 2).

To characterize the distributions, we compute l_{mol} and l_* using our molecular gas and stellar radial profiles. From the 38 galaxies with $i < 75^\circ$, we have selected VERTICO galaxies with Σ_{mol} and Σ_* radial profiles well described by an exponential profile and with $\Sigma_{\text{mol}} > 1 \text{ M}_{\odot}$

pc⁻² for all annuli within $0.25r_{25}$. These fits are shown by the green and red dashed lines in Figure 3.5. We have rejected annuli with $r_{\text{gal}} < 1.5$ kpc to avoid the central regions that may be susceptible to significant variations of α_{CO} (e.g., [100]), or to breaks in the exponential scale lengths (particularly for stars) due to bulges [109]. We obtain l_{mol} and l_{\star} for a subsample of 33 galaxies that fulfill the selection criteria mentioned above; the relation between them, colored by HI-Class, is shown in the left panel of Figure 3.6. We observe a fairly strong correlation between l_{mol} and l_{\star} (Pearson $r_p = 0.7$; $p\text{-value} < 0.01$). The left panel of Figure 3.6 also contains the OLS bisector fit (blue solid line) for $y = \alpha x$ weighted by the uncertainties for the l_{mol} and l_{\star} points. Columns (5) and (6) of Table 3.1 correspond to the l_{mol} and l_{\star} values, respectively, for the 33 galaxies included on this section.

We find that $l_{\text{mol}} = (0.62 \pm 0.05) \times l_{\star}$ ($\sim 3:5$ relation), much shallower than the almost 1:1 relation between l_{mol} and l_{\star} for (mostly) field EDGE-CALIFA galaxies (green-dashed line in left panel of Fig. 3.6). When we use a variable prescription of $\alpha_{\text{CO}}(\Sigma_{\text{total}})$ (Equation 4.6), we obtain $l_{\text{mol}} = (0.66 \pm 0.05) \times l_{\star}$, which is in agreement with the fixed α_{CO} . We note that while l_{mol} values for HI-Classes 0, I, and II tend to be similar to those for l_{\star} , they seem to concentrate significantly below the EDGE-CALIFA spirals trend for HI-Classes III and IV. This implies that the high-density environment of the Virgo Cluster has a measurable effect in compacting the spatial extension of the molecular gas.

Our results are consistent with studies performed in Virgo galaxies by [57], who analyze the relation between the CO-to-stellar (*i*-band) isophotal diameter ratio, $D(\text{CO})_{\text{iso}}/D(i)$, and HI deficiency in galaxies selected from the *Herschel* Reference Survey (HRS; [157]). They find a systematic decrease of $D(\text{CO})_{\text{iso}}/D(i)$ with increasing HI deficiency, which suggests that environmental effects act on both the molecular gas and HI simultaneously, particularly constraining

the H_2 content to galaxy centers (see also Fig. 3 and Fig. 4 in [155] for similar results). This may be attributed to the outside-in ram pressure detected previously in Virgo galaxies, which can compress the atomic gas and increase the molecular gas production (e.g., NGC 4548, 4522, 4330; [176–178]). This mechanism also could create a drag that causes gas to lose angular momentum and drift in. [166] also find a similar result for galaxies selected from the NGLS. Using $^{12}\text{CO}(J = 3 - 2)$ data, they find steeper H_2 radial profiles in Virgo galaxies than for their field counterparts.

3.4.2 Effective Radii and Environment

Comparison of scale lengths requires both the molecular and stellar radial distributions to be well described by an exponential. Non-parametric methods can help evaluate whether the assumption of an exponential disk may affect the conclusions above. The right panel of Figure 3.6 shows the relation between the effective radius of the molecular gas, $R_{\text{e,mol}}$, and the stars, $R_{\text{e},\star}$. These are the radii that enclose 50% of the total molecular gas and stellar mass, respectively, for the 38 VERTICO galaxies analyzed in this work. We determine the total mass of each by integrating the Σ_{mol} and Σ_{\star} radial profiles out to a distance of $\leq 1.2r_{25}$. The relation (Pearson $r_p = 0.5$; $p\text{-value} < 0.01$) between $R_{\text{e,mol}}$ and $R_{\text{e},\star}$ shows larger scatter than that between exponential scale lengths, but it nonetheless confirms the significant compactness of the molecular gas distribution compared to that of the stars. We also note that, in general, galaxies of higher HI-Class (particularly in HI-Class III) tend to have smaller $R_{\text{e,mol}}$ and are more compact relative to their stellar distribution.

In summary, the analysis of the Σ_{mol} radial profiles shows that VERTICO galaxies ($R_{\text{e,mol}} =$

$[0.61 \pm 0.04] \times R_{e,*}$) are approximately 30% smaller in CO relative to their stellar distributions than EDGE-CALIFA galaxies ($R_{e,\text{mol}} = [0.93 \pm 0.05] \times R_{e,*}$; see Chapter 2). When we use a variable $\alpha_{\text{CO}}(\Sigma_{\text{total}})$ (Equation 4.6), we obtain $l_{\text{mol}} = (0.66 \pm 0.04) \times l_*$, which agrees fairly well with the previous result. Similar results are found by [155], who show that VERTICO galaxies with larger HI deficiencies (i.e., upper HI-Classes) have steeper and less extended molecular gas radial profiles, suggesting that the processes behind the atomic gas removal are also producing more centrally concentrated molecular gas radial profiles.

Table 3.1 summarizes the properties of the 38 VERTICO galaxies selected for this work, together with the values for $R_{e,\text{mol}}$, and $R_{e,*}$ (hereafter R_e). In addition, columns (4) and (5) list M_{mol} (which are in good agreement with those included in [6]) and M_* , calculated from the radial profiles.

3.4.3 R_{mol} , SFE, and Environment

In this section we test how local and global physical parameters affect both the molecular-to-atomic gas ratio and the star formation efficiency of the molecular gas.

To understand the effect of the environmental processes of the cluster on gas and star formation properties for VERTICO, we need a comparison sample, that represents galaxies in low-density environments. We compare with two such samples: 1) 64 galaxies selected from spatially resolved surveys of spiral galaxies with $\log[M_*/M_\odot] = 9.1\text{--}11.5$ and morphologies spanning from Sa to Scd, EDGE-CALIFA survey; and 2) xGASS/xCOLD GASS (hereafter xGASS-CO; [67, 179]). For xGASS-CO we use the relations obtained in the analysis by [7] for main sequence (MS) galaxies. Each of these comparison samples have limitations that need to be kept

Name (1)	HI-Class (2)	$\log[M_{\text{mol}}/M_{\odot}]$ (3)	$\log[M_{\star}/M_{\odot}]$ (4)	l_{mol} (kpc) (5)	l_{\star} (kpc) (6)	$R_{\text{e,mol}}$ (kpc) (7)	$R_{\text{e},\star}$ (kpc) (8)
IC 3392	III	8.41±0.15	9.81±0.06	0.71±0.28	2.09±0.28	1.42 ±0.55	3.56±0.55
NGC 4064	III	8.44±0.19	10.01±0.09	0.67±0.54	2.50±0.53	1.17 ±1.05	4.27±1.05
NGC 4189	0	8.68±0.13	9.66±0.09	1.32±0.38	1.27±0.37	2.49 ±0.71	3.02±0.73
NGC 4254	I	9.87±0.10	10.41±0.08	2.36±0.65	2.48±0.65	4.09 ±1.29	4.22±1.33
NGC 4293	III	8.70±0.17	10.51±0.07	0.65±0.68	4.07±0.68	1.67 ±1.35	6.67±1.36
NGC 4294	I	7.91±0.07	9.57±0.05	2.26±0.45	3.88±0.41	2.69 ±0.81	6.58±0.79
NGC 4298	II	9.09±0.11	10.02±0.07	1.51±0.41	2.31±0.39	2.88 ±0.78	3.91±0.78
NGC 4299	I	7.53±0.17	9.27±0.08	1.31 ±0.43	2.7±0.44
NGC 4321	I	9.85±0.11	10.82±0.05	4.10±0.91	6.65±1.04	5.05 ±1.79	10.98±1.86
NGC 4351	I	7.81±0.16	9.36±0.12	0.86±0.38	1.43±0.37	1.53 ±0.74	2.64±0.74
NGC 4380	IV	8.58±0.11	10.17±0.07	2.39±0.60	3.15±0.52	3.54 ±1.08	5.22±1.04
NGC 4383	0	8.42±0.14	9.58±0.07	1.13±0.37	1.74±0.36	1.34 ±0.71	2.12±0.71
NGC 4394	IV	7.81±0.23	10.32±0.14	2.97 ±1.62	3.34±1.60
NGC 4405	III	8.30±0.17	9.62±0.11	0.51±0.29	1.03±0.28	0.94 ±0.56	1.98±0.56
NGC 4419	III	9.01±0.15	10.23±0.08	0.86±0.41	2.18±0.43	1.39 ±0.79	3.69±0.83
NGC 4424	II	8.36±0.15	9.93±0.06	0.98±0.45	2.97±0.45	1.42 ±0.88	4.97±0.88
NGC 4450	IV	8.65±0.11	10.69±0.07	1.79±0.64	3.13±0.64	2.24 ±1.27	4.42±1.27
NGC 4457	III	9.02±0.13	10.36±0.08	0.79±0.32	1.49±0.33	1.26 ±0.65	1.92±0.65
NGC 4501	II	9.69±0.12	10.99±0.08	3.44±0.84	3.68±0.83	4.78 ±1.67	5.69±1.67
NGC 4532	0	8.29±0.08	9.51±0.07	1.16±0.34	1.87±0.34	2.04 ±0.68	2.89±0.68
NGC 4535	I	9.46±0.13	10.58±0.06	5.72±1.42	6.34±0.96	6.14 ±2.05	10.48±1.76
NGC 4536	0	9.35±0.11	10.35±0.06	3.45±0.94	5.81±0.94	2.57 ±1.84	8.09±1.85
NGC 4548	IV	8.96±0.15	10.68±0.06	5.82±1.98	3.76±0.68	5.77 ±2.28	5.62±1.31
NGC 4561	0	7.31±0.13	9.33±0.07	1.57 ±1.91	1.58±0.37
NGC 4567	0	8.74±0.12	10.13±0.06	1.46±0.38	2.99±0.38	1.72 ±0.72	4.45±0.72
NGC 4568	0	9.43±0.12	10.38±0.06	1.59±0.55	3.85±0.57	2.51 ±1.10	6.35±1.11
NGC 4569	III	9.53±0.09	10.74±0.05	1.93±0.52	4.66±0.54	2.84 ±1.03	7.85±1.05
NGC 4579	IV	9.31±0.14	10.89±0.07	3.12±0.94	3.33±0.74	4.43 ±1.55	4.46±1.43
NGC 4580	III	8.58±0.15	9.94±0.07	0.66±0.27	1.65±0.25	1.41±0.51	2.84±0.51
NGC 4606	III	8.20±0.14	9.85±0.06	0.64±0.39	2.96±0.44	1.15 ±0.78	5.06±0.79
NGC 4651	0	8.77±0.16	10.27±0.11	1.17±0.63	2.26±0.64	2.12 ±1.26	2.99±1.26
NGC 4654	II	9.33±0.10	10.23±0.07	2.06±0.59	3.66±0.59	3.71 ±1.18	5.92±1.19
NGC 4689	IV	9.06±0.11	10.24±0.08	1.97±0.55	3.13±0.52	3.17 ±1.05	5.19±1.03
NGC 4694	II	8.29±0.07	9.92±0.07	1.07±0.38	2.04±0.39	2.43 ±0.76	2.98±0.77
NGC 4698	I	8.09±0.13	10.46±0.08	5.41 ±0.96	3.94±0.98
NGC 4713	0	8.33±0.11	9.51±0.08	1.13±0.32	1.73±0.31	1.83 ±0.63	2.95±0.63
NGC 4772	0	7.85±0.14	10.19±0.07	4.61 ±0.82	3.01±0.84
NGC 4808	0	8.74±0.11	9.61±0.08	1.24±0.33	1.76±0.33	2.36 ±0.67	2.94±0.67

Table 3.1: Main properties of the 38 VERTICO galaxies analyzed in this work. The columns are (1) galaxy name; (2) HI-Class from [5]; (3) logarithm of the total molecular gas mass derived as explained in Section 4.4.1.2; (4) logarithm of the total stellar mass derived as explained in Section 3.4.2; (5) exponential scale length of the molecular gas; (6) exponential scale length of the stars; (7) effective radius of the molecular gas; (8) effective radius of the stars.

in mind. The EDGE-CALIFA selected galaxies are mostly far-IR detected and rich in molecular gas (hence actively star-forming), and only a handful of them have resolved HI observations. The

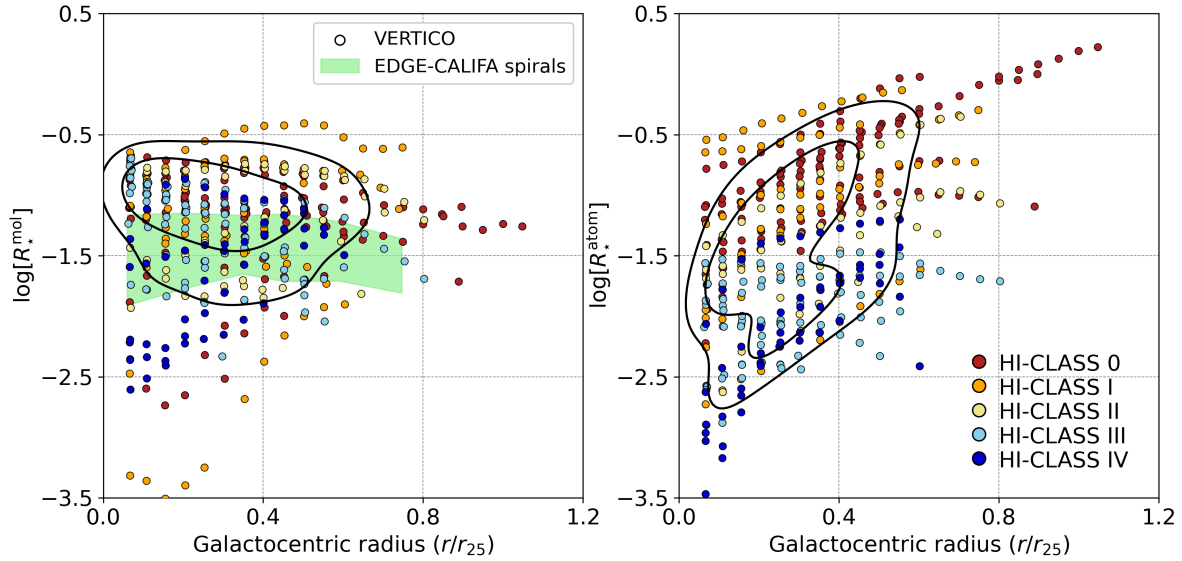


Figure 3.7: *Left:* The resolved molecular-to-stellar mass ratio R_*^{mol} colored by HI-Class vs galactocentric radius for annuli within the 38 VERTICO galaxies analyzed in this work. The black contours enclose, from outside-in, the 66% and 33% of the R_*^{mol} of the points. The green shaded area is the range covered by EDGE-CALIFA spiral galaxies within 1σ scatter about the mean values for radial bins of $0.1r_{25}$ wide. *Right:* The resolved atomic-to-stellar mass ratio R_*^{atom} vs galactocentric radius. Conventions are as in left panel.

xGASS-CO sample is the largest galaxy survey, but it is spatially unresolved.

We correct our calculations by the inclination of the galaxy (using a $\cos(i)$ factor) to represent physical “face-on” deprojected surface densities (see §4.3.1). The EDGE-CALIFA spiral galaxies included here were selected to have $i < 75^\circ$ (see Chapter 2).

3.4.3.1 R_{mol} vs Radius and Environment

The left and right panels of Figure 3.7 show the spatially resolved molecular-to-stellar $R_*^{\text{mol}} = \Sigma_{\text{mol}}/\Sigma_*$ and atomic-to-stellar $R_*^{\text{atom}} = \Sigma_{\text{atom}}/\Sigma_*$ ratios, in logarithmic space, as a function of galactocentric radius and colored by HI-Class. Looking at the black contours, which enclose 66% and 33% of the points, we note that R_*^{mol} follows a constant trend with radius and

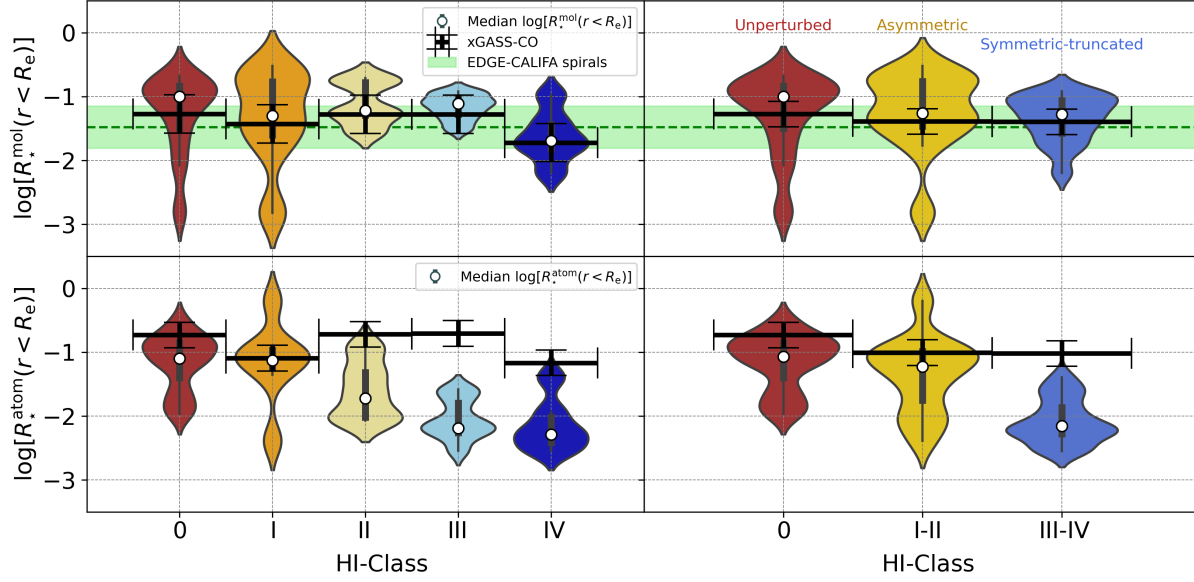


Figure 3.8: *Left:* The molecular-to-stellar mass ratio within R_e , $R_*^{\text{mol}}(r < R_e) = M_{\text{mol}}(r < R_e)/M_*(r < R_e)$ (top) and the atomic-to-stellar mass ratio within R_e , $R_*^{\text{atom}}(r < R_e) = M_{\text{atom}}(r < R_e)/M_*(r < R_e)$ (bottom), vs HI-Class defined by [5]. The black bars show the values obtained from the $M_{\text{mol}}/M_* - M_*$ and $M_{\text{atom}}/M_* - M_*$ relations for xGASS-CO MS galaxies from [7] using the mean stellar masses for the [5] HI-Classes listed in Table 3.2. The violin errorbars represent the distribution of values for each HI-Class. The white dot is the median value of the distribution. The shaded-green area in the top panel is the $R_*^{\text{mol}}(r < R_e)$ range covered by EDGE-CALIFA spiral galaxies within 1σ scatter. *Right:* $R_*^{\text{mol}}(r < R_e)$ (top) and the $R_*^{\text{atom}}(r < R_e)$ (bottom) vs HI-Class after clustering them in three broader groups: i) unperturbed galaxies (HI-Class 0), ii) asymmetric galaxies (HI-Classes I and II galaxies); and iii) symmetric-truncated galaxies (HI-Classes III and IV galaxies). Conventions are as in the left panel. While $R_*^{\text{mol}}(r < R_e)$ values for VERTICO galaxies are within the ranges covered by the xGASS-CO MS galaxies, $R_*^{\text{atom}}(r < R_e)$ values show a systematic decrease with increasing HI-Class.

it has similar values to those covered by EDGE-CALIFA spirals. We also note that most of the galaxies show a systematic inside-out increase in R_*^{atom} (Pearson $r_p = 0.53$ when considering all the points).

The top and bottom panels of Figure 3.8 show the molecular- and atomic-to-stellar mass ratios integrated out to R_e , $R_*^{\text{mol}}(r < R_e) = M_{\text{mol}}(r < R_e)/M_*(r < R_e)$ and $R_*^{\text{atom}}(r < R_e) = M_{\text{atom}}(r < R_e)/M_*(r < R_e)$, respectively, as a function of HI-Class. The upper panels show that the median $R_*^{\text{mol}}(r < R_e)$ values remain almost constant with HI-Class but with a possible

small decrease for HI-Class IV galaxies. These values are in good agreement with those expected from the $M_{\text{mol}}/M_{\star}-M_{\star}$ relation for xGASS-CO galaxies (black crosses; [7]), and with EDGE-CALIFA spirals (green-shaded area). Interestingly, $R_{\star}^{\text{atom}}(r < R_e)$ (bottom plots in Fig. 3.8) shows a systematic decrease from lower to upper HI-Classes. While HI-Classes 0 and I have atomic-to-stellar mass ratios with median values similar to that of xGASS-CO, HI-Classes II, III, and IV have significantly lower $R_{\star}^{\text{atom}}(r < R_e)$ values.

We test how our results change when adopting a variable $\alpha_{\text{CO}}(\Sigma_{\text{total}})$. Although R_{\star}^{mol} values decrease $\sim 0.2 - 0.3$ dex when using $\alpha_{\text{CO}}(\Sigma_{\text{total}})$ (particularly at $r0.6r_{25}$), we note that the R_{\star}^{mol} trend does not vary significantly compared to that for $\alpha_{\text{CO},\text{MW}}$; similarly, $R_{\star}^{\text{mol}}(r < R_e)$ values are still within the ranges covered by xGASS-CO when using the two α_{CO} prescriptions. Despite there being a clear deficit in the integrated HI content of the HI-perturbed galaxies, our VERTICO data reveal that these galaxies do *not* exhibit an appreciable deficit in H_2 mass.

The left panel of Figure 3.9 shows the spatially resolved molecular-to-atomic ratio $R_{\text{mol}} = \Sigma_{\text{mol}}/\Sigma_{\text{atom}}$, in logarithmic space, as a function of galactocentric radius and colored by HI-Class. To compute R_{mol} , we use the Σ_{mol} radial profiles derived from the 15 CO(2–1) datacubes to match VIVA’s HI angular resolution. In general, the figure shows a decreasing trend for R_{mol} with radius (Pearson $r_p = -0.5$; $p\text{-value} < 0.01$). We note that R_{mol} values for HI-Classes II, III, and IV (yellow, light blue, and blue solid dots, respectively) are on average higher than for HI-Classes 0 and I (red and orange solid dots, respectively). Looking at Figure 3.5, we note that while lower HI-Classes have similar Σ_{atom} to what is expected for normal field galaxies (e.g., $\Sigma_{\text{atom}} \approx 6 \text{ M}_{\odot} \text{ pc}^{-2}$; [30]), upper HI-Classes show notably lower atomic surface densities. Since HI-Classes II, III, and IV are HI deficient (as mentioned previously for $R_{\text{atom},\star}$), the enhancement of R_{mol} (at least within R_e) appears to be due mainly to their poor atomic gas content. The significant scatter

in R_{mol} , particularly at $r_{\text{gal}} \leq 0.3r_{25}$, may be due to the strong environmental effects experienced by some VERTICO galaxies. We also compute the molecular-to-atomic gas mass ratio within R_e , $R_{\text{mol}}(r < R_e) = M_{\text{mol}}(r < R_e)/M_{\text{atom}}(r < R_e)$. The right panel of Figure 3.9 shows the relation between $R_{\text{mol}}(r < R_e)$ (in logarithmic space) and HI-Class. Although with a dip in HI-Classes II and IV galaxies, there is a large systematic increase of $R_{\text{mol}}(r < R_e)$ from lower to upper HI-Classes which becomes even more clear for the broader HI groups in the left panel of Fig. 3.9. As noted previously for R_{\star}^{mol} , R_{mol} values decrease $\sim 0.2 - 0.3$ dex with $\alpha_{\text{CO}}(\Sigma_{\text{total}})$ at $r < 0.6r_{25}$. Similarly, $R_{\text{mol}}(r < R_e)$ values also decrease when using the variable α_{CO} prescription. However, we still observe a clear systematic decrease of R_{mol} with radius, and $R_{\text{mol}}(r < R_e)$ values are still within the ranges covered by xGASS-CO MS galaxies. This is consistent with the definition of HI-Classes by [5] for VIVA galaxies, and it confirms that the increase in ratios is a result of the deficiency in HI.

These results can be summarized as follows:

1. For unperturbed galaxies and with mild sign of HI- perturbation (e.g., HI-Classes 0 and I), $R_{\star}^{\text{mol}}(r < R_e)$ and $R_{\star}^{\text{atom}}(r < R_e)$ values are similar to those for xGASS-CO MS galaxies with similar stellar mass, and also have $R_{\text{mol}}(r < R_e)$ values comparable with the latter.
2. Asymmetric galaxies in HI or partially symmetric-truncated (HI-Classes II and III) have $R_{\star}^{\text{mol}}(r < R_e)$ values within the range covered by EDGE-CALIFA spirals and those expected from xGASS-CO relations. However, we note that $R_{\star}^{\text{atom}}(r < R_e)$ values are up to 1.5 dex lower than those for xGASS-CO MS galaxies. HI-Class II and III galaxies also have $R_{\text{mol}}(r < R_e)$ values significantly higher than those in stellar-mass matched xGASS-CO MS galaxies.

3. HI-symmetric-truncated galaxies (i.e., HI-Class IV) galaxies show a possible decrease in $R_{\star}^{\text{mol}}(r < R_e)$ compared with EDGE-CALIFA spirals, although still in good agreement with xGASS-CO MS galaxies. Similar to HI-Classes II and III, HI-Class IV has $R_{\star}^{\text{atom}}(r < R_e)$ values drastically lower than the latter (~ 1.0 dex lower). HI-Class IV galaxies also show an increase in $R_{\text{mol}}(r < R_e)$ values compared to lower HI-Classes (although a small decrease compared to HI-Class III) and to those expected for xGASS-CO MS galaxies.

These results suggest that even though environmental processes act on both the molecular and the atomic gas (at least within R_e), the latter is affected in a different manner than the former. Table 3.2, which includes a compilation of masses for all HI-Classes, indicates that VERTICO galaxies have lower M_{mol} compared to EDGE-CALIFA spirals (although the latter is slightly biased towards molecule-rich galaxies). VERTICO galaxies also seem to have lower M_{mol} values than those expected from the $M_{\text{mol}} - M_{\star}$ relation for main sequence xGASS-CO galaxies, although without significant variations with HI-Class or M_{\star} . We note that M_{atom} values for HI-Classes II, III, and IV are notably lower than for xGASS-CO. Similar results are found by [155], who do not observe a statistically significant correlation between H_2 and HI deficiencies. They also note that VERTICO galaxies tend to be H_2 deficient when compared to main sequence galaxies from xGASS-CO. These results suggest that even though environmental processes affect both the molecular and the atomic gas simultaneously, the level of HI perturbation in VERTICO galaxies does not necessarily modulate the molecular gas content. The large change in $R_{\text{mol}}(r < R_e)$ with environment (e.g., a factor of ~ 10 between HI-Classes 0 and III) also indicates that galaxy evolution simulations should factor this in if they want to trace HI/ H_2 phases in dense environments. Also, while R_{\star}^{atom} values for HI-Class IV galaxies are on average the lowest,

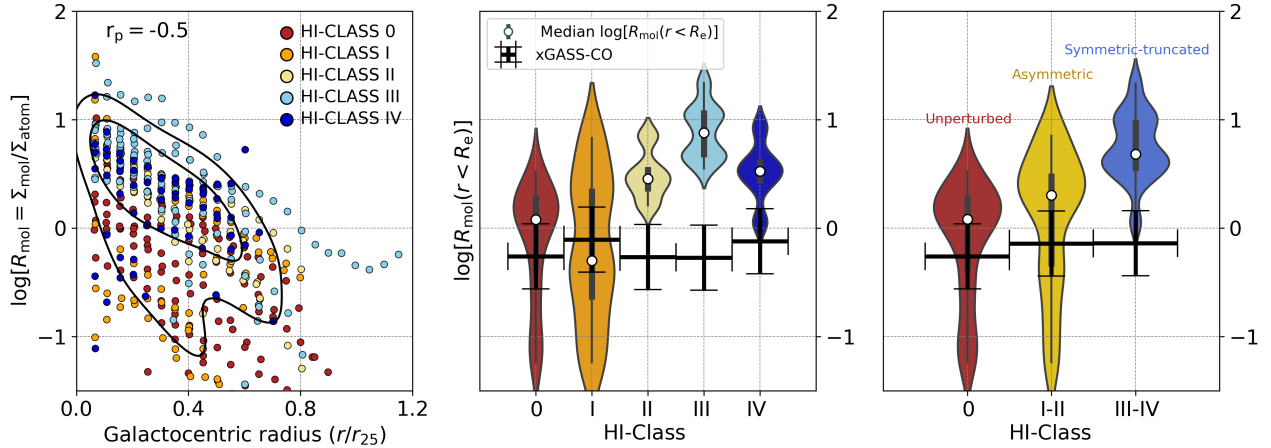


Figure 3.9: *Left*: The resolved molecular-to-atomic gas ratio $R_{\text{mol}} = \Sigma_{\text{mol}}/\Sigma_{\text{atom}}$ vs galactocentric radius, with circles colored by HI-Class. The black contours enclose, from outside-in, the 66% and 33% of the points. *Middle*: The molecular-to-atomic gas ratio, in logarithmic space, computed using the molecular and atomic gas masses within R_e , $R_{\text{mol}}(r < R_e) = M_{\text{mol}}(r < R_e)/M_{\text{atom}}(r < R_e)$, vs HI-Class. The black bars show the R_{mol} values obtained from the $M_{\text{mol}}/M_{\text{atom}}-M_{\star}$ relation for xGASS-CO MS galaxies from [7] using the mean stellar masses for the [5] HI-Classes listed in Table 3.2. There is an increase of $R_{\text{mol}}(r < R_e)$ that is up to about an order of magnitude going from lower to higher HI-Classes (e.g., from Class I to III); the more disturbed the HI the higher the molecular-to-atomic ratio within R_e . *Right*: $R_{\text{mol}}(r < R_e)$ vs HI-Class groups as in the right panel of Fig. 3.8. Conventions and symbols are as in Fig. 3.8.

particularly at $r=0.4r_{25}$, their R_{\star}^{mol} values show a significant decrease towards the centers. These results suggest that HI-Class IV galaxies could be tracing the population where the environment is starting to impact significantly the molecular gas content.

Although several environmental mechanisms could potentially explain the results previously shown, the most likely mechanism is ram pressure (at least in HI-Classes I-III). Out of the 38 VERTICO galaxies selected for this work, at least five of them are well studied cases of RPS: NGC 4501, NGC 4548, NGC 4569, NGC 4579, and NGC 4654 (e.g., [153, 180–183]; see also [184] and references therein). In particular, [166] report significantly higher R_{mol} values for Virgo galaxies than for field galaxies. They attribute this to environmental processes, either by inward flows of molecular gas, H_2 not being as efficiently stripped as the atomic gas, and/or

Galaxy Class	$\log[M_\star]$ (M_\odot)	$\log[M_{\text{mol}}]$ (M_\odot)	$\log[M_{\text{atom}}]$ (M_\odot)	$\log[\text{SFR}]$ ($M_\odot \text{ yr}^{-1}$)	$\log[M_{\text{mol}}^{\text{xGC}}]$ (M_\odot)	$\log[M_{\text{atom}}^{\text{xGC}}]$ (M_\odot)	$\log[M_{\text{mol}}]_{\text{xGC}}$ (M_\star)	$\log[M_{\text{atom}}]_{\text{xGC}}$ (M_\star)
(1)	(2)	(3)	(4)	(5)	(6)	(7)	(8)	(9)
Class 0	9.66±0.38	8.59±0.56	9.29±0.29	0.58±0.72	8.46±0.22	9.31±0.46	-1.28	-0.54
Class I	10.41±0.61	8.07±0.92	9.21±0.36	0.32±1.61	9.01±0.27	9.55±0.39	-1.61	-1.14
Class II	10.02±0.43	9.04±0.51	8.69±0.46	0.13±0.21	8.79±0.20	9.38±0.48	-1.27	-0.73
Class III	10.01±0.34	8.42±0.35	7.63±0.44	0.27±0.47	8.78±0.23	9.38±0.47	-1.27	-0.72
Class IV	10.5±0.27	8.73±0.41	8.66±0.24	0.24±0.54	9.13±0.26	9.61±0.39	-1.78	-1.18
EDGE-CALIFA	10.57±0.45	9.45±0.47	9.16±0.26	9.64±0.39	-1.89	-1.21

Table 3.2: Median and 1σ scatter values of the mass and star formation rate distributions for the galaxy groups in column (1). The columns are: (2) logarithm of the median stellar mass; (3) logarithm of median molecular gas mass; (4) logarithm of median atomic gas mass; from Class 0 to Class IV, atomic gas masses are taken from [6]; (5) logarithm of total median star formation rate; (6) logarithm of total molecular gas mass derived from the $M_{\text{mol}}-M_\star$ relation for main sequence xGASS-CO galaxies by [7], using the stellar mass from column (2); (7) logarithm of total atomic gas mass derived similarly as in column (6); (8) logarithm of the total molecular-to-stellar ratio derived from the $M_{\text{mol}}/M_\star-M_\star$ relation for xGASS-CO galaxies by [7], using the stellar mass from column (2), as shown by the black errorbars in the top panel of the right plot in Fig. 3.7; (9) logarithm of the total atomic-to-stellar ratio derived similarly as in column (8). For both columns (8) and (9), according to [7] the scatter is within ~ 0.3 dex.

HI migration to the galaxy center where it can be more easily converted into H_2 . This is also supported by [185], who analyze four jellyfish galaxies from the GAs Stripping Phenomena survey with MUSE (GASP; [186]). They propose that gas compression caused by ram pressure can trigger the conversion of large amounts of HI into the molecular phase in the disk, which may imply that HI is just partially stripped. The results found by [155] also support this idea, and suggest that RPS in VERTICO galaxies could potentially drive outside-in gas migration and may contribute to produce steeper H_2 radial profiles, as seen in [166]. However, thermal evaporation ([187]; see also [140] for a detailed description) or starvation have also been proposed to explain the effects of the environment in galaxies with symmetric-truncated HI radial profiles (e.g., HI-Class IV galaxies; see also § 5.1 in [155]). Observational and theoretical evidence has shown that thermal evaporation can complement the viscous stripping in removing the cold gas from the disk (e.g., [137, 188–190]). Consequently, it can affect the entire gas disk (all at the same time), leading to marginally truncated (but symmetric) gas disks with low surface density. Thermal

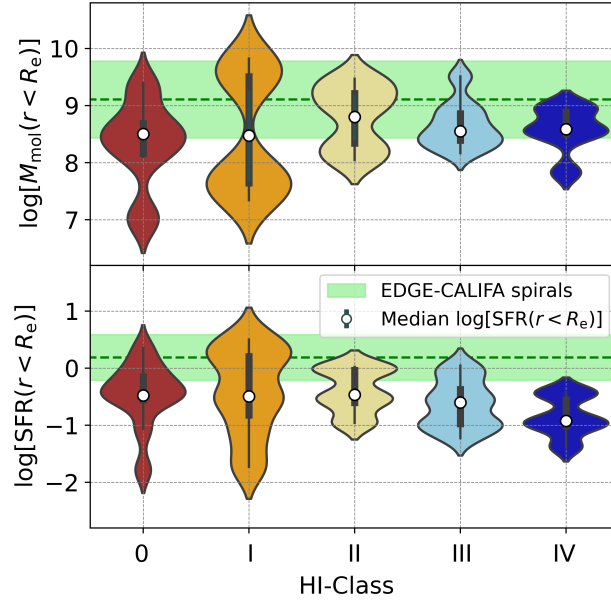


Figure 3.10: *Top*: The molecular gas mass within R_e , $M_{\text{mol}}(r < R_e)$ (M_{\odot}), vs HI-Class. *Bottom*: The star formation rate within R_e , $\text{SFR}(r < R_e)$ ($M_{\odot} \text{ yr}^{-1}$), vs HI-Class. Conventions are as in left panel of Fig. 3.8. While $M_{\text{mol}}(r < R_e)$ remains almost constant, there is a systematic decrease of $\text{SFR}(r < R_e)$ with HI-Class (particularly from HI-Classes II to IV).

evaporation is, therefore, a good candidate to explain the offset in $R_{\text{mol}}(r < R_e)$ for HI-Class IV galaxies (middle panel of Fig. 3.9) when compared to lower HI-Classes.

3.4.3.2 SFE vs Radius and Environment

Figure 3.10 shows the molecular gas mass within R_e , $M_{\text{mol}}(r < R_e)$ (top panel), and the star formation rate within R_e , $\text{SFR}(r < R_e)$ (bottom panel), vs HI-Class. Note that $M_{\text{mol}}(r < R_e)$ remains almost constant with HI-Class; on average, $M_{\text{mol}}(r < R_e)$ values for VERTICO galaxies are similar to the mean for EDGE-CALIFA spirals. Although the mean $\text{SFR}(r < R_e)$ does not vary significantly for HI-Classes 0 and I, we note a systematic decrease of the SFR with increasing HI-Class for Classes III to IV. The results shown in Figure 3.10 are consistent with the expected difference in the total molecular gas masses and star formation rates between galaxies

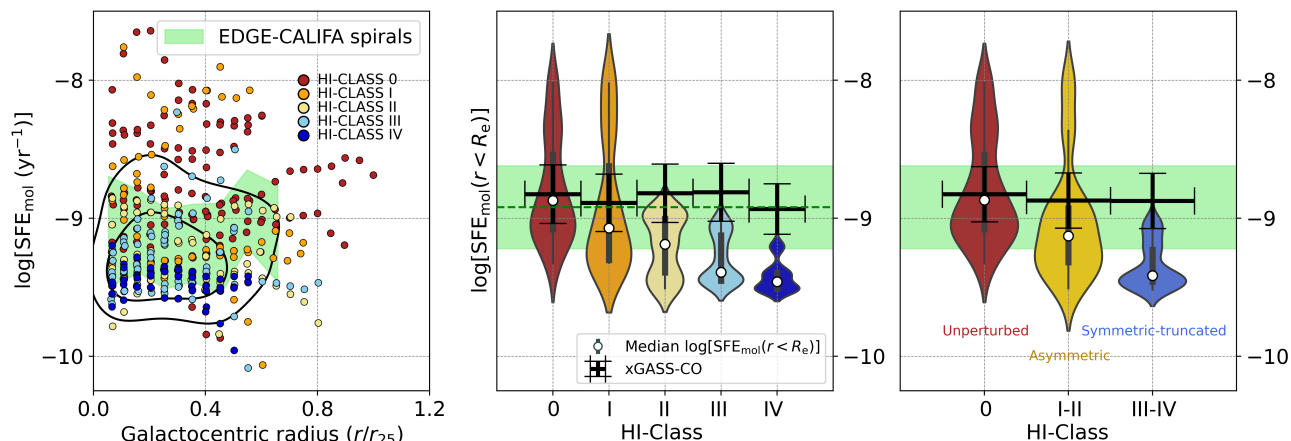


Figure 3.11: *Left*: The resolved star formation efficiency of the molecular gas, SFE_{mol} , vs galactocentric radius. The black contours enclose, from outside-in, the 66% and 33% of the points. *Middle*: The star formation efficiency of the molecular gas within R_e , $\text{SFE}_{\text{mol}}(r < R_e)$, vs HI-Class. The horizontal black bars are the $\text{SFR}/M_{\text{mol}}$ median values for HI-Classes 0, I, II, III, and IV VERTICO galaxies using the $\text{SFR}/M_{\text{mol}}-M_{\star}$ relation derived from the molecular depletion times, $\tau_{\text{dep}} = M_{\text{mol}}/\text{SFR}$, for xGASS-CO MS galaxies by [7]. The shaded-green area is the $\text{SFE}_{\text{mol}}(r < R_e)$ range covered by EDGE-CALIFA spiral galaxies within 1σ scatter. *Right*: $\text{SFE}_{\text{mol}}(r < R_e)$ vs HI-Groups. Conventions are as in left panel of Fig. 3.8. The results shown in Figs. 3.10 and 3.11 suggest that the systematic decrease of $\text{SFE}_{\text{mol}}(r < R_e)$ is a consequence of changes to the state of the gas or the star-formation process caused by the source of the morpho-kinematic perturbations that affect the HI in the outer disks of VERTICO galaxies.

from VERTICO and EDGE-CALIFA surveys. While the former includes galaxies with lower M_{mol} s than xGASS-CO main sequence galaxies, as shown in Table 3.2, the latter encompasses actively star-forming galaxies and rich in molecular gas (see [3] for more details of the sample selection), hence with higher molecular gas masses than main sequence galaxies.

The left panel of Figure 3.11 shows the spatially resolved $\text{SFE}_{\text{mol}} = \Sigma_{\text{SFR}}/\Sigma_{\text{mol}}$ as a function of galactocentric radius and colored by HI-Class. We do not observe a statistically significant correlation between the efficiencies and radius. We note that while higher HI-Classes have SFE_{mol} significantly below to the almost constant values for EDGE-CALIFA spirals, lower HI-Classes tend to be in fair agreement with the latter and scattered to much larger values (likely due to variations in Σ_{SFR} values within these HI-Classes; see Fig. 3.5). On average, lower HI-

Classes tend to have higher SFE_{mol} than upper HI-Classs for the r_{gal} range covered here. The middle and right panels of Figure 3.11 show the star formation efficiency of the molecular gas within R_e , $\text{SFE}_{\text{mol}}(r < R_e) = \text{SFR}(r < R_e)/M_{\text{mol}}(r < R_e)$, as a function of HI-Class. We note a systematic decrease of $\text{SFE}_{\text{mol}}(r < R_e)$ with HI-Class. Although $\text{SFE}_{\text{mol}}(r < R_e)$ values are mostly within the range covered by the control samples for HI-Classs 0 and I, HI-Classs II–IV have notably lower efficiencies (~ 0.3 – 0.5 orders of magnitude, or 2–3 times lower) than EDGE-CALIFA spirals (green shaded area) and xGASS-CO MS galaxies (black horizontal bars). We test how our efficiencies depend on the adopted α_{CO} prescription. Although SFE_{mol} values increase by ~ 1.1 – 1.3 dex when using $\alpha_{\text{CO}}(\Sigma_{\text{total}})$ in the region within $\sim 0.6r_{25}$, the SFE_{mol} trend does not vary significantly compared to that for $\alpha_{\text{CO},\text{MW}}$. Likewise, $\text{SFE}_{\text{mol}}(r < R_e)$ still shows a similar systematic decrease with HI-Class when adopting the two α_{CO} prescriptions. These results suggest that the systematic decrease of $\text{SFE}_{\text{mol}}(r < R_e)$ seen in Figure 3.11 is a consequence of changes to the star formation process caused by the source of the perturbations that affect the HI in the external regions of the disk.

It is interesting to compare our results with other galaxy-scale indicators of the star formation efficiency in VERTICO galaxies. For instance, [19] compute the best-fit power-law index of the resolved Kennicutt–Schmidt law, N_{rKS} , based on the resolved scaling relations between Σ_{SFR} and Σ_{mol} . Out of the 36 VERTICO galaxies with inclinations $i < 80^\circ$ included in [19], Figure 3.12 shows the $\text{SFE}_{\text{mol}}(r < R_e)$ vs N_{rKS} for 34 VERTICO galaxies for which they find N_{rKS} values statistically significant. We do not find a significant correlation between N_{rKS} and $\text{SFE}_{\text{mol}}(r < R_e)$. However, in observing the distributions of N_{rKS} colored by HI-Class, we note that HI-Classs III and IV (blue circles) tend to group at both lower N_{rKS} and $\text{SFE}_{\text{mol}}(r < R_e)$ than HI-Classs 0 and I (red circles), and vice versa. Since the resolved Kennicutt–Schmidt law

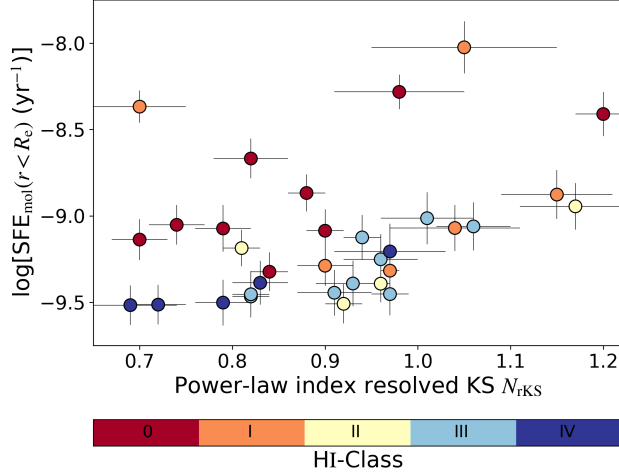


Figure 3.12: The star formation efficiency of the molecular mass within R_e , $\text{SFE}_{\text{mol}}(r < R_e)$, vs the best-fit power-law index of the resolved Kennicutt-Schmidt, N_{rKS} , from [19]. Although without a significant correlation between $\text{SFE}_{\text{mol}}(r < R_e)$ and N_{rKS} (Pearson $r_p = 0.3$), HI-Classes III and IV (blue circles) seem to group at both lower N_{rKS} and $\text{SFE}_{\text{mol}}(r < R_e)$ than HI-Classes 0 and I (red circles), and vice versa.

index quantifies changes in the molecular gas efficiencies through Σ_{mol} and Σ_{SFR} , lower efficiencies at the centers of HI-Classes II-IV reflect locally low $\Sigma_{\text{SFR}}/\Sigma_{\text{mol}}$ ratios, which drive N_{rKS} values below unity. [19] also show that, on average, the distribution of N_{rKS} in VERTICO galaxies peaks at lower values when compared to those for HERACLES [32] and PHANGS [191]. Our results are consistent with [19], who suggest that their sub-linear N_{rKS} values found in most of the VERTICO galaxies indicate a decrease in the efficiency of the molecular gas for regions with high Σ_{mol} and reflects the broad variety of physical conditions present in Virgo galaxies.

Our results show that VERTICO galaxies tend to be less efficient at converting molecular gas into stars when their atomic gas is strongly affected by environmental mechanisms, at least in the region within R_e . Analyzing 98 galaxies selected from the JCMT NGL survey, [192] show that Virgo galaxies have longer molecular gas depletion times, $\tau_{\text{dep}} = M_{\text{H}_2}/\text{SFR} = \text{SFE}_{\text{H}_2}^{-1}$, when compared to group galaxies selected from a sample of 485 local galaxies included in [193]. They

attribute this difference to a combination of environmental factors that increase the H_2 production and a decrease in the SFR in the presence of large amounts of molecular gas, which may reflect heating processes in the cluster environment or differences in the turbulent pressure. [150] find an increase in the CO surface brightness (an increase in Σ_{H_2}) in a region close to the galactic center subjected to intense ram pressure in the Virgo galaxy NGC 4402 (also confirmed by [168]), which seems to be tied to bright FUV and $H\alpha$ emission associated with intense star formation. [163] also observe an enhancement in the H_2 star formation efficiencies, $SFE = \Sigma_{SFR}/\Sigma_{H_2}$, of Fornax cluster galaxies (particularly at low masses) for galaxies on first passage through the cluster. They suggest that these changes might be driven by environmental mechanisms (e.g., RPS or tidal interactions). [194] analyze the atomic and molecular gas properties of massive Virgo galaxies ($M_\star > 10^9 M_\odot$), which are selected from the Extended Virgo Cluster Catalog (EVCC; [195]), within $r < 3R_{200}$ (R_{200} is the radius where the mean interior density is 200 times the critical density of the Universe). They find that Virgo galaxies have lower SFRs and higher $SFE_{H_2} = SFR/M_{H_2}$ compared to field galaxies with offsets from the main sequence of the star-forming galaxies $\Delta(MS) < 0.0$. In addition, they note that Virgo galaxies have both lower gas fractions (M_{H_2}/M_\star and M_{HI}/M_\star) and higher SFEs compared to field galaxies. [196] also find evidence of enhanced star formation on the leading side of four identified jellyfish galaxies selected from Perseus cluster using radio LOw Frequency ARray (LOFAR) continuum at 144 MHz and $H\alpha$ data. They find a positive correlation between $H\alpha + [NII]$ surface brightness and the orientation angle of sources with respect to the stripped tail, which is consistent with gas compression (i.e., the increasing of the star production) induced by ram pressure along the interface between the ICM and the galaxy. [197] analyze ALMA ACA $^{12}CO(J=1-0)$ and HI data for 31 galaxies selected from the Group Evolution Multiwavelength Study survey (GEMS; [198,

199]), finding that some members with highly asymmetric morphologies in CO and HI images (e.g., driven by tidal interactions and RPS) have a significant decrease in both SFR (e.g., due to gas becoming stable against gravitational collapse), and gas fractions, suggesting a decrease of Σ_{mol} due to the suppression of the HI-to-H₂ conversion. Numerical simulations have found that the star formation activity is generally amplified in galaxy centers by ram pressure (e.g., [200, 201]); particularly, some of them have shown that the star production can be boosted due to gas compression at the edges of the disks (e.g., [167, 202]).

Since our integrated efficiencies are computed within R_e , it is possible that the systematic decrease of $\text{SFE}_{\text{mol}}(r < R_e)$ with HI-Class could be in part caused by morphological quenching if most gas is driven into bulge-dominated galaxy centers. Morphological quenching ([139]) is able to produce a gravitational stabilization of the gas within the bulge region, preventing the fragmentation into bound star-forming clumps. Numerical simulations performed by [203] show that spheroids drive turbulence and increase the gas velocity dispersion, virial parameter, and turbulent gas pressure towards the galaxy centers, which are mostly dependent on the bulge mass (M_b). They note that the more massive the bulges are, the higher the level of turbulence. Therefore, the stellar spheroid stabilizes the ISM of the host galaxy by increasing the shear velocity and the gas velocity dispersion, thus preventing the gravitational instability of the gas reservoirs and suppressing the fragmentation responsible for the disruption of the ISM by stellar feedback. Morphological quenching has been shown to potentially operate not only on early-type massive galaxies with a strong bulge component, but it can also work at any M_* range (e.g., [204, 205]). However, some studies (e.g., [206, 207]) have noted that the regulation of the SFR in main sequence galaxies is more related to physical processes acting on the disk rather than the contribution from bulges.

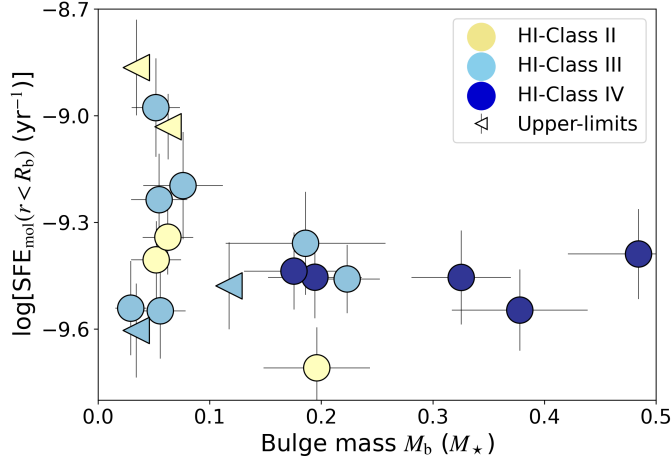


Figure 3.13: The star formation efficiency of the molecular mass within the radius of the bulge R_b , $SFE_{\text{mol}}(r < R_b)$, vs the bulge mass M_b (in units of the total stellar mass) for HI-Classes II, III, and IV. Symbols are colorcoded by HI-Class as in Figure 3.12. The horizontal arrows are upper-limits for M_b since no clear breaks in the stellar radial profiles due to bulges are identified; therefore, M_b in these cases is the mass enclosed within $0.1r_{25}$, which corresponds to $r_{\text{gal}} \approx 1.0$ kpc at the Virgo cluster distance (16.5 Mpc; [20]).

If the cluster environmental mechanisms act by pushing the molecular gas to central regions within the influence of the bulge, morphological quenching is then a good candidate to explain the $SFE_{\text{mol}}(r < R_e)$ decrease observed in higher HI-Classes via gas stabilization (at least in some VERTICO galaxies). Detailed studies of the molecular gas dynamics within the bulge region in Virgo galaxies are therefore important to establish the actual connection between the SFE_{mol} , the HI-Class, and the gravitational stability of the gas.

3.5 Summary and conclusions

We present a study of the molecular-to-atomic gas ratio, the star formation efficiency, and their dependence on other physical parameters in 38 galaxies selected from the VERTICO survey. We analyze $^{12}\text{CO}(J=2-1)$ datacubes with 9 angular resolution (except for the 13 NGC 4321 datacube) at 10 km s^{-1} channel width, along with HI velocities extracted from VIVA survey.

We implement spectral stacking of CO spectra to co-add them coherently by using HI velocities from the VIVA survey, and measure Σ_{mol} out to typical galactocentric radii of $r \approx 1.2 r_{25}$ by coherently averaging (stacking) spectra in elliptical annuli using the HI velocity as a reference in each pixel. We use a constant Milky Way CO-to-H₂ conversion factor prescription $\alpha_{\text{CO,MW}} = 4.3 M_{\odot} [\text{K km s}^{-1} \text{pc}^2]^{-1}$ ([83]), and a line Rayleigh-Jeans brightness temperature ratio of $R_{21} = I_{\text{CO}(2-1)}/I_{\text{CO}(1-0)} \sim 0.77$. Although the adoption of a variable α_{CO} has some impact on the molecular surface densities, it does not change the trends that we have found in this work. We warn that our exploration of the effects of α_{CO} dependence is limited and it deserves a more careful analysis in future VERTICO projects. We perform a systematic analysis to explore molecular disk sizes, molecular-to-atomic gas ratios, and the star formation efficiency of the molecular gas in VERTICO in comparison to field samples. Our main conclusions are as follows:

1. We determine the molecular and stellar exponential disk scale lengths, l_{mol} and l_{\star} , respectively, by fitting an exponential function to the Σ_{mol} and Σ_{\star} radial profiles for 33 VERTICO galaxies (see Fig. 3.6). We find that $l_{\text{mol}} = (0.62 \pm 0.05) l_{\star}$ ($\sim 3:5$ relation). When compared with the equivalent relation observed for galaxies selected from the field (e.g., EDGE-CALIFA survey; [1]), the CO emission in VERTICO galaxies is more centrally concentrated than the stellar surface density. Moreover, galaxies with a stronger degree of HI perturbation (as classified by [5]) tentatively show more compact CO distributions (this is particularly true for HI-Class III galaxies).
2. To test how the Virgo environment may be affecting the atomic-to-molecular gas transition, we compute molecular-to-stellar and atomic-to-stellar ratios as a function of galactocen-

tric radius (left and middle panels of Fig. 3.7). To control for the effects of stellar mass when comparing to a field sample, we use the results obtained from xGASS-CO for stellar masses matched to each subsample in VERTICO that has been broken into Yoon2017 HI-Classes. While the molecular-to-stellar mass ratio integrated out to R_e in VERTICO galaxies is completely consistent with the xGASS-CO sample, the atomic-to-stellar mass ratio integrated out to R_e shows a systematic decrease with increasing HI-Class, reflecting the known significant HI deficiencies in the high HI-Classes [5].

3. The resolved molecular-to-atomic gas ratio, R_{mol} , decreases with increasing galactocentric radius (left panel of Fig. 3.9) for all HI-Classes, as expected in galaxies. However, we find a systematic increase in the molecular-to-atomic gas ratio integrated out to R_e with increasing HI-Class (right panel of Fig. 3.9). Together with the previous point, these results suggest that although environmental processes act on the atomic and the molecular gas simultaneously, the atomic gas content is considerably more affected than the molecular gas content. Consequently, the morpho-kinematic HI features of VERTICO galaxies are not a good predictor for their molecular gas content.
4. There is a dependency of the star formation efficiency of the molecular gas within R_e on the morpho-kinematic HI features in VERTICO galaxies, but no strong systematic trends with galactocentric radius (Fig. 3.11). On average, VERTICO galaxies tend to be decreasingly efficient at converting their molecular gas into stars when their atomic gas is strongly perturbed by environmental effects. Although we do not find a statistically significant correlation between star formation efficiency within the bulge radius and the mass of the bulge we observe that galaxies with more centrally concentrated molecular gas tend

to be less efficient at converting their H_2 into stars when they host a more massive stellar bulge.

The general picture is that both the molecular and the atomic gas are affected by the Virgo environment, but in different manners (see also [140] and references therein). First, the mechanisms that remove HI in the cluster do not seem to significantly remove molecular gas. Instead, they appear to drive the molecular component toward the central regions, resulting in molecular disks with shorter scale lengths than their companion stellar disks. The removal of atomic gas results in galaxies that have high molecular-to-atomic ratios. However, these more centrally concentrated molecular regions with higher molecular-to-atomic ratios exhibit lower molecular star formation efficiencies than observed in field galaxies. A different (but also complementary) explanation is the removal of the molecular gas (e.g. by RPS acting preferentially in the more diffuse H_2 that is not strongly tied to GMCs) in combination with a simultaneous phase transition from HI-to- H_2 in the inner part of the galaxy triggered by the mechanisms that remove HI. The molecular gas removal also agrees with H_2 observations in the tails of jellyfish galaxies (e.g., [185]), which could otherwise be explained as a phase transition from HI-to- H_2 in the tail itself.

Future projects may complement the $^{12}\text{CO}(J=2-1)$ observations presented here with more accurate α_{CO} prescriptions (e.g., including metallicity indicators in Equation 4.6), the impact of the environment on the diffuse gas, or sub-kpc-scale CO observations within the bulge regions of high HI-Class galaxies. Also, detailed kinematic analyses are required to test the potential impact of environmental (or intrinsic) effects on the molecular gas stability, which may be decreasing the SFE in VERTICO galaxies.

Chapter 4: The EDGE-CALIFA survey: Molecular Gas and Star Formation Activity Across the Green Valley

4.1 Introduction

Star formation activity plays a key role in carving the appearance of galaxies in the local Universe. The production of stars is quantified through the star formation rate (SFR) which is in principle a function of the physical conditions in the dense interstellar medium (ISM). In the last decades, several studies have revealed a tight correlation between the integrated SFR and the stellar mass (M_*) in galaxies. The so-called star-formation main sequence (SFMS; e.g., [14, 40–43]) proposes a useful galaxy classification in terms of their star-formation status: “blue cloud” galaxies, which show a direct correlation between M_* and SFR for active star-forming galaxies; “red cloud,” where galaxies exhibit low SFRs and no M_* -SFR correlation; and the “green valley” (or transition galaxies; [208]). The bimodality of the SFMS suggests fundamental questions regarding the physical processes behind the transition from the SFMS to the green valley, which is mostly linked to the cessation of star formation activity.

The term “quenching” has been adopted to include the variety of mechanisms behind the cessation of star formation activity in galaxies. In particular, [44] suggest two different routes to classify quenching processes: “environmental quenching”, which is coupled to the local en-

vironmental conditions that may drive the decrease of (or cessation) SFR; and “mass quenching”, which refers to internal/intrinsic galaxy mechanisms affecting star formation. While environmental processes mostly take place in galaxies residing in high-density environments (e.g., galaxy clusters), encompassing a broad variety of environmental mechanisms (e.g., strangulation/starvation, [134, 135]; ram pressure stripping, [56], galaxy interactions, [136, 138]), intrinsic mechanisms are usually associated with the activation and regulation of the physical processes driving star formation activity. Intrinsic quenching mechanisms are also expected to act differently depending on the structural components within galaxies, resulting in variations in the SFR when comparing bulges, bars, or disks. These intrinsic mechanisms have been broadly associated with fast quenching processes (≤ 100 Myr; e.g. [209, 210]), or slow ageing (~ 0.5 –1 Gyr; e.g. [211]), which act in different ways to alter the physical conditions of the gas and span from strangulation (i.e, star formation continues until the reservoirs of cold gas are depleted; e.g., [212, 213]) gas removal, either due to active galactic nuclei (AGN) suppression (e.g., [21, 214]), or via stellar feedback (e.g., SNe winds; [21]).

Recent theoretical models have shown that some of these intrinsic mechanisms rely on modifying the physical properties of the ISM, therefore changing the efficiency by which the molecular gas is transformed into stars. [139] proposed “morphological quenching”, a process in which star formation is suppressed by the formation of a stellar spheroid. According to [139], morphological quenching reflects the stabilization of the disk by the dominant presence of a pressure-supported stellar spheroid, which replaces the stellar disk. The stabilization of the gas is a consequence of two effects: i) the steep potential well induced by the spheroid, and ii) the removal of the stellar disk, which is responsible to enhance the self-gravity of the perturbations in the disk. This process provides a mechanism through which early-type galaxies (ETGs) lose their

ability to form stars even in the presence of significant cold gas reservoirs (e.g., [215]). Gravitational instability is key to increase the SFR. In a simple model, stability is typically estimated by the Toomre Q parameter, $Q = \frac{\kappa\sigma}{\epsilon G\Sigma}$ [98], where σ is the one-dimensional dispersion velocity of the gas, σ_{gas} , and Σ is the surface density of an infinitely thin disk; κ is the epicyclic frequency, which is linked to the steepness of the gravitational potential, and is of order the angular velocity Ω . Axisymmetric instabilities, which create rings that break-up into clouds, can grow in the disks if $Q < 1$. [139] suggested that morphological quenching is the severe suppression of star-formation activity in a massive gaseous disk when it is embedded in a dominant bulge that stabilizes the gas (i.e., resulting in $Q \gg 1$). When compared with the star-formation activity in spirals, the difference in disk stability in ETGs arises from two main effects: i) the high central concentration of the stellar mass in ETGs increases κ , consequently increasing the tidal forces as well; and ii) the spheroidal distribution of stars dilutes the self-gravity of the gas, and therefore gravitational collapse cannot counteract the tidal forces, preventing the assembly of star-forming clumps. Also through numerical simulations, [203] show that spheroids drive turbulence and increase σ_{gas} , the virial parameter, and the turbulent pressure towards galaxy centers, which is mostly dependant on the bulge mass (M_{b}). They also find that turbulence increases for more compact and more massive bulges. Although morphological quenching represents a process capable to reduce the star formation during a well-defined time range of galaxies lifetime ($t \approx 7 - 11$ Gyr; [139]), it is still not clear at what degree the ageing in ETGs is driven by this mechanism, the reduction of the molecular gas content, or a combination of multiple processes.

By obtaining high-resolution CO data, the new generation of mm/submm telescopes have allowed us to analyze in detail how the physical conditions of the molecular gas change among the different structural components within galaxies in the local Universe. In addition, multiwave-

length galaxy surveys have revealed the interplay between the different components of the ISM and their role behind star formation activity. In this work, we present the Atacama Compact Array Extragalactic Database for Galaxy Evolution, the ACA EDGE survey. We investigate the star-formation activity in 60 nearby massive galaxies using Atacama Compact Array (ACA) observations of the CO(2-1) emission line in combination with optical Integrated Field Unit (IFU) data from the CALIFA survey [13].

This paper is organized as follows: Section 4.2 presents the main features of the ACA EDGE survey, including the sample selection, data processing, and the ancillary data. In Section 4.3 we explain the methods applied to analyze the data and the equations used to derive the physical quantities. Finally, in Section 4.4 we present our results and discussion, and in Section 4.5 we summarize the main conclusions. Throughout this work, we assume a Λ CDM cosmology, adopting the values $\Omega_\Lambda = 0.7$, $\Omega_{\text{DM}} = 0.3$ and $H_0 = 69.7 \text{ km s}^{-1} \text{ Mpc}^{-1}$.

4.2 OBSERVATIONS

4.2.1 The ACA EDGE sample

We used the ALMA large mm/submm Compact Array (ACA) to observe 60 galaxies drawn from the third public data release of the Calar Alto Legacy Integral Field Area survey Data Release 3 [216], in the context of the Extragalactic Database for Galaxy Evolution (EDGE) surveys. Previous CO surveys focus mainly (or exclusively) on “main sequence” or star forming galaxies selected either on their SFR/M_* , morphology, or IR brightness. ACA EDGE was designed to probe into the low SFR/M_* regime to probe processes associated with galaxy quenching. CALIFA observed over 800 galaxies with IFU spectroscopy at Calar Alto selected from a combination

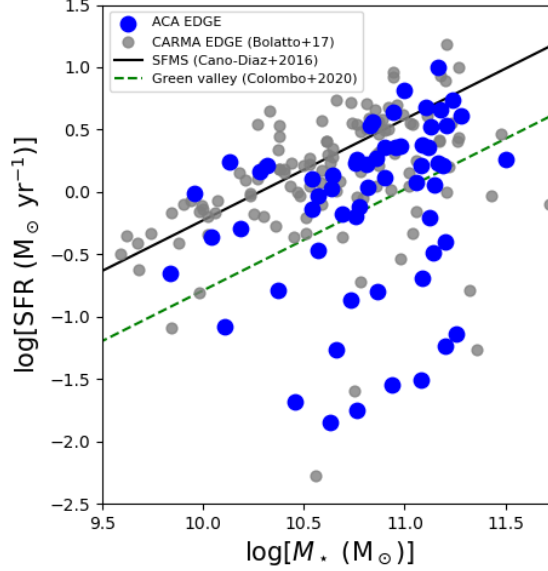


Figure 4.1: SFR- M_* relation for the 60 galaxies in the ACA EDGE survey (blue circles), sampling the whole range of $z = 0$ galaxy behavior for $\log[M_*/M_\odot] \approx 10 - 11.5$, including the star formation main sequence and quenched systems below it. Gray circles are the 126 galaxies CARMA EDGE galaxies included in [3]. The black-solid and dashed-green lines correspond to the best-linear fit for star-formation main sequence ([15]) and green valley ([14]) galaxies, respectively. ACA EDGE galaxies constitute a sample of the local universe with good statistical characteristics and are easy to volume-correct to characterize the star formation activity in nearby massive galaxies.

of the Sloan Digital Sky Survey (SDSS; [217,218]) and an extension of galaxies that fulfilled the observational setup (see [216] for more details), reflecting the $z = 0$ galaxy population with $\log[M_*/M_\odot] = 9 - 11.5$ in a statistically meaningful manner [73]. ACA EDGE targets a subsample of CALIFA galaxies with declination appropriate to observe with ALMA ($\delta < 30^\circ$) and stellar mass $M_* > 10^{10} M_\odot$, so that CO can be readily detected and metallicity effects are not too severe. We impose no selection on SFR in order to cover the full range of star formation activities in this mass range and enable the study of quenching. The ACA EDGE survey complements the main science goals of the CARMA EDGE survey ([3], galaxies also drawn from CALIFA; see Fig. 4.1), which encompasses CO observations for 126 CALIFA galaxies at $\sim 4.5''$ resolution but with significant biases. Although CARMA EDGE-selected galaxies cover a broader range of masses ($\log[M_*/M_\odot] = 9.1-11.5$), it mostly focused on late-type, far-IR detected galaxies that

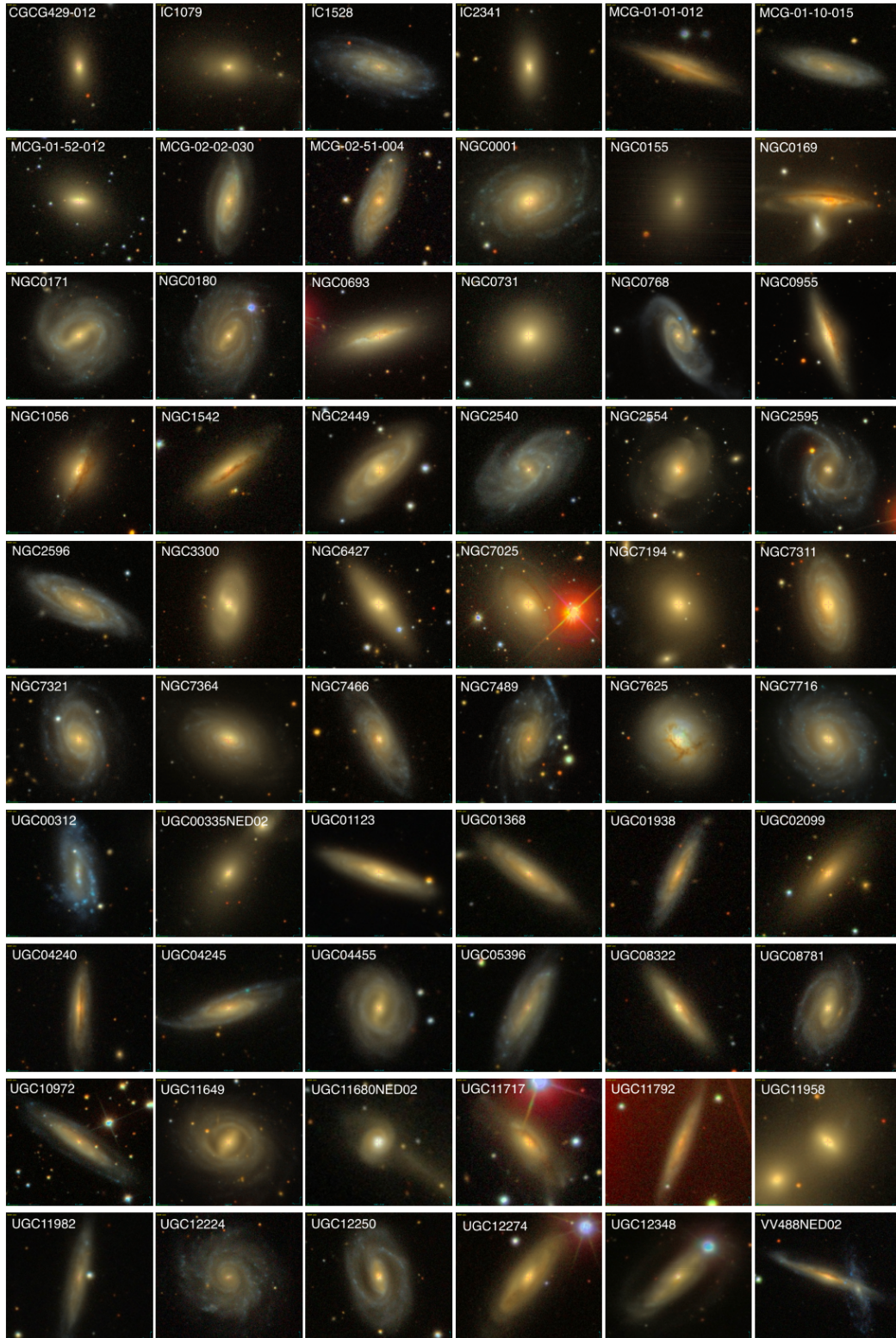


Figure 4.2: Menagerie of stellar distributions presented in the local Universe. SDSS r (red channel), i (green channel), and z -bands (blue channel) composite images for the 60 galaxies encompassed by the ACA EDGE survey. These local galaxies show a broad variety of morphologies, which is one of the main ACA EDGE goals to analyze the star-formation quenching mechanisms at different evolutionary stages.

are rich in molecular gas (hence actively star-forming), with morphological types mainly spanning from Sa to Scd. The ACA EDGE survey was designed to complement it by increasing the coverage of early-type galaxies, thus adding more red cloud galaxies to CARMA EDGE in order to drive more statistically significant results. A total of 60 galaxies were observed in CO(2–1) by the ALMA Cycle 7 project 2019.2.00029.S (P.I. A. D. Bolatto). The galaxies are listed in Table 4.1; SDSS images are shown in Figure 4.2. Optical inclinations and east-of-north position angles (PA) are taken from HyperLEDA¹ and recomputed (when applicable) using fits files from SDSS z -band photometry (see §4.3.1).

4.2.2 The CO data

CO observations of our ACA-only project were taken between December 2019 and September 2021, spending approximately between 15 and 43 minutes on-source for each source. We set a spectral bandwidth of ≈ 1980 MHz and a raw spectral resolution of ~ 1.938 MHz ≈ 2.5 km s⁻¹. The scheduling blocks were designed to detect the CO(2-1) emission line down to a root mean square (rms) spanning from ~ 12 to 18 mK at 10 km s⁻¹ channel width (corresponding to mass surface density of ~ 0.9 to 1.2 M_⊙ pc⁻²), and from $\sim 5''$ to 7'' angular resolution, depending on the declination of the source.

Each galaxy was observed in a Nyquist spaced mosaic (between 10 and 14 pointings) aligned with the major axis, covering the source out to r_{25} . As mentioned in the previous section, we obtained 7m ACA observations for 60, with an FoV $\sim 1.2'$.

¹<https://leda.univ-lyon1.fr/>

Name	R.A. (J2000)	Decl. (J2000)	i (deg)	P.A. (deg)	Redshift	rms (mK)	θ_{\min} (")	θ_{\max} (")	P.A.-beam (deg)	Distance (Mpc)	R_e (")	r_{25} (")
(1)	(2)	(3)	(4)	(5)	(6)	(7)	(8)	(9)	(10)	(11)	(12)	(13)
CGCG429-012	22 ^h 36 ^m 49.8 ^s	14°23'13."1	60	4	0.01751	12	5.3	9.7	-36.0	84	5.3	25.0
IC1079	14 ^h 56 ^m 36.1 ^s	09°22'11."1	50	81	0.02907	16	6.3	7.7	-83.0	114	19.3	43.4
IC1528	00 ^h 05 ^m 05.3 ^s	07°05'36."3	70	72	0.0125	13	4.6	8.2	-77.0	48	16.9	64.1
IC2341	08 ^h 23 ^m 41.4 ^s	21°26'05."5	60	2	0.01701	18	6.2	8.0	-72.0	75	8.0	35.2
MCG-01-01-012	23 ^h 59 ^m 10.8 ^s	04°11'30."6	90	70	0.01883	13	4.4	8.1	89.0	78	11.2	47.5
MCG-01-10-015	03 ^h 38 ^m 39.1 ^s	05°20'50."4	73	75	0.01343	12	5.1	8.3	-48.0	90	11.8	43.4
MCG-01-52-012	20 ^h 37 ^m 49.9 ^s	06°05'26."7	43	72	0.0127	14	5.0	8.4	-45.0	100	4.5	35.2
MCG-02-02-030	00 ^h 30 ^m 07.3 ^s	11°06'49."1	70	170	0.01179	13	4.4	8.3	-76.0	42	13.9	55.9
MCG-02-51-004	20 ^h 15 ^m 39.8 ^s	13°37'19."3	68	159	0.01876	12	5.2	8.1	-43.0	90	15.8	45.4
NGC0001	00 ^h 07 ^m 15.8 ^s	27°42'29."7	34	110	0.01511	15	4.9	11.7	-24.0	74	9.2	47.5
NGC0155	00 ^h 34 ^m 40.0 ^s	10°45'59."4	40	169	0.02053	13	5.1	7.9	-47.0	65	13.5	44.4
NGC0169	00 ^h 36 ^m 51.7 ^s	23°59'25."3	72	87	0.01525	15	5.0	10.1	-31.0	98	19.4	45.4
NGC0171	00 ^h 37 ^m 21.5 ^s	19°56'03."3	33	101	0.01277	14	4.9	8.0	-47.0	57	15.8	61.3
NGC0180	00 ^h 37 ^m 57.7 ^s	08°38'06."7	45	163	0.01743	13	5.6	8.9	-30.0	61	20.2	65.6
NGC0693	01 ^h 50 ^m 30.8 ^s	06°08'42."8	90	106	0.00498	17	5.1	8.9	-43.0	17	11.6	62.7
NGC0731	01 ^h 54 ^m 56.2 ^s	09°00'38."9	20	155	0.01296	12	5.1	8.2	-49.0	55	10.4	50.9
NGC0768	01 ^h 58 ^m 40.9 ^s	00°31'45."2	68	28	0.02308	13	5.3	8.3	-46.0	80	15.6	46.5
NGC0955	02 ^h 30 ^m 33.1 ^s	01°06'30."3	90	19	0.00489	17	5.2	8.5	-44.0	24	9.4	80.7
NGC1056	02 ^h 42 ^m 48.3 ^s	28°34'26."8	53	162	0.00528	15	4.8	10.9	-27.0	30	7.9	55.9
NGC1542	04 ^h 17 ^m 14.1 ^s	04°46'53."9	90	127	0.01235	18	4.8	8.2	-42.0	70	9.5	36.9
NGC2449	07 ^h 47 ^m 20.2 ^s	26°55'49."1	70	135	0.01652	15	6.0	7.6	-76.0	43	12.8	43.4
NGC2540	08 ^h 12 ^m 46.4 ^s	26°21'42."6	55	123	0.02088	17	5.7	9.7	-21.0	75	15.4	37.2
NGC2554	08 ^h 17 ^m 53.5 ^s	23°28'19."9	47	153	0.01365	18	5.9	8.3	-61.0	60	17.5	61.3
NGC2595	08 ^h 27 ^m 41.9 ^s	21°28'44."7	35	30	0.01429	18	5.8	8.5	-63.0	64	24.1	49.8
NGC2596	08 ^h 27 ^m 26.4 ^s	17°17'02."3	68	63	0.01964	17	5.3	8.5	-32.0	82	11.7	41.4
NGC3300	10 ^h 36 ^m 38.4 ^s	14°10'16."1	57	173	0.01012	16	5.8	7.7	-76.0	47	13.3	45.4
NGC6427	17 ^h 43 ^m 38.5 ^s	25°29'38."1	70	35	0.01088	15	4.9	10.3	-29.0	45	8.9	46.5
NGC7025	21 ^h 07 ^m 47.3 ^s	16°20'09."1	54	44	0.01639	13	4.9	9.1	-49.0	75	18.2	59.9
NGC7194	22 ^h 03 ^m 30.9 ^s	12°38'12."4	43	17	0.02713	13	5.6	9.5	-30.0	123	11.9	39.5
NGC7311	22 ^h 34 ^m 06.7 ^s	05°34'11."6	62	11	0.01495	13	5.1	8.9	-41.0	61	10.6	44.4
NGC7321	22 ^h 36 ^m 28.0 ^s	21°37'18."5	56	17	0.02372	14	4.9	9.7	-30.0	104	12.0	42.4
NGC7364	22 ^h 44 ^m 24.3 ^s	00°09'43."5	54	66	0.01605	14	4.5	8.4	86.0	68	10.6	49.8
NGC7466	23 ^h 02 ^m 03.4 ^s	27°03'10."1	66	25	0.02483	13	5.2	11.6	-19.0	92	12.6	46.5
NGC7489	23 ^h 07 ^m 32.6 ^s	22°59'53."6	63	165	0.02071	14	5.0	9.7	-30.0	70	16.6	36.9
NGC7625	23 ^h 20 ^m 30.0 ^s	17°13'35."0	40	45	0.00557	15	5.3	7.9	-53.0	24	9.8	44.4
NGC7716	23 ^h 36 ^m 31.4 ^s	00°17'50."2	44	34	0.00851	15	4.9	7.5	-69.0	36	14.2	54.6
UGC00312	00 ^h 31 ^m 23.9 ^s	08°28'00."6	63	7	0.01424	15	5.4	7.9	-57.0	57	13.3	44.4
UGC00335NED02	00 ^h 33 ^m 57.3 ^s	07°16'05."9	50	147	0.01812	13	5.4	9.0	-31.0	78	16.6	44.4
UGC01123	01 ^h 34 ^m 07.9 ^s	01°01'56."2	75	70	0.01615	12	5.2	8.4	-43.0	54	9.8	36.9
UGC01368	01 ^h 54 ^m 13.1 ^s	07°53'01."1	73	51	0.02653	12	5.5	7.0	-70.0	108	10.9	40.5
UGC01938	02 ^h 28 ^m 22.1 ^s	23°12'52."7	78	155	0.02108	14	5.2	9.4	-25.0	96	8.6	35.2
UGC02099	02 ^h 37 ^m 13.0 ^s	21°34'04."0	66	138	0.02737	14	5.4	10.4	-31.0	118	13.7	35.2
UGC04240	08 ^h 08 ^m 06.1 ^s	14°50'16."3	76	178	0.02886	12	5.3	8.3	87.0	163	10.2	37.8
UGC04245	08 ^h 08 ^m 45.7 ^s	18°11'39."0	70	107	0.01733	17	5.0	9.0	-32.0	75	14.5	42.4
UGC04455	08 ^h 31 ^m 32.8 ^s	01°11'51."8	47	13	0.03044	16	5.0	7.7	-81.0	128	7.9	25.0
UGC05396	10 ^h 01 ^m 40.4 ^s	10°45'23."0	75	145	0.01798	13	5.7	7.7	-87.0	76	13.9	44.4
UGC08322	13 ^h 15 ^m 00.9 ^s	12°43'31."0	73	36	0.0254	15	5.8	7.9	-82.0	98	8.5	33.7
UGC08781	13 ^h 52 ^m 22.7 ^s	21°32'22."0	50	161	0.02513	15	6.3	7.9	-61.0	115	12.0	47.5
UGC10972	17 ^h 46 ^m 21.8 ^s	26°32'36."9	78	55	0.01539	15	4.8	10.7	-28.0	63	19.0	62.7
UGC11649	20 ^h 55 ^m 27.6 ^s	01°13'30."9	42	90	0.01252	14	5.3	8.4	-42.0	60	14.5	43.4
UGC11680NED02	21 ^h 07 ^m 45.8 ^s	03°52'40."4	40	205	0.02615	12	4.7	8.3	89.0	111	9.9	20.8
UGC11717	21 ^h 18 ^m 35.4 ^s	19°43'07."0	60	39	0.02088	19	5.5	8.6	-54.0	90	11.8	36.1
UGC11792	21 ^h 42 ^m 12.7 ^s	05°36'55."1	78	160	0.01586	18	5.1	8.2	87.0	68	17.4	40.5
UGC11958	22 ^h 14 ^m 46.8 ^s	13°50'27."2	50	143	0.02618	13	5.5	9.8	-31.0	112	17.0	59.9
UGC11982	22 ^h 18 ^m 52.9 ^s	01°03'31."2	78	171	0.01554	14	4.5	8.3	-87.0	69	12.3	36.9
UGC12224	22 ^h 52 ^m 38.3 ^s	06°05'37."2	45	46	0.01156	13	5.2	8.9	-41.0	50	22.4	44.4
UGC12250	22 ^h 55 ^m 35.8 ^s	12°47'24."9	53	12	0.02405	12	5.4	9.4	-36.0	92	12.8	49.8
UGC12274	22 ^h 58 ^m 19.5 ^s	26°03'43."3	73	142	0.02538	13	5.0	11.4	-23.0	110	12.4	40.5
UGC12348	23 ^h 05 ^m 18.8 ^s	00°11'22."3	75	136	0.0251	13	5.1	7.1	-74.0	108	12.4	38.6
VV488NED02	22 ^h 56 ^m 50.8 ^s	08°58'03."1	82	73	0.01632	16	4.1	8.8	-86.0	70	13.3	62.7

Table 4.1: The ACA EDGE target sample. **Notes:** Column (1): galaxy name; (2) R.A. (J2000) of the galaxy optical center; (3) Decl. (J2000) of the galaxy optical center; (4) optical SDSS r -band inclination; (5) optical SDSS r -band position angle, calculated east of north; (6) stellar redshift; (7) root mean square flux in 10 km s⁻¹ channels; (8) minor axis of the synthesized beam; (9) major axis of the synthesized beam; (10) position angle of the synthesized beam; (11) distance; (12) effective radius; (13) optical size of the major axis measured at 25 mag arcsec⁻² in the B band. Columns (2) and (3) are drawn from the NASA/IPAC Extragalactic Database, NED. Column (4) is derived by finding the best fit for the SDSS z -band contours at $r \sim r_{25}$ as described in §4.3.1. Columns (5) and (6) are drawn from HyperLEDA. Column (11) is derived from column (6) assuming a Λ CDM cosmology with $\Omega_{\Lambda} = 0.7$, $\Omega_{\text{DM}} = 0.3$, and $H_0 = 69.7$ km s⁻¹ Mpc⁻¹. Column (12) is taken from CALIFA. Column (13) is taken from [8].

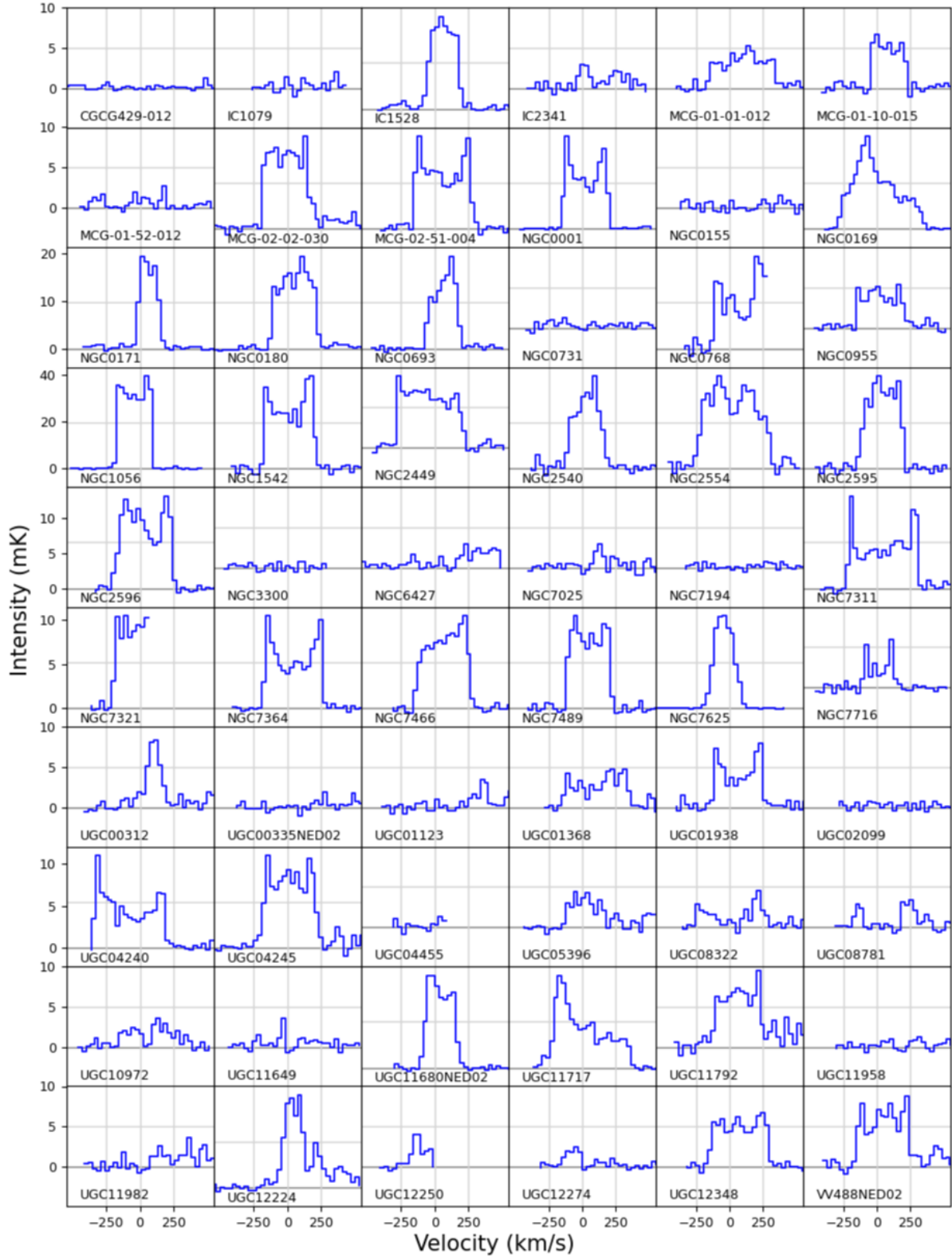


Figure 4.3: CO(2-1) spectra for ACA datacubes convolved to $1.1'$ and 30 km s^{-1} channel width for the 60 galaxies. The spectra are taken from the central pixel located at the optical center (columns 2 and 3 in Table 4.1), and velocities are centered on the stellar redshift.

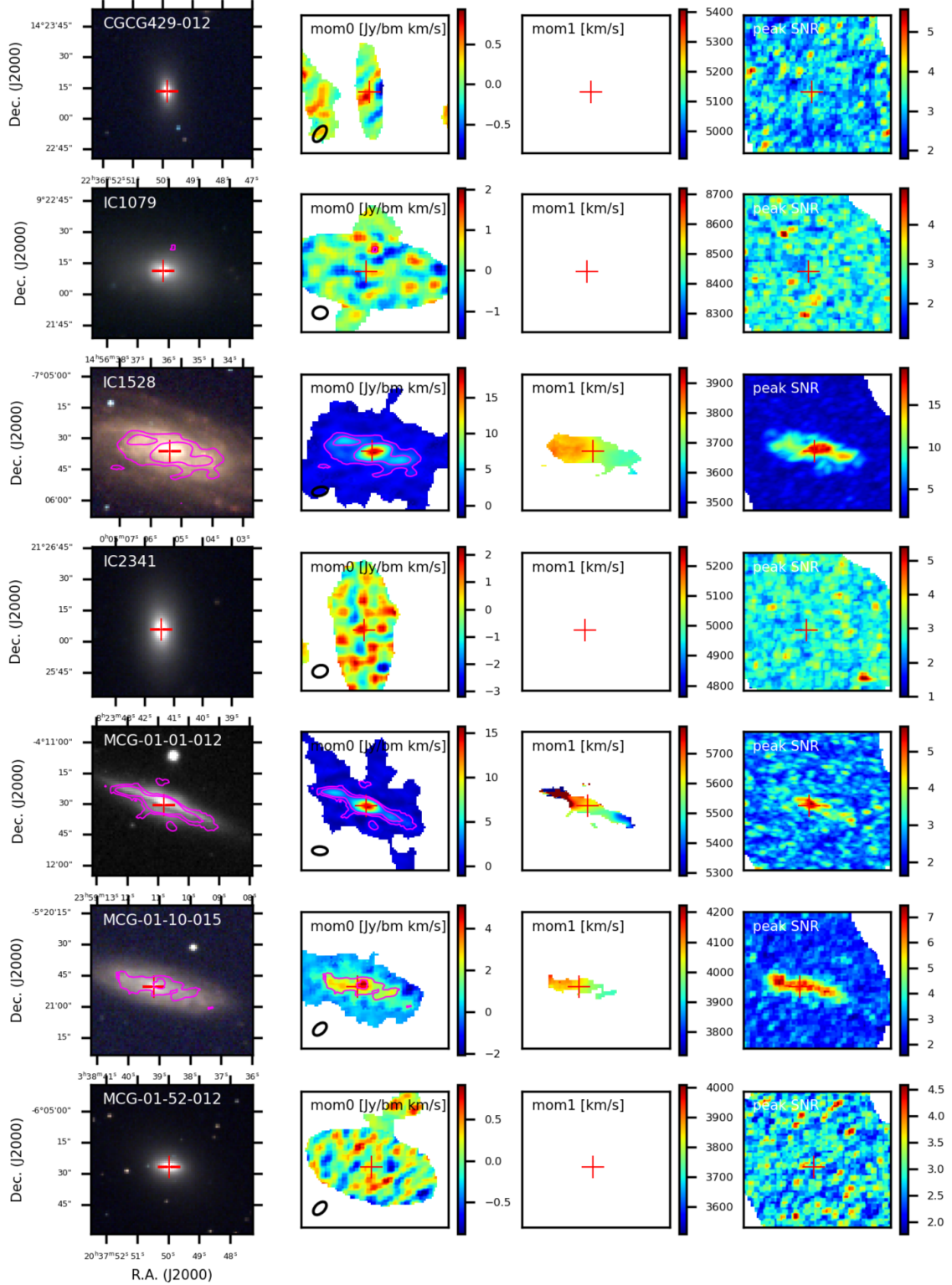


Figure 4.4: ACA EDGE data products for each galaxy. Panels cover an area of $1.25' \times 1.25'$. The first panel shows the SDSS *riz* multicolor image with contours from our integrated intensity masked map overlaid. Contours correspond to 2σ and 5σ CO(2-1) emission line levels. From left to right, the following panels show the CO(2-1) emission line intensity (moment 0, in units of $\text{Jy}/\text{beam km s}^{-1}$), velocity (moment 1, in units of km s^{-1}), and signal-to-noise peak maps, respectively. The red crosses are the optical centers (columns 2 and 3 of Table 4.1). The black ellipses in the left bottom corner are the beam size of the CO(2-1) data. Panels for the remainder of the survey can be found in the Appendix.

4.2.3 Data reduction and products

We used uv data delivered by ALMA and calibrated by the observatory pipeline [219], then we imaged the CO($J = 2-1$) emission from each target using the PHANGS–ALMA Imaging Pipeline Version 2.1 [220]. Both the calibration and imaging utilized the Common Astronomy Software Applications (CASA; [221]). The data were calibrated in CASA 5.6.1-8 for data taken in 2019 and 2020 and CASA 6.2.1-7 for data taken in 2021. We ran the PHANGS–ALMA imaging pipeline in CASA version 5.6.1-8.

Briefly, the PHANGS–ALMA imaging pipeline is designed to produce accurate images of extended spectral line emission. The pipeline combines all uv data for a given target on a common spectral grid, subtracts continuum emission, and then carries out a multi-step deconvolution. This includes an initial multi-scale clean (we used scales of 0, 5, and $10''$) with a relatively high $S/N \approx 4$ threshold, followed by a single scale clean that uses an automatically generated, more restrictive clean mask and cleans down to $S/N \approx 1$ by default. We used a Briggs weighting parameter of $= 0.5$ [222] to achieve a good compromise between synthesized beam size and signal to noise. We used a channel width of 5.08 km s^{-1} and adopted the local standard of rest (LSR) as our velocity reference frame, using the radio definition of velocity. After the initial imaging, the pipeline convolves the cube to have a round synthesized beam, converts the image to units of Kelvin, and downsamples the pixel gridding to save space while still Nyquist sampling the beam. See [220] for more details. We did not use the noise modeling or product creation portions of the PHANGS–ALMA pipeline, but instead used software based on previous EDGE work.

All cubes were visually inspected for obvious problems or imaging errors. We note that NGC 0768, NGC 6427, NGC 7321, and UGC 12250 have incomplete CO line coverage since

their emission peaks are located at the edge of the ACA spectral window. Although these galaxies have 5σ CO detections (see §4.4.1), the CO line emission flux should just be taken as lower-limits.

We calculate moment maps and radial profiles using a masked cube. The construction of our mask follows a two-step procedure. We first create a mask using the CO cube, following the procedure for a “diluted mask” detailed in [3]. This procedure includes in the mask areas around spectral peaks detected at $\geq 3.5\sigma$ significance (for more details, see [3, 223]). We put together a second mask using information that is independent of the CO cube. We then use three different procedures to generate this mask, and choose the one that recovers the most CO emission flux.

These procedures are:

- *H α mask (33 galaxies)*: We construct a mask using the central H α velocity map from CALIFA, and including around it a velocity region $[-FWHM,+FWHM]$ following the FWHM prescription from Figure 2 in [1]. H α spaxels with $SNR < 5$ in intensity are excluded from the mask. This approach assumes that the kinematics of the CO are similar to the kinematics of the H α (e.g., [79]).
- *Rotation mask (25 galaxies)*: We construct a mask assuming a very simple generic rotation curve that assumes the velocity is constant for $r > 5''$ and increases linearly inside this radius. We adopt the maximum apparent rotation velocity reported in HI by HyperLEDA ($v_{\max g}$ calculated from the 21-cm line, which we call $V_{\text{HI,max}}$ here; [224, 225]), and adopt the systemic stellar velocity from CALIFA. We include the same velocity region around this central velocity as for the previous mask. This mask only extends to $r = r_{25}$. The direction of rotation is decided based on the H α or CO velocity field (if available) or ultimately if neither are detected based on comparing the flux recovered between the two senses of

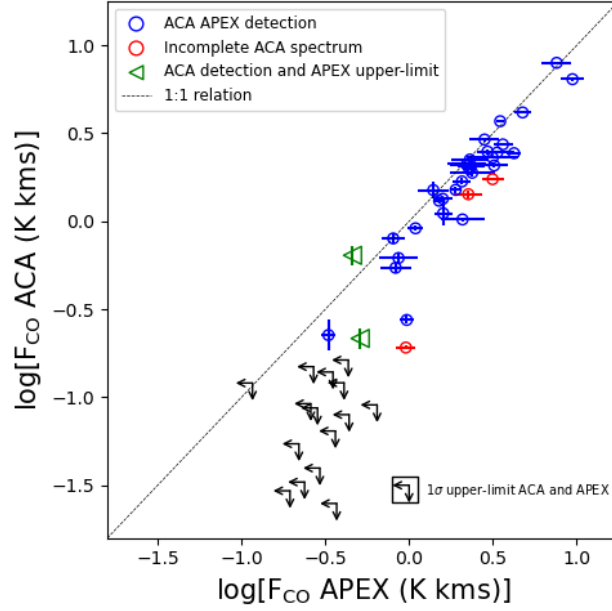


Figure 4.5: Comparison of the integrated CO($J=2-1$) emission line flux between ACA (this work) and APEX [14] datasets for 51 ACA galaxies. ACA fluxes are derived after convolving datacubes to match the APEX angular resolution ($26.3''$). The red dots correspond to NGC 0768, NGC 7321, and UGC 12250, which have incomplete ACA spectral coverage (see Fig. 4.3). The green arrows are UGC 08322 and UGC 12274, which are detected by ACA but not APEX (see Table 4.2). The figure shows good agreement between ACA and APEX fluxes. However, fluxes measured by APEX are on average $\sim 20\%$ brighter than in ACA, likely due to calibration differences. Note that a lack of a detection by ACA in a $26''$ beam does not imply the source is not detected by ACA: for interferometric data convolution results in removing visibilities in long baselines (and thus collecting area and sensitivity).

rotation. This approach assumes that the galaxy is predominantly rotating, and that the CO emission spans the same velocities as the HI.

- *Flat mask (2 galaxies)*: We construct a mask centered at the stellar systemic velocity, including all the channels inside the maximum apparent rotation velocity reported by HyperLEDA and extending out to $r = 0.5 r_{25}$. This approach does not assume any particular kinematics and is the most relaxed of the three, although it will also include more noise.

Our final step is to combine (through a logical OR operation) the best mask derived from this procedure with the dilated mask obtained from the CO, in order to obtain the final mask.

We generate moment 0 maps (integrated intensity of the spectrum along the spectral axis)

from the CO(2-1) spectral line cubes, in units of Jy/beam km s⁻¹, and after multiplying them by our mask (see Fig. 4.4). To obtain the uncertainties of the moment 0 maps, we compute the rms in the signal-free part of the spectrum in each spaxel, σ_i , and use the equation

$$u_i = \sigma_i \sqrt{N} \Delta v. \quad (4.1)$$

Here, N is the number of channels included by the mask and Δv is the channel width (in km s⁻¹). We also compute the velocity (moment 1) and peak signal-to-noise ratio (SNR_{peak}) maps.

The moment 1 maps (or CO velocity maps, in units of km s⁻¹) are derived by multiplying the CO datacubes by the mask and using

$$M_{1,i} = \frac{\sum I_{i,j} v_j}{M_{0,i}}, \quad (4.2)$$

where $I_{i,j}$ is the CO intensity in the j th spectral channel of the i th spaxel, v_j is the velocity of the j th channel, and M_0 is the moment 0 map. Finally, we blank the pixels outside the 2σ contour for M_0 . We also computed maps of the peak SNR, SNR_{peak,i}, at each position. We use the following equation:

$$\text{SNR}_{\text{peak}} = \frac{\max(I_{i,j})}{\sigma_i}, \quad (4.3)$$

where $\max(I_{i,j})$ is the maximum value of the CO intensity within the spectrum of the i th spaxel. Both velocity and SNR_{peak} maps are included in Figure 4.4.

We compare the ¹²CO(2-1) integrated fluxes for ACA EDGE galaxies to those from [14], who report ¹²CO(2-1) fluxes for 51 of our galaxies using APEX observations at 26.3'' resolution

and 30 km s^{-1} channel width (as part of the APEX EDGE survey). To do so, we convolve our CO datacubes to match the APEX angular resolution and we take the spectrum of the pixel located at the galaxy center, correcting by the recommended APEX main beam antenna efficiency (for the PI230 receiver at this frequency, $\eta_{\text{mb}} = 0.80$). Finally, we integrate the spectra over a spectral window defined by visual inspection (typically $\sim 500 \text{ km s}^{-1}$ wide). Uncertainties are computed by deriving the RMS from the signal-free part of the spectrum and using Equation 4.1. For non-detections, we estimate 1σ upper-limits by computing the RMS over the velocity window given by $V_{\text{HI,max}}$ and using Equation 4.1. Discrepancies between both measurements can in principle be attributed to inconsistencies in calibration, flux that is resolved out or lost due to imperfect deconvolution for ACA measurements, or pointing for APEX. Although there are some discrepancies between the two datasets and a handful of cases with incomplete ACA spectral coverage, Figure 4.5 shows that there is reasonable consistency between the ACA and APEX integrated CO fluxes. On average, we find that the median ACA-to-APEX flux ratio is 0.82.

4.2.4 The CALIFA survey and ancillary data

The Calar Alto Legacy Integral Field Area survey, CALIFA [13], comprises a sample of over 800 galaxies at $z \approx 0$. The data were acquired using the PMAS/PPAK IFU instrument [72] at the 3.5 m telescope of the Calar Alto Observatory. PMAS/PPAK uses 331 fibers each with a diameter of $2.7''$ in an hexagonal shape covering a FoV of a square arcminute. Its average spectral resolution is $\lambda/\Delta\lambda \sim 850$ at $\sim 5000\text{\AA}$ for a wavelength range that spans from $\lambda = 3745$ to 7300\AA . As mentioned in §5.3, CALIFA galaxies are angular size-selected such that their

isophotal diameters, D_{25} , match well with the PMAS/PPAK FoV. They range from 45'' to 80'' in the SDSS r -band [73]. The CALIFA survey uses a data reduction pipeline designed to produce datacubes with more than 5000 spectra with a sampling of 1'' \times 1''. For more details, see [216]. These cubes are processed using PIPE3D [74, 75] to generate maps of derived quantities.

The final data compilation also contains ancillary data, including information from HyperLEDA, NASA/IPAC Extragalactic Database (NED²), among others.

4.3 Methods and products

4.3.1 Basic equations and assumptions

To compute the extinction-corrected SFRs, we estimate the extinction (based on the Balmer decrement; see [3]) for each 1'' spaxel using the equation:

$$A_{\text{H}\alpha} = 5.86 \log \left(\frac{F_{\text{H}\alpha}}{2.86 F_{\text{H}\beta}} \right), \quad (4.4)$$

where $F_{\text{H}\alpha}$ and $F_{\text{H}\beta}$ are the fluxes of the respective Balmer lines, and the coefficients assume a [80] extinction curve and an unextinguished flux ratio of 2.86 for case B recombination. Then, the corresponding SFR (in $M_{\odot} \text{ yr}^{-1}$) is obtained using [81]

$$\text{SFR} = 1.6 \times 7.9 \times 10^{-42} F_{\text{H}\alpha} 10^{\frac{A_{\text{H}\alpha}}{2.5}}, \quad (4.5)$$

which includes a correction factor of 1.6 to move from a Salpeter IMF (as adopted by PIPE3D) to the more commonly used Kroupa IMF [82]. We do this to compare our results with those for

²<https://ned.ipac.caltech.edu/>

other galaxy surveys. We use this to compute the star formation rate surface density, Σ_{SFR} in $\text{M}_{\odot} \text{yr}^{-1} \text{kpc}^{-2}$, by dividing by the face-on area corresponding to a $1''$ spaxel, given the angular diameter distance to the galaxy. In order to produce smooth SFR maps, we process the $\text{H}\alpha$ and $\text{H}\beta$ fluxes applying the following recipe:

1. We select pixels with non-NaN values for $F_{\text{H}\alpha}$.
2. We adopt a minimum $\text{H}\alpha$ -to- $\text{H}\beta$ flux ratio, $F_{\text{H}\alpha}/F_{\text{H}\beta}$, of 2.86. Therefore, if $F_{\text{H}\alpha}/F_{\text{H}\beta} < 2.86$, then we impose $F_{\text{H}\alpha}/F_{\text{H}\beta} = 2.86$ (so $A_{\text{H}\alpha} = 0$).
3. If $F_{\text{H}\beta}$ is a NaN value for a given pixel, then we take the average value of $A_{\text{H}\alpha}$ (for pixels with $A_{\text{H}\alpha} > 0.0$) of the whole $A_{\text{H}\alpha}$ map.

We obtain the stellar mass surface density, Σ_{\star} , from the stellar maps derived by PIPE3D. We correct the maps from the spatial binning effect by applying the dezonification correction provided by PIPE3D datacubes. This is to weight the Σ_{\star} maps by the relative contribution to flux in the V -band for each spaxel to the flux intensity of the bin in which it is aggregated (for more details, see [75]). Finally, we mask the Σ_{\star} maps to avoid the flux contribution from field stars and we include the 1.6 correction factor to move from a Salpeter to a Kroupa IMF.

The molecular gas surface density, Σ_{mol} , is derived from the integrated CO intensity, $I_{\text{CO}(2-1)}$, by adopting a constant CO-to- H_2 conversion factor that is based on observations of the Milky Way: $X_{\text{CO}} = 2 \times 10^{20} \text{cm}^{-2} (\text{K km s}^{-1})^{-1}$, or equivalently $\alpha_{\text{CO,MW}} = 4.3 \text{M}_{\odot} (\text{K km s}^{-1} \text{pc}^2)^{-1}$ for the CO($J = 1 - 0$) line [83]. We also test how our results depend on our adopted prescription by using the CO-to- H_2 conversion factor from Equation 31 in [38]:

$$\alpha_{\text{CO}}(Z', \Sigma_{\text{total}}) = 2.9 \exp\left(\frac{+0.4}{Z' \Sigma_{\text{GMC}}^{100}}\right) \left(\frac{\Sigma_{\text{total}}}{100 \text{M}_{\odot} \text{pc}^2}\right)^{-\gamma}, \quad (4.6)$$

in $M_\odot (\text{K kms}^{-1} \text{pc}^{-2})^{-1}$. $\gamma \approx 0.5$ for $\Sigma_{\text{total}} > 100 M_\odot \text{pc}^{-2}$ and $\gamma = 0$ otherwise. Additionally, the metallicity is normalized to the solar one, $Z' = [\text{O}/\text{H}]/[\text{O}/\text{H}]_\odot$, where $[\text{O}/\text{H}]_\odot = 4.9 \times 10^{-4}$ [86], $\Sigma_{\text{GMC}}^{100}$ is the average surface density of molecular gas in units of $100 M_\odot \text{pc}^{-2}$, and Σ_{total} is the combined gas plus stellar surface density on kpc scales. We are also interested in the global variations of $\alpha_{\text{CO}}(Z', \Sigma_{\text{total}})$. To do so, we adopt $\Sigma_{\text{GMC}}^{100} = 1$ and derive Z' using the metallicity-stellar mass relation (based on the O3N2 calibrator; [85]) for CALIFA galaxies from [226]. We use the following expression to obtain Σ_{mol}

$$\Sigma_{\text{mol}} = \frac{\alpha_{\text{CO}}}{R_{21}} \cos(i) I_{\text{CO}(2-1)}, \quad (4.7)$$

which adopts the average line luminosity ratio of $R_{21} = I_{\text{CO}(2-1)}/I_{\text{CO}(1-0)} = 0.65$ based on [32] and [227], measured at kpc scales; i is the inclination of the galaxy. This equation takes into account the mass correction due to the cosmic abundance of helium. Although i is generally drawn from HyperLEDA, we use SDSS z -band images to obtain a better constraint on the inclination (particularly for galaxies with $i > 60^\circ$). To do so, we fit an ellipse to the SDSS z -band contour for a major axis $A_{\text{maj}} \sim 1.2r_{25}$. We obtain the ratio between the minor and major axes, $A_{\text{min}}/A_{\text{maj}}$, and compute the inclination by taking $i = \arccos[A_{\text{min}}/A_{\text{maj}}]$ (see column 4 in Table 4.1). This assumes an infinitely thin disk and introduces errors for $i > 85^\circ$, but we discard highly inclined galaxies from our analysis anyway since most derived quantities are highly uncertain.

To compute the global values of the molecular gas mass, M_{mol} , M_\star , and SFR (Q_i quantities), we use the following equation:

$$Q_i = \int_A \Sigma_i(r) dA, \quad (4.8)$$

where A is the area within a circle defined by the geometrical parameters included in Table 4.1 (with radius r_{25} and centered at the optical center); Σ_i is the surface densities for the pixels within A and $i = \text{SFR, mol, or } \star$.

We integrate the surface densities for the molecular gas, stars (assuming that they are distributed along a thin disk), and the SFR to obtain the stellar mass, molecular gas mass, and the SFR within the bulge:

$$M_{b,i} = 2\pi \int_0^{R_b} \Sigma_i(r) r dr, \quad (4.9)$$

where R_b is the bulge radius for the stellar component (see §4.3.3 for more details), and $i = \text{mol, } \star, \text{ or SFR}$. We then calculate the integrated ratios as the ratio of the integrated masses and the SFR.

Finally, we compute the resolved SFE_{mol} (in units of yr^{-1}) for each pixel,

$$\text{SFE}_{\text{mol}} = \frac{\Sigma_{\text{SFR}}}{\Sigma_{\text{mol}}}. \quad (4.10)$$

In a similar way, we calculate the resolved molecular-to-stellar mass fraction, $rR_{\star}^{\text{mol}} = \Sigma_{\text{mol}}/\Sigma_{\star}$, and the specific star formation rate, $\text{sSFR} = \Sigma_{\text{SFR}}/\Sigma_{\star}$ (in units of yr^{-1}).

4.3.2 Radial profiles

We obtain stellar and molecular gas radial profiles for a subsample of 30 galaxies with inclinations $\leq 70^\circ$ and 5σ integrated CO detections (see §4.4.1), which represent well the distributions of stellar masses and morphologies of the full ACA EDGE sample (see Table 4.2). We also select spaxels with 3σ CO detections. We derive these profiles by measuring the average

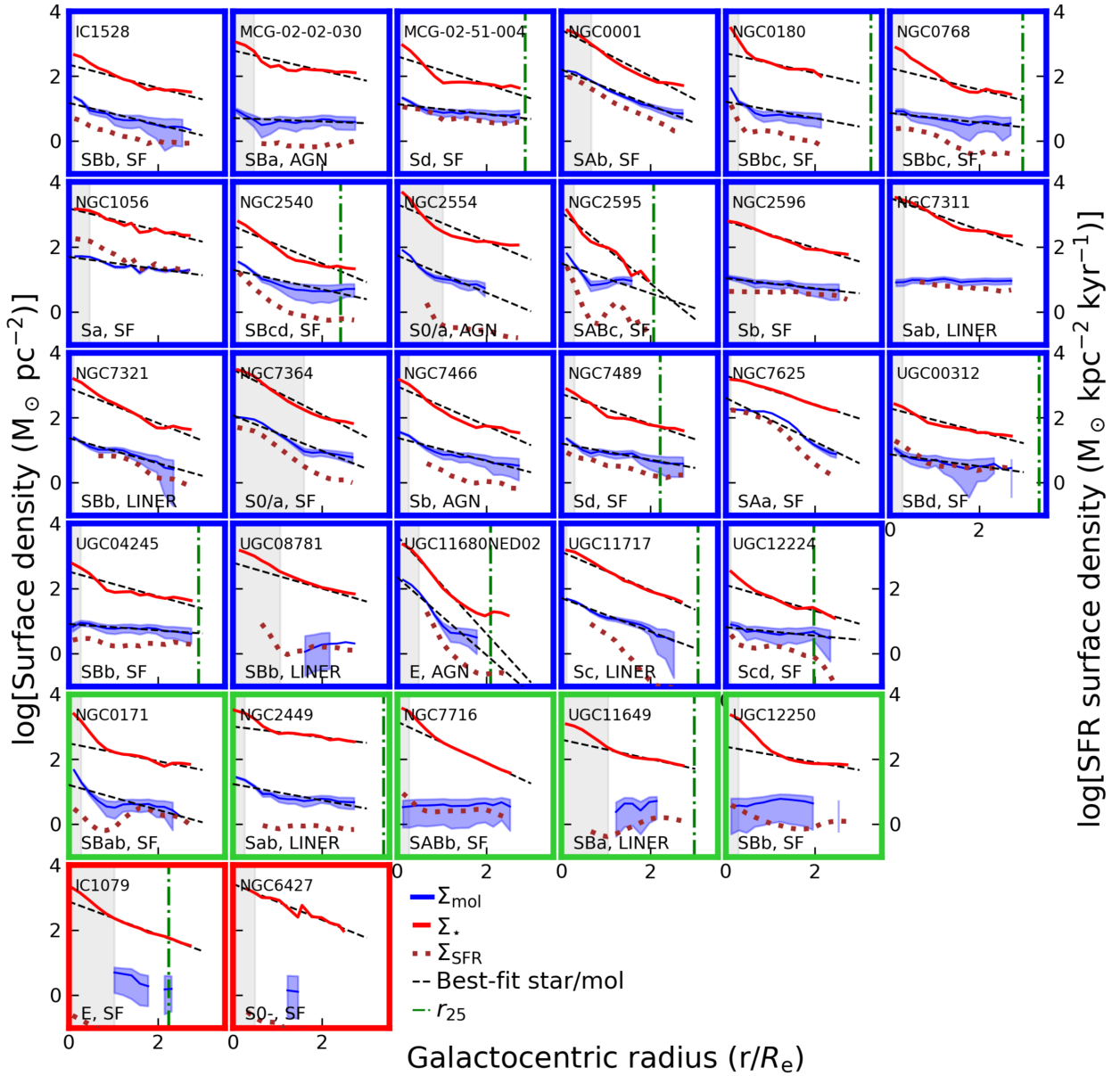


Figure 4.6: Stellar (Σ_* ; red solid line) and molecular gas (Σ_{mol} ; blue solid line) surface densities, in units of $M_\odot \text{ pc}^{-2}$, as a function of galactocentric radius, in units of the stellar effective radius (R_e), for the 30 ACA EDGE galaxies with 5σ CO detections and inclinations $i \leq 70^\circ$. The blue shaded area is the Σ_{mol} uncertainty. The brown dotted line is the SFR surface density, Σ_{SFR} . The gray shaded area is the region within the bulge radius, R_{bulge} . Dashed black lines correspond to the best exponential function fit for stellar and molecular gas radial profiles, from top to bottom. The dashed green line corresponds to $r = r_{25}$. The code on the left bottom corner corresponds to the Hubble type and the nuclear activity (columns 5 and 6 in Table 4.2, respectively). SFRs at $r < 0.5R_e$ have been removed for LINER and AGN galaxies since $\text{H}\alpha$ in this region is susceptible to LINER/AGN contamination (see §4.4.2.2). Galaxies are classified based on their quenching stage as defined in §4.4.1, i.e., in main sequence (blue panels), green valley (green panels), and red cloud (red panels). When using stellar profiles as a benchmark, we note a systematic flattening of the molecular gas profiles with quenching stage. See also Fig. 4.12.

Name	$\log[M_*$ (M_\odot) (2)	$\log[\text{SFR}]$ ($M_\odot \text{ yr}^{-1}$) (3)	$\log[M_{\text{mol}}]$ (M_\odot) (4)	Morph. Class (5)	Nuclear (6)	Quenching Stage (7)	l_* (kpc) (8)	l_{CO} (kpc) (9)	R_b (kpc) (10)	M_b (M_\odot/M_*) (11)
CGCG429-012	10.46	-1.68	<6.77	E0	...	RS
IC1079	11.2	-1.23	8.86±0.17	E	...	RS	9.12±0.98	...	10.99±1.07	0.14±0.19
IC1528 ^a	10.76	0.23	8.83±0.02	SBb	...	MS, SF	4.8±2.01	5.13±1.25	0.52±0.39	0.01±0.38
IC2341	10.86	-0.8	<7.4	S0-	...	RS
MCG-01-01-012	11.19	0.21	7.58±0.02	SAab	...	GV
MCG-01-10-015	9.95	-0.01	8.32±0.03	Sd	...	MS
MCG-01-52-012	10.37	-0.79	<6.56	S0-	...	GV
MCG-02-02-030 ^a	10.81	0.03	8.52±0.02	SBa	AGN	MS, QnR	3.95±1.43	23.27±49.75	1.35±0.28	0.1±0.07
MCG-02-51-004 ^a	10.94	0.64	9.19±0.02	Sd	...	MS, SF	6.93±0.74	19.56±5.93	0.87±0.69	0.02±0.36
NGC0001 ^a	10.84	0.57	9.87±0.02	SAb	SF	MS, SF	2.01±0.28	2.6±0.47	2.25±0.33	0.39±0.15
NGC0155 ^a	11.08	-1.51	<7.45	S0	...	RS, fR
NGC0169	11.24	0.73	9.54±0.01	SAab	LINER	MS
NGC0171 ^a	10.77	-0.12	8.98±0.02	SBab	...	GV, cQ	6.94±4.06	4.94±1.06	1.27±0.44	0.15±0.05
NGC0180	11.08	0.21	9.62±0.02	SBbc	...	MS	8.5±3.9	10.16±2.15	1.74±0.6	0.12±0.0
NGC0693	9.84	-0.65	6.86±0.02	S0/a	...	MS
NGC0731	10.94	-1.55	<6.84	E	...	RS
NGC0768 ^a	10.86	0.27	9.25±0.02	SBbc	...	MS, SF	7.92±2.74	17.97±6.58	1.87±0.6	0.13±0.09
NGC0955	10.11	-1.08	6.53±0.04	Sab	...	GV
NGC1056 ^a	10.28	0.16	8.6±0.01	Sa	SF	MS, SF	1.47±1.2	2.66±3.95	0.56±0.12	0.08±0.04
NGC1542 ^a	10.57	-0.03	6.34±0.47	Sab	SF	MS, MX
NGC2449 ^a	11.13	-0.2	9.03±0.02	Sab	LINER	GV, MX	6.97±10.57	4.63±2.16	0.72±0.27	0.03±0.16
NGC2540	10.54	0.11	9.47±0.03	SBcd	...	MS	4.23±0.42	8.09±1.54	0.74±0.56	0.02±0.37
NGC2554 ^a	11.11	0.68	9.4±0.02	S0/a	AGN	MS, nR	3.89±0.43	3.85±0.68	5.25±0.51	0.47±0.35
NGC2595	10.9	0.12	9.57±0.02	SABc	...	MS	2.96±0.19	7.07±1.45	2.17±0.75	0.24±0.0
NGC2596	10.76	0.26	9.13±0.02	Sb	...	MS	4.84±0.8	12.95±6.32	3.07±0.46	0.16±0.07
NGC3300 ^a	10.76	-1.75	<6.84	SAB	...	RS, fR
NGC6427	10.63	-1.85	7.39±0.17	S0-	...	RS	1.51±0.57	...	0.97±0.19	0.14±0.0
NGC7025 ^a	11.17	0.23	<7.6	Sa	LINER	MS, nR
NGC7194 ^a	11.25	-1.14	<7.86	E	LINER	RS, fR
NGC7311 ^a	11.12	0.36	9.1±0.02	Sab	LINER	MS, cQ	2.77±0.58	...	0.99±0.31	0.06±0.14
NGC7321 ^a	11.13	0.53	9.41±0.02	SBb	LINER	MS, QnR	4.86±1.02	6.8±1.15	0.72±0.61	0.02±0.41
NGC7364 ^a	11.18	0.66	9.58±0.02	S0/a	...	MS, SF	2.18±0.29	2.76±0.47	5.55±0.35	0.75±0.47
NGC7466 ^a	10.95	0.36	9.56±0.02	Sb	AGN	MS, SF	4.05±0.38	6.91±1.1	1.51±0.56	0.1±0.13
NGC7489 ^a	10.83	0.54	9.42±0.02	Sd	SF	MS, SF	5.27±0.64	9.78±2.21	1.68±0.57	0.07±0.11
NGC7625 ^a	10.32	0.21	9.33±0.02	SAa	SF	MS, SF	1.13±0.81	0.74±0.35	0.14±0.11	0.01±0.43
NGC7716 ^a	10.69	-0.18	7.86±0.08	SABb	...	GV, cQ	1.69±0.9	...	0.69±0.25	0.2±0.1
UGC00312 ^a	10.13	0.24	8.42±0.06	SBd	SF	MS, SF	4.45±1.09	8.72±4.18	1.08±0.37	0.04±0.14
UGC00335NED02	10.66	-1.26	<7.58	E	LINER	RS
UGC01123	10.73	-0.87	<6.73	Sab	...	RS
UGC01368	11.21	0.53	8.93±0.03	Sab	...	MS
UGC01938	10.64	0.13	8.68±0.03	Sbc	...	MS
UGC02099	11.14	-0.49	<7.58	S0	...	RS
UGC04240	10.98	0.37	9.19±0.02	S	...	MS
UGC04245	10.54	-0.14	9.02±0.02	SBb	...	MS	6.04±0.95	23.75±14.75	1.45±0.53	0.05±0.14
UGC04455	11.5	0.26	<7.51	SBa	...	GV
UGC05396	10.81	0.23	8.36±0.05	Scd	SF	MS
UGC08322	11.15	0.06	8.67±0.05	Sa	...	GV
UGC08781 ^a	11.09	0.37	8.65±0.13	SBb	LINER	MS, cQ	7.29±1.59	...	7.1±0.67	0.23±0.12
UGC10972 ^a	10.75	-0.19	8.26±0.058	Scd	LINER	GV, cQ
UGC11649	10.57	-0.47	7.76±0.19	SBa	LINER	GV	6.12±3.3	...	4.45±0.42	0.08±0.05
UGC11680NED02	11.17	1.0	9.82±0.02	E	AGN	MS	1.55±0.17	1.95±0.18	2.64±0.54	0.52±0.12
UGC11717 ^a	11.28	0.61	9.6±0.02	Sc	LINER	MS, MX	3.79±0.73	4.36±0.58	0.65±0.52	0.02±0.41
UGC11792	10.64	0.02	8.67±0.02	Sc	SF	MS
UGC11958	11.2	-0.4	<7.22	E	LINER	RS
UGC11982	10.04	-0.36	7.53±0.12	SBcd	...	MS
UGC12224	10.18	-0.3	9.22±0.02	Scd	SF	MS	5.94±1.91	18.32±10.46	0.67±0.54	0.02±0.36
UGC12250	11.06	0.08	8.65±0.1	SBb	...	GV	10.39±5.26	...	1.71±0.57	0.17±0.09
UGC12274 ^a	11.09	-0.69	8.47±0.09	S	LINER	RS, nR
UGC12348	11.0	0.81	9.05±0.02	Sa	AGN	MS
VV488NED02	10.9	0.36	8.43±0.03	SBc	SF	MS

Table 4.2: Main properties of the ACA EDGE galaxies. Column (1): galaxy name. Column (2) and (3): logarithmic of the total stellar masses and SFRs from CALIFA. Column (4): logarithmic of the total molecular gas mass as derived explained in §4.3.1. Column (5): morphological classification drawn from NED. Column (6): emission line diagnostics for the optical nucleus spectrum for CALIFA galaxies by [4], who classify them into star-forming (SF), active galactic nuclei (AGN), and LINER-type galaxies. These groups are also complemented by the type-I and type-II AGN classification by [9]. Column (7): Galaxy classification according to their quenching stage as explained in §4.4.1.1: main sequence (MS), green valley (GV), and red cloud (RS). Columns (8) and (9): exponential scale lengths of the molecular gas and stars, respectively, as derived in §4.4.1.2. Columns (10) and (11): radius and mass of bulges, as derived in §4.3.3. ^aGalaxies with two-dimensional emission line classification (column 7) from [10], who classify galaxies in star-forming (SF), quiescent-nuclear-ring (QnR), centrally quiescent (cQ), mixed (MX), nearly retired (nR), and fully retired (fR).

azimuthal CO, stellar, and SFR surface densities in elliptical annuli in the CO(2-1) datacubes. Figure 4.6 shows the molecular gas radial profiles (blue solid line) and their $\pm 1\sigma$ uncertainties (blue shaded areas), which are corrected by inclination (i.e., multiplied by a factor of $\cos(i)$). Annuli are centered on the optical galaxy position and aligned with the centered major-axis position angle (column 5 in Table 4.1). We compute the average $I_{\text{CO}(2-1)}$ for a given annulus by summing the velocity-integrated CO line emission intensities from the total pixels within an annulus $\sim 5''$, wide (average of the minor beam axes), and then we use Equation 4.7 (adopting the constant α_{CO} prescription; see §4.3.1) to obtain the molecular gas surface density, Σ_{mol} .

We implement the same method (averaging over all pixels in an annulus) for the SFR and stars. Stellar and SFR radial profiles are shown in Fig. 4.6 by the red solid and brown dotted lines, respectively. We remove SFRs at $r < 0.5R_e$ for galaxies classified as LINER or AGN (bottom-left corner legend in Fig. 4.6) since $\text{H}\alpha$ in this region is susceptible to LINER/AGN contamination (see §4.4.2.2 for more details).

4.3.3 Bulge radii and masses

In order to test the star-formation quenching mechanisms within the bulge region (see §4.4.2.2), we derive the radius of the bulge, R_b , for the 30 ACA EDGE galaxies included in Figure 4.6. We characterize the bulge-dominated region by identifying the galactocentric radius where there is a break with respect to the stellar radial profiles. Similar to [2], we adopt $R_b = 1$ kpc for spiral galaxies where we do not identify a clear break. Since previous studies have shown that bulges for spirals are typically ≤ 1.5 kpc (e.g., [1, 109, 228]), we use the stellar and SFR maps at CALIFA’s native resolution of $2.7''$ to obtain the best physical resolution available (~ 0.9 kpc at

the median distance of ACA EDGE galaxies). Bulge radius distributions for main sequence and green valley galaxies are centered at $\log[R_b/(\text{kpc})] \sim 0.15$ and ~ -0.1 , which are slightly larger than those found by [229], who compute the radius for the central regions (including small bulges and nuclei) of 74 galaxies nearby galaxies selected from PHANGS. By implementing a photometric decomposition using GALFIT [44], they obtain a mean value of $\log[R_{\text{center}}/r_{25}] \sim -1.5$, which on average is lower than that of our main sequence galaxies ($\log[R_{\text{center}}/r_{25}] \sim -1.0$). The vast majority of PHANGS galaxies corresponds to late-type spiral galaxies which cover a lower stellar mass range ($9.25 \leq \log[M_*/M_\odot] \leq 11.25$) than ACA EDGE, which could result in shorter bulge radii. Finally, red cloud galaxies have the largest bulge radii, with R_b distributions centered at $\log[R_B/(\text{kpc})] \sim 0.35$. These results are consistent with observational evidence. For instance, [230] present a catalog of bulge, disk, and total stellar mass estimates for $\sim 660,000$ galaxies from SDSS DR7, based on g and r -band photometry published in [231] and using GIM2D [232]. By fitting Sérsic profiles (n_S ; [233]) to elliptical, disk, and bulge+disk, they find a Sérsic index distribution centered at larger values for the former ($n_S \sim 5$) when compared to the latter two groups ($n_S \sim 1$). In addition, [228] implement a 2D photometric decomposition using GASP2D [234, 235] for 404 CALIFA galaxies using g , r , and i SDSS images, including 28 ACA EDGE galaxies in their analysis. We obtain a close 1:1 relation when comparing the two sets of bulge radii (OLS $R_{b,\text{CALIFA}} = [0.83 \pm 0.10] \times R_{b,\text{ACAEDGE}}$), which also show a strong correlation between them (Pearson $r_p = 0.92$; $p\text{-value} \ll 0.01$).

Using R_b , we compute the bulge mass, M_b , in terms of the total stellar mass, after numerically integrating the stellar profiles using Equation 4.9. Table 4.2 summarizes the properties of the 60 ACA EDGE galaxies, together with the values of R_b and M_b (columns 10 and 11). Columns (4), (8), and (9) list M_{mol} , l_* , and l_{mol} , respectively; the latter two are calculated from

radial profiles in §4.4.1.2.

4.4 Results and Discussion

In the next subsections we present the main properties of the 60 galaxies included in the ACA EDGE survey. To do so, we divide our results in global (i.e., quantities derived from integrated measurements) and spatially resolved (i.e., quantities derived from pixel measurements). Unless otherwise mentioned, we estimate the molecular gas related quantities by adopting a constant Milky Way CO-to-H₂ conversion factor (see §4.3.1).

4.4.1 Global quantities and relations

4.4.1.1 SFR versus stellar and molecular gas masses

The top left panel of Figure 4.7 shows the SFR- M_* relation, color-coded by M_{mol} , using the global values (pixels at $r < r_{25}$) of SFR and M_* (see §4.3.1). On average, we note that galaxies near the SFMS (black line; [15]) tend to have higher molecular gas masses, although there is not a clear region on the SFR- M_* relation associated with low values of M_{mol} (see color-coded symbols). In order to characterize the behaviour of the molecular gas as a function of the difference between the SFR and the SFMS, $\Delta\text{SFMS} = \text{SFMS} - \log[\text{SFR}]$, we classify our galaxies in three different groups based on their quenching stage, as shown by shaded areas in top left panel of Figure 4.7:

1. Main sequence (36 galaxies; blue shaded area), which are galaxies with $-0.5 \text{ dex} < \Delta\text{SFMS}$.
2. Green valley (11 galaxies; green shaded area), encompassing galaxies with $-1.0 \text{ dex} <$

$$\Delta\text{SFMS} \leq -0.5 \text{ dex.}$$

3. Red cloud (13 galaxies; red shaded area), which includes galaxies with $\Delta\text{SFMS} \leq -1.0$ dex.

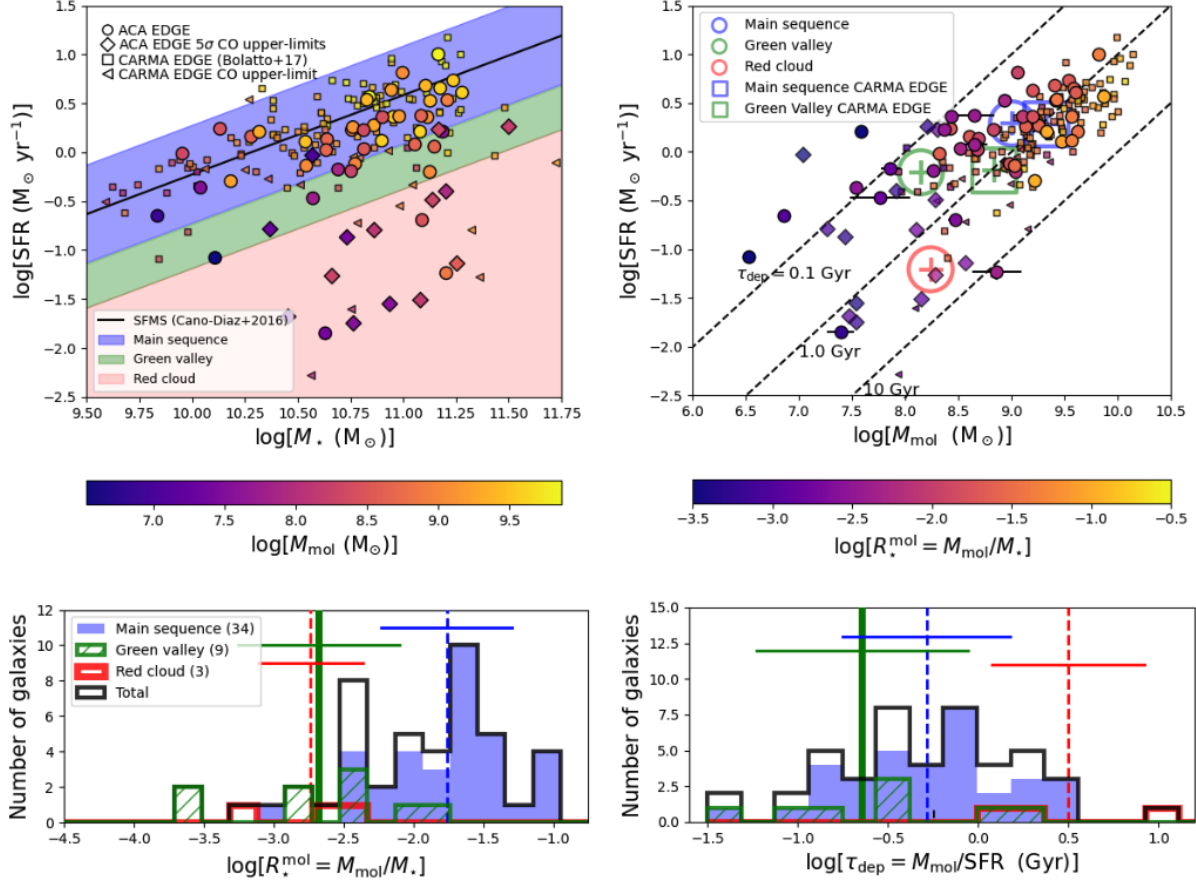


Figure 4.7: *Top left*: SFR- M_* diagram integrated over CALIFA SFR and stellar maps, color-coded by the total molecular gas mass, M_{mol} . The solid black line is the SFMS fit by [15]. Blue, green, and red dashed areas define main sequence, green valley, and red cloud galaxies, respectively, as defined by the bands (see §4.4.1 for more details). *Top right*: SFR- M_{mol} relation color-coded by stellar mass. The dashed black lines, from top to bottom, correspond to molecular gas depletion times $\tau_{\text{dep}} = 0.1, 1.0,$ and 10 Gyr , respectively. Blue, green, and red circles are the centroids of SFR and M_{mol} values for galaxies with 5σ CO detections (filled circles) of the groups as defined by the bands in the top left panel. The blue and green squares correspond to the centroid of SFR and M_{mol} values for main sequence and green valley CARMA EDGE detected galaxies. *Bottom*: Distributions for the molecular-to-stellar mass fraction ($R_*^{\text{mol}} = M_{\text{mol}}/M_*$; left) and the molecular gas depletion time ($\tau_{\text{mol}} = M_{\text{mol}}/\text{SFR}$; right) for the three categories (excluding CO upper-limits), as defined in top left panel. Vertical and horizontal lines correspond to the average values and the standard deviations of the distributions, respectively. The plots suggest that while the transition from main sequence to green valley galaxies is mostly driven by gas removal/depletion, the movement from the latter to the red cloud may be determined by a reduction in the star formation efficiency of the molecular gas ($\text{SFE}_{\text{mol}} = \tau_{\text{dep}}^{-1}$).

We choose these boundaries based on the typical values of the main-sequence/green valley distribution scatters reported in recent studies, which span from ~ 0.2 to 0.7 dex (e.g., [14, 15, 236–239]). The bottom left panel of Figure 4.7 shows the distribution of the molecular-to-stellar mass fraction, $R_{\star}^{\text{mol}} = M_{\text{mol}}/M_{\star}$, of the three groups for galaxies with 5σ CO detections. Main sequence galaxies have the highest molecular gas masses (with an average $\log[R_{\star}^{\text{mol}}] \sim -1.6$ dex; blue dashed line), while on average both green valley and red cloud galaxies have fractions about an order of magnitude lower (green solid and red dashed lines).

The top right panel of Fig. 4.7 shows the SFR- M_{mol} relation, color-coded by M_{\star} . The three dashed black lines correspond to three different molecular depletion times, $\tau_{\text{dep}} = M_{\text{mol}}/\text{SFR} = 0.1, 1.0, \text{ and } 10$ Gyr, going from top to bottom, respectively. It is interesting to note that although most ACA EDGE galaxies are well represented by the $\tau_{\text{dep}} = 1$ Gyr line, there is not a characteristic molecular depletion time for the whole sample. This is confirmed when we analyze the molecular gas depletion time distributions of the three groups (bottom right panel of Fig. 4.7); red cloud galaxies have τ_{dep} around 3 and 6 times longer than main sequence and green valley galaxies, respectively. However, these results have to be considered carefully due to the small number of CO-detected red cloud galaxies.

Our results are consistent with [14], who analyze $^{12}\text{CO}(2-1)$ APEX data at $26.3''$ resolution (i.e., the region within R_e) for 472 EDGE galaxies. They note a strong correlation between ΔSFMS and the star formation efficiency of the molecular gas, $\text{SFE}_{\text{mol}} = \tau_{\text{dep}}^{-1}$, suggesting a scenario where the transition of galaxies from the main sequence to the green valley is primarily driven by the molecular gas lost. In addition, they propose that changes in the SFE_{mol} of the remaining cold gas is what modulates a galaxy’s retirement from the green valley to the red cloud. Analyzing a compilation of ~ 8000 galaxies from MaNGA, [239] also note that the SFE

decreases as galaxies move out of the main sequence to the red cloud and pass through the green valley, which is confirmed by several studies (e.g., [111, 240]).

4.4.1.2 Exponential scale lengths

If gas removal/depletion is one of the main processes modulating the transition from main sequence to green valley galaxies, it should impact the distribution of the molecular gas. To test this, we compute the exponential scale lengths for the molecular gas, l_{mol} , and the stars, l_{\star} , for the ACA EDGE galaxies in Figure 4.6. Figure 4.8 shows the comparison between l_{mol} and l_{\star} for main sequence ACA EDGE galaxies with $i < 70^\circ$ and 5σ CO detections (see §4.3.2). Galaxies are color-coded by their quenching stage according to the classification explained in Figure 4.7. Out of the 30 galaxies with molecular gas and stellar radial profiles, we have selected 23 galaxies with decreasing Σ_{mol} profiles (i.e., $\Sigma_{\text{mol}}(r < 1 \text{ kpc}) > \Sigma_{\text{mol}}(r = r_{\text{max}})$), where r_{max} is the largest radius at which we have a 5σ CO detection. Since we also restrict the $\Sigma_{\star}(r)$ exponential fit to the stellar disk, we do not consider annuli within prominent bulges (i.e., E and S0 galaxies; [109]) and bars (i.e., SB, Sab, and Sbc galaxies). These fits for Σ_{mol} and Σ_{\star} profiles are shown by the black dashed lines in Figure 4.6. We observe a significant correlation between l_{mol} and l_{\star} for main sequence and green valley galaxies (blue and green circles; Pearson $r_p = 0.6$; p -value < 0.01). When we compute an ordinary least-square (OLS; blue solid line in Fig. 4.8) bisector fit for the model $y = \alpha x$ for main sequence galaxies with at least 5σ l_{mol} measurements (symbols with enhanced color in Fig. 4.8), we obtain $l_{\text{mol}} = (1.24 \pm 0.05) \times l_{\star}$. We test how this relation varies with angular resolution by fitting the CO radial profiles derived from CO moment 0 maps smoothed at $10''$ beamsize. Although molecular length scales are slightly larger than for stars

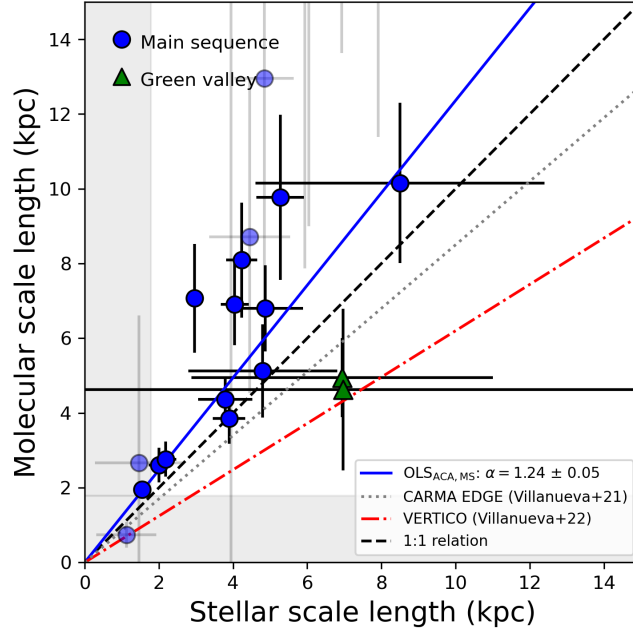


Figure 4.8: Comparison between the stellar, l_* , and molecular, l_{mol} , scale lengths, computed by fitting exponential profiles to the respective surface densities as a function of galactocentric radius. Blue circles and green triangles correspond to 23 ACA EDGE galaxies with $\Sigma_{\text{mol}} > 1 \text{ M}_{\odot} \text{ pc}^{-2}$ for all the annuli within 1 kpc. The blue solid line is the best fit for the model $y = \alpha x$ for main sequence, omitting galaxies with low-quality l_{mol} fits (symbols with pale colors). The gray dotted and orange-dotted lines are the best fit relation for CARMA EDGE [1] and VERTICO [2], respectively. The shaded gray area correspond to the median physical resolution of ACA EDGE galaxies. On average, the figure shows a $\sim 6:5$ relation between the molecular and stellar scale lengths.

$l_{\text{mol}} = (1.15 \pm 0.05) \times l_*$, the best linear relation is still above unity.

While several studies have found a close 1:1 relation between the molecular gas and stars in main sequence star-forming galaxy samples based on galaxies selected from the field (e.g., [108]; BIMA [109]; HERACLES, [30]; CARMA EDGE, [1,3]), quenching mechanisms have the potential to affect the distribution of the molecular gas, atomic gas, and stars in different ways. On the one hand, environmental mechanisms (e.g., ram pressure stripping, galaxy interactions, among others) have been shown to compact the spatial extent of the molecular gas, particularly in high-density environments (e.g., galaxy clusters; [155, 241]). For instance, [2] find a $\sim 3:5$ relation for the molecular and stellar scale lengths in a subsample of 28 Virgo Cluster galaxies selected from VERTICO [6]. On the other hand, intrinsic mechanisms tend to operate either by

removing (e.g., via AGN activity), re-distributing (e.g., via stellar feedback), or depleting (e.g., via starvation) the cold gas reservoirs. Figure 4.6 shows a broad variety of radial profiles that could be explained by a different combination of mechanisms depending on the galaxy quenching stage. The best relation between molecular gas and stellar scale lengths for ACA EDGE main sequence galaxies (blue solid circles in Fig. 4.8) is close to a 6:5 relation. Although this is still consistent with the almost $\sim 1:1$ relation from [1], l_{mol} values for ACA EDGE galaxies are slightly larger when compared to CARMA EDGE spirals. This seems to be a consequence of the lower molecular gas content in the central regions of the former than the latter (as shown by the M_{mol} centroids in upper-right panel of Figure 4.7), producing flatter Σ_{mol} profiles in ACA EDGE galaxies than those for CARMA EDGE.

4.4.2 Spatially resolved relations

4.4.2.1 SFR versus stellar and molecular gas surface densities

The left panel of Figure 4.9 shows Σ_{SFR} versus Σ_{\star} (the so-called resolved SFMS, rSFMS; e.g., [15, 70, 119, 242]), both in units of $M_{\odot} \text{ kpc}^{-2}$ and color-coded by the resolved star formation efficiency of the molecular gas, $\text{SFE}_{\text{mol}} = \Sigma_{\text{SFR}}/\Sigma_{\text{mol}}$. The figure includes pixels from the 30 ACA EDGE galaxies with 5σ global CO detections and $i < 70^{\circ}$. Similarly to §4.4.1, we classify pixels according to the quenching stage of the host galaxy as main sequence (blue contours), green valley (green contours), and red cloud (red contours). Although there is not a remarkable difference in the Σ_{\star} range covered by the main sequence and green valley pixels, there is a mild decrease in Σ_{SFR} from the former ($\log[\Sigma_{\text{SFR}}] \sim -2.7$ dex) to the latter ($\log[\Sigma_{\text{SFR}}] \sim -3.0$ dex). However, red cloud pixels have the lowest SFR of all groups. To compare our results

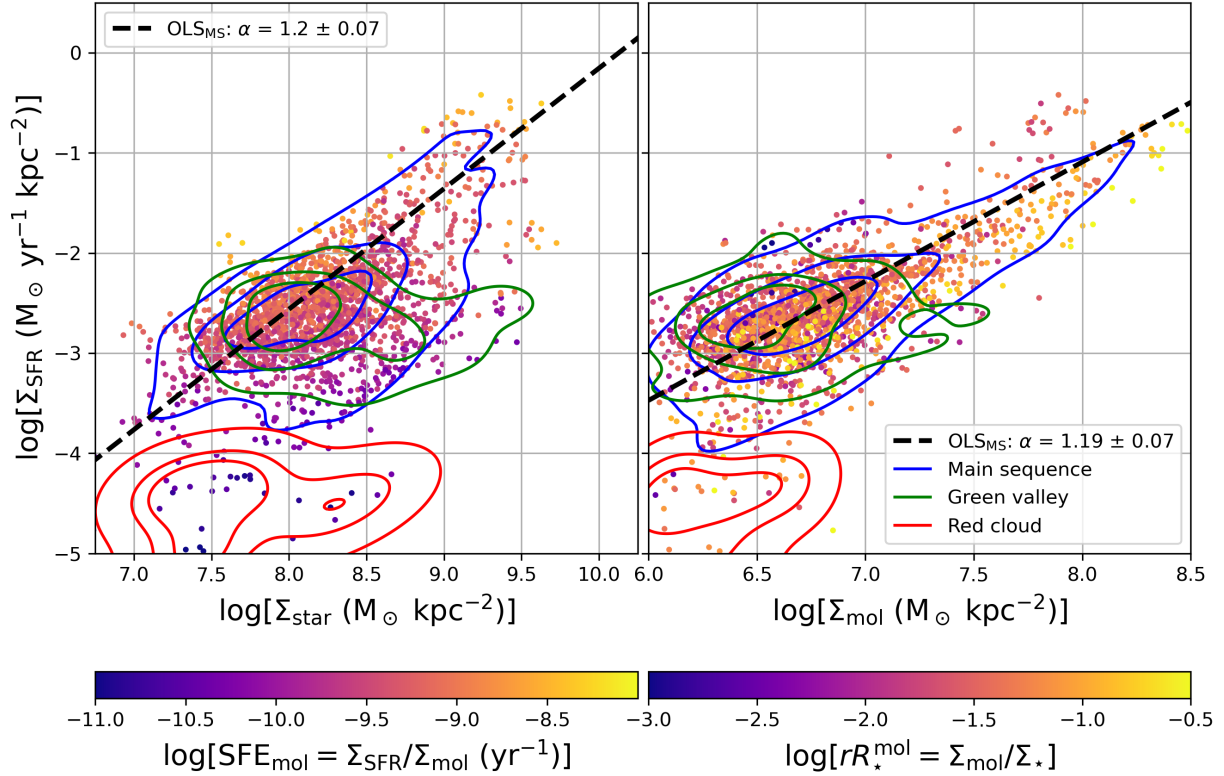


Figure 4.9: *Left*: SFR surface density, Σ_{SFR} , versus stellar surface density, Σ_{\star} , color-coded by the resolved star formation efficiency of the molecular gas, $\text{SFE} = \Sigma_{\text{SFR}}/\Sigma_{\text{mol}}$, for pixels with 5σ CO detections and selected from the 30 galaxies included in Figure 4.6. Blue and green density contours are 90%, 60%, and 30% of the points for main sequence and green valley galaxies. *Right*: The resolved SFR- M_{mol} relation, color-coded by the resolved molecular-to-stellar mass gas fraction, $rR_{\star}^{\text{mol}} = \Sigma_{\text{mol}}/\Sigma_{\star}$. Conventions are as in left panel. The black dashed lines corresponds to the OLS bisector fit for main sequence galaxies using the model $y = \alpha x + \beta$ for the resolved SFMS (left) and the resolved Kennicutt-Schmidt (right) relations. While the left panel exhibits an increasing in Σ_{\star} for pixels transiting from the main sequence to the green valley, the right panel shows that pixels from these two populations cover a similar parameter space although with a mild decreasing in Σ_{SFR} . This suggests that changes in star formation activity during the transition are driven not only by a lowering in the molecular gas, but also due to a decrease of the star formation efficiency.

with previous studies, we compute an OLS bisector fit for main sequence pixels using the model

$y = \alpha x + \beta$; we obtain $\log[\Sigma_{\text{SFR}}] = (1.20 \pm 0.07) \times \log[\Sigma_{\star}] - (12.18 \pm 0.60)$ (dashed black

line in left panel of Fig. 4.9). Our rSFMS best-fit slope, α_{rSFMS} , is slightly higher than those

for CARMA EDGE ($\alpha_{\text{rSFMS}} \approx 1.01$; [3]), PHANGS ($\alpha_{\text{rSFMS}} \approx 1.04$; [191]), and other galaxy

sample (see [243] and references therein). However, our results are consistent with the val-

ues found in several studies based on galaxy samples similar to ACA EDGE (e.g. [70]). For

instance, [242] analyze the rSFMS properties of $\sim 15,000$ spaxels in a sample of 29 galaxies selected from the ALMA-MaNGA QUEnching and STar formation (ALMaQUEST) survey [244]. Covering the same range of stellar masses, ALMaQUEST was designed to investigate the star-formation activity in galaxies from the green valley to the starburst regime, complementing surveys with a better representation of galaxy properties in the local Universe (e.g., CARMA EDGE). Implementing an orthogonal distance regression (ODR) fit for the rSFMS, [242] find $\log[\Sigma_{\text{SFR}}] = (1.37 \pm 0.01) \times \log[\Sigma_{\star}] - (13.12 \pm 0.10)$, thus resulting in a steeper rSFMS slope (clearly above unity) for high stellar mass galaxies.

Similarly to the rSFMS, the widely-studied resolved Kennicutt-Schmidt relation (rKS; e.g., [12, 19, 30, 78, 191, 245, 246]) presents a complementary way to investigate how the SFR depends on the ISM. The right panel of Figure 4.9 contains the rKS relation for ACA EDGE galaxies, color-coded by the resolved molecular-to-stellar mass fraction, $rR_{\star}^{\text{mol}} = \Sigma_{\text{mol}}/\Sigma_{\star}$, and density contours as in the left panel. It is interesting to note that the OLS bisector fit for main sequence galaxies also yields a rKS best-fit slope value, α_{rKS} , above the unity ($\log[\Sigma_{\text{SFR}}] = (1.19 \pm 0.07) \times \log[\Sigma_{\text{mol}}] - (10.62 \pm 0.98)$; dashed black line in right panel of Fig. 4.9). Although our α_{rKS} is higher when compared to that for CARMA EDGE ($\alpha_{\text{rKS}} \approx 1.01$; [3]), PHANGS ($\alpha_{\text{rKS}} \approx 1.03$; [191]), and other galaxy samples from the literature (see [243] and references therein), it is consistent with the ODR fit for ALMaQUEST galaxies ($\log[\Sigma_{\text{SFR}}] = (1.23 \pm 0.01) \times \log[\Sigma_{\text{mol}}] - (10.49 \pm 0.06)$; [242]). We note however that these results are very sensitive to the adopted α_{CO} prescription. For instance, [246] show that different assumptions of the CO-to-H₂ conversion factor can result in $\alpha_{\text{rKS}} = 0.9 - 1.2$, which translates into uncertainties up to 25% in the CO related quantities of PHANGS galaxies. We also observe a systematic decrease in both Σ_{SFR} and Σ_{mol} from the main sequence to the green valley galaxies. In combination with the

results shown in the left panel, this may suggest that although the transition from main sequence to the green valley is primarily driven by gas removal, an increase in Σ_* is also required to alter the ability of the molecular gas to form stars.

4.4.2.2 SFE and bulge properties

To understand which mechanisms may be driving the star-formation quenching in ACA EDGE galaxies, we analyze the impact of bulges on the star formation efficiency of the molecular gas. It is important to mention that SFR estimators derived from $H\alpha$ have to be taken carefully since they are susceptible to contamination due to AGN activity, jets, shocks and post-Asymptotic Giant Branch stars [9]. To perform our analysis only on star-forming pixels, we have used the nuclear activity of CALIFA galaxies from [4] (column 5 in Table 4.2), who classify galaxies according to the emission-line diagnostic of the optical nucleus in star-forming (SF), AGN, and LINER-type galaxies. We complement the AGN classification using [9], who group CALIFA galaxies as Type-I (galaxies with a broad $H\alpha$ width, i.e. $\text{FWHM} > 1000 \text{ km s}^{-1}$) or Type-II (galaxies above the [247] line on the BPT diagram and $H\alpha$ line width $> 3\text{\AA}$) AGNs. Although galaxies may host an AGN and actively form stars, we classify galaxies as SF if no nuclear activity is detected. We adopt this since we do not see significant variations between the results for only confirmed SF galaxies and SF+not-detected nuclear activity galaxies.

The top panel of Figure 4.10 shows the resolved SFE_{mol} as a function of galactocentric radius (in units of r_{25}), color-coded by the quenching stage of the host galaxy, for SF-pixels within R_b . The figure also includes the SFE_{mol} pixels within the centers (including bulge and nucleus) of PHANGS-ALMA galaxies drawn from [229] (black crosses), which complement well the pa-

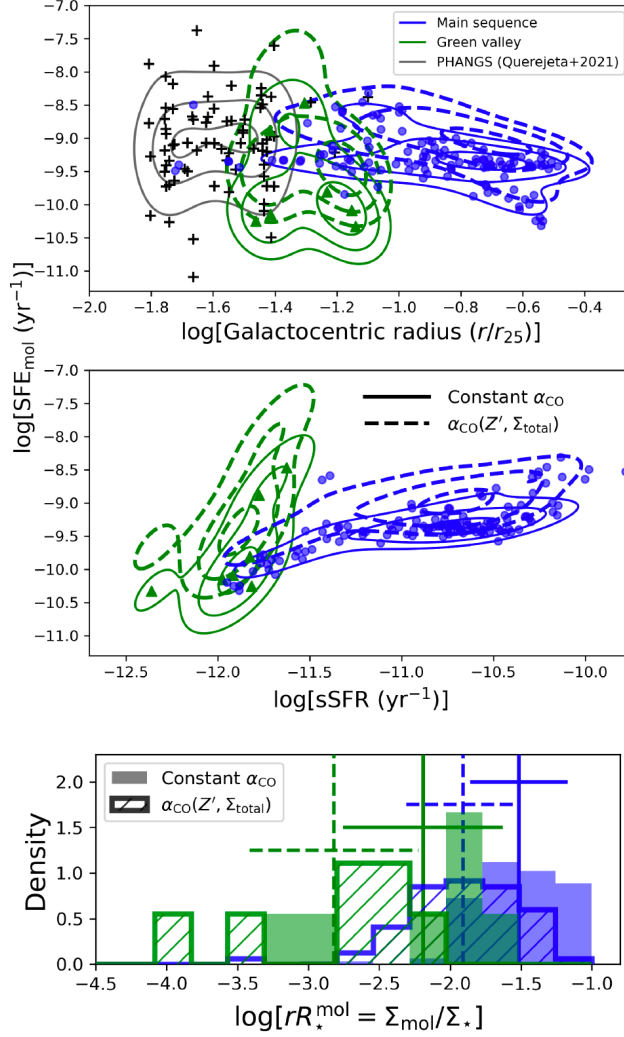


Figure 4.10: *Top:* The resolved SFE_{mol} versus galactocentric radius for SF pixels within R_b , color-coded by quenching stage. Black crosses are pixels drawn for PHANGS-ALMA spirals. Solid blue and green lines correspond to 90%, 60%, and 30% density contours of main sequence and green valley pixels, respectively. Dashed lines are density contours for pixels when adopting a variable $\alpha_{\text{CO}}(Z', \Sigma_{\text{total}})$ prescription (see Eq. 4.6). *Middle:* The resolved SFE_{mol} versus the resolved specific star formation rate, sSFR, for the same groups as in top panel. *Bottom:* Distribution of the resolved molecular-to-stellar mass fraction, rR_{\star}^{mol} , for main sequence and green valley galaxies included in the upper panel. The vertical and horizontal lines are the mean and the standard deviation values of the distributions, respectively. We note that the spatially resolved SFE_{mol} , sSFR, and rR_{\star}^{mol} within the bulges have a systematic decrease with quenching stage, and these trends seem to not depend on the adopted α_{CO} prescription.

parameter space covered by ACA EDGE pixels at small galactocentric radii. On average, ACA EDGE green valley pixels have lower efficiencies compared to those for PHANGS and ACA EDGE main sequence galaxies, with the two latter covering a similar range of SFE_{mol} . To test how these results depend on the α_{CO} prescription, we compute the SFE_{mol} by adopting a variable

$\alpha_{\text{CO}}(Z', \Sigma_{\text{total}})$ (see Equation 4.6), as shown in the top panel of Figure 4.10 by dashed contours. On average, $\alpha_{\text{CO}}(Z', \Sigma_{\text{total}})$ values are lower than for the fixed prescription at $r \leq 1.5R_e$; consequently, SFE_{mol} are higher when derived from $\alpha_{\text{CO}}(Z', \Sigma_{\text{total}})$. We note that green valley galaxies have a slightly higher increase in the efficiencies than main sequence galaxies (~ 0.3 dex) with the variable α_{CO} , although with the former still having lower SFE_{mol} than the latter. The middle panel of Figure 4.10 shows the SFE_{mol} as a function of the specific star-formation rate, $\text{sSFR} = \Sigma_{\text{SFR}}/\Sigma_{\star}$, for ACA EDGE pixels within the bulge region. We note a systematic increase of the efficiencies with sSFR , going from low SFE_{mol} values for green valley galaxies ($\log[\text{SFE}_{\text{mol}}] \sim -10.3$ and $\log[\text{sSFR}] \sim -12$), to high SFE_{mol} values for main sequence galaxies ($\log[\text{SFE}_{\text{mol}}] \sim -9.3$ and $\log[\text{sSFR}] \sim -10.5$). Even though efficiencies are higher when compared to those derived from the fixed α_{CO} , these tendencies do not change when adopting the variable α_{CO} prescription (as shown by dashed contours in top and middle panels of Figure 4.10). These results are in agreement with several studies reporting lower star formation efficiencies in bulge dominated galaxies (e.g., [124, 240, 248]). For instance, [249] report a decrease in the SFRs with sSFR within bulges of CALIFA galaxies at any M_{\star} . [250] also find a clear correlation between the star formation efficiency and sSFR in galaxies without prominent bulges and with the same morphological type. In addition, they note a strong connection between massive bulges and low SFE.

Are the differences in SFE_{mol} between main sequence and green valley bulges primarily driven by gas depletion/removal? To test this, we compute the resolved molecular-to-stellar mass fraction, $rR_{\star}^{\text{mol}} = \Sigma_{\text{mol}}/\Sigma_{\star}$, for pixels within the bulge region from these two groups. The bottom panel of Figure 4.10 shows the distribution of rR_{\star}^{mol} of pixels within bulges and adopting the fixed (hatched histograms) and variable (solid histograms) α_{CO} prescriptions. On average,

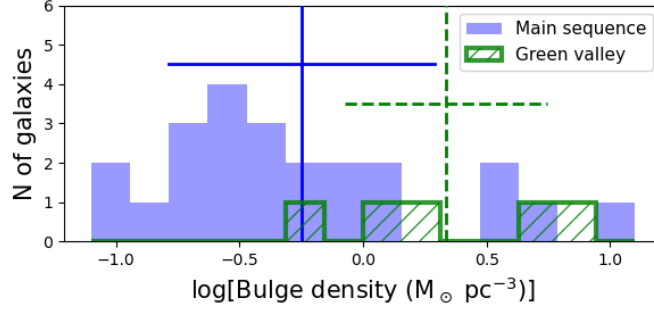


Figure 4.11: Distributions of the bulge density (in units of $M_{\odot} \text{pc}^{-3}$), for the 23 main sequence and 5 green valley galaxies included in Figure 4.6. The vertical and horizontal lines are the mean and the standard deviation values of the distributions, respectively. Although we do not see a statistically significant difference between green valley and main sequence bulge densities, we note that the former have on average denser bulges than the latter.

rR_{\star}^{mol} values of green valley pixels are ~ 3 times lower than those within main sequence bulges when adopting the fixed α_{CO} . Although we note a displacement to the left of the mean rR_{\star}^{mol} values of the pixel distributions when adopting the variable α_{CO} , the tendencies do not change significantly (rR_{\star}^{mol} values for green valley galaxies are ~ 5 times lower than for main sequence galaxies).

Similarly to the morphological quenching proposed by [139], numerical simulations performed by [203] show that bulges drive turbulence and increase the gas velocity dispersion, σ_{gas} , virial parameter, and turbulent pressure, P_{turb} , towards the galaxy centers. They note that the more compact and more massive (therefore, the more dense) the bulges are, then the higher the level of turbulence. The star-formation activity is, therefore, “dynamically suppressed” in the innermost parts of bulge-dominant galaxies due to an increase of the gas turbulence that prevents the gravitational instabilities. Figure 4.11 shows the distribution of the bulge density, ρ_{b} , for main sequence and green valley galaxies. To compute ρ_{b} , we assume an spheroidal distribution of the bulge, i.e. we use $\rho_{\text{b}} = M_{\text{b}} / (\frac{4}{3}\pi R_{\text{b}}^3)$. Although with a poor representation of green valley galaxies, Figure 4.11 shows that, on average, green valley bulges tend to be more dense than those for

main sequence galaxies. These results suggest that, when compared to main sequence pixels, the lower SFE_{mol} values within green valley bulges are not just a consequence of a poor molecular gas content. In addition, dynamical suppression may be reducing the star-formation rate in these regions due to an increase in Σ_{\star} with quenching stage (green valley bulges are ~ 3 times more dense than for main sequence galaxies).

4.4.2.3 What drives star-formation quenching in ACA EDGE galaxies?

The six panels in Figure 4.12 show the resolved SFE_{mol} (top panels), rR_{\star}^{mol} (middle panels), and the specific star formation rate, $\text{sSFR} = \Sigma_{\text{SFR}}/\Sigma_{\star}$ (bottom panels), versus galactocentric radius (in radial bins of $0.3R_e$, ~ 1.5 kpc resolution at the mean distance) for the 30 galaxies included in Figure 4.6. In order to better understand the different mechanisms behind star-formation quenching in ACA EDGE galaxies, we split the panels of Figure 4.12 into two groups. Panels A, C, and E include SF galaxies (hereafter no nuclear activity galaxies, NNA; i.e., pixels from galaxies without LINER/AGN activity), split by their quenching stage (i.e., main sequence, green valley, and red cloud). Panels B, D, and F include pixels from NNA, LINER, and AGN galaxies (shaded purple, orange, and yellow regions, respectively), according to their nuclear activity (column 5 in Table 4.2).

On average, the SFE_{mol} remains almost constant with radius for NNA main sequence, green valley, and red cloud galaxies (panel A). These results are consistent with [1]; while they do not observe significant variations of SFE_{mol} with radius in the CARMA EDGE sample, they also note a systematic decrease in the efficiencies from late- to early-type galaxies. In addition, panel A shows that green valley galaxies have a mild increase in SFE_{mol} with radius. While main

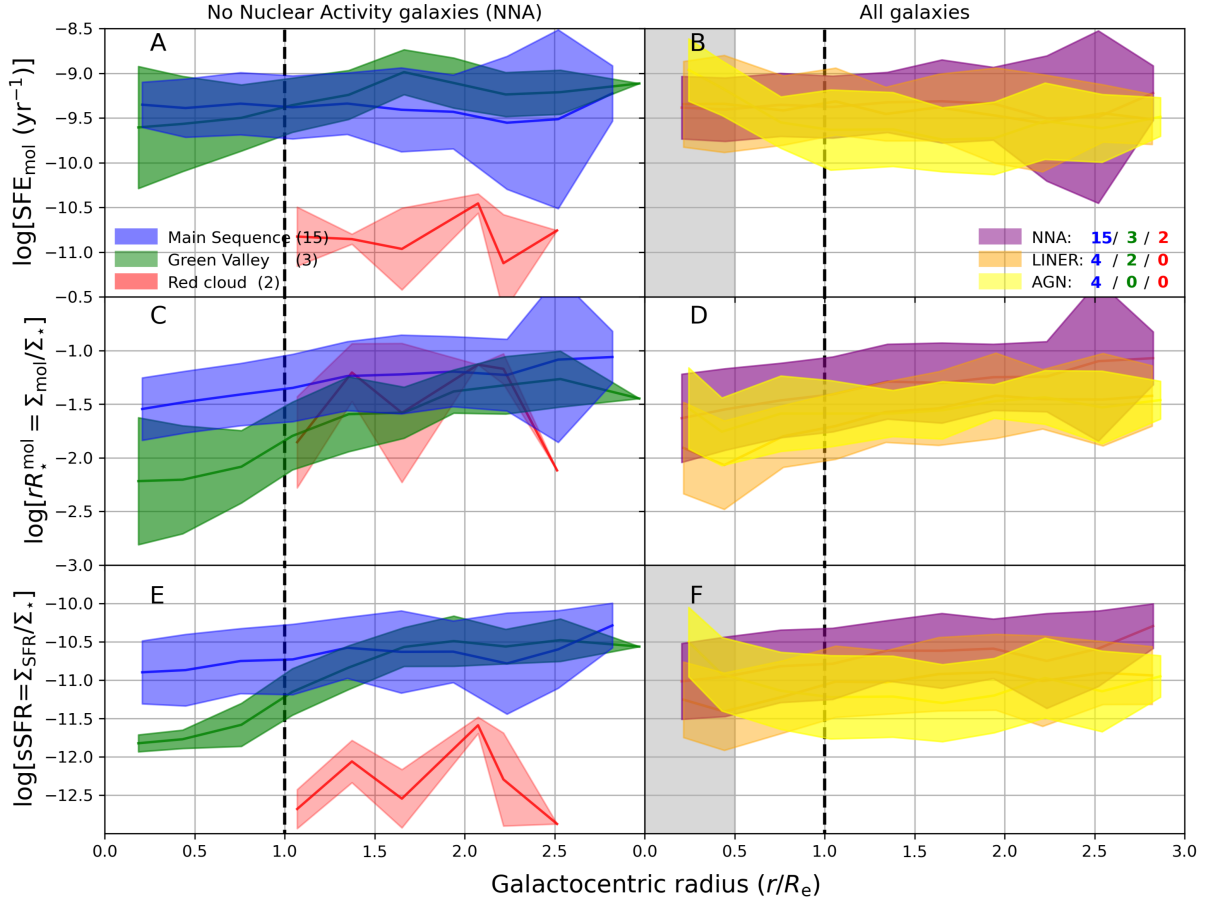


Figure 4.12: The resolved star formation efficiency of the molecular gas, $\text{SFE}_{\text{mol}} = \Sigma_{\text{SFR}}/\Sigma_{\text{mol}}$ (panels A and B), the resolved molecular-to-stellar mass fraction, $rR_*^{\text{mol}} = \Sigma_{\text{mol}}/\Sigma_*$ (panels C and D), and the specific star formation rate, $\text{sSFR} = \Sigma_{\text{SFR}}/\Sigma_*$ (panels E and F), in radial bins of $0.3R_e$ (~ 1.5 kpc) versus galactocentric radius for pixels from the 30 galaxies included in Figure 4.6. The figure is color-coded according to the three main groups. Panels A, C, and E encompass pixels from 20 galaxies classified as SF (or with No Nuclear Activity, NNA; see column 5 in Table 4.2), split by their quenching stage (i.e., main sequence, green valley, and red cloud) of the host galaxy. Panels B, D, and F include pixels from 30 ACA EDGE galaxies grouped according to the nuclear activity of the host galaxy. The grey shaded areas correspond to the regions where our $\text{H}\alpha$ -based SFR estimator is susceptible to AGN/LINER contamination, so SFR and quantities related are only taken as upper-limits. In all panels, the vertical extent of the shaded areas is the 1σ scatter distribution for any group. Also, the vertical black dashed lines are located at $r = R_e$, which we use to divide galaxy regions in central and disk pixels. While efficiencies in main sequence galaxies remain almost constant with galactocentric radius, in green valley galaxies we note a systematic increase of SFE_{mol} , rR_*^{mol} , and sSFR , with increasing radius. We also observe slightly higher SFE_{mol} in the regions near the centers ($0.5R_e \leq r \leq 1.2R_e$) of AGNs when compared to their outskirts.

sequences and green valley galaxies have similar rR_*^{mol} for $r \geq 1.8R_e$ (see panel C), the latter have significantly lower rR_*^{mol} than the former at $r \leq 1.5R_e$. molecular-to-stellar mass fractions for green valley galaxies can reach values even ~ 0.8 dex below than those for main sequence at $r \leq 0.5R_e$. Similarly, sSFR s show almost the same radial trends than that of rR_*^{mol} (see panel

E). The sSFR for green valleys is about an order of magnitude below main sequences (~ 1.2 dex). These results suggest that what is driving the star-formation quenching in green valley galaxies is more related to a decrease of the SFR (e.g., via changes in the stellar potential) rather than gas removal and/or depletion alone.

Similar to panel A of Figure 4.12, panel B shows that NNA galaxies (mostly dominated by the main sequence) have on average flat SFE_{mol} profiles. Although both LINER and AGN galaxies have remarkably high efficiencies in the central regions ($r \leq 0.5R_e$; grey shaded area in panels B and F), these values have to be considered carefully due to LINER/AGN contamination (as explained in §4.4.2.2). Consequently, SFE_{mol} (and quantities related) must be considered only as upper-limits for these two groups within this region. While LINERs and SFs show a flat SFE_{mol} profile for $r \geq 0.5R_e$, AGNs seem to have significantly lower the efficiencies in the range $0.75R_e \leq r \leq 2.0R_e$ than LINER/NNA galaxies, which finally flatten down at larger galactocentric radii. When analyzing rR_{\star}^{mol} as a function of galactocentric radius (shown in panel D), we observe a systematic inside-out increase of the molecular fractions for the three groups with radius. However, LINERs/AGNs have rR_{\star}^{mol} values slightly lower than NNA galaxies ($\sim 0.2 - 0.5$ dex below) for the galactocentric radius range covered here. We also note that, on average, sSFR has a similar behaviour as SFE_{mol} , particularly for AGN galaxies which show a slight decrease of the sSFR with radius (similar as the one seen for SFE_{mol}). This may be suggesting that AGN activity mitigates the star formation activity, although not necessarily by impacting the H_2 reservoirs (e.g., [209, 210]).

Our results are consistent with CALIFA-based studies reporting lower molecular gas fractions in centers of AGN hosting galaxies when compared to their outskirts (e.g., [9, 239, 248]). However, observational evidence has also shown that the gas content in AGN hosts can be

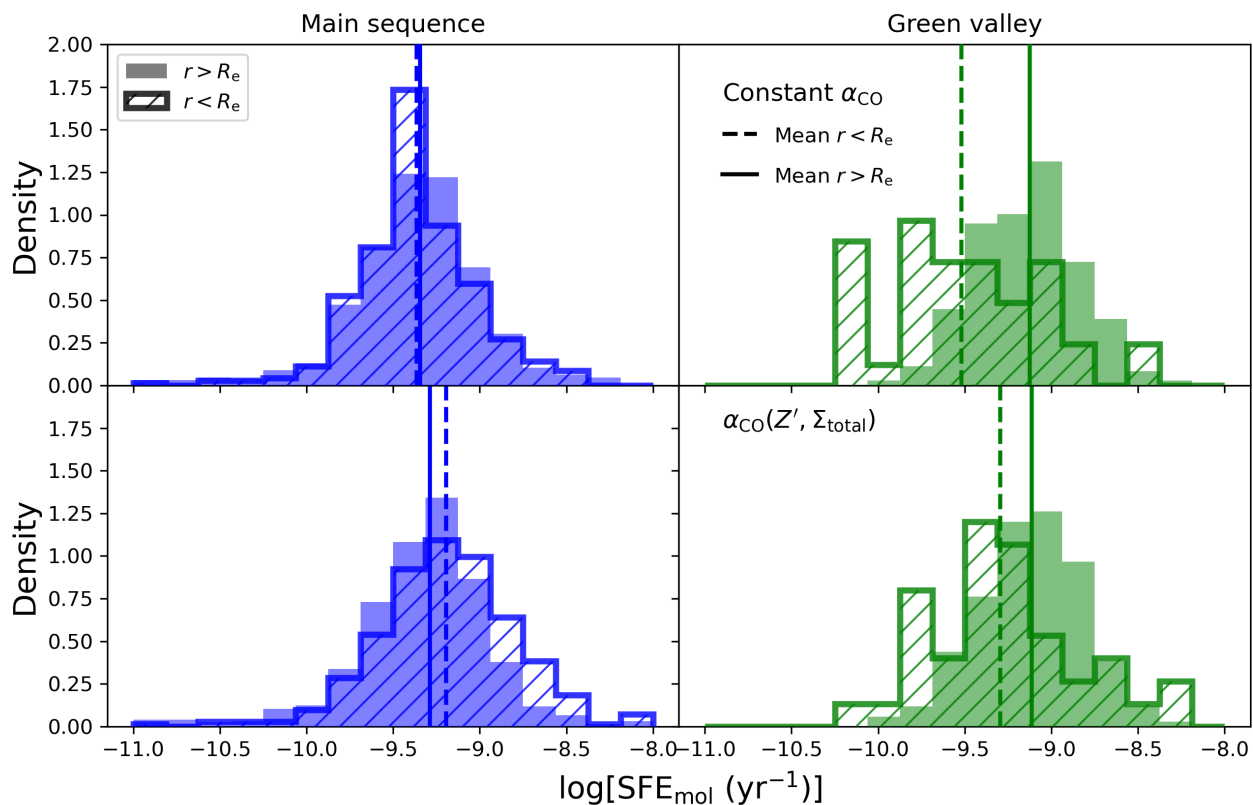


Figure 4.13: SFE_{mol} distributions for pixels from no nuclear activity galaxies (NNA), split in main sequence (blue bars) and green valley (green bars) galaxies (from left to right panels, respectively). The two groups are split by two radial bins according to the breaks identified in Fig. 4.12, thus between pixels within the central (hatched unfilled bars) and outer (solid bars) regions. To compute the SFE_{mol} , we adopt a fixed CO-to- H_2 conversion factor (top panels), and the variable $\alpha_{\text{CO}}(Z', \Sigma_{\text{total}})$ from Equation 4.6 (bottom panels). While the distributions of SFE_{mol} for main sequences pixels within the two radial bins are similar when adopting the two α_{CO} prescriptions, green valleys show a more clear bimodal behaviour when using a constant α_{CO} .

similar (or even higher) than galaxies without nuclear activity, either by analyzing the atomic (e.g., [251–253]), or molecular (e.g., [67, 254–256]) gas reservoirs.

These results suggest that the cessation of the star-formation activity has different modes depending on galaxy substructures, morphological type, and nuclear activity. NNA main sequence and green valley galaxies have SFE_{mol} consistent with local star-forming spirals (e.g., [1, 2]), which on average remain constant with radius. Nevertheless, green valley galaxies show signs of an inside-out increase in their efficiencies. To better understand these differences, we

compute the SFE distributions for NNA galaxies by splitting them in central pixels (i.e., pixels at $r < R_e$) and outer pixels (i.e., pixels at $r > R_e$). We also test how these distributions change with the two α_{CO} prescriptions included in this work (as shown in Figure 4.13). The distribution of SFE_{mol} for main sequence galaxies is almost identical when we split their pixels in two radial bins at $r = R_e$. When adopting the fixed α_{CO} (top panels), green valley and red cloud pixels show a clear bimodal behaviour. We test how the SFE distributions change by using the variable $\alpha_{\text{CO}}(Z', \Sigma_{\text{total}})$ (bottom panels). Interestingly, we note that green valley galaxies show mild bimodal distributions. We perform a Student's t -test to verify if the distribution of SFE_{mol} values in green valley galaxies are drawn from the same parent population. We obtain $|t| = 0.89$ for green valley (degrees of freedom = 222) pixel distributions, which is below the critical t -value $t_{\alpha=0.05} \approx 1.96$; we thus can reject the null hypothesis that the two green valley groups are drawn from the same underlying distribution with 95% confidence. Although these results suggest that morphological quenching may be acting after the gas removal stage in green valley galaxies (e.g., [14]), the small difference between these two distributions may be caused by the poor spatial resolution of our CO observations (~ 1.5 kpc) when compared to the physical scale required to resolve bulges in ACA EDGE galaxies (≤ 500 pc). In addition, some studies (e.g., [206, 207]) have discarded a scenario where bulges play a key role in controlling the star-formation activity, suggesting that this could be reflecting physical processes more associated with galaxy disks.

A similar analysis is shown in Figure 4.14. This figure includes the SFE_{mol} distributions for two radial bins, i.e. for pixels within $r < 1.2R_e$ (hatched histograms) and at $r > 1.2R_e$ (solid histograms), in NNA (purple bars), LINER (orange bars), and AGN (yellow bars) galaxies. We also test how the distributions change with the two α_{CO} prescriptions. To avoid SFR contamination due to AGN/LINER, we reject pixels at $r < 0.5R_e$. While NNA, LINER, and AGN pixels

have similar distributions for the two radial bins and using the fixed α_{CO} (top panels of Fig. 4.14), we note signs of a bimodal behaviour for AGNs when adopting the variable $\alpha_{\text{CO}}(Z', \Sigma_{\text{total}})$ prescription (bottom left panel). We perform a Student's t -test to verify if the AGN distributions are drawn from the same parent population; we obtain $|t| = 1.89$ (degrees of freedom = 140), which is lower than the critical t -value $t_{\alpha=0.05} \approx 1.97$. We thus can reject the null hypothesis that the two AGN groups are drawn from the same underlying distribution. Although SFE_{mol} values for AGNs are consistent with observational evidence showing that optical and radio selected AGNs tend to have similar/lower SFRs than typical main sequence galaxies (e.g., [9, 239, 257]), which appears to be mainly due in SFR within galaxy centers (e.g., [10, 239, 258]), these results could be also supporting the idea of a slightly enhancement of the star formation in these regions. However, studies have shown that the impact of AGN ionization can reach as far out as 10s of kpc (e.g., [259–261]). Although unlikely, the high efficiencies at the centers of ACA EDGE AGNs may thus respond to SFR values still susceptible to AGN contamination, even after excluding pixels at $r < 0.5R_e$.

Morphological quenching has shown to be a good candidate to explain the decrease of the SFE_{mol} observed in green valley ACA EDGE galaxies, perhaps via gas stabilization or dynamical suppression (e.g., [139, 203, 262]), increasing the turbulent velocity dispersion of the gas (e.g., [263]), as a sequence of short lived AGN (e.g., [209, 210]), or a combination of mechanisms. However, the similarity of the SFE distributions shown in the bottom panels of Figures 4.13 and 4.14 (particularly for green valley galaxies) suggest that these processes have a minimal impact on the efficiencies. These mechanisms seem to respond to non long-standing processes and may only complement the gas depletion and/or removal. Further studies based on CO data within galaxy centers with both higher resolution and sensitivity than those presented in this work

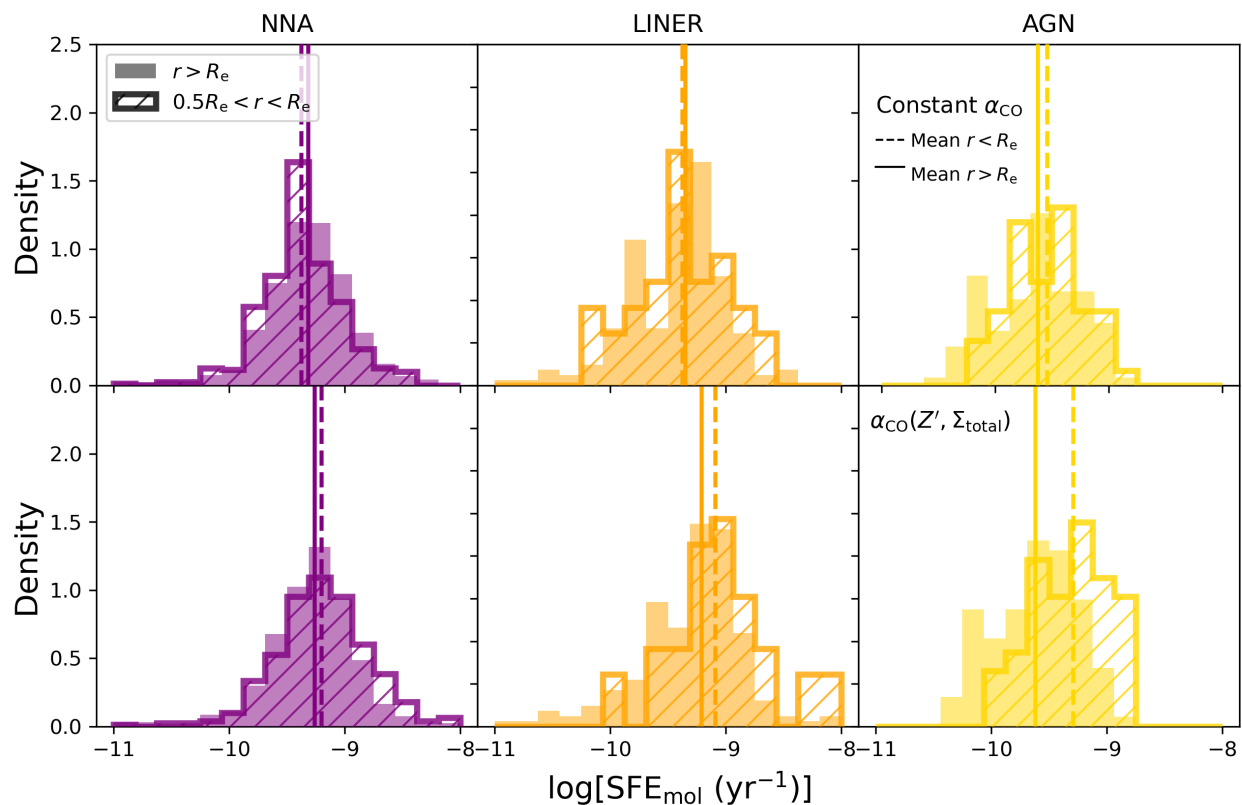


Figure 4.14: SFE_{mol} distributions for pixels from star-forming (i.e., no nuclear activity galaxies, NNA; purple bars), LINER (orange bars), and AGN (yellow bars) galaxies (from left to right panels, respectively). Conventions are as in Fig. 4.13. While NNA and LINER pixels have similar SFE_{mol} distributions for the two radial bins and when testing the two α_{CO} prescriptions, we note a mild bimodal behaviour for AGNs.

(e.g., at physical scales ≤ 500 pc) could give us more information about the dynamical state of the molecular gas within bulges of green valley and red cloud galaxies. These are essential to disentangle the actual connection between the SFE_{mol} and the gravitational stability of the gas, or the effects of AGN in the star-formation activity in detail.

4.5 Summary and conclusions

We present a systematic study of the star formation efficiency and its dependence on other physical parameters in 60 galaxies from the ACA EDGE survey. We analyze $^{12}\text{CO}(J=2-1)$ data

cubes and optical IFU data from CALIFA. Compared to other local galaxy surveys, ACA EDGE is designed to mitigate selection effects based on CO brightness and morphological type. This results in a less biased galaxy survey and an ideal sample to investigate the effects of the star-formation quenching on massive local galaxies. We conduct a detailed analysis to characterize the main properties of the molecular gas by deriving global (e.g., integrated masses and SFRs) and resolved quantities out to typical galactocentric radii of $r \approx 3R_e$. We use a constant Milky Way CO-to-H₂ conversion factor $\alpha_{\text{CO,MW}} = 4.3 \text{ M}_\odot (\text{K km s}^{-1} \text{ pc}^2)^{-1}$ [83] and a Rayleigh-Jeans brightness temperature line ratio of $R_{21} = I_{\text{CO}(2-1)}/I_{\text{CO}(1-0)} \sim 0.65$. We also test the impact of the CO-to-H₂ conversion factor adopted in our results by using the variable $\alpha_{\text{CO}}(Z', \Sigma_{\text{total}})$ from [38]. We conduct a systematic analysis to explore molecular and stellar scale lengths, bulge physical properties, molecular-to-stellar mass fractions, and the SFE of the molecular gas in ACA EDGE galaxies to compare them with the current literature. Our main conclusions are enumerated as follows:

1. We compute the molecular depletion times, τ_{dep} , of ACA EDGE galaxies. Although the majority of galaxies have $\tau_{\text{dep}} \sim 1$ Gyr, we find that molecular depletion times varies significantly with distance of the SFR to the star formation main sequence line, ΔSFMS (i.e., or quenching stage). Classifying galaxies as main sequence ($-0.5 \text{ dex} \leq \Delta\text{SFMS} \leq 0.5 \text{ dex}$), green valley ($-1.0 \text{ dex} < \Delta\text{SFMS} \leq -0.5 \text{ dex}$), and red cloud ($\Delta\text{SFMS} \leq -1.0 \text{ dex}$) galaxies, we note a systematic decrease in the molecular-to-stellar mass fraction, R_\star^{mol} , and an increase in τ_{dep} with quenching stage (see Fig. 4.7).
2. We determine the molecular and stellar exponential disk scale lengths, l_{mol} and l_\star , respectively (see Fig. 4.8). We fit an exponential function to 23 molecular gas surface density,

Σ_{mol} , and 30 stellar surface density, Σ_{\star} , radial profiles from ACA EDGE galaxies with 5σ CO detections and inclinations $< 70^\circ$. We find a close 6:5 relation between l_{mol} and l_{\star} ($l_{\star} = [1.24 \pm 0.05] \times l_{\text{mol}}$), which is consistent with previous results from the literature for main sequence spirals (e.g., HERACLES, CARMA EDGE).

3. We derive the $\Sigma_{\text{SFR}}-\Sigma_{\star}$ and $\Sigma_{\text{SFR}}-\Sigma_{\text{mol}}$ relations, the resolved star formation main sequence (rSFMS) and the resolved Kennicutt-Schmidt (rKS) relations, respectively (see Fig. 4.9). We find slopes of $\alpha_{\text{rSFMS}} = [1.20 \pm 0.07]$ and $\alpha_{\text{rKS}} = [1.19 \pm 0.07]$ for the rSFMS and rKS. Although our slopes are larger than those of spiral star-forming galaxies selected from the field (e.g., CARMA EDGE, PHANGS), they are consistent with those found for early-type red cloud galaxy surveys (e.g., ALMaQUEST). However, we remark that these slopes are very sensitive to the fitting method and the α_{CO} prescription adopted, among others.
4. We compute the resolved star-formation efficiency of the molecular gas, SFE_{mol} , within the bulge region of 23 main sequence and 5 green valley ACA EDGE galaxies. We find that SFE_{mol} values within green valley bulges tend to be lower than for main sequence galaxies. The results suggest that in addition to poor molecular gas content, dynamical suppression may be reducing the star-formation rate in the bulge region of green valley galaxies due to an increasing in Σ_{\star} with quenching stage (see Fig. 4.10).
5. We compute radial profiles for SFE_{mol} , the resolved molecular-to-stellar mass fraction $rR_{\star}^{\text{mol}} = \Sigma_{\text{mol}}/\Sigma_{\star}$, and the resolved specific star formation rate $\text{sSFR} = \Sigma_{\text{SFR}}/\Sigma_{\star}$, for pixels grouped according to their quenching stage and their nuclear activity (see Fig. 4.12). We note a systematic decrease in SFE_{mol} , rR_{\star}^{mol} , and sSFR with quenching stage. We also observe a slightly inside-out decrease in the efficiencies in green valley galaxies up

to $r \approx R_e$; from this point on, SFE_{mol} increases until it reaches similar values than those almost constant for main sequences. Although the efficiencies of green valley galaxy centers are more similar to those of the outer disks when we use the variable $\alpha_{\text{CO}}(Z', \Sigma_{\text{total}})$ prescription, on average their SFE_{mol} distributions show lower efficiencies in their central regions when compared to their outskirts (see Fig. 4.13).

Our results suggest that gas depletion/removal does not completely explain the star-formation quenching processes in ACA EDGE galaxies. Complementary mechanisms (such as morphological quenching and/or AGN feedback) are therefore required to change the physical properties of the molecular gas, which could impact its ability to form stars in galaxies transiting through the green valley. The inside-out nature of these processes is reflected by the decreasing of the SFE_{mol} in the central regions of green valley galaxies, although this change is dependant on the α_{CO} prescription adopted. Future projects should focus on increasing the early-type galaxy coverage to improve the statistical significance of these results. In addition, high resolution CO observations in the central parts of green valley and red cloud galaxies are essential to better understand how these mechanisms may impact the stability of the gas at physical scales comparable to those of molecular clouds (≤ 100 pc).

Chapter 5: Conclusions & Future Work

Throughout this thesis, we have tried to give a general picture about the main factors that affect the star formation activity in galaxies within the local Universe. Based on an holistic approach, we have analyzed our data by implementing a common methodology in order to perform a reliable comparison between galaxies from different samples. Investigating a variety of galaxy samples, which were designed based on morphology, environment, stellar mass, among others, we have been able to reach the following conclusions, summarized in the following subsections:

5.1 About the Star-formation Efficiency in EDGE-CALIFA galaxies

Using CO(1-0) and optical IFU data, we perform a systematic study of the star formation efficiency and its dependence on other physical parameters in 81 galaxies from the EDGE-CALIFA survey. Although EDGE-CALIFA-selected galaxies are mostly far-IR detected and rich in molecular gas, the sample was designed to cover a representation of galaxy morphologies and stellar masses in the local Universe, while at the same time permitting statistically significant results. By analyzing the EDGE-CALIFA survey, we were able to construct a “control” sample to compare with the two other galaxy surveys, VERTICO (Chapter 3) and EDGE ACA (Chapter 4).

As a good representation of the local Universe, we found that the molecular gas and stars in EDGE-CALIFA galaxies are similarly distributed as a function of galactocentric radius in galaxy

disks, with an almost 1:1 relation between the molecular and the stellar scale lengths. As also seen in other local galaxy surveys (e.g. HERACLES), we find that the star-formation efficiency shows a smooth exponential decline with galactocentric radius, with a systematic increase in the average efficiencies from early to late type galaxies. We also note a clear relationship between resolved efficiencies, the star-formation rate, and the dynamical equilibrium pressure, particularly in the innermost regions of galactic disks; these results support a self-regulated scenario in which the star formation acts to restore the pressure balance in active star-forming regions. Finally, under the assumption of a constant velocity dispersion for the gas, we do not find clear correlations between the efficiencies and gravitational instabilities.

Among the main limitations of this study, fixed prescriptions for both the velocity dispersion of the gas and the atomic gas surface density seem to be the most important ones. In addition, it is possible that a larger sample of galaxies may be required to derive more statistically significant results. In this regards, the EDGE-CALIFA survey will keep expanding its galaxy coverage, adding complementary HI and higher angular resolution CO data. Future local galaxy surveys will be incorporated into the EDGE database (e.g. the ACA EDGE survey or the APEX EDGE sample; see Chapter 4), allowing us to attenuate some of these limitations and to extend this analysis to sources that are less bright in CO (e.g., earlier galaxy types), contributing to a more extensive and representative galaxy sample of the local Universe.

5.2 About galaxy cluster environmental effects in VERTICO galaxies

Analyzing $^{12}\text{CO}(J=2-1)$, HI, WISE, and GALEX data, we present a study of the star formation efficiency and its dependence on other physical parameters in 38 galaxies selected from

the VERTICO survey. The VERTICO sample was designed to investigate the impact of quenching processes on late-type galaxies selected from the Virgo cluster and undergoing different environmental mechanisms. Using the control sample constructed in Chapter 2 (which is based mostly on EDGE-CALIFA spirals), we were able to test how the physical properties and quantities related to the molecular gas of VERTICO galaxies compare to those for star-forming field galaxies.

Compared to EDGE-CALIFA spirals, we find that the molecular gas in VERTICO galaxies tends to be more centrally concentrated than the stellar component. Interestingly, galaxies with a stronger degree of perturbation in the atomic gas seem to have more compact CO distribution than those with unaffected HI. We also compute the molecular-to-stellar and atomic-to-stellar ratios as a function of galactocentric radius. We note that while the molecular-to-stellar mass ratio in the central regions of VERTICO galaxies remains almost constant independent of the perturbation level of HI, the atomic-to-stellar mass ratio shows a systematic decrease with increasing HI content. The results suggest that although environmental processes act on the atomic and the molecular gas simultaneously, the atomic gas content is considerably more affected than the molecular gas content. Consequently, the morpho-kinematic HI features of VERTICO galaxies are not a good predictor for their molecular gas content. Additionally, we observe that VERTICO galaxies tend to be decreasingly efficient at converting their molecular gas into stars when their atomic gas is strongly perturbed by environmental effects. Although there is no clear correlation between star formation efficiency within the bulge radius and the mass of the bulge, we observe that galaxies with more centrally concentrated molecular gas tend to be less efficient at converting their H_2 into stars when they host a more massive stellar bulge.

Our study shows that both the molecular and the atomic gas are affected by the Virgo

environment, although in dissimilar ways. While the mechanisms that remove HI in the cluster do not seem to significantly remove molecular gas, they tend to drive the molecular component toward the central regions. Nevertheless, these more centrally concentrated molecular regions with higher molecular-to-atomic ratios exhibit lower molecular star formation efficiencies than observed in field galaxies. It is also possible that the removal of the molecular gas (e.g. by ram pressure stripping acting preferentially in the more diffuse H₂ that is not strongly tied to GMCs) in combination with a simultaneous phase transition from HI-to-H₂ in the inner part of the galaxy triggered by the mechanisms that remove HI.

In addition to increasing the angular resolution of CO and HI observations, more suitable SFR prescriptions might be required to get better constraints on the effects of ram pressure on the star-formation efficiency. On the one hand, CO and HI data at higher angular resolutions would allow us to test the gravitational stability of the gas at physical scales comparable to molecular clouds (~ 100 pc). In this way, we could thus verify if the low efficiencies in central regions of highly HI-perturbed VERTICO galaxies are a result of gas stabilization. On the other hand, gas compression can enhance the SFE_{mol} , particularly for the galaxy face directly affected by ram pressure. Although the VERTICO project has SFR maps based on NUV+WISE3+WISE4, these trace the star formation on timescales > 100 Myr. They are thus not optimal to track variations of the SFE_{mol} on scales of ~ 10 Myr, i.e. those expected during the hydrodynamic interaction of galaxies with the environment suggested by numerical simulations [202]. H α and H β data to derive SFR maps seem to be a more suitable for this purpose. Future projects on VERTICO galaxies should therefore include high resolution HI, CO, and H α -H β data (e.g. VLA, ALMA, VLT) to address –at least at some degree– these limitations.

5.3 About the Star Formation Activity in ACA EDGE galaxies

We introduce the ACA EDGE survey, an extension of the original EDGE-CALIFA sample designed to study the star formation efficiency and its dependence on other physical parameters in 60 massive galaxies from the CALIFA survey. Compared to other local galaxy surveys, ACA EDGE galaxies were chosen to mitigate selection effects based on CO brightness and morphological type. This results in a less biased galaxy survey and an ideal sample to investigate the effects of the star-formation quenching on massive local galaxies. Using Atacama millimeter-submillimeter Compact Array $^{12}\text{CO}(J = 2 - 1)$ and optical IFU data, we conduct a detailed analysis to characterize the main properties of the molecular gas by deriving global (e.g., integrated masses and SFRs) and spatially-resolved quantities.

To test how intrinsic mechanisms affect the star-formation efficiency in galaxies at different evolutionary stages, we classify them according to their distance to the star formation main sequence, with the latter representing the tight correlation between the star-formation rate and the total stellar mass for normal star-forming galaxies. We also compute the molecular gas depletion time (an estimate of the time that a galaxy will continue producing stars until the molecular gas is depleted), and the molecular-to-stellar fraction. Classifying galaxies as main sequence (i.e., normal star-forming galaxies), green valley (i.e., galaxies with mild sign of star-formation quenching), and red sequence (i.e., galaxies with low or null star formation activity), we find that while both main sequence and green valley galaxies have significantly lower molecular-to-stellar fractions than main sequence galaxies, the former show clearly higher depletion times than the former. Compared to EDGE-CALIFA spirals, the molecular gas scale lengths in ACA EDGE main sequence galaxies are slightly higher (although still consistent) and the stellar scale lengths

in ACA EDGE main sequence galaxies. We also compute the resolved star-formation efficiency of the molecular gas within the bulge region of 23 main sequence and 5 green valley ACA EDGE galaxies with low inclinations and detected in CO, finding that the efficiencies within green valley bulges tend to be lower than for main sequence galaxies. Similarly to Chapter 2, we also note a systematic increase in the average efficiencies with quenching stage (i.e., from early- to late-type galaxies). Although the efficiencies of green valley galaxy centers are more similar to those of the outer disks when we use a variable CO-to-H₂ conversion factor, on average they show lower efficiencies in their central regions when compared to their outskirts.

Although with some limitations, our results suggest that gas depletion and/or removal does not completely explain the effects of star-formation quenching processes on ACA EDGE galaxies. Complementary mechanisms (such as morphological quenching) are thus required to change the physical properties of the molecular gas, which could impact its ability to form stars in galaxies transiting through the green valley. The inside-out nature of these processes is reflected by the decrease of the star-formation efficiency in the central regions of green valley galaxies, although the degree in this change depends on the α_{CO} prescription adopted. To mitigate some of the limitations in our analysis, future projects should focus on increasing the early-type galaxy coverage to improve the statistical significance of these results. As mentioned in section of Chapter 4, out of the 145 galaxies originally selected for the ALMA program, only 60 were finally observed. However, the EDGE collaboration has re-submitted new proposals during ALMA Cycle 10 to increase the sample of CO detected green valley and red sequence galaxies. On the one hand, the proposal *The Star Formation Quenching ACA Survey of the Local Universe* proposes ACA CO($J=2-1$) observations of 79 green valley galaxies selected from CALIFA. The selection is based on galaxies with a broad variety of star formation quenching patterns as defined

in [10], indicating different modalities in which quenching happens in galaxies (e.g., classifying galaxies if they are dominated by star formation, centrally quiescent, with quiescent ring-like patterns, mixed effects, or completely quiescent). In a nutshell, the proposal will use ACA to assemble the optimal dataset to answer two main questions: which are the mechanisms that cause galaxies to quench their star formation following exactly these patterns? Does an evolutionary pathway between the quenching stages exist?. On the other hand, the large ALMA program *The Local Universe ALMA Survey* will produce (if accepted) a dataset with ~ 300 pc resolution in 522 galaxies, covering a stellar masses range of $\log[M_*/M_\odot] = 8.5 - 11.5$, and spanning a large volume of the local Universe, thus reducing the cosmic variance. Among other things, the combination of homogeneous ALMA and IFU data from CALIFA will enable us to probe the roles of gas loss, gas stabilization, and AGN in quenching, and testing galaxy evolution models with unparalleled statistical power. Also, we will be able to create the next generation of scaling relations by describing the resolved relation between the SFR, gas, and stellar surface densities as a function of kinematics, star formation history, and stellar properties. In addition, the large amount of proven galaxy environments/morphologies will allow us to perform an extensive benchmarking of baryonic physics in cosmological simulations.

Finally, and summarizing most of the points explored in this section, future high resolution CO observations in the central parts of green valley and red sequence galaxies are essential to understand better how these mechanisms may impact the stability of the gas at physical scales comparable to those of molecular clouds (≤ 100 pc).

5.4 Future projects

As part of my future projects, I will be analyzing ALMA-JWST-HST observations for the [C II] Resolved Ism in STar-forming galaxies with ALma, the CRISTAL¹ project. I will be working on the characterization of the physical conditions within molecular clouds and HII regions using the combination of optical, mid-infrared and submillimeter data at high redshift (i.e., $z = 4-5$). The resulting [C II], $H\alpha$, and IR will be very helpful to quantify the star formation activity and account for the dust extinction in individual regions at different evolutionary stages and cosmological epochs. In particular, I will contribute to the characterization of CRISTAL galaxies from two different points of view:

- *Modeling and constraining the kinematics of CRISTAL galaxies:* To first order, galaxies are rotationally supported disk systems. The observed line-of-sight velocity distributions are expected to show a regular rotation pattern in the form of the so-called “spider diagram”, with the position angle (PA) of the minimum and maximum velocities aligned with the optical major axis. Nevertheless, several physical processes can disturb this regular behavior. While kinematic perturbations can be a consequence of external factors (e.g., ram-pressure stripping) or galactic mergers, they can also depart from regular rotation due to internal instabilities induced by their structural components (e.g., bars and spiral arms). It is thus necessary to perform a detailed study of the possible kinematic perturbations in both stars and gas to disentangle perturbations due to internal and external processes. To investigate this, I will perform a modeling of the rotation curves (RC) for the ionized and the stellar gas components. While computing this, we will obtain accurate estimations of

¹<https://www.alma-cristal.info/>

the position angles (PA) of each component, allowing us to carry out a detailed comparison between them and the photometric PAs. Studies have shown that, when compared with non-interacting samples, galaxies currently (or recently) undergoing a merger event are commonly characterized by morpho-kinematic misalignments between the stellar and ionized gas components. CRISTAL galaxies give us a unique opportunity to quantify the fraction of rotating disk systems and compare them with the fraction observed at low-redshift (e.g., CALIFA survey; Barrera-Ballesteros et al. 2015 [264]), therefore verifying if the mechanisms driving the galaxy assembly at early stages of the Universe have evolved with time.

- *Characterizing the distribution and physical conditions of the gas, dust, and stars on kiloparsec scales:* Several studies have shown a close 1:1 relationship between the spatial distribution of the molecular gas and stars in local galaxies selected from the field. However, as we have seen in this thesis, this tight correlation can be affected by intrinsic (e.g., the influence of bulge, bars, spiral arms) or environmental mechanisms (e.g., like those in galaxy clusters). These factors can potentially alter the star-formation efficiency of the available molecular gas, either by boosting the production of star (e.g., due to gas compression or gas funneling) or mitigating the star formation activity (e.g., by stabilization or gas removal). In order to characterize these mechanisms, I will perform an extensive analysis of the distribution of ionized gas, dust, and stars and how they are related to each other by computing the radial profiles of these quantities and computing prompts for the star-formation efficiency. I will obtain length scales for the gas, dust, and stars and compare their relations with those observed at low redshift. I will also verify if the most important

factors altering the star-formation in CRISTAL galaxies match well those affecting galaxies in the local Universe by comparing these results with those already published in my previous work (e.g., EDGE-CALIFA and VERTICO surveys).

These projects will not only further our knowledge on the physical conditions of the ISM appropriate for the star formation activity at kpc scales, but it will also improve the statistics since so far this was only possible in star forming sites within the Local Group. In addition, the data combination in CRISTAL galaxies will help us to understand the different star-formation quenching mechanisms acting at different evolutionary stages of the Universe.

Appendix A: Emission line intensity, velocity, and peak-SNR maps for ACA EDGE galaxies

Figures [A.1](#) to [A.8](#) in this appendix follow the same format as [Figure 4.4](#), and show the products for 53 galaxies included in the ACA EDGE survey.

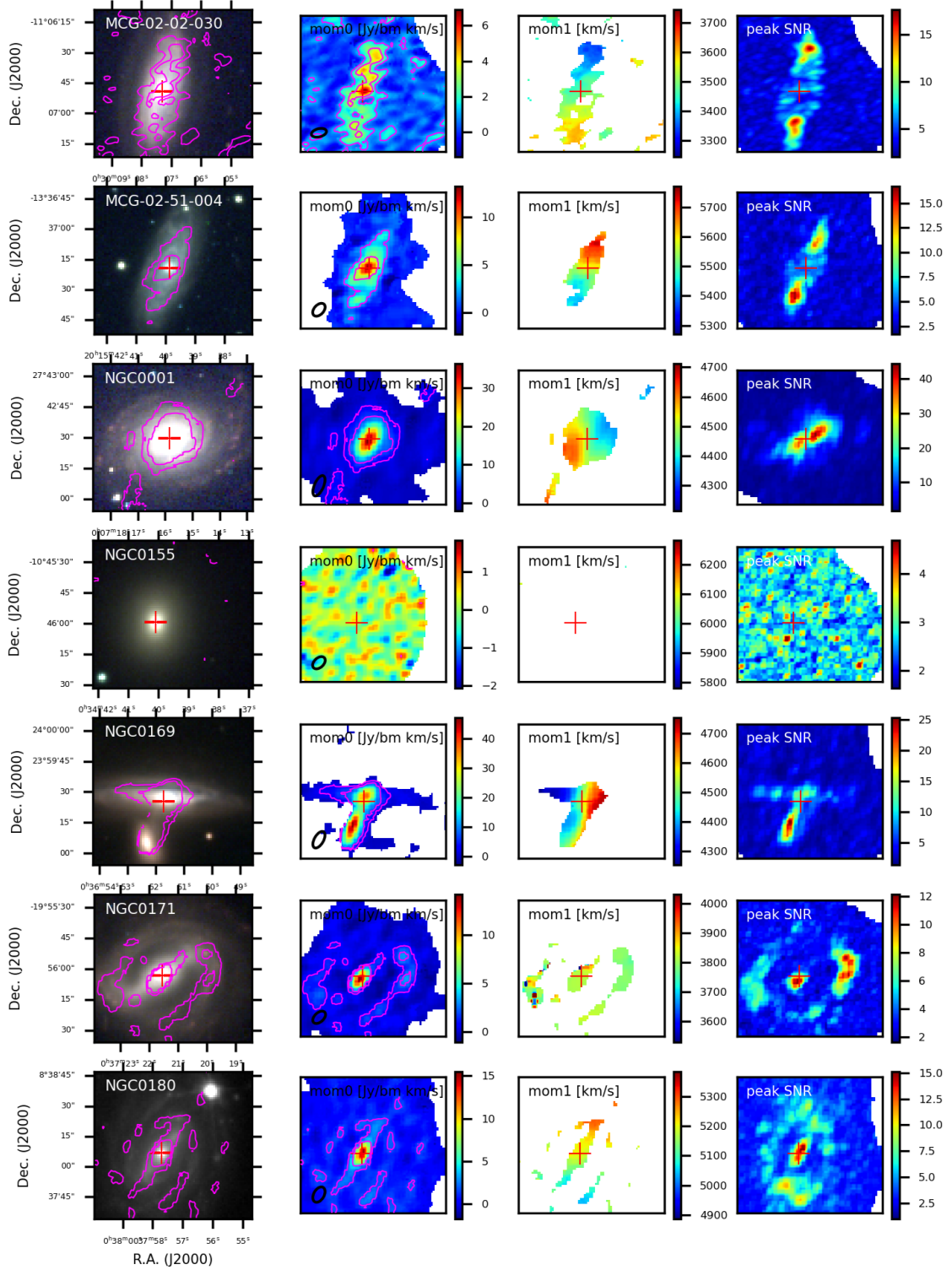


Figure A.1: Images for ACA EDGE galaxies. See caption in Figure 4.4.

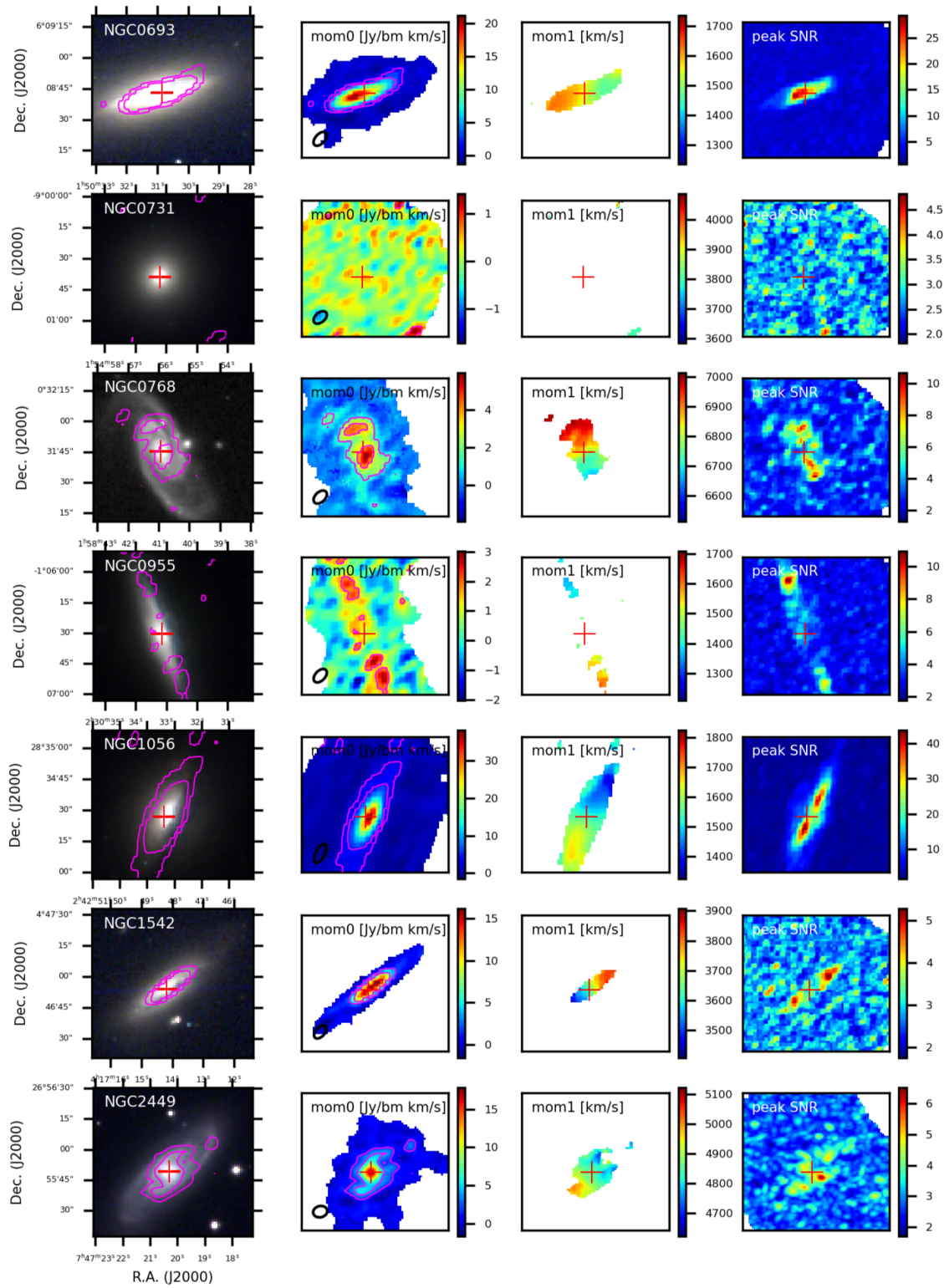


Figure A.2: Images for ACA EDGE galaxies. See caption in Figure 4.4.

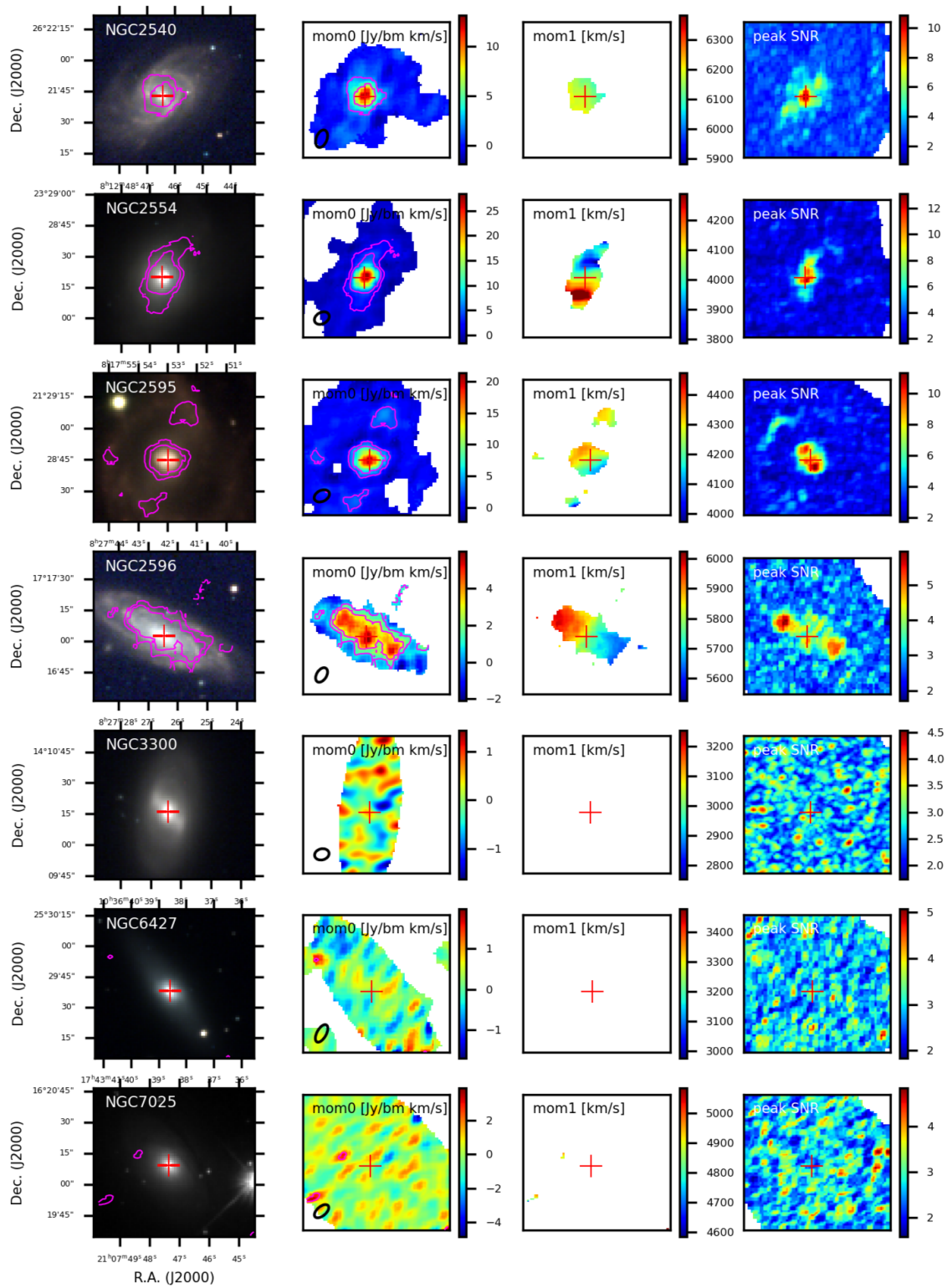


Figure A.3: Images for ACA EDGE galaxies. See caption in Figure 4.4.

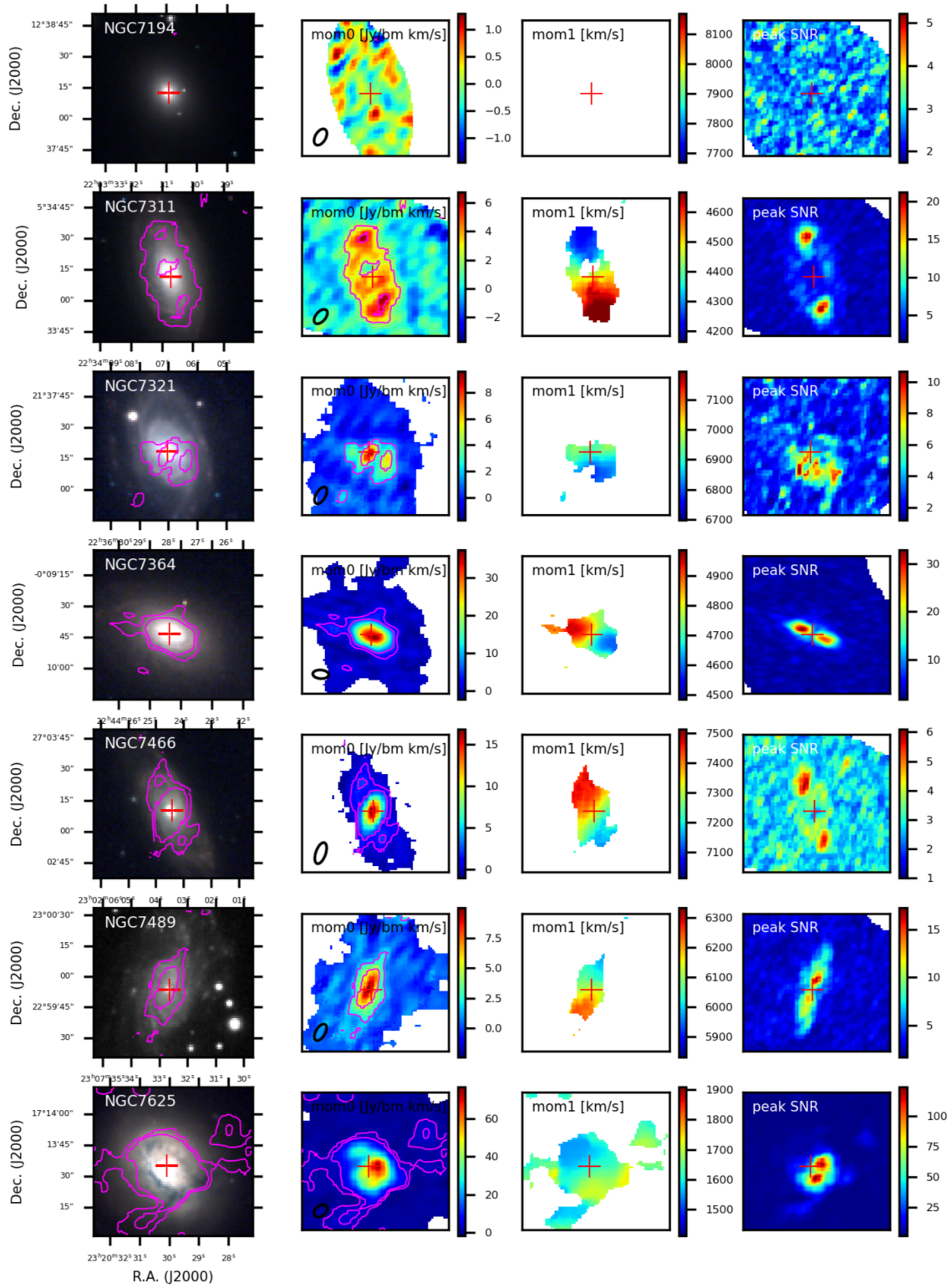


Figure A.4: Images for ACA EDGE galaxies. See caption in Figure 4.4.

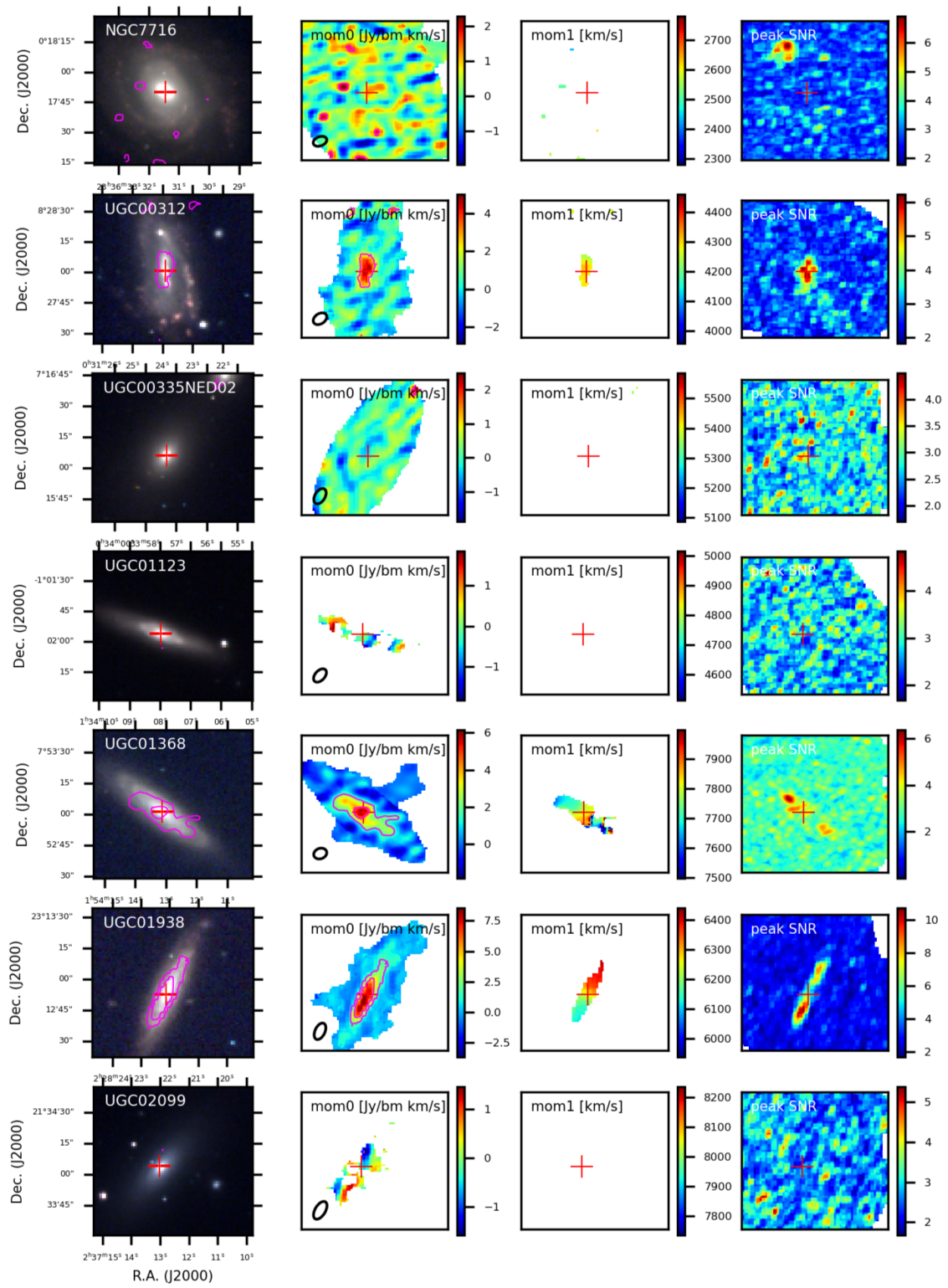


Figure A.5: Images for ACA EDGE galaxies. See caption in Figure 4.4.

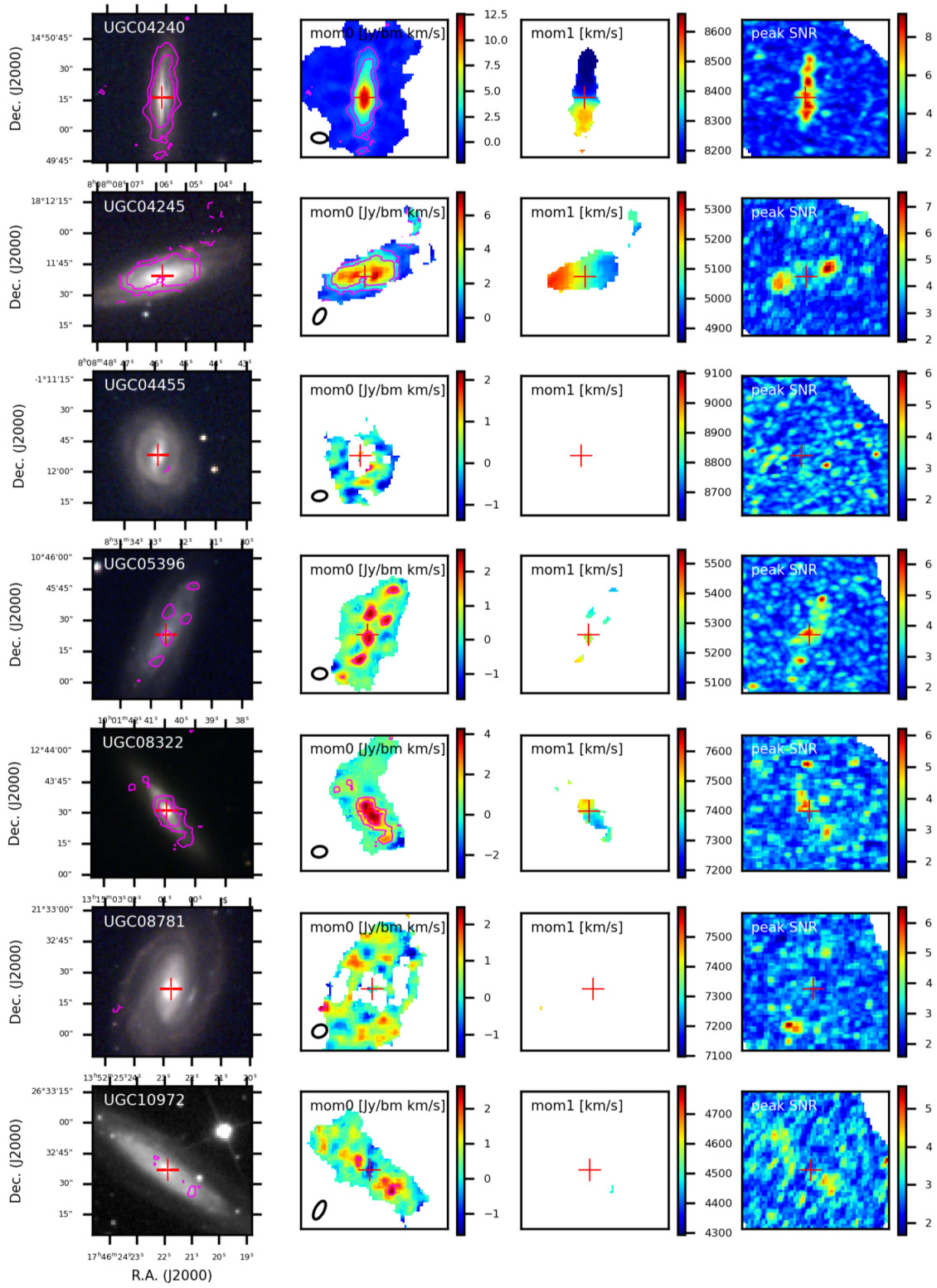


Figure A.6: Images for ACA EDGE galaxies. See caption in Figure 4.4.

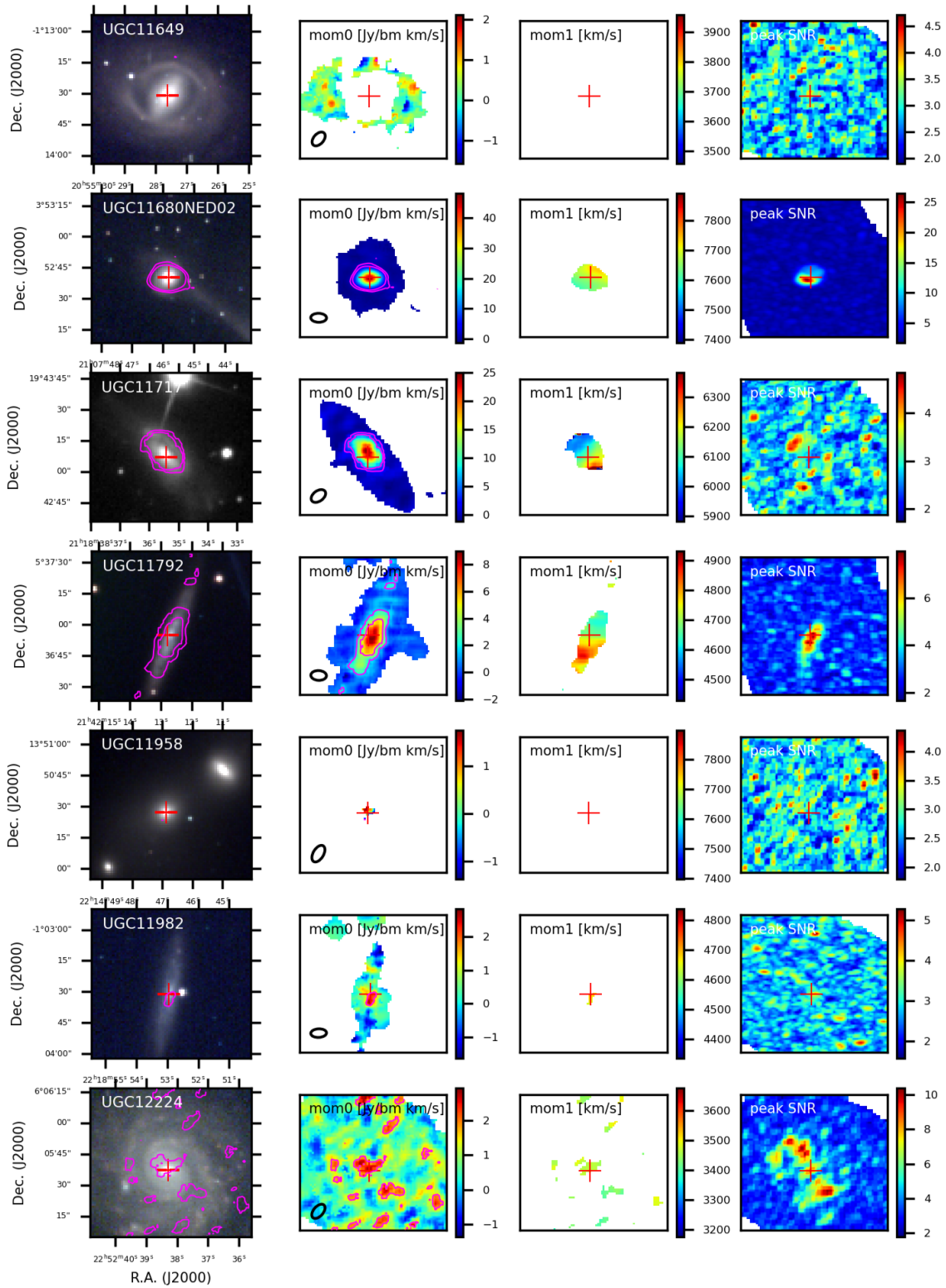


Figure A.7: Images for ACA EDGE galaxies. See caption in Figure 4.4.

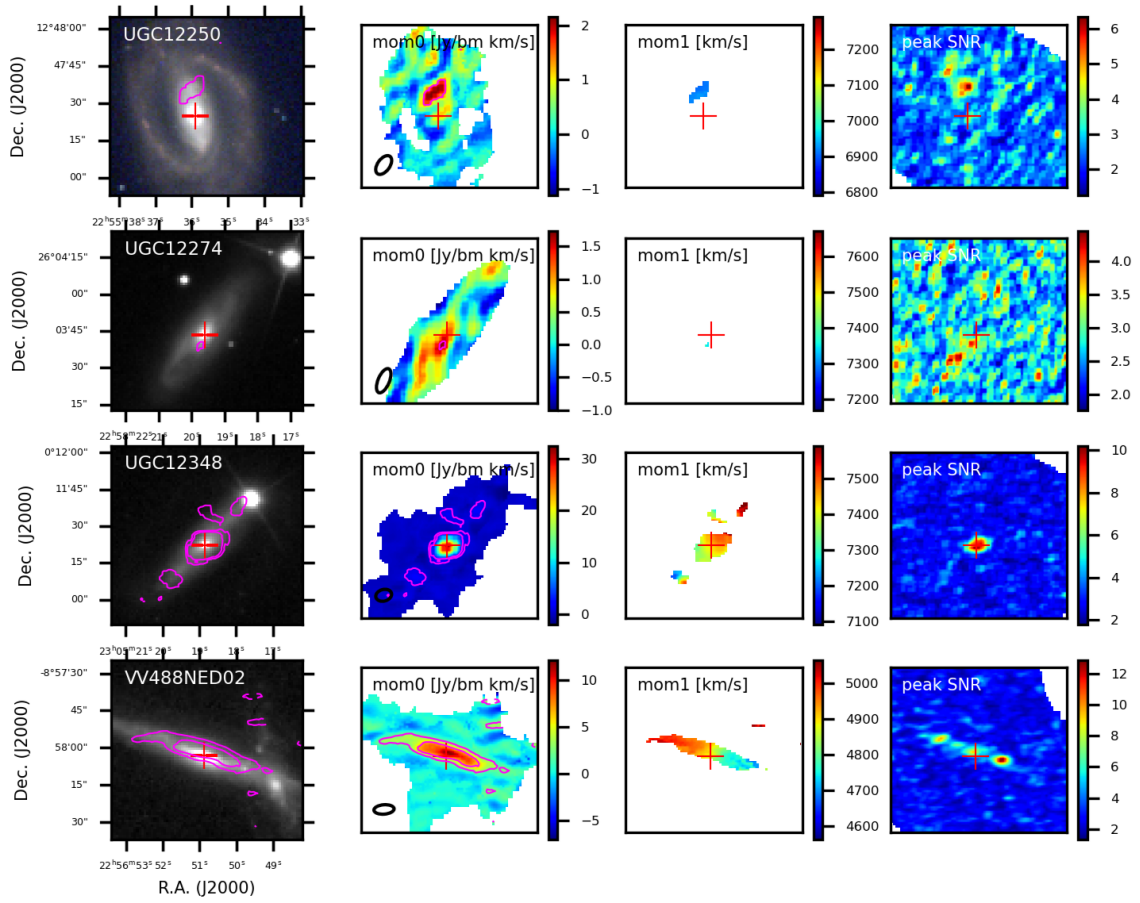


Figure A.8: Images for ACA EDGE galaxies. See caption in Figure 4.4.

Appendix B: Facilities and Software used in this Thesis

B.0.1 Facilities

- ALMA Observatory
- APEX telescope
- Calar Alto Observatory
- CARMA Observatory
- GALEX space telescope
- VLA Observatory
- WISE space telescope

B.0.2 Software

- `astropy` [[265](#)]
- `CASA` [[266](#)]
- `Numpy` [[267](#)]
- `Pipe3D` [[75](#)]

- Scikit-learn [\[268\]](#)
- SciPy [\[269\]](#)
- seaborn [\[270\]](#)

Bibliography

- [1] V. Villanueva, A. Bolatto, S. Vogel, R. C. Levy, S. F. Sánchez, J. Barrera-Ballesteros, T. Wong, E. Rosolowsky, D. Colombo, M. Rubio, Y. Cao, V. Kalinova, A. Leroy, D. Utomo, R. Herrera-Camus, L. Blitz, and Y. Luo. The EDGE-CALIFA Survey: The Resolved Star Formation Efficiency and Local Physical Conditions. *ApJ*, 923(1):60, December 2021.
- [2] Vicente Villanueva, Alberto D. Bolatto, Stuart Vogel, Tobias Brown, Christine D. Wilson, Nikki Zabel, Sara Ellison, Adam R. H. Stevens, María Jesús Jiménez Donaire, Kristine Spekkens, Mallory Tharp, Timothy A. Davis, Laura C. Parker, Ian D. Roberts, Dhruv Basra, Alessandro Boselli, Barbara Catinella, Aeree Chung, Luca Cortese, Bumhyun Lee, and Adam Watts. VERTICO. IV. Environmental Effects on the Gas Distribution and Star Formation Efficiency of Virgo Cluster Spirals. *ApJ*, 940(2):176, December 2022.
- [3] Alberto D. Bolatto, Tony Wong, Dyas Utomo, Leo Blitz, Stuart N. Vogel, Sebastián F. Sánchez, Jorge Barrera-Ballesteros, Yixian Cao, Dario Colombo, Helmut Dannerbauer, Rubén García-Benito, Rodrigo Herrera-Camus, Bernd Husemann, Veselina Kalinova, Adam K. Leroy, Gigi Leung, Rebecca C. Levy, Damián Mast, Eve Ostriker, Erik Rosolowsky, Karin M. Sandstrom, Peter Teuben, Glenn van de Ven, and Fabian Walter. The EDGE-CALIFA Survey: Interferometric Observations of 126 Galaxies with CARMA. *ApJ*, 846(2):159, Sep 2017.
- [4] B. García-Lorenzo, I. Márquez, J. K. Barrera-Ballesteros, J. Masegosa, B. Husemann, J. Falcón-Barroso, M. Lyubenova, S. F. Sánchez, J. Walcher, D. Mast, R. García-Benito, J. Méndez-Abreu, G. van de Ven, K. Spekkens, L. Holmes, A. Monreal-Ibero, A. del Olmo, B. Ziegler, J. Bland-Hawthorn, P. Sánchez-Blázquez, J. Iglesias-Páramo, J. A. L. Aguerri, P. Papaderos, J. M. Gomes, R. A. Marino, R. M. González Delgado, C. Cortijo-Ferrero, A. R. López-Sánchez, S. Bekeraïté, L. Wisotzki, and D. Bomans. Ionized gas kinematics of galaxies in the CALIFA survey. I. Velocity fields, kinematic parameters of the dominant component, and presence of kinematically distinct gaseous systems. *A&A*, 573:A59, January 2015.
- [5] Hyein Yoon, Aeree Chung, Rory Smith, and Yara L. Jaffé. A History of H I Stripping in Virgo: A Phase-space View of VIVA Galaxies. *ApJ*, 838(2):81, April 2017.
- [6] Toby Brown, Christine D. Wilson, Nikki Zabel, Timothy A. Davis, Alessandro Boselli, Aeree Chung, Sara L. Ellison, Claudia D. P. Lagos, Adam R. H. Stevens, Luca Cortese,

- Yannick M. Bahé, Dhruv Bisaria, Alberto D. Bolatto, Claire R. Cashmore, Barbara Catinella, Ryan Chown, Benedikt Diemer, Pascal J. Elahi, Maan H. Hani, María J. Jiménez-Donaire, Bumhyun Lee, Katya Leidig, Angus Mok, Karen Pardos Olsen, Laura C. Parker, Ian D. Roberts, Rory Smith, Kristine Spekkens, Mallory Thorp, Stephanie Tonnesen, Evan Vienneau, Vicente Villanueva, Stuart N. Vogel, James Wadsley, Charlotte Welker, and Hyein Yoon. VERTICO: The Virgo Environment Traced in CO Survey. *ApJ*, 257(2):21, December 2021.
- [7] Amelie Saintonge and Barbara Catinella. The cold interstellar medium of galaxies in the Local Universe. *arXiv e-prints*, page arXiv:2202.00690, February 2022.
- [8] Gerard de Vaucouleurs, Antoinette de Vaucouleurs, Jr. Corwin, Herold G., Ronald J. Buta, Georges Paturel, and Pascal Fouque. *Third Reference Catalogue of Bright Galaxies*. 1991.
- [9] Eduardo A. D. Lacerda, Sebastián F. Sánchez, R. Cid Fernandes, Carlos López-Cobá, Carlos Espinosa-Ponce, and L. Galbany. Galaxies hosting an active galactic nucleus: a view from the CALIFA survey. *MNRAS*, 492(3):3073–3090, March 2020.
- [10] V. Kalinova, D. Colombo, S. F. Sánchez, K. Kodaira, R. García-Benito, R. González Delgado, E. Rosolowsky, and E. A. D. Lacerda. Star formation quenching stages of active and non-active galaxies. *A&A*, 648:A64, April 2021.
- [11] F. F. S. van der Tak, S. C. Madden, P. Roelfsema, L. Armus, M. Baes, J. Bernard-Salas, A. Bolatto, S. Bontemps, C. Bot, C. M. Bradford, and et al. Probing the baryon cycle of galaxies with spica mid- and far-infrared observations. *Publications of the Astronomical Society of Australia*, 35:e002, 2018.
- [12] F. Bigiel, A. Leroy, F. Walter, E. Brinks, W. J. G. de Blok, B. Madore, and M. D. Thornley. The Star Formation Law in Nearby Galaxies on Sub-Kpc Scales. *AJ*, 136(6):2846–2871, Dec 2008.
- [13] S. F. Sánchez, R. C. Kennicutt, A. Gil de Paz, G. van de Ven, J. M. Vílchez, L. Wisotzki, C. J. Walcher, D. Mast, J. A. L. Aguerri, S. Albiol-Pérez, A. Alonso-Herrero, J. Alves, J. Bakos, T. Bartáková, J. Bland-Hawthorn, A. Boselli, D. J. Bomans, A. Castillo-Morales, C. Cortijo-Ferrero, A. de Lorenzo-Cáceres, A. Del Olmo, R. J. Dettmar, A. Díaz, S. Ellis, J. Falcón-Barroso, H. Flores, A. Gallazzi, B. García-Lorenzo, R. González Delgado, N. Gruel, T. Haines, C. Hao, B. Husemann, J. Iglésias-Páramo, K. Jahnke, B. Johnson, B. Jungwiert, V. Kalinova, C. Kehrig, D. Kupko, Á. R. López-Sánchez, M. Lyubenova, R. A. Marino, E. Mármol-Queraltó, I. Márquez, J. Masegosa, S. Meidt, J. Mendez-Abreu, A. Monreal-Ibero, C. Montijo, A. M. Mourão, G. Palacios-Navarro, P. Papaderos, A. Pasquali, R. Peletier, E. Pérez, I. Pérez, A. Quirrenbach, M. Relaño, F. F. Rosales-Ortega, M. M. Roth, T. Ruiz-Lara, P. Sánchez-Blázquez, C. Sengupta, R. Singh, V. Stanishev, S. C. Trager, A. Vazdekis, K. Viironen, V. Wild, S. Zibetti, and B. Ziegler. CALIFA, the Calar Alto Legacy Integral Field Area survey. I. Survey presentation. *A&A*, 538:A8, Feb 2012.
- [14] D. Colombo, S. F. Sanchez, A. D. Bolatto, V. Kalinova, A. Weiß, T. Wong, E. Rosolowsky, S. N. Vogel, J. Barrera-Ballesteros, H. Dannerbauer, Y. Cao, R. C. Levy, D. Utomo, and

- L. Blitz. The EDGE-CALIFA survey: exploring the role of molecular gas on galaxy star formation quenching. *A&A*, 644:A97, December 2020.
- [15] M. Cano-Díaz, S. F. Sánchez, S. Zibetti, Y. Ascasibar, J. Bland-Hawthorn, B. Ziegler, R. M. González Delgado, C. J. Walcher, R. García-Benito, D. Mast, M. A. Mendoza-Pérez, J. Falcón-Barroso, L. Galbany, B. Husemann, C. Kehrig, R. A. Marino, P. Sánchez-Blázquez, C. López-Cobá, Á. R. López-Sánchez, and J. M. Vilchez. Spatially Resolved Star Formation Main Sequence of Galaxies in the CALIFA Survey. *ApJL*, 821(2):L26, April 2016.
- [16] Aeree Chung, J. H. van Gorkom, Jeffrey D. P. Kenney, Hugh Crowl, and Bernd Vollmer. VLA Imaging of Virgo Spirals in Atomic Gas (VIVA). I. The Atlas and the H I Properties. *AJ*, 138(6):1741–1816, December 2009.
- [17] O. Ivy Wong, Jeffrey D. P. Kenney, Eric J. Murphy, and George Helou. The search for shock-excited h2 in virgo spirals experiencing ram pressure stripping. *The Astrophysical Journal*, 783(2):109, feb 2014.
- [18] R. R. Rafikov. The local axisymmetric instability criterion in a thin, rotating, multicomponent disc. *MNRAS*, 323(2):445–452, May 2001.
- [19] María J. Jiménez-Donaire, Toby Brown, Christine D. Wilson, Ian D. Roberts, Nikki Zabel, Sara L. Ellison, Mallory Thorp, Vicente Villanueva, Ryan Chown, Dhruv Bisaria, Alberto D. Bolatto, Alessandro Boselli, Barbara Catinella, Aeree Chung, Luca Cortese, Timothy A. Davis, Claudia D. P. Lagos, Bumhyun Lee, Laura C. Parker, Kristine Spekkens, Adam R. H. Stevens, and Jiayi Sun. VERTICO. III. The Kennicutt-Schmidt relation in Virgo cluster galaxies. *A&A*, 671:A3, March 2023.
- [20] Simona Mei, John P. Blakeslee, Patrick Côté, John L. Tonry, Michael J. West, Laura Ferrarese, Andrés Jordán, Eric W. Peng, André Anthony, and David Merritt. The ACS Virgo Cluster Survey. XIII. SBF Distance Catalog and the Three-dimensional Structure of the Virgo Cluster. *ApJ*, 655(1):144–162, January 2007.
- [21] Benjamin D. Oppenheimer, Romeel Davé, Dušan Kereš, Mark Fardal, Neal Katz, Juna A. Kollmeier, and David H. Weinberg. Feedback and recycled wind accretion: assembling the $z = 0$ galaxy mass function. *MNRAS*, 406(4):2325–2338, August 2010.
- [22] P. Di Matteo, F. Combes, A. L. Melchior, and B. Semelin. Star formation efficiency in galaxy interactions and mergers: a statistical study. *A&A*, 468(1):61–81, June 2007.
- [23] Frédéric Bournaud and Bruce G. Elmegreen. Unstable Disks at High Redshift: Evidence for Smooth Accretion in Galaxy Formation. *ApJL*, 694(2):L158–L161, April 2009.
- [24] D. B. Sanders, N. Z. Scoville, and P. M. Solomon. Giant molecular clouds in the galaxy. II. Characteristics of discrete features. *ApJ*, 289:373–387, February 1985.
- [25] Gerard de Vaucouleurs. Classification and Morphology of External Galaxies. *Handbuch der Physik*, 53:275, January 1959.

- [26] Jr. Kennicutt, Robert C. The Star Formation Law in Galactic Disks. *ApJ*, 344:685, Sep 1989.
- [27] Jr. Kennicutt, Robert C. The Global Schmidt Law in Star-forming Galaxies. *ApJ*, 498(2):541–552, May 1998.
- [28] Tony Wong and Leo Blitz. The Relationship between Gas Content and Star Formation in Molecule-rich Spiral Galaxies. *ApJ*, 569(1):157–183, Apr 2002.
- [29] Jr. Kennicutt, Robert C., Daniela Calzetti, Fabian Walter, George Helou, David J. Hollenbach, Lee Armus, George Bendo, Daniel A. Dale, Bruce T. Draine, Charles W. Engelbracht, Karl D. Gordon, Moire K. M. Prescott, Michael W. Regan, Michele D. Thornley, Caroline Bot, Elias Brinks, Erwin de Blok, Dulia de Mello, Martin Meyer, John Moustakas, Eric J. Murphy, Kartik Sheth, and J. D. T. Smith. Star Formation in NGC 5194 (M51a). II. The Spatially Resolved Star Formation Law. *ApJ*, 671(1):333–348, December 2007.
- [30] Adam K. Leroy, Fabian Walter, Elias Brinks, Frank Bigiel, W. J. G. de Blok, Barry Madore, and M. D. Thornley. The Star Formation Efficiency in Nearby Galaxies: Measuring Where Gas Forms Stars Effectively. *AJ*, 136(6):2782–2845, Dec 2008.
- [31] F. Bigiel, A. K. Leroy, F. Walter, E. Brinks, W. J. G. de Blok, C. Kramer, H. W. Rix, A. Schrubba, K. F. Schuster, A. Usero, and H. W. Wiesemeyer. A Constant Molecular Gas Depletion Time in Nearby Disk Galaxies. *ApJL*, 730(2):L13, April 2011.
- [32] Adam K. Leroy, Fabian Walter, Karin Sandstrom, Andreas Schrubba, Juan-Carlos Munoz-Mateos, Frank Bigiel, Alberto Bolatto, Elias Brinks, W. J. G. de Blok, Sharon Meidt, Hans-Walter Rix, Erik Rosolowsky, Eva Schinnerer, Karl-Friedrich Schuster, and Antonio Usero. Molecular Gas and Star Formation in nearby Disk Galaxies. *AJ*, 146(2):19, August 2013.
- [33] Lisa M. Young, Martin Bureau, Timothy A. Davis, Françoise Combes, Richard M. McDermid, Katherine Alatalo, Leo Blitz, Maxime Bois, Frédéric Bournaud, Michele Cappellari, Roger L. Davies, P. T. de Zeeuw, Eric Emsellem, Sadegh Khochfar, Davor Krajnović, Harald Kuntschner, Pierre-Yves Lablanche, Raffaella Morganti, Thorsten Naab, Tom Oosterloo, Marc Sarzi, Nicholas Scott, Paolo Serra, and Anne-Marie Weijmans. The ATLAS^{3D} project - IV. The molecular gas content of early-type galaxies. *MNRAS*, 414(2):940–967, June 2011.
- [34] Timothy A. Davis, Katherine Alatalo, Marc Sarzi, Martin Bureau, Lisa M. Young, Leo Blitz, Paolo Serra, Alison F. Crocker, Davor Krajnović, Richard M. McDermid, Maxime Bois, Frédéric Bournaud, Michele Cappellari, Roger L. Davies, Pierre-Alain Duc, P. Tim de Zeeuw, Eric Emsellem, Sadegh Khochfar, Harald Kuntschner, Pierre-Yves Lablanche, Raffaella Morganti, Thorsten Naab, Tom Oosterloo, Nicholas Scott, and Anne-Marie Weijmans. The ATLAS^{3D} project - X. On the origin of the molecular and ionized gas in early-type galaxies. *MNRAS*, 417(2):882–899, October 2011.

- [35] Alison Crocker, Melanie Krips, Martin Bureau, Lisa M. Young, Timothy A. Davis, Estelle Bayet, Katherine Alatalo, Leo Blitz, Maxime Bois, Frédéric Bournaud, Michele Cappellari, Roger L. Davies, P. T. de Zeeuw, Pierre-Alain Duc, Eric Emsellem, Sadegh Khochfar, Davor Krajnović, Harald Kuntschner, Pierre-Yves Lablanche, Richard M. McDermid, Raffaella Morganti, Thorsten Naab, Tom Oosterloo, Marc Sarzi, Nicholas Scott, Paolo Serra, and Anne-Marie Weijmans. The ATLAS^{3D} project - XI. Dense molecular gas properties of CO-luminous early-type galaxies. *MNRAS*, 421(2):1298–1314, April 2012.
- [36] Katherine Alatalo, Timothy A. Davis, Martin Bureau, Lisa M. Young, Leo Blitz, Alison F. Crocker, Estelle Bayet, Maxime Bois, Frédéric Bournaud, Michele Cappellari, Roger L. Davies, P. T. de Zeeuw, Pierre-Alain Duc, Eric Emsellem, Sadegh Khochfar, Davor Krajnović, Harald Kuntschner, Pierre-Yves Lablanche, Raffaella Morganti, Richard M. McDermid, Thorsten Naab, Tom Oosterloo, Marc Sarzi, Nicholas Scott, Paolo Serra, and Anne-Marie Weijmans. The ATLAS^{3D} project - XVIII. CARMA CO imaging survey of early-type galaxies. *MNRAS*, 432(3):1796–1844, July 2013.
- [37] Mark R. Krumholz, Christopher F. McKee, and Jason Tumlinson. The Star Formation Law in Atomic and Molecular Gas. *ApJ*, 699(1):850–856, July 2009.
- [38] Alberto D. Bolatto, Mark Wolfire, and Adam K. Leroy. The CO-to-H₂ Conversion Factor. *ARA&A*, 51(1):207–268, August 2013.
- [39] D. C. J. Bock. CARMA: Combined Array for Research in Millimeter-Wave Astronomy. In D. C. Backer, J. M. Moran, and J. L. Turner, editors, *Revealing the Molecular Universe: One Antenna is Never Enough*, volume 356 of *Astronomical Society of the Pacific Conference Series*, page 17, December 2006.
- [40] J. Brinchmann, S. Charlot, S. D. M. White, C. Tremonti, G. Kauffmann, T. Heckman, and J. Brinkmann. The physical properties of star-forming galaxies in the low-redshift Universe. *MNRAS*, 351(4):1151–1179, July 2004.
- [41] E. Daddi, M. Dickinson, G. Morrison, R. Chary, A. Cimatti, D. Elbaz, D. Frayer, A. Renzini, A. Pope, D. M. Alexander, F. E. Bauer, M. Giavalisco, M. Huynh, J. Kurk, and M. Mignoli. Multiwavelength Study of Massive Galaxies at $z \sim 2$. I. Star Formation and Galaxy Growth. *ApJ*, 670(1):156–172, November 2007.
- [42] Katherine E. Whitaker, Pieter G. van Dokkum, Gabriel Brammer, and Marijn Franx. The Star Formation Mass Sequence Out to $z = 2.5$. *ApJL*, 754(2):L29, August 2012.
- [43] Amelie Saintonge, Barbara Catinella, Luca Cortese, Reinhard Genzel, Riccardo Giovanelli, Martha P. Haynes, Steven Janowiecki, Carsten Kramer, Katharina A. Lutz, David Schiminovich, Linda J. Tacconi, Stijn Wuyts, and Gioacchino Accurso. Molecular and atomic gas along and across the main sequence of star-forming galaxies. *MNRAS*, 462(2):1749–1756, October 2016.
- [44] Ying-jie Peng, Simon J. Lilly, Katarina Kovač, Micol Bolzonella, Lucia Pozzetti, Alvio Renzini, Gianni Zamorani, Olivier Ilbert, Christian Knobel, Angela Iovino, Christian Maier, Olga Cucciati, Lidia Tasca, C. Marcella Carollo, John Silverman, Pawel Kampczyk,

- Loic de Ravel, David Sanders, Nicholas Scoville, Thierry Contini, Vincenzo Mainieri, Marco Scodeggio, Jean-Paul Kneib, Olivier Le Fèvre, Sandro Bardelli, Angela Bongiorno, Karina Caputi, Graziano Coppa, Sylvain de la Torre, Paolo Franzetti, Bianca Garilli, Fabrice Lamareille, Jean-Francois Le Borgne, Vincent Le Brun, Marco Mignoli, Enrique Perez Montero, Roser Pello, Elena Ricciardelli, Masayuki Tanaka, Laurence Tresse, Daniela Vergani, Niraj Welikala, Elena Zucca, Pascal Oesch, Umami Abbas, Luke Barnes, Rongmon Bordoloi, Dario Bottini, Alberto Cappi, Paolo Cassata, Andrea Cimatti, Marco Fumana, Gunther Hasinger, Anton Koekemoer, Alexei Leauthaud, Dario Maccagni, Christian Marinoni, Henry McCracken, Pierdomenico Memeo, Baptiste Meneux, Preethi Nair, Cristiano Porciani, Valentina Presotto, and Roberto Scaramella. Mass and Environment as Drivers of Galaxy Evolution in SDSS and zCOSMOS and the Origin of the Schechter Function. *ApJ*, 721(1):193–221, September 2010.
- [45] B. S. Koribalski, L. Staveley-Smith, and V. A. Kilborn et al.. The 1000 Brightest HIPASS Galaxies: HI Properties. *AJ*, 128(1):16–46, July 2004.
- [46] M. J. Meyer, M. A. Zwaan, and R. L. Webster et al.. The HIPASS catalogue - I. Data presentation. *MNRAS*, 350(4):1195–1209, June 2004.
- [47] Jr. Oemler, Augustus. The Systematic Properties of Clusters of Galaxies. Photometry of 15 Clusters. *ApJ*, 194:1–20, November 1974.
- [48] Tomotsugu Goto, Chisato Yamauchi, Yutaka Fujita, Sadanori Okamura, Maki Sekiguchi, Ian Smail, Mariangela Bernardi, and Percy L. Gomez. The morphology-density relation in the Sloan Digital Sky Survey. *MNRAS*, 346(2):601–614, December 2003.
- [49] Daniel Thomas, Claudia Maraston, Kevin Schawinski, Marc Sarzi, and Joseph Silk. Environment and self-regulation in galaxy formation. *MNRAS*, 404(4):1775–1789, June 2010.
- [50] A. Dressler. Galaxy morphology in rich clusters: implications for the formation and evolution of galaxies. *ApJ*, 236:351–365, March 1980.
- [51] Alan Dressler, Jr. Oemler, Augustus, Warrick J. Couch, Ian Smail, Richard S. Ellis, Amy Barger, Harvey Butcher, Bianca M. Poggianti, and Ray M. Sharples. Evolution since $z = 0.5$ of the Morphology-Density Relation for Clusters of Galaxies. *ApJ*, 490(2):577–591, December 1997.
- [52] Avishai Dekel and Yuval Birnboim. Galaxy bimodality due to cold flows and shock heating. *MNRAS*, 368(1):2–20, May 2006.
- [53] Michele Cappellari, Eric Emsellem, Davor Krajnović, Richard M. McDermid, Paolo Serra, Katherine Alatalo, Leo Blitz, Maxime Bois, Frédéric Bournaud, M. Bureau, Roger L. Davies, Timothy A. Davis, P. T. de Zeeuw, Sadegh Khochfar, Harald Kuntschner, Pierre-Yves Lablanche, Raffaella Morganti, Thorsten Naab, Tom Oosterloo, Marc Sarzi, Nicholas Scott, Anne-Marie Weijmans, and Lisa M. Young. The ATLAS^{3D} project - VII. A new look at the morphology of nearby galaxies: the kinematic morphology-density relation. *MNRAS*, 416(3):1680–1696, September 2011.

- [54] Peter Behroozi, Risa H. Wechsler, Andrew P. Hearin, and Charlie Conroy. UNIVERSEMACHINE: The correlation between galaxy growth and dark matter halo assembly from $z = 0-10$. *MNRAS*, 488(3):3143–3194, September 2019.
- [55] Ruby J. Wright, Claudia del P Lagos, Chris Power, Adam R. H. Stevens, Luca Cortese, and Rhys J. J. Poulton. An orbital perspective on the starvation, stripping, and quenching of satellite galaxies in the EAGLE simulations. *MNRAS*, July 2022.
- [56] James E. Gunn and III Gott, J. Richard. On the Infall of Matter Into Clusters of Galaxies and Some Effects on Their Evolution. *ApJ*, 176:1, August 1972.
- [57] A. Boselli, L. Cortese, M. Boquien, S. Boissier, B. Catinella, G. Gavazzi, C. Lagos, and A. Saintonge. Cold gas properties of the Herschel Reference Survey. III. Molecular gas stripping in cluster galaxies. *A&A*, 564:A67, April 2014.
- [58] Robert C. Kennicutt and Neal J. Evans. Star Formation in the Milky Way and Nearby Galaxies. *ARA&A*, 50:531–608, Sep 2012.
- [59] Piero Madau and Mark Dickinson. Cosmic Star-Formation History. *ARA&A*, 52:415–486, Aug 2014.
- [60] Mark G. Wolfire, David Hollenbach, and Christopher F. McKee. The Dark Molecular Gas. *ApJ*, 716(2):1191–1207, June 2010.
- [61] Desika Narayanan, Mark R. Krumholz, Eve C. Ostriker, and Lars Hernquist. A general model for the CO-H₂ conversion factor in galaxies with applications to the star formation law. *MNRAS*, 421(4):3127–3146, April 2012.
- [62] S. J. Lilly, O. Le Fèvre, A. Renzini, G. Zamorani, M. Scodreggio, T. Contini, C. M. Carollo, G. Hasinger, J. P. Kneib, A. Iovino, V. Le Brun, C. Maier, V. Mainieri, M. Mignoli, J. Silverman, L. A. M. Tasca, M. Bolzonella, A. Bongiorno, D. Bottini, P. Capak, K. Caputi, A. Cimatti, O. Cucciati, E. Daddi, R. Feldmann, P. Franzetti, B. Garilli, L. Guzzo, O. Ilbert, P. Kampczyk, K. Kovac, F. Lamareille, A. Leauthaud, J. F. Le Borgne, H. J. McCracken, C. Marinoni, R. Pello, E. Ricciardelli, C. Scarlata, D. Vergani, D. B. Sanders, E. Schinnerer, N. Scoville, Y. Taniguchi, S. Arnouts, H. Aussel, S. Bardelli, M. Brusa, A. Cappi, P. Ciliegi, A. Finoguenov, S. Foucaud, A. Franceschini, C. Halliday, C. Impney, C. Knobel, A. Koekemoer, J. Kurk, D. Maccagni, S. Maddox, B. Marano, G. Marconi, B. Meneux, B. Mobasher, C. Moreau, J. A. Peacock, C. Porciani, L. Pozzetti, R. Scaramella, D. Schiminovich, P. Shopbell, I. Smail, D. Thompson, L. Tresse, G. Vettolani, A. Zanichelli, and E. Zucca. zCOSMOS: A Large VLT/VIMOS Redshift Survey Covering $0 < z < 3$ in the COSMOS Field. *ApJ*, 172(1):70–85, September 2007.
- [63] Shadab Alam, Franco D. Albareti, Carlos Allende Prieto, F. Anders, Scott F. Anderson, Timothy Anderton, Brett H. Andrews, Eric Armengaud, Éric Aubourg, Stephen Bailey, Sarbani Basu, Julian E. Bautista, Rachael L. Beaton, Timothy C. Beers, Chad F. Bender, Andreas A. Berlind, Florian Beutler, Vaishali Bhardwaj, Jonathan C. Bird, Dmitry Bizyaev, Cullen H. Blake, Michael R. Blanton, Michael Blomqvist, John J. Bochanski, Adam S. Bolton, Jo Bovy, A. Shelden Bradley, W. N. Brandt, D. E. Brauer, J. Brinkmann,

Peter J. Brown, Joel R. Brownstein, Angela Burden, Etienne Burtin, Nicolás G. Busca, Zheng Cai, Diego Capozzi, Aurelio Carnero Rosell, Michael A. Carr, Ricardo Carrera, K. C. Chambers, William James Chaplin, Yen-Chi Chen, Cristina Chiappini, S. Drew Chojnowski, Chia-Hsun Chuang, Nicolas Clerc, Johan Comparat, Kevin Covey, Rupert A. C. Croft, Antonio J. Cuesta, Katia Cunha, Luiz N. da Costa, Nicola Da Rio, James R. A. Davenport, Kyle S. Dawson, Nathan De Lee, Timothée Delubac, Rohit Deshpande, Saurav Dhital, Letícia Dutra-Ferreira, Tom Dwelly, Anne Ealet, Garrett L. Ebelke, Edward M. Edmondson, Daniel J. Eisenstein, Tristan Ellsworth, Yvonne Elsworth, Courtney R. Epstein, Michael Eracleous, Stephanie Escoffier, Massimiliano Esposito, Michael L. Evans, Xiaohui Fan, Emma Fernández-Alvar, Diane Feuillet, Nurten Filiz Ak, Hayley Finley, Alexis Finoguenov, Kevin Flaherty, Scott W. Fleming, Andreu Font-Ribera, Jonathan Foster, Peter M. Frinchaboy, J. G. Galbraith-Frew, Rafael A. García, D. A. García-Hernández, Ana E. García Pérez, Patrick Gaulme, Jian Ge, R. Génova-Santos, A. Georgakakis, Luan Ghezzi, Bruce A. Gillespie, Léo Girardi, Daniel Goddard, Satya Gontcho A. Gontcho, Jonay I. González Hernández, Eva K. Grebel, Paul J. Green, Jan Niklas Grieb, Nolan Grieves, James E. Gunn, Hong Guo, Paul Harding, Sten Hasselquist, Suzanne L. Hawley, Michael Hayden, Fred R. Hearty, Saskia Hekker, Shirley Ho, David W. Hogg, Kelly Holley-Bockelmann, Jon A. Holtzman, Klaus Honscheid, Daniel Huber, Joseph Huehnerhoff, Inese I. Ivans, Linhua Jiang, Jennifer A. Johnson, Karen Kinemuchi, David Kirkby, Francisco Kitaura, Mark A. Klaene, Gillian R. Knapp, Jean-Paul Kneib, Xavier P. Koenig, Charles R. Lam, Ting-Wen Lan, Dustin Lang, Pierre Laurent, Jean-Marc Le Goff, Alexie Leauthaud, Khee-Gan Lee, Young Sun Lee, Timothy C. Licquia, Jian Liu, Daniel C. Long, Martín López-Corredoira, Diego Lorenzo-Oliveira, Sara Lucatello, Britt Lundgren, Robert H. Lupton, III Mack, Claude E., Suvrath Mahadevan, Marcio A. G. Maia, Steven R. Majewski, Elena Malanushenko, Viktor Malanushenko, A. Machado, Marc Manera, Qingqing Mao, Claudia Maraston, Robert C. Marchwinski, Daniel Margala, Sarah L. Martell, Marie Martig, Karen L. Masters, Savita Mathur, Cameron K. McBride, Peregrine M. McGehee, Ian D. McGreer, Richard G. McMahan, Brice Ménard, Marie-Luise Menzel, Andrea Merloni, Szabolcs Mészáros, Adam A. Miller, Jordi Miralda-Escudé, Hironao Miyatake, Antonio D. Montero-Dorta, Surhud More, Eric Morganson, Xan Morice-Atkinson, Heather L. Morrison, Benôit Mosser, Demitri Muna, Adam D. Myers, Kirpal Nandra, Jeffrey A. Newman, Mark Neyrinck, Duy Cuong Nguyen, Robert C. Nichol, David L. Nidever, Pasquier Noterdaeme, Sebastián E. Nuza, Julia E. O’Connell, Robert W. O’Connell, Ross O’Connell, Ricardo L. C. Ogando, Matthew D. Olmstead, Audrey E. Oravetz, Daniel J. Oravetz, Keisuke Osumi, Russell Owen, Deborah L. Padgett, Nikhil Padmanabhan, Martin Paegert, Nathalie Palanque-Delabrouille, Kaike Pan, John K. Parejko, Isabelle Pâris, Changbom Park, Petchara Pattarakijwanich, M. Pellejero-Ibanez, Joshua Pepper, Will J. Percival, Ismael Pérez-Fournon, Ignasi P´rez-Ra´fols, Patrick Petitjean, Matthew M. Pieri, Marc H. Pinsonneault, Gustavo F. Porto de Mello, Francisco Prada, Abhishek Prakash, Adrian M. Price-Whelan, Pavlos Protopapas, M. Jordan Raddick, Mubdi Rahman, Beth A. Reid, James Rich, Hans-Walter Rix, Annie C. Robin, Constance M. Rockosi, Thaíse S. Rodrigues, Sergio Rodríguez-Torres, Natalie A. Roe, Ashley J. Ross, Nicholas P. Ross, Graziano Rossi, John J. Ruan, J. A. Rubiño-Martín, Eli S. Rykoff, Salvador Salazar-Albornoz, Mara Salvato, Lado Samushia, Ariel G. Sánchez, Basilio Santiago, Conor Sayres, Ricardo P. Schiavon, David J. Schlegel, Sarah J. Schmidt,

- Donald P. Schneider, Mathias Schultheis, Axel D. Schwope, C. G. Scóccola, Caroline Scott, Kris Sellgren, Hee-Jong Seo, Aldo Serenelli, Neville Shane, Yue Shen, Matthew Shetrone, Yiping Shu, V. Silva Aguirre, Thirupathi Sivarani, M. F. Skrutskie, Anže Slosar, Verne V. Smith, Flávia Sobreira, Diogo Souto, Keivan G. Stassun, Matthias Steinmetz, Dennis Stello, Michael A. Strauss, Alina Streblyanska, Nao Suzuki, Molly E. C. Swanson, Jonathan C. Tan, Jamie Tayar, Ryan C. Terrien, Aniruddha R. Thakar, Daniel Thomas, Neil Thomas, Benjamin A. Thompson, Jeremy L. Tinker, Rita Tojeiro, Nicholas W. Troup, Mariana Vargas-Magaña, Jose A. Vazquez, Licia Verde, Matteo Viel, Nicole P. Vogt, David A. Wake, Ji Wang, Benjamin A. Weaver, David H. Weinberg, Benjamin J. Weiner, Martin White, John C. Wilson, John P. Wisniewski, W. M. Wood-Vasey, Christophe Ye'che, Donald G. York, Nadia L. Zakamska, O. Zamora, Gail Zasowski, Idit Zehavi, Gong-Bo Zhao, Zheng Zheng, Xu Zhou, Zhimin Zhou, Hu Zou, and Guangtun Zhu. The Eleventh and Twelfth Data Releases of the Sloan Digital Sky Survey: Final Data from SDSS-III. *ApJ*, 219(1):12, July 2015.
- [64] E. Wisnioski, N. M. Förster Schreiber, S. Wuyts, E. Wuyts, K. Bandara, D. Wilman, R. Genzel, R. Bender, R. Davies, M. Fossati, P. Lang, J. T. Mendel, A. Beifiori, G. Brammer, J. Chan, M. Fabricius, Y. Fudamoto, S. Kulkarni, J. Kurk, D. Lutz, E. J. Nelson, I. Momcheva, D. Rosario, R. Saglia, S. Seitz, L. J. Tacconi, and P. G. van Dokkum. The KMOS^{3D} Survey: Design, First Results, and the Evolution of Galaxy Kinematics from 0.7 z \leq 2.7. *ApJ*, 799(2):209, February 2015.
- [65] N. M. Förster Schreiber, R. Genzel, N. Bouché, G. Cresci, R. Davies, P. Buschkamp, K. Shapiro, L. J. Tacconi, E. K. S. Hicks, S. Genel, A. E. Shapley, D. K. Erb, C. C. Steidel, D. Lutz, F. Eisenhauer, S. Gillessen, A. Sternberg, A. Renzini, A. Cimatti, E. Daddi, J. Kurk, S. Lilly, X. Kong, M. D. Lehnert, N. Nesvadba, A. Verma, H. McCracken, N. Arimoto, M. Mignoli, and M. Onodera. The SINS Survey: SINFONI Integral Field Spectroscopy of $z \sim 2$ Star-forming Galaxies. *ApJ*, 706(2):1364–1428, December 2009.
- [66] Amélie Saintonge, Guinevere Kauffmann, Jing Wang, Carsten Kramer, Linda J. Tacconi, Christof Buchbender, Barbara Catinella, Javier Graciá-Carpio, Luca Cortese, Silvia Fabbello, Jian Fu, Reinhard Genzel, Riccardo Giovanelli, Qi Guo, Martha P. Haynes, Timothy M. Heckman, Mark R. Krumholz, Jenna Lemonias, Cheng Li, Sean Moran, Nemesio Rodriguez-Fernandez, David Schiminovich, Karl Schuster, and Albrecht Sievers. COLD GASS, an IRAM legacy survey of molecular gas in massive galaxies - II. The non-universality of the molecular gas depletion time-scale. *MNRAS*, 415(1):61–76, July 2011.
- [67] Amélie Saintonge, Barbara Catinella, Linda J. Tacconi, Guinevere Kauffmann, Reinhard Genzel, Luca Cortese, Romeel Davé, Thomas J. Fletcher, Javier Graciá-Carpio, Carsten Kramer, Timothy M. Heckman, Steven Janowiecki, Katharina Lutz, David Rosario, David Schiminovich, Karl Schuster, Jing Wang, Stijn Wuyts, Sanchayeeta Borthakur, Isabella Lamperti, and Guido W. Roberts-Borsani. xCOLD GASS: The Complete IRAM 30 m Legacy Survey of Molecular Gas for Galaxy Evolution Studies. *ApJ*, 233(2):22, December 2017.

- [68] Scott M. Croom, Jon S. Lawrence, Joss Bland-Hawthorn, Julia J. Bryant, Lisa Fogarty, Samuel Richards, Michael Goodwin, Tony Farrell, Stan Miziarski, Ron Heald, D. Heath Jones, Steve Lee, Matthew Colless, Sarah Brough, Andrew M. Hopkins, Amanda E. Bauer, Michael N. Birchall, Simon Ellis, Anthony Horton, Sergio Leon-Saval, Geraint Lewis, Á. R. López-Sánchez, Seong-Sik Min, Christopher Trinh, and Holly Trowland. The Sydney-AAO Multi-object Integral field spectrograph. *MNRAS*, 421(1):872–893, March 2012.
- [69] Kevin Bundy, Matthew A. Bershad, David R. Law, Renbin Yan, Niv Drory, Nicholas MacDonald, David A. Wake, Brian Cherinka, José R. Sánchez-Gallego, Anne-Marie Weijmans, Daniel Thomas, Christy Tremonti, Karen Masters, Lodovico Coccato, Aleksandar M. Diamond-Stanic, Alfonso Aragón-Salamanca, Vladimir Avila-Reese, Carles Badenes, Jesús Falcón-Barroso, Francesco Belfiore, Dmitry Bizyaev, Guillermo A. Blanc, Joss Bland-Hawthorn, Michael R. Blanton, Joel R. Brownstein, Nell Byler, Michele Cappellari, Charlie Conroy, Aaron A. Dutton, Eric Emsellem, James Etherington, Peter M. Frinchaboy, Hai Fu, James E. Gunn, Paul Harding, Evelyn J. Johnston, Guinevere Kauffmann, Karen Kinemuchi, Mark A. Klaene, Johan H. Knapen, Alexie Leauthaud, Cheng Li, Lihwai Lin, Roberto Maiolino, Viktor Malanushenko, Elena Malanushenko, Shude Mao, Claudia Maraston, Richard M. McDermid, Michael R. Merrifield, Robert C. Nichol, Daniel Oravetz, Kaike Pan, John K. Parejko, Sebastian F. Sanchez, David Schlegel, Audrey Simmons, Oliver Steele, Matthias Steinmetz, Karun Thanjavur, Benjamin A. Thompson, Jeremy L. Tinker, Remco C. E. van den Bosch, Kyle B. Westfall, David Wilkinson, Shelley Wright, Ting Xiao, and Kai Zhang. Overview of the SDSS-IV MaNGA Survey: Mapping nearby Galaxies at Apache Point Observatory. *ApJ*, 798(1):7, January 2015.
- [70] Lihwai Lin, Hsi-An Pan, Sara L. Ellison, Francesco Belfiore, Yong Shi, Sebastián F. Sánchez, Bau-Ching Hsieh, Kate Rowlands, S. Ramya, Mallory D. Thorp, Cheng Li, and Roberto Maiolino. The ALMaQUEST Survey: The Molecular Gas Main Sequence and the Origin of the Star-forming Main Sequence. *ApJL*, 884(2):L33, October 2019.
- [71] Adam K. Leroy, Eva Schinnerer, Annie Hughes, Erik Rosolowsky, Jérôme Pety, Andreas Schruba, Antonio Usero, Guillermo A. Blanc, Mélanie Chevance, Eric Emsellem, Christopher M. Faesi, Cinthya N. Herrera, Daizhong Liu, Sharon E. Meidt, Miguel Querejeta, Toshiki Saito, Karin M. Sandstrom, Jiayi Sun, Thomas G. Williams, Gagandeep S. Anand, Ashley T. Barnes, Erica A. Behrens, Francesco Belfiore, Samantha M. Benincasa, Ivana Bešlić, Frank Bigiel, Alberto D. Bolatto, Jakob S. den Brok, Yixian Cao, Rupali Chandar, Jérémy Chastenet, I-Da Chiang, Enrico Congiu, Daniel A. Dale, Sinan Deger, Cosima Eibensteiner, Oleg V. Egorov, Axel García-Rodríguez, Simon C. O. Glover, Kathryn Grasha, Jonathan D. Henshaw, I-Ting Ho, Amanda A. Kepley, Jaeyeon Kim, Ralf S. Klessen, Kathryn Kreckel, Eric W. Koch, J. M. Diederik Kruijssen, Kirsten L. Larson, Janice C. Lee, Laura A. Lopez, Josh Machado, Ness Mayker, Rebecca McElroy, Eric J. Murphy, Eve C. Ostriker, Hsi-An Pan, Ismael Pessa, Johannes Puschig, Alessandro Razza, Patricia Sánchez-Blázquez, Francesco Santoro, Amy Sardone, Fabian Scheuermann, Kazimierz Sliwa, Mattia C. Sormani, Sophia K. Stuber, David A. Thilker, Jordan A. Turner, Dyas Utomo, Elizabeth J. Watkins, and Bradley Whitmore. PHANGS-

ALMA: Arcsecond CO(2-1) Imaging of Nearby Star-Forming Galaxies. *arXiv e-prints*, page arXiv:2104.07739, April 2021.

- [72] Martin M. Roth, Andreas Kelz, Thomas Fechner, Thomas Hahn, Svend-Marian Bauer, Thomas Becker, Petra Böhm, Lise Christensen, Frank Dionies, Jens Paschke, Emil Popow, Dieter Wolter, Jürgen Schmall, Uwe Laux, and Werner Altmann. PMAS: The Potsdam Multi-Aperture Spectrophotometer. I. Design, Manufacture, and Performance. *PASA*, 117(832):620–642, June 2005.
- [73] C. J. Walcher, L. Wisotzki, S. Bekeraité, B. Husemann, J. Iglesias-Páramo, N. Bäckmann, J. Barrera Ballesteros, C. Catalán-Torrecilla, C. Cortijo, A. del Olmo, B. Garcia Lorenzo, J. Falcón-Barroso, L. Jilkova, V. Kalinova, D. Mast, R. A. Marino, J. Méndez-Abreu, A. Pasquali, S. F. Sánchez, S. Trager, S. Zibetti, J. A. L. Aguerri, J. Alves, J. Bland-Hawthorn, A. Boselli, A. Castillo Morales, R. Cid Fernandes, H. Flores, L. Galbany, A. Gallazzi, R. García-Benito, A. Gil de Paz, R. M. González-Delgado, K. Jahnke, B. Jungwiert, C. Kehrig, M. Lyubenova, I. Márquez Perez, J. Masegosa, A. Monreal Ibero, E. Pérez, A. Quirrenbach, F. F. Rosales-Ortega, M. M. Roth, P. Sanchez-Blazquez, K. Spekkens, E. Tundo, G. van de Ven, M. A. W. Verheijen, J. V. Vilchez, and B. Ziegler. CALIFA: a diameter-selected sample for an integral field spectroscopy galaxy survey. *A&A*, 569:A1, September 2014.
- [74] S. F. Sánchez, E. Pérez, P. Sánchez-Blázquez, J. J. González, F. F. Rosales-Ortega, M. Cano-Díaz, C. López-Cobá, R. A. Marino, A. Gil de Paz, M. Mollá, A. R. López-Sánchez, Y. Ascasibar, and J. Barrera-Ballesteros. Pipe3D, a pipeline to analyze Integral Field Spectroscopy Data: I. New fitting philosophy of FIT3D. , 52:21–53, April 2016.
- [75] S. F. Sánchez, E. Pérez, P. Sánchez-Blázquez, R. García-Benito, H. J. Ibarra-Mede, J. J. González, F. F. Rosales-Ortega, L. Sánchez-Menguiano, Y. Ascasibar, T. Bitsakis, D. Law, M. Cano-Díaz, C. López-Cobá, R. A. Marino, A. Gil de Paz, A. R. López-Sánchez, J. Barrera-Ballesteros, L. Galbany, D. Mast, V. Abril-Melgarejo, and A. Roman-Lopes. Pipe3D, a pipeline to analyze Integral Field Spectroscopy Data: II. Analysis sequence and CALIFA dataproducts. , 52:171–220, April 2016.
- [76] Edwin E. Salpeter. The Luminosity Function and Stellar Evolution. *ApJ*, 121:161, January 1955.
- [77] S. F. Sánchez, F. F. Rosales-Ortega, J. Iglesias-Páramo, M. Mollá, J. Barrera-Ballesteros, R. A. Marino, E. Pérez, P. Sánchez-Blázquez, R. González Delgado, R. Cid Fernandes, A. de Lorenzo-Cáceres, J. Mendez-Abreu, L. Galbany, J. Falcon-Barroso, D. Miralles-Caballero, B. Husemann, R. García-Benito, D. Mast, C. J. Walcher, A. Gil de Paz, B. García-Lorenzo, B. Jungwiert, J. M. Vílchez, Lucie Jílková, M. Lyubenova, C. Cortijo-Ferrero, A. I. Díaz, L. Wisotzki, I. Márquez, J. Bland-Hawthorn, S. Ellis, G. van de Ven, K. Jahnke, P. Papaderos, J. M. Gomes, M. A. Mendoza, and Á. R. López-Sánchez. A characteristic oxygen abundance gradient in galaxy disks unveiled with CALIFA. *A&A*, 563:A49, March 2014.

- [78] Andreas Schruba, Adam K. Leroy, Fabian Walter, Frank Bigiel, Elias Brinks, W. J. G. de Blok, Gaelle Dumas, Carsten Kramer, Erik Rosolowsky, Karin Sandstrom, Karl Schuster, Antonio Usero, Axel Weiss, and Helmut Wiesemeyer. A Molecular Star Formation Law in the Atomic-gas-dominated Regime in Nearby Galaxies. *AJ*, 142(2):37, Aug 2011.
- [79] Rebecca C. Levy, Alberto D. Bolatto, Peter Teuben, Sebastián F. Sánchez, Jorge K. Barrera-Ballesteros, Leo Blitz, Dario Colombo, Rubén García-Benito, Rodrigo Herrera-Camus, Bernd Husemann, Veselina Kalinova, Tian Lan, Gigi Y. C. Leung, Damián Mast, Dyas Utomo, Glenn van de Ven, Stuart N. Vogel, and Tony Wong. The EDGE-CALIFA Survey: Molecular and Ionized Gas Kinematics in Nearby Galaxies. *ApJ*, 860(2):92, Jun 2018.
- [80] Jason A. Cardelli, Geoffrey C. Clayton, and John S. Mathis. The Relationship between Infrared, Optical, and Ultraviolet Extinction. *ApJ*, 345:245, October 1989.
- [81] Daniel Rosa-González, Elena Terlevich, and Roberto Terlevich. An empirical calibration of star formation rate estimators. *MNRAS*, 332(2):283–295, May 2002.
- [82] J. S. Speagle, C. L. Steinhardt, P. L. Capak, and J. D. Silverman. A Highly Consistent Framework for the Evolution of the Star-Forming “Main Sequence” from $z \sim 0$ -6. *ApJ*, 214(2):15, October 2014.
- [83] Fabian Walter, Elias Brinks, W. J. G. de Blok, Frank Bigiel, Jr. Kennicutt, Robert C., Michele D. Thornley, and Adam Leroy. THINGS: The H I Nearby Galaxy Survey. *AJ*, 136(6):2563–2647, December 2008.
- [84] J. K. Barrera-Ballesteros, S. F. Sánchez, T. Heckman, T. Wong, A. Bolatto, E. Ostriker, E. Rosolowsky, L. Carigi, S. Vogel, R. C. Levy, D. Colombo, Yufeng Luo, and Yixian Cao. The EDGE-CALIFA survey: self-regulation of star formation at kpc scales. *MNRAS*, 503(3):3643–3659, May 2021.
- [85] R. A. Marino, F. F. Rosales-Ortega, S. F. Sánchez, A. Gil de Paz, J. Vílchez, D. Miralles-Caballero, C. Kehrig, E. Pérez-Montero, V. Stanishev, J. Iglesias-Páramo, A. I. Díaz, A. Castillo-Morales, R. Kennicutt, A. R. López-Sánchez, L. Galbany, R. García-Benito, D. Mast, J. Mendez-Abreu, A. Monreal-Ibero, B. Husemann, C. J. Walcher, B. García-Lorenzo, J. Masegosa, A. Del Olmo Orozco, A. M. Mourão, B. Ziegler, M. Mollá, P. Papaderos, P. Sánchez-Blázquez, R. M. González Delgado, J. Falcón-Barroso, M. M. Roth, G. van de Ven, and Califa Team. The O3N2 and N2 abundance indicators revisited: improved calibrations based on CALIFA and T_e -based literature data. *A&A*, 559:A114, November 2013.
- [86] W. H. Baumgartner and R. F. Mushotzky. Oxygen Abundances in the Milky Way Using X-Ray Absorption Measurements toward Galaxy Clusters. *ApJ*, 639(2):929–940, March 2006.
- [87] Bruce G. Elmegreen. A Pressure and Metallicity Dependence for Molecular Cloud Correlations and the Calibration of Mass. *ApJ*, 338:178, Mar 1989.

- [88] D. Tamburro, H. W. Rix, A. K. Leroy, M. M. Mac Low, F. Walter, R. C. Kennicutt, E. Brinks, and W. J. G. de Blok. What is Driving the H I Velocity Dispersion? *AJ*, 137(5):4424–4435, May 2009.
- [89] B. G. Elmegreen and A. Parravano. When Star Formation Stops: Galaxy Edges and Low Surface Brightness Disks. *ApJL*, 435:L121, November 1994.
- [90] R. Herrera-Camus, A. Bolatto, M. Wolfire, E. Ostriker, B. Draine, A. Leroy, K. Sandstrom, L. Hunt, R. Kennicutt, D. Calzetti, J. D. Smith, K. Croxall, M. Galametz, I. de Looze, D. Dale, A. Crocker, and B. Groves. Thermal Pressure in the Cold Neutral Medium of Nearby Galaxies. *ApJ*, 835(2):201, February 2017.
- [91] D. B. Fisher, A. D. Bolatto, H. White, K. Glazebrook, R. G. Abraham, and D. Obreschkow. Testing Feedback-regulated Star Formation in Gas-rich, Turbulent Disk Galaxies. *ApJ*, 870(1):46, January 2019.
- [92] Andreas Schruba, J. M. Diederik Kruijssen, and Adam K. Leroy. How Galactic Environment Affects the Dynamical State of Molecular Clouds and Their Star Formation Efficiency. *ApJ*, 883(1):2, September 2019.
- [93] Jiayi Sun, Adam K. Leroy, Eve C. Ostriker, Annie Hughes, Erik Rosolowsky, Andreas Schruba, Eva Schinnerer, Guillermo A. Blanc, Christopher Faesi, J. M. Diederik Kruijssen, and et al. Dynamical equilibrium in the molecular ism in 28 nearby star-forming galaxies. *The Astrophysical Journal*, 892(2):148, Apr 2020.
- [94] Michiel Kregel, Pieter C. van der Kruit, and Richard de Grijs. Flattening and truncation of stellar discs in edge-on spiral galaxies. *MNRAS*, 334(3):646–668, August 2002.
- [95] Joseph Silk. Feedback, Disk Self-Regulation, and Galaxy Formation. *ApJ*, 481(2):703–709, May 1997.
- [96] Bruce G. Elmegreen. The Initial Stellar Mass Function from Random Sampling in a Turbulent Fractal Cloud. *ApJ*, 486(2):944–954, Sep 1997.
- [97] Massimo Persic, Paolo Salucci, and Fulvio Stel. The universal rotation curve of spiral galaxies — I. The dark matter connection. *MNRAS*, 281(1):27–47, July 1996.
- [98] A. Toomre. On the gravitational stability of a disk of stars. *ApJ*, 139:1217–1238, May 1964.
- [99] Kristen L. Shapiro, Joris Gerssen, and Roeland P. van der Marel. Observational Constraints on Disk Heating as a Function of Hubble Type. *AJ*, 126(6):2707–2716, December 2003.
- [100] K. M. Sandstrom, A. K. Leroy, F. Walter, A. D. Bolatto, K. V. Croxall, B. T. Draine, C. D. Wilson, M. Wolfire, D. Calzetti, R. C. Kennicutt, G. Aniano, J. Donovan Meyer, A. Usero, F. Bigiel, E. Brinks, W. J. G. de Blok, A. Crocker, D. Dale, C. W. Engelbracht, M. Galametz, B. Groves, L. K. Hunt, J. Koda, K. Kreckel, H. Linz, S. Meidt, E. Pellegrini, H. W. Rix, H. Roussel, E. Schinnerer, A. Schruba, K. F. Schuster, R. Skibba, T. van der Laan, P. Appleton, L. Armus, B. Brandl, K. Gordon, J. Hinz, O. Krause, E. Montiel,

- M. Sauvage, A. Schmiedeke, J. D. T. Smith, and L. Vigroux. The CO-to-H₂ Conversion Factor and Dust-to-gas Ratio on Kiloparsec Scales in Nearby Galaxies. *ApJ*, 777(1):5, November 2013.
- [101] Adam K. Leroy, Fabian Walter, Frank Bigiel, Antonio Usero, Axel Weiss, Elias Brinks, W. J. G. de Blok, Robert C. Kennicutt, Karl-Friedrich Schuster, Carsten Kramer, H. W. Wiesemeyer, and H el ene Roussel. Heracles: The HERA CO Line Extragalactic Survey. *AJ*, 137(6):4670–4696, June 2009.
- [102] L. Blitz and F. H. Shu. The origin and lifetime of giant molecular cloud complexes. *ApJ*, 238:148–157, May 1980.
- [103] Akiko Kawamura, Yoji Mizuno, Tetsuhiro Minamidani, Miroslav D. Filipovi c, Lister Staveley-Smith, Sungeun Kim, Norikazu Mizuno, Toshikazu Onishi, Akira Mizuno, and Yasuo Fukui. The Second Survey of the Molecular Clouds in the Large Magellanic Cloud by NANTEN. II. Star Formation. *ApJ*, 184(1):1–17, September 2009.
- [104] P. Gratier, J. Braine, N. J. Rodriguez-Fernandez, K. F. Schuster, C. Kramer, E. Corbelli, F. Combes, N. Brouillet, P. P. van der Werf, and M. R ollig. Giant molecular clouds in the Local Group galaxy M 33*. *A&A*, 542:A108, June 2012.
- [105] Leo Blitz and Erik Rosolowsky. The Initial Mass Function of GMCs. *arXiv e-prints*, pages astro-ph/0411520, November 2004.
- [106] Eve C. Ostriker, Christopher F. McKee, and Adam K. Leroy. Regulation of Star Formation Rates in Multiphase Galactic Disks: A Thermal/Dynamical Equilibrium Model. *ApJ*, 721(2):975–994, October 2010.
- [107] Leo Blitz and Erik Rosolowsky. The Role of Pressure in GMC Formation II: The H₂-Pressure Relation. *ApJ*, 650(2):933–944, October 2006.
- [108] Judith S. Young, Shuding Xie, Linda Tacconi, Pat Knezek, Paul Viscuso, Lowell Tacconi-Garman, Nick Scoville, Steve Schneider, F. Peter Schloerb, Steve Lord, Amy Lesser, Jeff Kenney, Yi-Long Huang, Nick Devereux, Mark Claussen, James Case, John Carpenter, Mike Berry, and Lori Allen. The FCRAO Extragalactic CO Survey. I. The Data. *ApJ*, 98:219, May 1995.
- [109] Michael W. Regan, Michele D. Thornley, Tamara T. Helfer, Kartik Sheth, Tony Wong, Stuart N. Vogel, Leo Blitz, and Douglas C. J. Bock. The BIMA Survey of Nearby Galaxies. I. The Radial Distribution of CO Emission in Spiral Galaxies. *ApJ*, 561(1):218–237, November 2001.
- [110] Crystal L. Martin and Jr. Kennicutt, Robert C. Star Formation Thresholds in Galactic Disks. *ApJ*, 555(1):301–321, Jul 2001.
- [111] Sebasti an F. S anchez. Spatially Resolved Spectroscopic Properties of Low-Redshift Star-Forming Galaxies. *ARA&A*, 58(1):annurev, August 2020.

- [112] S. F. Sanchez, C. J. Walcher, C. Lopez-Coba, J. K. Barrera-Ballesteros, A. Mejia-Narvaez, C. Espinosa-Ponce, and A. Camps-Fariña. From global to spatially resolved in low-redshift galaxies. *arXiv e-prints*, page arXiv:2009.00424, September 2020.
- [113] Janice C. Lee, Armando Gil de Paz, Christy Tremonti, Jr. Kennicutt, Robert C., Samir Salim, Matthew Bothwell, Daniela Calzetti, Julianne Dalcanton, Daniel Dale, Chad Engelbracht, S. J. José G. Funes, Benjamin Johnson, Shoko Sakai, Evan Skillman, Liese van Zee, Fabian Walter, and Daniel Weisz. Comparison of $H\alpha$ and UV Star Formation Rates in the Local Volume: Systematic Discrepancies for Dwarf Galaxies. *ApJ*, 706(1):599–613, November 2009.
- [114] Kazuyuki Muraoka, Kazuo Sorai, Yusuke Miyamoto, Moe Yoda, Kana Morokuma-Matsui, Masato I. N. Kobayashi, Mayu Kuroda, Hiroyuki Kaneko, Nario Kuno, Tsutomu T. Takeuchi, Hiroyuki Nakanishi, Yoshimasa Watanabe, Takahiro Tanaka, Atsushi Yasuda, Yoshiyuki Yajima, Shugo Shibata, Dragan Salak, Daniel Espada, Naoko Matsumoto, Yuto Noma, Shoichiro Kita, Ryusei Komatsuzaki, Ayumi Kajikawa, Yu Yashima, Hsi-An Pan, Nagisa Oi, Masumichi Seta, and Naomasa Nakai. CO Multi-line Imaging of Nearby Galaxies (COMING). VI. Radial variations in star formation efficiency. , 71:S15, December 2019.
- [115] Kazuo Sorai, Nario Kuno, Kazuyuki Muraoka, Yusuke Miyamoto, Hiroyuki Kaneko, Hiroyuki Nakanishi, Naomasa Nakai, Kazuki Yanagitani, Takahiro Tanaka, Yuya Sato, Dragan Salak, Michiko Umei, Kana Morokuma-Matsui, Naoko Matsumoto, Saeko Ueno, Hsi-An Pan, Yuto Noma, Tsutomu T. Takeuchi, Moe Yoda, Mayu Kuroda, Atsushi Yasuda, Yoshiyuki Yajima, Nagisa Oi, Shugo Shibata, Masumichi Seta, Yoshimasa Watanabe, Shoichiro Kita, Ryusei Komatsuzaki, Ayumi Kajikawa, Yu Yashima, Suchetha Cooray, Hiroyuki Baji, Yoko Segawa, Takami Tashiro, Miho Takeda, Nozomi Kishida, Takuya Hatakeyama, Yuto Tomiyasu, and Chey Saita. CO multi-line imaging of nearby galaxies (COMING). IV. Overview of the project. , 71:S14, December 2019.
- [116] B. G. Elmegreen. Star Formation at Compressed Interfaces in Turbulent Self-gravitating Clouds. *ApJL*, 419:L29, December 1993.
- [117] Sara L. Ellison, Mallory D. Thorp, Lihwai Lin, Hsi-An Pan, Asa F. L. Bluck, Jillian M. Scudder, Hossen Teimoorinia, Sebastian F. Sánchez, and Mark Sargent. The ALMaQUEST survey - III. Scatter in the resolved star-forming main sequence is primarily due to variations in star formation efficiency. *MNRAS*, 493(1):L39–L43, March 2020.
- [118] Biprateep Dey, Erik Rosolowsky, Yixian Cao, Alberto Bolatto, Sebastian F. Sanchez, Dyas Utomo, Dario Colombo, Veselina Kalinova, Tony Wong, Leo Blitz, Stuart Vogel, Jason Loeppky, and Rubén García-Benito. The EDGE-CALIFA survey: exploring the star formation law through variable selection. *MNRAS*, 488(2):1926–1940, September 2019.
- [119] S. F. Sánchez, J. K. Barrera-Ballesteros, D. Colombo, T. Wong, A. Bolatto, E. Rosolowsky, S. Vogel, R. Levy, V. Kalinova, P. Alvarez-Hurtado, Y. Luo, and Y. Cao. The EDGE-CALIFA survey: the local and global relations between Σ_* , Σ_{SFR} , and Σ_{mol} that regulate star formation. *MNRAS*, 503(2):1615–1635, May 2021.

- [120] Chang-Goo Kim, Eve C. Ostriker, and Woong-Tae Kim. Three-dimensional Hydrodynamic Simulations of Multiphase Galactic Disks with Star Formation Feedback. I. Regulation of Star Formation Rates. *ApJ*, 776(1):1, October 2013.
- [121] Eve C. Ostriker and Rahul Shetty. Maximally Star-forming Galactic Disks. I. Starburst Regulation Via Feedback-driven Turbulence. *ApJ*, 731(1):41, April 2011.
- [122] Dyas Utomo, Alberto D. Bolatto, Tony Wong, Eve C. Ostriker, Leo Blitz, Sebastian F. Sanchez, Dario Colombo, Adam K. Leroy, Yixian Cao, Helmut Dannerbauer, Ruben Garcia-Benito, Bernd Husemann, Veselina Kalinova, Rebecca C. Levy, Damian Mast, Erik Rosolowsky, and Stuart N. Vogel. The EDGE-CALIFA Survey: Variations in the Molecular Gas Depletion Time in Local Galaxies. *ApJ*, 849(1):26, November 2017.
- [123] Vadim A. Semenov, Andrey V. Kravtsov, and Nickolay Y. Gnedin. The Physical Origin of Long Gas Depletion Times in Galaxies. *ApJ*, 845(2):133, August 2017.
- [124] D. Colombo, V. Kalinova, D. Utomo, E. Rosolowsky, A. D. Bolatto, R. C. Levy, T. Wong, S. F. Sanchez, A. K. Leroy, E. Ostriker, L. Blitz, S. Vogel, D. Mast, R. García-Benito, B. Husemann, H. Dannerbauer, L. Ellmeier, and Y. Cao. The EDGE-CALIFA survey: the influence of galactic rotation on the molecular depletion time across the Hubble sequence. *MNRAS*, 475(2):1791–1808, April 2018.
- [125] Shuhei Koyama, Yusei Koyama, Takuji Yamashita, Masao Hayashi, Hideo Matsuhara, Takao Nakagawa, Shigeru V. Namiki, Tomoko L. Suzuki, Nao Fukagawa, Tadayuki Kodama, Lihwai Lin, Kana Morokuma-Matsui, Rhythm Shimakawa, and Ichi Tanaka. Do Galaxy Morphologies Really Affect the Efficiency of Star Formation During the Phase of Galaxy Transition? *ApJ*, 874(2):142, April 2019.
- [126] Deidre A. Hunter, Dana Ficut-Vicas, Trisha Ashley, Elias Brinks, Phil Cigan, Bruce G. Elmegreen, Volker Heesen, Kimberly A. Herrmann, Megan Johnson, Se-Heon Oh, Michael P. Rupen, Andreas Schrubba, Caroline E. Simpson, Fabian Walter, David J. Westpfahl, Lisa M. Young, and Hong-Xin Zhang. Little Things. *AJ*, 144(5):134, November 2012.
- [127] Bruce G. Elmegreen and Deidre A. Hunter. A Star Formation Law for Dwarf Irregular Galaxies. *ApJ*, 805(2):145, June 2015.
- [128] Alessandro B. Romeo. From massive spirals to dwarf irregulars: a new set of tight scaling relations for cold gas and stars driven by disc gravitational instability. *MNRAS*, 491(4):4843–4851, February 2020.
- [129] Sami Dib, Sacha Hony, and Guillermo Blanc. The extended law of star formation: the combined role of gas and stars. *MNRAS*, 469(2):1521–1531, August 2017.
- [130] Yong Shi, George Helou, Lin Yan, Lee Armus, Yanling Wu, Casey Papovich, and Sabrina Stierwalt. Extended Schmidt Law: Role of Existing Stars in Current Star Formation. *ApJ*, 733(2):87, June 2011.

- [131] K. Pearson. On lines and planes of closest fit to systems of points in space. *Philosophical Magazine*, 2:559–572, 1901.
- [132] Sebastián F. Sánchez. Spatially Resolved Spectroscopic Properties of Low-Redshift Star-Forming Galaxies. *ARA&A*, 58(1):annurev, August 2020.
- [133] S. F. Sanchez, C. J. Walcher, C. Lopez-Coba, J. K. Barrera-Ballesteros, A. Mejia-Narvaez, C. Espinosa-Ponce, and A. Camps-Fariña. From global to spatially resolved in low-redshift galaxies. *arXiv e-prints*, page arXiv:2009.00424, September 2020.
- [134] R. B. Larson, B. M. Tinsley, and C. N. Caldwell. The evolution of disk galaxies and the origin of S0 galaxies. *ApJ*, 237:692–707, May 1980.
- [135] Michael L. Balogh and Simon L. Morris. $H\alpha$ photometry of Abell 2390. *MNRAS*, 318(3):703–714, November 2000.
- [136] Ben Moore, Neal Katz, George Lake, Alan Dressler, and Augustus Oemler. Galaxy harassment and the evolution of clusters of galaxies. *Nature*, 379(6566):613–616, February 1996.
- [137] Alessandro Boselli and Giuseppe Gavazzi. Environmental Effects on Late-Type Galaxies in Nearby Clusters. *PASA*, 118(842):517–559, April 2006.
- [138] R. Smith, J. I. Davies, and A. H. Nelson. How effective is harassment on infalling late-type dwarfs? *MNRAS*, 405(3):1723–1735, July 2010.
- [139] Marie Martig, Frédéric Bournaud, Romain Teyssier, and Avishai Dekel. Morphological Quenching of Star Formation: Making Early-Type Galaxies Red. *ApJ*, 707(1):250–267, December 2009.
- [140] L. Cortese, B. Catinella, and R. Smith. The Dawes Review 9: The role of cold gas stripping on the star formation quenching of satellite galaxies. *PASA*, 38:e035, August 2021.
- [141] M. A. W. Verheijen and R. Sancisi. The Ursa Major cluster of galaxies. IV. HI synthesis observations. *A&A*, 370:765–867, May 2001.
- [142] M. P. Haynes and R. Giovanelli. Neutral hydrogen in isolated galaxies. IV. Results for the Arecibo sample. *AJ*, 89:758–800, June 1984.
- [143] Toby Brown, Barbara Catinella, Luca Cortese, Claudia del P. Lagos, Romeel Davé, Virginia Kilborn, Martha P. Haynes, Riccardo Giovanelli, and Mika Rafieferantsoa. Cold gas stripping in satellite galaxies: from pairs to clusters. *MNRAS*, 466(2):1275–1289, April 2017.
- [144] Adam R. H. Stevens and Toby Brown. Physical drivers of galaxies’ cold-gas content: exploring environmental and evolutionary effects with Dark Sage. *MNRAS*, 471(1):447–462, October 2017.

- [145] Adam B. Watts, Barbara Catinella, Luca Cortese, and Chris Power. xGASS: Robust quantification of asymmetries in global H I spectra and their relationship to environmental processes. *MNRAS*, 492(3):3672–3684, March 2020.
- [146] Adam B. Watts, Chris Power, Barbara Catinella, Luca Cortese, and Adam R. H. Stevens. Global H I asymmetries in IllustrisTNG: a diversity of physical processes disturb the cold gas in galaxies. *MNRAS*, 499(4):5205–5219, December 2020.
- [147] D. Cs. Molnár, P. Serra, T. van der Hulst, T. H. Jarrett, A. Boselli, L. Cortese, J. Healy, E. de Blok, M. Cappellari, K. M. Hess, G. I. G. Józsa, R. M. McDermid, T. A. Oosterloo, and M. A. W. Verheijen. The Westerbork Coma Survey. A blind, deep, high-resolution H I survey of the Coma cluster. *A&A*, 659:A94, March 2022.
- [148] Timothy A. Davis, Katherine Alatalo, Martin Bureau, Michele Cappellari, Nicholas Scott, Lisa M. Young, Leo Blitz, Alison Crocker, Estelle Bayet, Maxime Bois, Frédéric Bournaud, Roger L. Davies, P. T. de Zeeuw, Pierre-Alain Duc, Eric Emsellem, Sadegh Khochfar, Davor Krajnović, Harald Kuntschner, Pierre-Yves Lablanche, Richard M. McDermid, Raffaella Morganti, Thorsten Naab, Tom Oosterloo, Marc Sarzi, Paolo Serra, and Anne-Marie Weijmans. The ATLAS^{3D} Project - XIV. The extent and kinematics of the molecular gas in early-type galaxies. *MNRAS*, 429(1):534–555, February 2013.
- [149] Michele Fumagalli, Mark R. Krumholz, J. Xavier Prochaska, Giuseppe Gavazzi, and Alessandro Boselli. Molecular Hydrogen Deficiency in H I-poor Galaxies and its Implications for Star Formation. *ApJ*, 697(2):1811–1821, June 2009.
- [150] Bumhyun Lee, Aeree Chung, Stephanie Tonnesen, Jeffrey D. P. Kenney, O. Ivy Wong, B. Vollmer, Glen R. Petitpas, Hugh H. Crowl, and Jacqueline van Gorkom. The effect of ram pressure on the molecular gas of galaxies: three case studies in the Virgo cluster. *MNRAS*, 466(2):1382–1398, April 2017.
- [151] Bumhyun Lee and Aeree Chung. The ALMA Detection of Extraplanar ¹³CO in a Ram-pressure-stripped Galaxy and Its Implication. *ApJL*, 866(1):L10, October 2018.
- [152] Nikki Zabel, Timothy A. Davis, Matthew W. L. Smith, Natasha Maddox, George J. Bendo, Reynier Peletier, Enrichetta Iodice, Aku Venhola, Maarten Baes, Jonathan I. Davies, Ilse de Looze, Haley Gomez, Marco Grossi, Jeffrey D. P. Kenney, Paolo Serra, Freeke van de Voort, Catherine Vlahakis, and Lisa M. Young. The ALMA Fornax Cluster Survey I: stirring and stripping of the molecular gas in cluster galaxies. *MNRAS*, 483(2):2251–2268, February 2019.
- [153] T. Lizée, B. Vollmer, J. Braine, and F. Nehlig. Gas compression and stellar feedback in the tidally interacting and ram-pressure stripped Virgo spiral galaxy NGC 4654. *A&A*, 645:A111, January 2021.
- [154] Adam R. H. Stevens, Claudia del P. Lagos, Luca Cortese, Barbara Catinella, Benedikt Diemer, Dylan Nelson, Annalisa Pillepich, Lars Hernquist, Federico Marinacci, and Mark

- Vogelsberger. Molecular hydrogen in IllustrisTNG galaxies: carefully comparing signatures of environment with local CO and SFR data. *MNRAS*, 502(3):3158–3178, April 2021.
- [155] Nikki Zabel, Toby Brown, Christine D. Wilson, Timothy A. Davis, Luca Cortese, Laura C. Parker, Alessandro Boselli, Barbara Catinella, Ryan Chown, Aeree Chung, Tirna Deb, Sara L. Ellison, María J. Jiménez-Donaire, Bumhyun Lee, Ian D. Roberts, Kristine Spekkens, Adam R. H. Stevens, Mallory Thorp, Stephanie Tonnesen, and Vicente Vilanueva. VERTICO II: How H I-identified Environmental Mechanisms Affect the Molecular Gas in Cluster Galaxies. *ApJ*, 933(1):10, July 2022.
- [156] Eun Jung Chung and Sungeun Kim. H I and H₂ properties and star formation efficiency of NGC 4654 in the cluster environment. , 66(1):11, February 2014.
- [157] A. Boselli, L. Ciesla, V. Buat, and et al. FIR colours and SEDs of nearby galaxies observed with Herschel. *A&A*, 518:L61, July 2010.
- [158] Rein Herm Warmels. *HI properties of spiral galaxies in the Virgo cluster*. 1986.
- [159] V. Cayatte, J. H. van Gorkom, C. Balkowski, and C. Kotanyi. VLA Observations of Neutral Hydrogen in Virgo Cluster Galaxies. I. The Atlas. *AJ*, 100:604, September 1990.
- [160] A. Loni, P. Serra, D. Kleiner, L. Cortese, B. Catinella, B. Koribalski, T. H. Jarrett, D. Cs. Molnar, T. A. Davis, E. Iodice, K. Lee-Waddell, F. Loi, F. M. Maccagni, R. Peletier, A. Popping, M. Ramatsoku, M. W. L. Smith, and N. Zabel. A blind ATCA HI survey of the Fornax galaxy cluster. Properties of the HI detections. *A&A*, 648:A31, April 2021.
- [161] Andreas Schrubba, Adam K. Leroy, Fabian Walter, Karin Sandstrom, and Erik Rosolowsky. The Scale Dependence of the Molecular Gas Depletion Time in M33. *ApJ*, 722(2):1699–1706, October 2010.
- [162] Rebecca A. Koopmann and Jeffrey D. P. Kenney. H α Morphologies and Environmental Effects in Virgo Cluster Spiral Galaxies. *ApJ*, 613(2):866–885, October 2004.
- [163] N. Zabel, T. A. Davis, M. Sarzi, Boris Nedelchev, M. Chevance, J. M. Diederik Kruijssen, E. Iodice, M. Baes, G. J. Bendo, E. Maria Corsini, I. De Looze, P. Tim de Zeeuw, D. A. Gadotti, M. Grossi, R. Peletier, F. Pinna, Paolo Serra, F. van de Voort, A. Venhola, S. Viaene, and C. Vlahakis. ALFoCS + Fornax3D: resolved star formation in the Fornax cluster with ALMA and MUSE. *MNRAS*, 496(2):2155–2182, August 2020.
- [164] T. N. Reynolds, B. Catinella, L. Cortese, T. Westmeier, G. R. Meurer, L. Shao, D. Obreschkow, J. Román, L. Verdes-Montenegro, N. Deg, H. Dénes, B. Q. For, D. Kleiner, B. S. Koribalski, K. Lee-Waddell, C. Murugesan, S. H. Oh, J. Rhee, K. Spekkens, L. Staveley-Smith, A. R. H. Stevens, J. M. van der Hulst, J. Wang, O. I. Wong, B. W. Holwerda, A. Bosma, J. P. Madrid, and K. Bekki. WALLABY pilot survey: H I gas disc truncation and star formation of galaxies falling into the Hydra I cluster. *MNRAS*, 510(2):1716–1732, February 2022.

- [165] Bärbel S. Koribalski, L. Staveley-Smith, T. Westmeier, P. Serra, K. Spekkens, O. I. Wong, K. Lee-Waddell, C. D. P. Lagos, D. Obreschkow, E. V. Ryan-Weber, M. Zwaan, V. Kilborn, G. Bekiaris, K. Bekki, F. Bigiel, A. Boselli, A. Bosma, B. Catinella, G. Chauhan, M. E. Cluver, M. Colless, H. M. Courtois, R. A. Crain, W. J. G. de Blok, H. Dénes, A. R. Duffy, A. Elagali, C. J. Fluke, B. Q. For, G. Heald, P. A. Henning, K. M. Hess, B. W. Holwerda, C. Howlett, T. Jarrett, D. H. Jones, M. G. Jones, G. I. G. Józsa, R. Jurek, E. Jütte, P. Kamphuis, I. Karachentsev, J. Kerp, D. Kleiner, R. C. Kraan-Korteweg, Á. R. López-Sánchez, J. Madrid, M. Meyer, J. Mould, C. Murugesan, R. P. Norris, S. H. Oh, T. A. Oosterloo, A. Popping, M. Putman, T. N. Reynolds, J. Rhee, A. S. G. Robotham, S. Ryder, A. C. Schröder, Li Shao, A. R. H. Stevens, E. N. Taylor, J. M. van der Hulst, L. Verdes-Montenegro, B. P. Wakker, J. Wang, M. Whiting, B. Winkel, and C. Wolf. WALLABY - an SKA Pathfinder HI survey. , 365(7):118, July 2020.
- [166] Angus Mok, C. D. Wilson, J. H. Knapen, J. R. Sánchez-Gallego, E. Brinks, and E. Rosolowsky. The JCMT Nearby Galaxies Legacy Survey - XI. Environmental variations in the atomic and molecular gas radial profiles of nearby spiral galaxies. *MNRAS*, 467(4):4282–4292, June 2017.
- [167] E. Roediger, M. Bruggen, M. S. Owers, H. Ebeling, and M. Sun. Star formation in shocked cluster spirals and their tails. *MNRAS*, 443:L114–L118, September 2014.
- [168] W. J. Cramer, J. D. P. Kenney, J. R. Cortes, Cortes P. C., C. Vlahakis, P. Jáchym, E. Pompei, and M. Rubio. ALMA Evidence for Ram Pressure Compression and Stripping of Molecular Gas in the Virgo Cluster Galaxy NGC 4402. *ApJ*, 901(2):95, October 2020.
- [169] C. D. Wilson, B. E. Warren, F. P. Israel, S. Serjeant, D. Attewell, G. J. Bendo, H. M. Butner, P. Chanial, D. L. Clements, J. Golding, V. Heesen, J. Irwin, J. Leech, H. E. Matthews, S. Mühle, A. M. J. Mortier, G. Petitpas, J. R. Sánchez-Gallego, E. Sinukoff, K. Shorten, B. K. Tan, R. P. J. Tilanus, A. Usero, M. Vaccari, T. Wiegert, M. Zhu, D. M. Alexander, P. Alexander, M. Azimlu, P. Barmby, R. Brar, C. Bridge, E. Brinks, S. Brooks, K. Coppin, S. Côté, P. Côté, S. Courteau, J. Davies, S. Eales, M. Fich, M. Hudson, D. H. Hughes, R. J. Ivison, J. H. Knapen, M. Page, T. J. Parkin, D. Rigopoulou, E. Rosolowsky, E. R. Seaquist, K. Spekkens, N. Tanvir, J. M. van der Hulst, P. van der Werf, C. Vlahakis, T. M. Webb, B. Weferling, and G. J. White. The JCMT Nearby Galaxies Legacy Survey — VIII. CO data and the $L_{CO(3-2)}-L_{FIR}$ correlation in the SINGS sample. *MNRAS*, 424(4):3050–3080, August 2012.
- [170] Adam K. Leroy, Eva Schinnerer, Annie Hughes, Erik Rosolowsky, Jérôme Pety, Andreas Schruba, Antonio Usero, Guillermo A. Blanc, Mélanie Chevance, Eric Emsellem, Christopher M. Faesi, Cinthya N. Herrera, Daizhong Liu, Sharon E. Meidt, Miguel Querejeta, Toshiki Saito, Karin M. Sandstrom, Jiayi Sun, Thomas G. Williams, Gagandeep S. Anand, Ashley T. Barnes, Erica A. Behrens, Francesco Belfiore, Samantha M. Benincasa, Ivana Bešlić, Frank Bigiel, Alberto D. Bolatto, Jakob S. den Brok, Yixian Cao, Rupali Chandar, Jérémy Chastenet, I-Da Chiang, Enrico Congiu, Daniel A. Dale, Sinan Deger, Cosima Eibensteiner, Oleg V. Egorov, Axel García-Rodríguez, Simon C. O. Glover, Kathryn Grasha, Jonathan D. Henshaw, I-Ting Ho, Amanda A. Kepley, Jaeyeon Kim,

- Ralf S. Klessen, Kathryn Kreckel, Eric W. Koch, J. M. Diederik Kruijssen, Kirsten L. Larson, Janice C. Lee, Laura A. Lopez, Josh Machado, Ness Mayker, Rebecca McElroy, Eric J. Murphy, Eve C. Ostriker, Hsi-An Pan, Ismael Pessa, Johannes Puschignig, Alessandro Razza, Patricia Sánchez-Blázquez, Francesco Santoro, Amy Sardone, Fabian Scheuermann, Kazimierz Sliwa, Mattia C. Sormani, Sophia K. Stuber, David A. Thilker, Jordan A. Turner, Dyas Utomo, Elizabeth J. Watkins, and Bradley Whitmore. PHANGS-ALMA: Arcsecond CO(2-1) Imaging of Nearby Star-Forming Galaxies. *arXiv e-prints*, page arXiv:2104.07739, April 2021.
- [171] J. P. McMullin, B. Waters, D. Schiebel, W. Young, and K. Golap. CASA Architecture and Applications. In R. A. Shaw, F. Hill, and D. J. Bell, editors, *Astronomical Data Analysis Software and Systems XVI*, volume 376 of *Astronomical Society of the Pacific Conference Series*, page 127, October 2007.
- [172] Adam K. Leroy, Annie Hughes, Daizhong Liu, Jérôme Pety, Erik Rosolowsky, Toshiki Saito, Eva Schinnerer, Andreas Schrubba, Antonio Usero, Christopher M. Faesi, Cinthya N. Herrera, Mélanie Chevance, Alexander P. S. Hygate, Amanda A. Kepley, Eric W. Koch, Miguel Querejeta, Kazimierz Sliwa, David Will, Christine D. Wilson, Gagandeep S. Anand, Ashley Barnes, Francesco Belfiore, Ivana Bešlić, Frank Bigiel, Guillermo A. Blanc, Alberto D. Bolatto, Mèdèric Boquien, Yixian Cao, Rupali Chandar, Jérémy Chastenet, I-Da Chiang, Enrico Congiu, Daniel A. Dale, Sinan Deger, Jakob S. den Brok, Cosima Eibensteiner, Eric Emsellem, Axel García-Rodríguez, Simon C. O. Glover, Kathryn Grasha, Brent Groves, Jonathan D. Henshaw, María J. Jiménez Donaire, Jaeyeon Kim, Ralf S. Klessen, Kathryn Kreckel, J. M. Diederik Kruijssen, Kirsten L. Larson, Janice C. Lee, Ness Mayker, Rebecca McElroy, Sharon E. Meidt, Angus Mok, Hsi-An Pan, Johannes Puschignig, Alessandro Razza, Patricia Sánchez-Blázquez, Karin M. Sandstrom, Francesco Santoro, Amy Sardone, Fabian Scheuermann, Jiayi Sun, David A. Thilker, Jordan A. Turner, Leonardo Ubeda, Dyas Utomo, Elizabeth J. Watkins, and Thomas G. Williams. PHANGS-ALMA Data Processing and Pipeline. *ApJ*, 255(1):19, July 2021.
- [173] Adam K. Leroy, Karin M. Sandstrom, Dustin Lang, Alexia Lewis, Samir Salim, Erica A. Behrens, Jérémy Chastenet, I-Da Chiang, Molly J. Gallagher, Sarah Kessler, and Dyas Utomo. A $z = 0$ Multiwavelength Galaxy Synthesis. I. A WISE and GALEX Atlas of Local Galaxies. *ApJ*, 244(2):24, October 2019.
- [174] G. Aniano, B. T. Draine, K. D. Gordon, and K. Sandstrom. Common-Resolution Convolution Kernels for Space- and Ground-Based Telescopes. *PASA*, 123(908):1218, October 2011.
- [175] Pavel Kroupa. On the variation of the initial mass function. *MNRAS*, 322(2):231–246, April 2001.
- [176] B. Vollmer, V. Cayatte, A. Boselli, C. Balkowski, and W. J. Duschl. Kinematics of the anemic cluster galaxy NGC 4548. Is stripping still active? *A&A*, 349:411–423, September 1999.
- [177] B. Vollmer, J. Braine, C. Pappalardo, and P. Hily-Blant. Ram-pressure stripped molecular gas in the Virgo spiral galaxy NGC 4522. *A&A*, 491(2):455–464, November 2008.

- [178] B. Vollmer, M. Soida, J. Braine, A. Abramson, R. Beck, A. Chung, H. H. Crawl, J. D. P. Kenney, and J. H. van Gorkom. Ram pressure stripping of the multiphase ISM and star formation in the Virgo spiral galaxy NGC 4330. *A&A*, 537:A143, January 2012.
- [179] Barbara Catinella, Amélie Saintonge, Steven Janowiecki, Luca Cortese, Romeel Davé, Jenna J. Lemonias, Andrew P. Cooper, David Schiminovich, Cameron B. Hummels, Silvia Fabello, Katinka Geréb, Virginia Kilborn, and Jing Wang. xGASS: total cold gas scaling relations and molecular-to-atomic gas ratios of galaxies in the local Universe. *MNRAS*, 476(1):875–895, May 2018.
- [180] V. Cayatte, C. Kotanyi, C. Balkowski, and J. H. van Gorkom. A Very Large Array Survey of Neutral Hydrogen in Virgo Cluster Spirals. III. Surface Density Profiles of the Gas. *AJ*, 107:1003, March 1994.
- [181] A. Boselli, S. Boissier, L. Cortese, A. Gil de Paz, M. Seibert, B. F. Madore, V. Buat, and D. C. Martin. The Fate of Spiral Galaxies in Clusters: The Star Formation History of the Anemic Virgo Cluster Galaxy NGC 4569. *ApJ*, 651(2):811–821, November 2006.
- [182] B. Vollmer, O. I. Wong, J. Braine, A. Chung, and J. D. P. Kenney. The influence of the cluster environment on the star formation efficiency of 12 Virgo spiral galaxies. *A&A*, 543:A33, July 2012.
- [183] A. Boselli, J. C. Cuillandre, M. Fossati, S. Boissier, D. Bomans, G. Consolandi, G. Anselmi, L. Cortese, P. Côté, P. Durrell, L. Ferrarese, M. Fumagalli, G. Gavazzi, S. Gwyn, G. Hensler, M. Sun, and E. Toloba. Spectacular tails of ionized gas in the Virgo cluster galaxy NGC 4569. *A&A*, 587:A68, March 2016.
- [184] Alessandro Boselli, Matteo Fossati, and Ming Sun. Ram pressure stripping in high-density environments. , 30(1):3, December 2022.
- [185] Alessia Moretti, Rosita Paladino, Bianca M. Poggianti, Paolo Serra, Mpati Ramatsoku, Andrea Franchetto, Tirna Deb, Marco Gullieuszik, Neven Tomičić, Matilde Mingozzi, Benedetta Vulcani, Mario Radovich, Daniela Bettoni, and Jacopo Fritz. The High Molecular Gas Content, and the Efficient Conversion of Neutral into Molecular Gas, in Jellyfish Galaxies. *ApJL*, 897(2):L30, July 2020.
- [186] Bianca M. Poggianti, Alessia Moretti, Marco Gullieuszik, Jacopo Fritz, Yara Jaffé, Daniela Bettoni, Giovanni Fasano, Callum Bellhouse, George Hau, Benedetta Vulcani, Andrea Biviano, Alessandro Omizzolo, Angela Paccagnella, Mauro D’Onofrio, Antonio Cava, Y. K. Sheen, Warrick Couch, and Matt Owers. GASP. I. Gas Stripping Phenomena in Galaxies with MUSE. *ApJ*, 844(1):48, July 2017.
- [187] L. L. Cowie and A. Songaila. Thermal evaporation of gas within galaxies by a hot intergalactic medium. *Nature*, 266:501–503, April 1977.
- [188] M. Bureau and C. Carignan. Environment, Ram Pressure, and Shell Formation in Holmberg II. *AJ*, 123(3):1316–1333, March 2002.

- [189] E. Roediger and G. Hensler. Ram pressure stripping of disk galaxies. From high to low density environments. *A&A*, 433(3):875–895, April 2005.
- [190] S. Randall, P. Nulsen, W. R. Forman, C. Jones, M. Machacek, S. S. Murray, and B. Maughan. Chandra’s View of the Ram Pressure Stripped Galaxy M86. *ApJ*, 688(1):208–223, November 2008.
- [191] I. Pessa, E. Schinnerer, F. Belfiore, E. Emsellem, A. K. Leroy, A. Schrubba, J. M. D. Kruijssen, H. A. Pan, G. A. Blanc, P. Sanchez-Blazquez, F. Bigiel, M. Chevance, E. Congiu, D. Dale, C. M. Faesi, S. C. O. Glover, K. Grasha, B. Groves, I. Ho, M. Jiménez-Donaire, R. Klessen, K. Kreckel, E. W. Koch, D. Liu, S. Meidt, J. Pety, M. Querejeta, E. Rosolowsky, T. Saito, F. Santoro, J. Sun, A. Usero, E. J. Watkins, and T. G. Williams. Star formation scaling relations at ~ 100 pc from PHANGS: Impact of completeness and spatial scale. *A&A*, 650:A134, June 2021.
- [192] Angus Mok, C. D. Wilson, J. Golding, B. E. Warren, F. P. Israel, S. Serjeant, J. H. Knapen, J. R. Sánchez-Gallego, P. Barmby, G. J. Bendo, E. Rosolowsky, and P. van der Werf. The JCMT nearby galaxies legacy survey - X. Environmental effects on the molecular gas and star formation properties of spiral galaxies. *MNRAS*, 456(4):4384–4406, March 2016.
- [193] A. M. Garcia. General study of group membership. II. Determination of nearby groups. , 100:47–90, July 1993.
- [194] Kana Morokuma-Matsui, Tadayuki Kodama, Tomoki Morokuma, Kouichiro Nakanishi, Yusei Koyama, Takuji Yamashita, Shuhei Koyama, and Takashi Okamoto. A Phase-space View of Cold-gas Properties of Virgo Cluster Galaxies: Multiple Quenching Processes at Work? *ApJ*, 914(2):145, June 2021.
- [195] Suk Kim, Soo-Chang Rey, Helmut Jerjen, Thorsten Lisker, Eon-Chang Sung, Youngdae Lee, Jiwon Chung, Mina Pak, Wonhyeong Yi, and Woong Lee. The Extended Virgo Cluster Catalog. *ApJ*, 215(2):22, December 2014.
- [196] I. D. Roberts, R. J. van Weeren, R. Timmerman, A. Botteon, M. Gendron-Marsolais, A. Ignesti, and H. J. A. Rottgering. LoTSS jellyfish galaxies. III. The first identification of jellyfish galaxies in the Perseus cluster. *A&A*, 658:A44, February 2022.
- [197] Bumhyun Lee, Jing Wang, Aeree Chung, Luis C. Ho, Ran Wang, Tomonari Michiyama, Juan Molina, Yongjung Kim, Li Shao, Virginia Kilborn, Shun Wang, Dawoon E. Kim, B. Catinella, L. Cortese, N. Deg, H. Dénes, A. Elagali, Bi-Qing For, D. Kleiner, B. S. Koribalski, K. Lee-Waddell, J. Rhee, K. Spekkens, T. Westmeier, O. I. Wong, F. Bigiel, A. Bosma, B. W. Holwerda, J. M. van der Hulst, Sambit Roychowdhury, L. Verdes-Montenegro, and M. A. Zwaan. ALMA/ACA CO Survey of the IC 1459 and NGC 4636 Groups: Environmental Effects on the Molecular Gas of Group Galaxies. *arXiv e-prints*, page arXiv:2204.06022, April 2022.
- [198] John P. F. Osmond and Trevor J. Ponman. The GEMS project: X-ray analysis and statistical properties of the group sample. *MNRAS*, 350(4):1511–1535, June 2004.

- [199] Duncan A. Forbes, Trevor Ponman, Frazer Pearce, John Osmond, Virginia Kilborn, Sarah Brough, Somak Raychaudhury, Carole Mundell, Trevor Miles, and Katie Kern. The Group Evolution Multiwavelength Study (GEMS): The Sample and Datasets. *PASA*, 23(1):38–49, March 2006.
- [200] Stephanie Tonnesen and Greg L. Bryan. Star formation in ram pressure stripped galactic tails. *MNRAS*, 422(2):1609–1624, May 2012.
- [201] Kenji Bekki. Galactic star formation enhanced and quenched by ram pressure in groups and clusters. *MNRAS*, 438(1):444–462, February 2014.
- [202] A. Boselli, M. Fossati, and M. Sun. Ram Pressure Stripping in High-Density Environments. *arXiv e-prints*, page arXiv:2109.13614, September 2021.
- [203] Jindra Gensior, J. M. Diederik Kruijssen, and Benjamin W. Keller. Heart of darkness: the influence of galactic dynamics on quenching star formation in galaxy spheroids. *MNRAS*, 495(1):199–223, June 2020.
- [204] C. Catalán-Torrecilla, A. Gil de Paz, A. Castillo-Morales, J. Iglesias-Páramo, S. F. Sánchez, R. C. Kennicutt, P. G. Pérez-González, R. A. Marino, C. J. Walcher, B. Husemann, R. García-Benito, D. Mast, R. M. González Delgado, J. C. Muñoz-Mateos, J. Bland-Hawthorn, D. J. Bomans, A. Del Olmo, L. Galbany, J. M. Gomes, C. Kehrig, Á. R. López-Sánchez, M. A. Mendoza, A. Monreal-Ibero, M. Pérez-Torres, P. Sánchez-Blázquez, J. M. Vilchez, and Califa Collaboration. Star formation in the local Universe from the CALIFA sample. I. Calibrating the SFR using integral field spectroscopy data. *A&A*, 584:A87, December 2015.
- [205] C. Catalán-Torrecilla, A. Gil de Paz, A. Castillo-Morales, J. Méndez-Abreu, J. Falcón-Barroso, S. Bekeraite, L. Costantin, A. de Lorenzo-Cáceres, E. Florido, R. García-Benito, B. Husemann, J. Iglesias-Páramo, R. C. Kennicutt, D. Mast, S. Pascual, T. Ruiz-Lara, L. Sánchez-Menguiano, S. F. Sánchez, C. J. Walcher, J. Bland-Hawthorn, S. Duarte Pueras, R. A. Marino, J. Masegosa, P. Sánchez-Blázquez, and CALIFA Collaboration. Star Formation in the Local Universe from the CALIFA Sample. II. Activation and Quenching Mechanisms in Bulges, Bars, and Disks. *ApJ*, 848(2):87, October 2017.
- [206] Robin H. W. Cook, Luca Cortese, Barbara Catinella, and Aaron Robotham. xGASS: The impact of photometric bulges on the scatter of HI scaling relations. *MNRAS*, 490(3):4060–4079, December 2019.
- [207] Robin H. W. Cook, Luca Cortese, Barbara Catinella, and Aaron Robotham. xGASS: the role of bulges along and across the local star-forming main sequence. *MNRAS*, 493(4):5596–5605, April 2020.
- [208] Samir Salim, R. Michael Rich, Stéphane Charlot, Jarle Brinchmann, Benjamin D. Johnson, David Schiminovich, Mark Seibert, Ryan Mallery, Timothy M. Heckman, Karl Forster, Peter G. Friedman, D. Christopher Martin, Patrick Morrissey, Susan G. Neff, Todd Small, Ted K. Wyder, Luciana Bianchi, José Donas, Young-Wook Lee, Barry F. Madore, Bruno

- Milliard, Alex S. Szalay, Barry Y. Welsh, and Sukyoung K. Yi. UV Star Formation Rates in the Local Universe. *ApJ*, 173(2):267–292, December 2007.
- [209] Asa F. L. Bluck, Roberto Maiolino, Sebastian F. Sánchez, Sara L. Ellison, Mallory D. Thorp, Joanna M. Piotrowska, Hossen Teimoorinia, and Kevin A. Bundy. Are galactic star formation and quenching governed by local, global, or environmental phenomena? *MNRAS*, 492(1):96–139, February 2020.
- [210] Asa F. L. Bluck, Roberto Maiolino, Joanna M. Piotrowska, James Trussler, Sara L. Ellison, Sebastian F. Sánchez, Mallory D. Thorp, Hossen Teimoorinia, Jorge Moreno, and Christopher J. Conselice. How do central and satellite galaxies quench? - Insights from spatially resolved spectroscopy in the MaNGA survey. *MNRAS*, 499(1):230–268, November 2020.
- [211] Pablo Corcho-Caballero, Yago Ascasibar, Sebastián F. Sánchez, and Ángel R. López-Sánchez. Ageing and quenching through the ageing diagram: predictions from simulations and observational constraints. *MNRAS*, 520(1):193–209, March 2023.
- [212] Daisuke Kawata and John S. Mulchaey. Strangulation in Galaxy Groups. *ApJL*, 672(2):L103, January 2008.
- [213] Y. Peng, R. Maiolino, and R. Cochrane. Strangulation as the primary mechanism for shutting down star formation in galaxies. *Nature*, 521(7551):192–195, May 2015.
- [214] M. J. Page, M. Symeonidis, J. D. Vieira, B. Altieri, A. Amblard, V. Arumugam, H. Aussel, T. Babbedge, A. Blain, J. Bock, A. Boselli, V. Buat, N. Castro-Rodríguez, A. Cava, P. Charnial, D. L. Clements, A. Conley, L. Conversi, A. Cooray, C. D. Dowell, E. N. Dubois, J. S. Dunlop, E. Dwek, S. Dye, S. Eales, D. Elbaz, D. Farrah, M. Fox, A. Franceschini, W. Gear, J. Glenn, M. Griffin, M. Halpern, E. Hatziminaoglou, E. Ibar, K. Isaak, R. J. Ivison, G. Lagache, L. Levenson, N. Lu, S. Madden, B. Maffei, G. Mainetti, L. Marchetti, H. T. Nguyen, B. O’Halloran, S. J. Oliver, A. Omont, P. Panuzzo, A. Papageorgiou, C. P. Pearson, I. Pérez-Fournon, M. Pohlen, J. I. Rawlings, D. Rigopoulou, L. Riguccini, D. Rizzo, G. Rodighiero, I. G. Roseboom, M. Rowan-Robinson, M. Sánchez Portal, B. Schulz, D. Scott, N. Seymour, D. L. Shupe, A. J. Smith, J. A. Stevens, M. Trichas, K. E. Tugwell, M. Vaccari, I. Valtchanov, M. Viero, L. Vigroux, L. Wang, R. Ward, G. Wright, C. K. Xu, and M. Zemcov. The suppression of star formation by powerful active galactic nuclei. *Nature*, 485(7397):213–216, May 2012.
- [215] Marie Martig, Alison F. Crocker, Frédéric Bournaud, Eric Emsellem, Jared M. Gabor, Katherine Alatalo, Leo Blitz, Maxime Bois, Martin Bureau, Michele Cappellari, Roger L. Davies, Timothy A. Davis, Avishai Dekel, P. T. de Zeeuw, Pierre-Alain Duc, Jesus Falcón-Barroso, Sadegh Khochfar, Davor Krajnović, Harald Kuntschner, Raffaella Morganti, Richard M. McDermid, Thorsten Naab, Tom Oosterloo, Marc Sarzi, Nicholas Scott, Paolo Serra, Kristen Shapiro Griffin, Romain Teyssier, Anne-Marie Weijmans, and Lisa M. Young. The ATLAS^{3D} project - XXII. Low-efficiency star formation in early-type galaxies: hydrodynamic models and observations. *MNRAS*, 432(3):1914–1927, July 2013.
- [216] S. F. Sánchez, R. García-Benito, S. Zibetti, C. J. Walcher, B. Husemann, M. A. Mendoza, L. Galbany, J. Falcón-Barroso, D. Mast, J. Aceituno, J. A. L. Aguerri, J. Alves,

- A. L. Amorim, Y. Ascasibar, D. Barrado-Navascues, J. Barrera-Ballesteros, S. Bekeraïtè, J. Bland-Hawthorn, M. Cano Díaz, R. Cid Fernandes, O. Cavichia, C. Cortijo, H. Dannerbauer, M. Demleitner, A. Díaz, R. J. Dettmar, A. de Lorenzo-Cáceres, A. del Olmo, A. Galazzi, B. García-Lorenzo, A. Gil de Paz, R. González Delgado, L. Holmes, J. Iglésias-Páramo, C. Kehrig, A. Kelz, R. C. Kennicutt, B. Kleemann, E. A. D. Lacerda, R. López Fernández, A. R. López Sánchez, M. Lyubenova, R. Marino, I. Márquez, J. Mendez-Abreu, M. Mollá, A. Monreal-Ibero, R. Ortega Minakata, J. P. Torres-Papaqui, E. Pérez, F. F. Rosales-Ortega, M. M. Roth, P. Sánchez-Blázquez, U. Schilling, K. Spekkens, N. Vale Asari, R. C. E. van den Bosch, G. van de Ven, J. M. Vilchez, V. Wild, L. Wisotzki, A. Yıldırım, and B. Ziegler. CALIFA, the Calar Alto Legacy Integral Field Area survey. IV. Third public data release. *A&A*, 594:A36, October 2016.
- [217] Donald G. York, J. Adelman, Jr. Anderson, John E., Scott F. Anderson, James Annis, Neta A. Bahcall, J. A. Bakken, Robert Barkhouser, Steven Bastian, Eileen Berman, William N. Boroski, Steve Bracker, Charlie Briegel, John W. Briggs, J. Brinkmann, Robert Brunner, Scott Burles, Larry Carey, Michael A. Carr, Francisco J. Castander, Bing Chen, Patrick L. Colestock, A. J. Connolly, J. H. Crocker, István Csabai, Paul C. Czarapata, John Eric Davis, Mamoru Doi, Tom Dombeck, Daniel Eisenstein, Nancy Ellman, Brian R. Elms, Michael L. Evans, Xiaohui Fan, Glenn R. Federwitz, Larry Fiscelli, Scott Friedman, Joshua A. Frieman, Masataka Fukugita, Bruce Gillespie, James E. Gunn, Vijay K. Gurbani, Ernst de Haas, Merle Haldeman, Frederick H. Harris, J. Hayes, Timothy M. Heckman, G. S. Hennessy, Robert B. Hindsley, Scott Holm, Donald J. Holmgren, Chi-hao Huang, Charles Hull, Don Husby, Shin-Ichi Ichikawa, Takashi Ichikawa, Željko Ivezić, Stephen Kent, Rita S. J. Kim, E. Kinney, Mark Klaene, A. N. Kleinman, S. Kleinman, G. R. Knapp, John Korienek, Richard G. Kron, Peter Z. Kunszt, D. Q. Lamb, B. Lee, R. French Leger, Siriluk Limmongkol, Carl Lindenmeyer, Daniel C. Long, Craig Loomis, Jon Loveday, Rich Lucinio, Robert H. Lupton, Bryan MacKinnon, Edward J. Mannery, P. M. Mantsch, Bruce Margon, Peregrine McGehee, Timothy A. McKay, Avery Meiksin, Aronne Merelli, David G. Monet, Jeffrey A. Munn, Vijay K. Narayanan, Thomas Nash, Eric Neilsen, Rich Neswold, Heidi Jo Newberg, R. C. Nichol, Tom Nicinski, Mario Nonino, Norio Okada, Sadanori Okamura, Jeremiah P. Ostriker, Russell Owen, A. George Pauls, John Peoples, R. L. Peterson, Donald Petravick, Jeffrey R. Pier, Adrian Pope, Ruth Pordes, Angela Prosapio, Ron Rechenmacher, Thomas R. Quinn, Gordon T. Richards, Michael W. Richmond, Claudio H. Rivetta, Constance M. Rockosi, Kurt Ruthmansdorfer, Dale Sandford, David J. Schlegel, Donald P. Schneider, Maki Sekiguchi, Gary Sergey, Kazuhiro Shimasaku, Walter A. Siegmund, Stephen Smee, J. Allyn Smith, S. Snedden, R. Stone, Chris Stoughton, Michael A. Strauss, Christopher Stubbs, Mark SubbaRao, Alexander S. Szalay, Istvan Szapudi, Gyula P. Szokoly, Anirudda R. Thakar, Christy Tremonti, Douglas L. Tucker, Alan Uomoto, Dan Vanden Berk, Michael S. Vogeley, Patrick Waddell, Shu-i. Wang, Masaru Watanabe, David H. Weinberg, Brian Yanny, Naoki Yasuda, and SDSS Collaboration. The Sloan Digital Sky Survey: Technical Summary. *AJ*, 120(3):1579–1587, September 2000.
- [218] Shadab Alam, Franco D. Albareti, Carlos Allende Prieto, F. Anders, Scott F. Anderson, Timothy Anderton, Brett H. Andrews, Eric Armengaud, Éric Aubourg, Stephen Bailey,

Sarbani Basu, Julian E. Bautista, Rachael L. Beaton, Timothy C. Beers, Chad F. Bender, Andreas A. Berlind, Florian Beutler, Vaishali Bhardwaj, Jonathan C. Bird, Dmitry Bizyaev, Cullen H. Blake, Michael R. Blanton, Michael Blomqvist, John J. Bochanski, Adam S. Bolton, Jo Bovy, A. Shelden Bradley, W. N. Brandt, D. E. Brauer, J. Brinkmann, Peter J. Brown, Joel R. Brownstein, Angela Burden, Etienne Burtin, Nicolás G. Busca, Zheng Cai, Diego Capozzi, Aurelio Carnero Rosell, Michael A. Carr, Ricardo Carrera, K. C. Chambers, William James Chaplin, Yen-Chi Chen, Cristina Chiappini, S. Drew Chojnowski, Chia-Hsun Chuang, Nicolas Clerc, Johan Comparat, Kevin Covey, Rupert A. C. Croft, Antonio J. Cuesta, Katia Cunha, Luiz N. da Costa, Nicola Da Rio, James R. A. Davenport, Kyle S. Dawson, Nathan De Lee, Timothée Delubac, Rohit Deshpande, Saurav Dhital, Letícia Dutra-Ferreira, Tom Dwelly, Anne Ealet, Garrett L. Ebelke, Edward M. Edmondson, Daniel J. Eisenstein, Tristan Ellsworth, Yvonne Elsworth, Courtney R. Epstein, Michael Eracleous, Stephanie Escoffier, Massimiliano Esposito, Michael L. Evans, Xiaohui Fan, Emma Fernández-Alvar, Diane Feuillet, Nurten Filiz Ak, Hayley Finley, Alexis Finoguenov, Kevin Flaherty, Scott W. Fleming, Andreu Font-Ribera, Jonathan Foster, Peter M. Frinchaboy, J. G. Galbraith-Frew, Rafael A. García, D. A. García-Hernández, Ana E. García Pérez, Patrick Gaulme, Jian Ge, R. Génova-Santos, A. Georgakakis, Luan Ghezzi, Bruce A. Gillespie, Léo Girardi, Daniel Goddard, Satya Gontcho A. Gontcho, Jonay I. González Hernández, Eva K. Grebel, Paul J. Green, Jan Niklas Grieb, Nolan Grieves, James E. Gunn, Hong Guo, Paul Harding, Sten Hasselquist, Suzanne L. Hawley, Michael Hayden, Fred R. Hearty, Saskia Hekker, Shirley Ho, David W. Hogg, Kelly Holley-Bockelmann, Jon A. Holtzman, Klaus Honscheid, Daniel Huber, Joseph Huehnerhoff, Inese I. Ivans, Linhua Jiang, Jennifer A. Johnson, Karen Kinemuchi, David Kirkby, Francisco Kitaura, Mark A. Klaene, Gillian R. Knapp, Jean-Paul Kneib, Xavier P. Koenig, Charles R. Lam, Ting-Wen Lan, Dustin Lang, Pierre Laurent, Jean-Marc Le Goff, Alexie Leauthaud, Khee-Gan Lee, Young Sun Lee, Timothy C. Licquia, Jian Liu, Daniel C. Long, Martín López-Corredoira, Diego Lorenzo-Oliveira, Sara Lucatello, Britt Lundgren, Robert H. Lupton, III Mack, Claude E., Suvrath Mahadevan, Marcio A. G. Maia, Steven R. Majewski, Elena Malanushenko, Viktor Malanushenko, A. Manchado, Marc Manera, Qingqing Mao, Claudia Maraston, Robert C. Marchwinski, Daniel Margala, Sarah L. Martell, Marie Martig, Karen L. Masters, Savita Mathur, Cameron K. McBride, Peregrine M. McGehee, Ian D. McGreer, Richard G. McMahon, Brice Ménard, Marie-Luise Menzel, Andrea Merloni, Szabolcs Mészáros, Adam A. Miller, Jordi Miralda-Escudé, Hironao Miyatake, Antonio D. Montero-Dorta, Surhud More, Eric Morganson, Xan Morice-Atkinson, Heather L. Morrison, Benoit Mosser, Demitri Muna, Adam D. Myers, Kirpal Nandra, Jeffrey A. Newman, Mark Neyrinck, Duy Cuong Nguyen, Robert C. Nichol, David L. Nidever, Pasquier Noterdaeme, Sebastián E. Nuza, Julia E. O'Connell, Robert W. O'Connell, Ross O'Connell, Ricardo L. C. Ogando, Matthew D. Olmstead, Audrey E. Oravetz, Daniel J. Oravetz, Keisuke Osumi, Russell Owen, Deborah L. Padgett, Nikhil Padmanabhan, Martin Paegert, Nathalie Palanque-Delabrouille, Kaike Pan, John K. Parejko, Isabelle Pâris, Changbom Park, Petchara Pattarakijwanich, M. Pellejero-Ibanez, Joshua Pepper, Will J. Percival, Ismael Pérez-Fournon, Ignasi Pérez-Ràfols, Patrick Petitjean, Matthew M. Pieri, Marc H. Pinsonneault, Gustavo F. Porto de Mello, Francisco Prada, Abhishek Prakash, Adrian M. Price-Whelan, Pavlos Protopapas, M. Jordan Raddick, Mubdi Rahman, Beth A. Reid, James Rich, Hans-Walter Rix, Annie C. Robin, Con-

- stance M. Rockosi, Tháise S. Rodrigues, Sergio Rodríguez-Torres, Natalie A. Roe, Ashley J. Ross, Nicholas P. Ross, Graziano Rossi, John J. Ruan, J. A. Rubiño-Martín, Eli S. Rykoff, Salvador Salazar-Albornoz, Mara Salvato, Lado Samushia, Ariel G. Sánchez, Basilio Santiago, Conor Sayres, Ricardo P. Schiavon, David J. Schlegel, Sarah J. Schmidt, Donald P. Schneider, Mathias Schultheis, Axel D. Schwoppe, C. G. Scóccola, Caroline Scott, Kris Sellgren, Hee-Jong Seo, Aldo Serenelli, Neville Shane, Yue Shen, Matthew Shetrone, Yiping Shu, V. Silva Aguirre, Thirupathi Sivarani, M. F. Skrutskie, Anže Slosar, Verne V. Smith, Flávia Sobreira, Diogo Souto, Keivan G. Stassun, Matthias Steinmetz, Dennis Stello, Michael A. Strauss, Alina Streblyanska, Nao Suzuki, Molly E. C. Swanson, Jonathan C. Tan, Jamie Tayar, Ryan C. Terrien, Aniruddha R. Thakar, Daniel Thomas, Neil Thomas, Benjamin A. Thompson, Jeremy L. Tinker, Rita Tojeiro, Nicholas W. Troup, Mariana Vargas-Magaña, Jose A. Vazquez, Licia Verde, Matteo Viel, Nicole P. Vogt, David A. Wake, Ji Wang, Benjamin A. Weaver, David H. Weinberg, Benjamin J. Weiner, Martin White, John C. Wilson, John P. Wisniewski, W. M. Wood-Vasey, Christophe Ye'che, Donald G. York, Nadia L. Zakamska, O. Zamora, Gail Zasowski, Idit Zehavi, Gong-Bo Zhao, Zheng Zheng, Xu Zhou, Zhimin Zhou, Hu Zou, and Guangtun Zhu. The Eleventh and Twelfth Data Releases of the Sloan Digital Sky Survey: Final Data from SDSS-III. *ApJ*, 219(1):12, July 2015.
- [219] Todd R. Hunter, Remy Indebetouw, Crystal L. Brogan, Kristin Berry, Chin-Shin Chang, Harold Francke, Vincent C. Geers, Laura Gómez, John E. Hibbard, Elizabeth M. Humphreys, Brian R. Kent, Amanda A. Kepley, Devaky Kunneriath, Andrew Lipnicky, Ryan A. Loomis, Brian S. Mason, Joseph S. Masters, Luke T. Maud, Dirk Muders, Jose Sabater, Kanako Sugimoto, László Szűcs, Eugene Vasiliev, Liza Videla, Eric Villard, Stewart J. Williams, Rui Xue, and Ilsang Yoon. The ALMA Interferometric Pipeline Heuristics. *arXiv e-prints*, page arXiv:2306.07420, June 2023.
- [220] Adam K. Leroy, Annie Hughes, Daizhong Liu, Jérôme Pety, Erik Rosolowsky, Toshiki Saito, Eva Schinnerer, Andreas Schrubba, Antonio Usero, Christopher M. Faesi, Cinthya N. Herrera, Mélanie Chevance, Alexander P. S. Hygate, Amanda A. Kepley, Eric W. Koch, Miguel Querejeta, Kazimierz Sliwa, David Will, Christine D. Wilson, Gagandeep S. Anand, Ashley Barnes, Francesco Belfiore, Ivana Bešlić, Frank Bigiel, Guillermo A. Blanc, Alberto D. Bolatto, Mèdèric Boquien, Yixian Cao, Rupali Chandar, Jérémy Chastenet, I-Da Chiang, Enrico Congiu, Daniel A. Dale, Sinan Deger, Jakob S. den Brok, Cosima Eibensteiner, Eric Emsellem, Axel García-Rodríguez, Simon C. O. Glover, Kathryn Grasha, Brent Groves, Jonathan D. Henshaw, María J. Jiménez Donaire, Jaeyeon Kim, Ralf S. Klessen, Kathryn Kreckel, J. M. Diederik Kruijssen, Kirsten L. Larson, Janice C. Lee, Ness Mayker, Rebecca McElroy, Sharon E. Meidt, Angus Mok, Hsi-An Pan, Johannes Puschignig, Alessandro Razza, Patricia Sánchez-BI'azquez, Karin M. Sandstrom, Francesco Santoro, Amy Sardone, Fabian Scheuermann, Jiayi Sun, David A. Thilker, Jordan A. Turner, Leonardo Ubeda, Dyas Utomo, Elizabeth J. Watkins, and Thomas G. Williams. PHANGS-ALMA Data Processing and Pipeline. *ApJ*, 255(1):19, July 2021.
- [221] CASA Team, Ben Bean, Sanjay Bhatnagar, Sandra Castro, Jennifer Donovan Meyer, Bjorn Emonts, Enrique Garcia, Robert Garwood, Kumar Golap, Justo Gonzalez Villalba, Pamela Harris, Yohei Hayashi, Josh Hoskins, Mingyu Hsieh, Preshanth Jagannathan, Wataru

- Kawasaki, Aard Keimpema, Mark Kettenis, Jorge Lopez, Joshua Marvil, Joseph Masters, Andrew McNichols, David Mehringer, Renaud Miel, George Moellenbrock, Federico Montesino, Takeshi Nakazato, Juergen Ott, Dirk Petry, Martin Pokorny, Ryan Raba, Urvasi Rau, Darrell Schiebel, Neal Schweighart, Srikrishna Sekhar, Kazuhiko Shimada, Des Small, Jan-Willem Steeb, Kanako Sugimoto, Ville Suoranta, Takahiro Tsutsumi, Ilse M. van Bommel, Marjolein Verkouter, Akeem Wells, Wei Xiong, Arpad Szomoru, Morgan Griffith, Brian Glendenning, and Jeff Kern. CASA, the Common Astronomy Software Applications for Radio Astronomy. *PASA*, 134(1041):114501, November 2022.
- [222] Daniel Shenon Briggs. *High fidelity deconvolution of moderately resolved sources*. PhD thesis, New Mexico Institute of Mining and Technology, January 1995.
- [223] Erik Rosolowsky and Adam Leroy. Bias-free Measurement of Giant Molecular Cloud Properties. *PASA*, 118(842):590–610, April 2006.
- [224] L. Bottinelli, L. Gouguenheim, and G. Paturel. HI line studies of galaxies. I - General catalogue of 21-cm line data. , 47:171–192, January 1982.
- [225] L. Bottinelli, L. Gouguenheim, P. Fouque, and G. Paturel. An extragalactic data base II. The HI data. , 82:391–488, March 1990.
- [226] S. F. Sánchez, J. K. Barrera-Ballesteros, L. Sánchez-Menguiano, C. J. Walcher, R. A. Marino, L. Galbany, J. Bland-Hawthorn, M. Cano-Díaz, R. García-Benito, C. López-Cobá, S. Zibetti, J. M. Vilchez, J. Iglésias-Páramo, C. Kehrig, A. R. López Sánchez, S. Duarte Puertas, and B. Ziegler. The mass-metallicity relation revisited with CALIFA. *MNRAS*, 469(2):2121–2140, August 2017.
- [227] J. S. den Brok, D. Chatzigiannakis, F. Bigiel, J. Puschnig, A. T. Barnes, A. K. Leroy, M. J. Jiménez-Donaire, A. Usero, E. Schinnerer, E. Rosolowsky, C. M. Faesi, K. Grasha, A. Hughes, J. M. D. Kruijssen, D. Liu, L. Neumann, J. Pety, M. Querejeta, T. Saito, A. Schruba, and S. Stuber. New constraints on the $^{12}\text{CO}(2-1)/(1-0)$ line ratio across nearby disc galaxies. *MNRAS*, 504(3):3221–3245, July 2021.
- [228] J. Méndez-Abreu, T. Ruiz-Lara, L. Sánchez-Menguiano, A. de Lorenzo-Cáceres, L. Costantin, C. Catalán-Torrecilla, E. Florido, J. A. L. Aguerri, J. Bland-Hawthorn, E. M. Corsini, R. J. Dettmar, L. Galbany, R. García-Benito, R. A. Marino, I. Márquez, R. A. Ortega-Minakata, P. Papaderos, S. F. Sánchez, P. Sánchez-Blazquez, K. Spekkens, G. van de Ven, V. Wild, and B. Ziegler. Two-dimensional multi-component photometric decomposition of CALIFA galaxies. *A&A*, 598:A32, February 2017.
- [229] M. Querejeta, E. Schinnerer, S. Meidt, J. Sun, A. K. Leroy, E. Emsellem, R. S. Klessen, J. C. Muñoz-Mateos, H. Salo, E. Laurikainen, I. Bešlić, G. A. Blanc, M. Chevance, D. A. Dale, C. Eibensteiner, C. Faesi, A. García-Rodríguez, S. C. O. Glover, K. Grasha, J. Henshaw, C. Herrera, A. Hughes, K. Kreckel, J. M. D. Kruijssen, D. Liu, E. J. Murphy, H. A. Pan, J. Pety, A. Razza, E. Rosolowsky, T. Saito, A. Schruba, A. Usero, E. J. Watkins, and T. G. Williams. Stellar structures, molecular gas, and star formation across the PHANGS sample of nearby galaxies. *A&A*, 656:A133, December 2021.

- [230] J. Trevor Mendel, Luc Simard, Michael Palmer, Sara L. Ellison, and David R. Patton. A catalog of bulge, disk, and total stellar mass estimates for the sloan digital sky survey. *The Astrophysical Journal Supplement Series*, 210(1):3, dec 2013.
- [231] Luc Simard, J. Trevor Mendel, David R. Patton, Sara L. Ellison, and Alan W. McConnachie. A catalog of bulge+disk decompositions and updated photometry for 1.12 million galaxies in the sloan digital sky survey. *The Astrophysical Journal Supplement Series*, 196(1):11, aug 2011.
- [232] Luc Simard, Christopher N. A. Willmer, Nicole P. Vogt, Vicki L. Sarajedini, Andrew C. Phillips, Benjamin J. Weiner, David C. Koo, Myungshin Im, Garth D. Illingworth, and S. M. Faber. The DEEP Groth Strip Survey. II. Hubble Space Telescope Structural Parameters of Galaxies in the Groth Strip. *ApJ*, 142(1):1–33, September 2002.
- [233] Jose Luis Sersic. *Atlas de Galaxias Australes*. 1968.
- [234] J. Méndez-Abreu, J. A. L. Aguerri, E. M. Corsini, and E. Simonneau. Structural properties of disk galaxies: The intrinsic equatorial ellipticity of bulges. *arXiv e-prints*, page arXiv:0802.0010, January 2008.
- [235] J. Méndez-Abreu, V. P. Debattista, E. M. Corsini, and J. A. L. Aguerri. Secular- and merger-built bulges in barred galaxies. *A&A*, 572:A25, December 2014.
- [236] Kevin Schawinski, C. Megan Urry, Brooke D. Simmons, Lucy Fortson, Sugata Kaviraj, William C. Keel, Chris J. Lintott, Karen L. Masters, Robert C. Nichol, Marc Sarzi, Ramin Skibba, Ezequiel Treister, Kyle W. Willett, O. Ivy Wong, and Sukyoung K. Yi. The green valley is a red herring: Galaxy Zoo reveals two evolutionary pathways towards quenching of star formation in early- and late-type galaxies. *MNRAS*, 440(1):889–907, May 2014.
- [237] Yu-Yen Chang, Arjen van der Wel, Elisabete da Cunha, and Hans-Walter Rix. Stellar Masses and Star Formation Rates for 1M Galaxies from SDSS+WISE. *ApJ*, 219(1):8, July 2015.
- [238] Joss Bland-Hawthorn and Ortwin Gerhard. The Galaxy in Context: Structural, Kinematic, and Integrated Properties. *ARA&A*, 54:529–596, September 2016.
- [239] S. F. Sánchez, V. Avila-Reese, H. Hernandez-Toledo, E. Cortes-Suárez, A. Rodríguez-Puebla, H. Ibarra-Medel, M. Cano-Díaz, J. K. Barrera-Ballesteros, C. A. Negrete, A. R. Calette, A. de Lorenzo-Cáceres, R. A. Ortega-Minakata, E. Aquino, O. Valenzuela, J. C. Clemente, T. Storchi-Bergmann, R. Riffel, J. Schimoia, R. A. Riffel, S. B. Rembold, J. R. Brownstein, K. Pan, R. Yates, N. Mallmann, and T. Bitsakis. SDSS IV MaNGA - Properties of AGN Host Galaxies. , 54:217–260, April 2018.
- [240] S. F. Sánchez, C. J. Walcher, C. Lopez-Cobá, J. K. Barrera-Ballesteros, A. Mejía-Narváez, C. Espinosa-Ponce, and A. Camps-Fariña. From Global to Spatially Resolved in Low-Redshift Galaxies. , 57:3–38, April 2021.
- [241] A. Boselli, L. Cortese, and M. Boquien. Cold gas properties of the Herschel Reference Survey. I. $^{12}\text{CO}(1-0)$ and HI data. *A&A*, 564:A65, April 2014.

- [242] Sara L. Ellison, Lihwai Lin, Mallory D. Thorp, Hsi-An Pan, Jillian M. Scudder, Sebastian F. Sánchez, Asa F. L. Bluck, and Roberto Maiolino. The ALMaQUEST Survey - V. The non-universality of kpc-scale star formation relations and the factors that drive them. *MNRAS*, 501(4):4777–4797, March 2021.
- [243] Sebastián F. Sánchez, Daysi C. Gómez Medina, J. K. Barrera-Ballesteros, L. Galbany, A. Bolatto, and T. Wong. The local and global relations between Σ_* , Σ_{SFR} and Σ_{mol} that regulate star-formation. *IAU Symposium*, 373:3–10, January 2023.
- [244] Lihwai Lin, Sara L. Ellison, Hsi-An Pan, Mallory D. Thorp, Yung-Chau Su, Sebastián F. Sánchez, Francesco Belfiore, M. S. Bothwell, Kevin Bundy, Yan-Mei Chen, Alice Concas, Bau-Ching Hsieh, Pei-Ying Hsieh, Cheng Li, Roberto Maiolino, Karen Masters, Jeffrey A. Newman, Kate Rowlands, Yong Shi, Rebecca Smethurst, David V. Stark, Ting Xiao, and Po-Chieh Yu. ALMaQUEST. IV. The ALMA-MaNGA QUEnching and STar Formation (ALMaQUEST) Survey. *ApJ*, 903(2):145, November 2020.
- [245] S. F. Sánchez, C. J. Walcher, C. Lopez-Cobá, J. K. Barrera-Ballesteros, A. Mejía-Narváez, C. Espinosa-Ponce, and A. Camps-Fariña. From Global to Spatially Resolved in Low-Redshift Galaxies. , 57:3–38, April 2021.
- [246] Jiayi Sun, Adam K. Leroy, Eve C. Ostriker, Sharon Meidt, Erik Rosolowsky, Eva Schinnerer, Christine D. Wilson, Dyas Utomo, Francesco Belfiore, Guillermo A. Blanc, Eric Emsellem, Christopher Faesi, Brent Groves, Annie Hughes, Eric W. Koch, Kathryn Kreckel, Daizhong Liu, Hsi-An Pan, Jérôme Pety, Miguel Querejeta, Alessandro Razza, Toshiki Saito, Amy Sardone, Antonio Usero, Thomas G. Williams, Frank Bigiel, Alberto D. Bolatto, Mélanie Chevance, Daniel A. Dale, Jindra Gensior, Simon C. O. Glover, Kathryn Grasha, Jonathan D. Henshaw, María J. Jiménez-Donaire, Ralf S. Klessen, J. M. Diederik Kruijssen, Eric J. Murphy, Lukas Neumann, Yu-Hsuan Teng, and David A. Thilker. Star Formation Laws and Efficiencies across 80 Nearby Galaxies. *ApJL*, 945(2):L19, March 2023.
- [247] L. J. Kewley, M. A. Dopita, R. S. Sutherland, C. A. Heisler, and J. Trevena. Theoretical Modeling of Starburst Galaxies. *ApJ*, 556(1):121–140, July 2001.
- [248] Sara L. Ellison, Tony Wong, Sebastian F. Sánchez, Dario Colombo, Alberto Bolatto, Jorge Barrera-Ballesteros, Rubén García-Benito, Veselina Kalinova, Yufeng Luo, Monica Rubio, and Stuart N. Vogel. The EDGE-CALIFA survey: central molecular gas depletion in AGN host galaxies - a smoking gun for quenching? *MNRAS*, 505(1):L46–L51, July 2021.
- [249] C. Catalán-Torrecilla, A. Gil de Paz, A. Castillo-Morales, J. Méndez-Abreu, J. Falcón-Barroso, S. Bekeraite, L. Costantin, A. de Lorenzo-Cáceres, E. Florido, R. García-Benito, B. Husemann, J. Iglesias-Páramo, R. C. Kennicutt, D. Mast, S. Pascual, T. Ruiz-Lara, L. Sánchez-Menguiano, S. F. Sánchez, C. J. Walcher, J. Bland-Hawthorn, S. Duarte Puer-tas, R. A. Marino, J. Masegosa, P. Sánchez-Blázquez, and CALIFA Collaboration. Star Formation in the Local Universe from the CALIFA Sample. II. Activation and Quenching Mechanisms in Bulges, Bars, and Disks. *ApJ*, 848(2):87, October 2017.

- [250] Stephen Eales, Oliver Eales, and Pieter de Vis. Do bulges stop stars forming? *MNRAS*, 491(1):69–79, January 2020.
- [251] Luis C. Ho, Jeremy Darling, and Jenny E. Greene. Properties of Active Galaxies Deduced from H I Observations. *ApJ*, 681(1):128–140, July 2008.
- [252] Silvia Fabello, Guinevere Kauffmann, Barbara Catinella, Riccardo Giovanelli, Martha P. Haynes, Timothy M. Heckman, and David Schiminovich. Arecibo Legacy Fast ALFA H I data stacking - II. H I content of the host galaxies of active galactic nuclei. *MNRAS*, 416(3):1739–1744, September 2011.
- [253] Sara L. Ellison, Toby Brown, Barbara Catinella, and Luca Cortese. Atomic gas fractions in active galactic nucleus host galaxies. *MNRAS*, 482(4):5694–5703, February 2019.
- [254] R. Maiolino, M. Ruiz, G. H. Rieke, and P. Papadopoulos. Molecular Gas, Morphology, and Seyfert Galaxy Activity. *ApJ*, 485(2):552–569, August 1997.
- [255] Michael J. Koss, Benjamin Strittmatter, Isabella Lamperti, Taro Shimizu, Benny Trakhtenbrot, Amelie Saintonge, Ezequiel Treister, Claudia Cicone, Richard Mushotzky, Kyuseok Oh, Claudio Ricci, Daniel Stern, Tonima Tasnim Ananna, Franz E. Bauer, George C. Privon, Rudolf E. Bär, Carlos De Breuck, Fiona Harrison, Kohei Ichikawa, Meredith C. Powell, David Rosario, David B. Sanders, Kevin Schawinski, Li Shao, C. Megan Urry, and Sylvain Veilleux. BAT AGN Spectroscopic Survey. XX. Molecular Gas in Nearby Hard-X-Ray-selected AGN Galaxies. *ApJ*, 252(2):29, February 2021.
- [256] Federico Esposito, Livia Vallini, Francesca Pozzi, Viviana Casasola, Matilde Mingozzi, Cristian Vignali, Carlotta Gruppioni, and Francesco Salvestrini. AGN impact on the molecular gas in galactic centres as probed by CO lines. *MNRAS*, 512(1):686–711, May 2022.
- [257] Sara L. Ellison, Hossen Teimoorinia, David J. Rosario, and J. Trevor Mendel. The star formation rates of active galactic nuclei host galaxies. *MNRAS*, 458(1):L34–L38, May 2016.
- [258] Sara L. Ellison, Sebastian F. Sánchez, Hector Ibarra-Medel, Braulio Antonio, J. Trevor Mendel, and Jorge Barrera-Ballesteros. Star formation is boosted (and quenched) from the inside-out: radial star formation profiles from MaNGA. *MNRAS*, 474(2):2039–2054, February 2018.
- [259] S. Veilleux, P. L. Shopbell, D. S. Rupke, J. Bland-Hawthorn, and G. Cecil. A Search for Very Extended Ionized Gas in Nearby Starburst and Active Galaxies. *AJ*, 126(5):2185–2208, November 2003.
- [260] B. Husemann, L. Wisotzki, S. F. Sánchez, and K. Jahnke. Extended emission-line regions in low-redshift quasars. Dependence on nuclear spectral properties. *A&A*, 488(1):145–149, September 2008.

- [261] N. P. H. Nesvadba, M. Polletta, M. D. Lehnert, J. Bergeron, C. De Breuck, G. Lagache, and A. Omont. The dynamics of the ionized and molecular interstellar medium in powerful obscured quasars at $z \geq 3.5$. *MNRAS*, 415(3):2359–2372, August 2011.
- [262] Jindra Gensior and J. M. Diederik Kruijssen. The elephant in the bathtub: when the physics of star formation regulate the baryon cycle of galaxies. *MNRAS*, 500(2):2000–2011, January 2021.
- [263] B. Vollmer and R. I. Davies. The quenching of star formation in accretion-driven clumpy turbulent tori of active galactic nuclei. *A&A*, 556:A31, August 2013.
- [264] J. K. Barrera-Ballesteros, B. García-Lorenzo, J. Falcón-Barroso, G. van de Ven, M. Lyubenova, V. Wild, J. Méndez-Abreu, S. F. Sánchez, I. Marquez, J. Masegosa, A. Monreal-Ibero, B. Ziegler, A. del Olmo, L. Verdes-Montenegro, R. García-Benito, B. Husemann, D. Mast, C. Kehrig, J. Iglesias-Paramo, R. A. Marino, J. A. L. Aguerri, C. J. Walcher, J. M. Vílchez, D. J. Bomans, C. Cortijo-Ferrero, R. M. González Delgado, J. Bland-Hawthorn, D. H. McIntosh, and S. Bekeraité. Tracing kinematic (mis)alignments in CALIFA merging galaxies. Stellar and ionized gas kinematic orientations at every merger stage. *A&A*, 582:A21, October 2015.
- [265] Astropy Collaboration, A. M. Price-Whelan, B. M. Sipőcz, H. M. Günther, P. L. Lim, S. M. Crawford, S. Conseil, D. L. Shupe, M. W. Craig, N. Dencheva, A. Ginsburg, J. T. VanderPlas, L. D. Bradley, D. Pérez-Suárez, M. de Val-Borro, T. L. Aldcroft, K. L. Cruz, T. P. Robitaille, E. J. Tollerud, C. Ardelean, T. Babej, Y. P. Bach, M. Bachetti, A. V. Bakanov, S. P. Bamford, G. Barentsen, P. Barmby, A. Baumbach, K. L. Berry, F. Biscani, M. Boquien, K. A. Bostroem, L. G. Bouma, G. B. Brammer, E. M. Bray, H. Breytenbach, H. Buddelmeijer, D. J. Burke, G. Calderone, J. L. Cano Rodríguez, M. Cara, J. V. M. Cardoso, S. Cheedella, Y. Copin, L. Corrales, D. Crichton, D. D’Avella, C. Deil, É. Depagne, J. P. Dietrich, A. Donath, M. Droettboom, N. Earl, T. Erben, S. Fabbro, L. A. Ferreira, T. Finethy, R. T. Fox, L. H. Garrison, S. L. J. Gibbons, D. A. Goldstein, R. Gommers, J. P. Greco, P. Greenfield, A. M. Groener, F. Grollier, A. Hagen, P. Hirst, D. Homeier, A. J. Horton, G. Hosseinzadeh, L. Hu, J. S. Hunkeler, Ž. Ivezić, A. Jain, T. Jenness, G. Kanarek, S. Kendrew, N. S. Kern, W. E. Kerzendorf, A. Khvalko, J. King, D. Kirkby, A. M. Kulkarni, A. Kumar, A. Lee, D. Lenz, S. P. Littlefair, Z. Ma, D. M. Macleod, M. Mastropietro, C. McCully, S. Montagnac, B. M. Morris, M. Mueller, S. J. Mumford, D. Muna, N. A. Murphy, S. Nelson, G. H. Nguyen, J. P. Ninan, M. Nöthe, S. Ogaz, S. Oh, J. K. Parejko, N. Parley, S. Pascual, R. Patil, A. A. Patil, A. L. Plunkett, J. X. Prochaska, T. Rastogi, V. Reddy Janga, J. Sabater, P. Sakurikar, M. Seifert, L. E. Sherbert, H. Sherwood-Taylor, A. Y. Shih, J. Sick, M. T. Silbiger, S. Singanamalla, L. P. Singer, P. H. Sladen, K. A. Sooley, S. Sornarajah, O. Streicher, P. Teuben, S. W. Thomas, G. R. Tremblay, J. E. H. Turner, V. Terrón, M. H. van Kerkwijk, A. de la Vega, L. L. Watkins, B. A. Weaver, J. B. Whitmore, J. Woillez, V. Zabalza, and Astropy Contributors. The Astropy Project: Building an Open-science Project and Status of the v2.0 Core Package. *AJ*, 156(3):123, September 2018.
- [266] J. P. McMullin, B. Waters, D. Schiebel, W. Young, and K. Golap. CASA Architecture and Applications. In R. A. Shaw, F. Hill, and D. J. Bell, editors, *Astronomical Data Analysis*

Software and Systems XVI, volume 376 of *Astronomical Society of the Pacific Conference Series*, page 127, October 2007.

- [267] Charles R. Harris, K. Jarrod Millman, Stéfan J. van der Walt, Ralf Gommers, Pauli Virtanen, David Cournapeau, Eric Wieser, Julian Taylor, Sebastian Berg, Nathaniel J. Smith, Robert Kern, Matti Picus, Stephan Hoyer, Marten H. van Kerkwijk, Matthew Brett, Allan Haldane, Jaime Fernández del Río, Mark Wiebe, Pearu Peterson, Pierre Gérard-Marchant, Kevin Sheppard, Tyler Reddy, Warren Weckesser, Hameer Abbasi, Christoph Gohlke, and Travis E. Oliphant. Array programming with NumPy. *Nature*, 585(7825):357–362, September 2020.
- [268] F. Pedregosa, G. Varoquaux, A. Gramfort, V. Michel, B. Thirion, O. Grisel, M. Blondel, P. Prettenhofer, R. Weiss, V. Dubourg, J. Vanderplas, A. Passos, D. Cournapeau, M. Brucher, M. Perrot, and E. Duchesnay. Scikit-learn: Machine learning in Python. *Journal of Machine Learning Research*, 12:2825–2830, 2011.
- [269] Pauli Virtanen, Ralf Gommers, Travis E. Oliphant, Matt Haberland, Tyler Reddy, David Cournapeau, Evgeni Burovski, Pearu Peterson, Warren Weckesser, Jonathan Bright, Stéfan J. van der Walt, Matthew Brett, Joshua Wilson, K. Jarrod Millman, Nikolay Mayorov, Andrew R. J. Nelson, Eric Jones, Robert Kern, Eric Larson, C J Carey, İlhan Polat, Yu Feng, Eric W. Moore, Jake VanderPlas, Denis Laxalde, Josef Perktold, Robert Cimrman, Ian Henriksen, E. A. Quintero, Charles R. Harris, Anne M. Archibald, Antônio H. Ribeiro, Fabian Pedregosa, Paul van Mulbregt, and SciPy 1.0 Contributors. SciPy 1.0: Fundamental Algorithms for Scientific Computing in Python. *Nature Methods*, 17:261–272, 2020.
- [270] Michael L. Waskom. seaborn: statistical data visualization. *Journal of Open Source Software*, 6(60):3021, 2021.